Cosmology on the Edge of Λ-Cold Dark Matter

José Luis Bernal

Tesis Doctoral

Cosmology on the Edge of Λ-Cold Dark Matter

Memoria presentada por José Luis Bernal para optar al grado de Doctor por la Universitat de Barcelona

Programa de doctorado en Física

Directora	Tutor	Doctorando
Dra. Licia Verde	Dr. Alberto Manrique	José Luis Bernal

Barcelona, 2019

Cosmology on the Edge of Λ-Cold Dark Matter

José Luis Bernal

Acknowledgements

First and foremost, I would like to express my most sincere gratitude to my Ph.D advisor, Licia Verde for all her help, teachings and support during these years. She has always been an example to follow, and only through the freedom she gave me and the trust she placed on me I have been able to develop as a scientist the way I did.

I would also like to particularly thank other two mentors I had during my doctorate: Antonio J. Cuesta, who guided me through the first steps of my career; and Alvise Raccanelli, who taught me how fun it can be to be curious and embrace new projects to end up being as eclectic as possible. I extend also this gratitude to all my scientific collaborators, especially to John A. Peacock and Marc Kamionkowski, for welcoming me on their research groups in the University of Edinburgh and Johns Hopkins University in Baltimore, respectively.

I would like to thank all the members of Licia Verde's group I have coincided with, especially my fellow doctoral student Nicola Bellomo, who has traveled this path with me almost from its very beginning, and started with me that adventure that the ICC PhD meetings have been, but also Raúl Jiménez, Emilio Bellini, Fergus Simpson, Benedict Kalus, David Valcin, Katie Short, Héctor Gil-Marín, Ali Rida Khalife, Samuel Brieden, Davide Bianchi, and Ilia Musco. I learned so much while having lots of fun from every discussion we had.

I thank the secretary units both at the department pf the Universitat de Barcelona and at the Institut de Ciències del Cosmos, especially José Ramón Rodríguez, for being so helpful whenever I had an administrative process to deal with. I thank the Spanish Ministerio de Economía y Competitividad for his financial support.

A huge thanks to all my friends, for anchoring me to reality when physics and the doctorate became science fiction.

Y finalmente:

a mi familia, por su ánimo y apoyo durante todo el doctorado,

e por suposto á miña compañeira, por cada paso e cada voo.

Abstract

The successful standard model of cosmology, Λ-Cold Dark Matter (ΛCDM), is supported by a massive amount of extremely precise observations, which it is able to reproduce with great accuracy. Nonetheless, ΛCDM is a phenomenological model which does not answer some of the most fundamental questions about the Universe, such as the nature of dark matter or dark energy. Moreover, when this model is used to interpret the observations, there are some persistent tensions between independent experiments that, in the case of being free of unaccounted-for systematics, would require a different model in order to be solved.

This doctoral thesis collects both published and on going research addressing these issues. Concretely, three main different topics are covered: the tension on the Hubble constant between the direct measurements using the distance ladder and the inferred value obtained from observations of the Planck collaboration when ΛCDM is assumed; the role of primordial black holes as seeds of the supermassive black holes, or as candidates for being a significant fraction of the dark matter; and the potential of radio-continuum surveys and intensity mapping experiments, with the corresponding optimal strategies to probe ΛCDM and constrain deviations from it.

Therefore, the work collected here aims to investigate both the tensions of ΛCDM and the questions left unanswered in a critical way, from an agnostic point of view. In addition, it intends to set the basis for future research on these lines when more precise observations become available, and contribute to future tests of the standard model of cosmology in regimes that have not been probed so far.

Resumen

La cosmología es la disciplina científica que estudia el Universo como un todo, con el fin de entender su origen, composición y evolución. Por tanto, esta ciencia involucra el estudio de procesos físicos a todas las escalas, yendo desde la física de partículas hasta la distribución de materia en las escalas más grandes del Universo. Actualmente, la cosmología está viviendo un momento de esplendor, pues en las últimas décadas ha pasado de ser una disciplina principalmente teórica, sin observaciones con las que contrastar los modelos, a tener acceso a una cantidad ingente de observaciones. Esto ha permitido realizar medidas con una precisión imprecedente, dando paso a lo que se conoce como 'cosmología de precisión'.

Este gran esfuerzo observacional ha confirmado y promovido también la cosmología teórica, aumentando de manera significativa nuestro conocimiento sobre el cosmos en todas las fases de su evolución. Todo este conocimiento ha sido recogido en lo que se conoce como el modelo cosmológico estándar, ΛCDM (Λ + materia oscura fría, por sus siglas en inglés). Este modelo se basa en la teoría del Big Bang, asumiendo que la Relatividad General es una descripción correcta de la gravedad a todas las escalas, y determina que la materia oscura fría (materia no relativista que interacciona con el resto del Universo únicamente de manera gravitacional) conforma la mayor parte de la materia existente en el Universo. Además, describe la expansión acelerada del Universo en sus últimos estadíos de evolución con una constante cosmológica.

ΛCDM reproduce con éxito la gran mayoría de las observaciones. Sin embargo, todavía hay ciertas discrepancias entre experimentos que, de confirmarse que no están producidas por errores sistemáticos en las medidas, serían una prueba irrefutable de la necesidad de otro modelo cosmológico. En cualquier caso, existe una diferencia entre modelizar y entender, y ΛCDM es un modelo fenomenológico. Como tal, deja sin responder muchas preguntas acerca de la naturaleza del Universo. Por ejemplo, no incluye una descripción microscópica de qué genera la expansión acelerada del Universo, o sobre la naturaleza de la materia oscura.

Esta tesis (cuyo título en castellano es 'Cosmología al límite de Λ-Cold Dark Matter'), recoge parte de mi investigación, centrada en el estudio de las pequeñas incongruencias presentes en el modelo cosmológico estándar. Además, se discuten y proponen posibles estrategias para optimizar el desempeño de futuros experimentos.

El Capítulo 1 presenta una introducción a la cosmología, los pilares básicos del modelo cosmológico estándar y las observaciones que han permitido confirmarlo y establecerlo. Además, también se discuten las tensiones existentes entre distintos experimentos, así como el estado actual de las cuestiones teóricas que aún no han sido respondidas.

En el Capítulo 2 se discute la tensión entre las medidas directas de la velocidad de expansión del Universo (H_0) y los valores que se infieren a partir de observaciones del fondo de radiación de microondas cuando se utiliza ΛCDM para reconstruir la evolución del Universo. Además, se incluye una reconstrucción independiente de cualquier modelo de la expansión del Universo en sus últimos estadíos de evolución, lo que permite compararlo con ΛCDM e identificar las posibles fuentes de la tensión en H_0. En este Capítulo también se presenta el concepto de la regla de distancias estándar a bajo redshift (así como su medida correspondiente) y un método estadístico para analizar al mismo tiempo observaciones de distintos experimentos de una manera conservadora, sin importar el grado de tensión entre dichos experimentos y considerando la posible presencia de errores sistemáticos en las medidas.

El Capítulo 3 se centra en el estudio de los agujeros negro primordiales como posibles candidatos para conformar una fracción significativa de la materia oscura, así como para explicar el origen de los agujeros negros supermasivos que se han detectado en momentos tempranos de la evolución del Universo. En concreto, se discute el impacto que tendría el hecho de que la materia oscura estuviera compuesta de agujeros negros primordiales en el resto de parámetros cosmológicos. Además, se presenta una vía para identificar agujeros negros primordiales en el caso de que estos fueran las semillas de los agujeros negros supermasivos.

El Capítulo 4, por el contrario, trata sobre el prometedor potencial que tienen los experimentos de mapeo y cartografiado de la estructura a gran escala para avanzar nuestro conocimiento del Universo. En concreto, se discuten dos tipos de experimentos ligeramente distintos a los cartografiados de galaxias espectroscópicos y fotométricos: cartografiados de galaxias utilizando el continuo de la emisión en radio y experimentos de mapeos de intensidades. Estos dos tipos de experimentos permiten observar el cielo a mayor velocidad y son sensibles también a fuentes mucho menos brillantes que los cartografiados de galaxias espectroscópicos y fotométricos. Además, mediante la utilización de técnicas de mapeo de intensidad, es posible observar momentos de la evolución del Universo que no han podido ser observados hasta el momento, porque otras técnicas observacionales son incapaces de acceder a ellos. En este Capítulo, por tanto, se estudia el potencial de dichos experimentos, proponiendo estrategias para optimizar el análisis de sus observaciones y los correspondientes resultados.

Finalmente, todo el trabajo incluido en esta tesis se pone en común en el Capítulo 5, donde además se presentan las principales conclusiones de mi investigación y se proponen diferentes maneras de profundizar en ella y continuarla. Es en este Capítulo donde quedan patentes las sinergias entre distintos tipos de experimentos y donde se puede ver que el resto de Capítulos no son extractos de investigaciones aisladas. Al contrario, pese a centrarse en distintos temas de la cosmología actual, todos los trabajos científicos incluidos en esta tesis se complementan entre ellos porque tienen un mismo objetivo global: la comprensión y resolución de las tensiones y problemas abiertos que conlleva ΛCDM. Por esta razón, todos mis trabajos están interrelacionados y son necesarios para una comprensión global de los problemas discutidos en esta tesis.

La investigación recogida en esta tesis, así como los resultados que se presentan, serán de utilidad para futuros proyectos científicos. En particular, este trabajo contribuye a la mejor comprensión de lo que necesita el modelo ΛCDM para describir mejor el Universo, así como posibles soluciones para sus problemas y estrategias para explotar observaciones tomadas por experimentos futuros, con el fin de optimizar sus resultados y así maximizar nuestro conocimiento y comprensión del Universo.

Contents

1. Introduction

Cosmology is the science that studies the Universe as a whole, with the aim of understanding its origin, composition and evolution. Involving all ranges of scales, from particle physics to the distribution of matter at the largest causally connected distances, and beyond, cosmology takes a statistical approach, and assumes that the Universe we live in is the evolution of a single realization drawn from all possible initial conditions, which have a certain probability distribution function, given by the cosmological model.

We currently live in a golden era for cosmology. During the last few decades, there has been a tremendous experimental effort to probe our Universe, reaching an astonishing level of precision and establishing cosmology as a robust science, the so-called "precision cosmology". During these years, cosmology has transitioned from a data-starved to a data-driven science. This transformation possibly started with the first measurement of the Cosmic Microwave Background (CMB) temperature anisotropies by the COBE collaboration in 1992 (Smoot et al., 1992). Subsequently, other CMB experiments took over, such as balloon experiments, as BOOMERANG (Netterfield et al., 2002) and MAXIMA-1 (Hanany et al., 2000) which improved the measurement of the temperature anisotropies; or ground-based telescopes as DASI, which detected the CMB polarization anisotropies for the first time (Kovac et al., 2002), and ACBAR, which measured the high multipoles of the temperature angular power spectrum with the highest precision at the time (Kuo et al., 2004), among many others. CMB experiments have reached astonishing precision with satellite telescopes like WMAP (Bennett et al., 2013; Hinshaw et al., 2013) and the very recent Planck (Planck Collaboration et al., 2018), which has exploited almost all the accessible information in the primary CMB temperature anisotropies). After them, the observational effort will continue with the CMB Stage 4 (Abazajian et al., 2016), a joint strategy from the Bicep/Keck, SPT, ACT, Polarbear and Simons Observatory collaborations with the aim to build multiple ground-based telescopes coordinately to push CMB cosmology to the next level, especially focusing on polarization measurements.

Likewise, other cosmological probes target the late Universe. Among these, one of the first and most important probes are standard candles such as supernovae type Ia (SNeIa), which provided the fist evidence of the accelerated expansion of the Universe (Riess et al., 1998; Perlmutter et al., 1999), and nowadays constrain the evolution of dark energy (Betoule et al., 2014; Scolnic et al., 2018). Soon after the first evidence of the accelerated expansion of the Universe, galaxy clustering and Baryon Acoustic Oscillations (BAO) became a cornerstone of cosmology. BAO are standard rulers, which yield an extremely robust geometric measurement of the expansion history of the Universe. The BAO peak was first detected in the galaxy number count perturbations by the SDSS (Eisenstein et al., 2005) and 2dF (Cole et al., 2005) collaborations. Subsequent experiments have improved the BAO scale measurements from galaxy number counts, reaching percent level precision (Alam et al., 2017b). The BAO scale has also been measured at earlier times using the distribution of quasars and the Lyman-α forest (Gil-Marín et al., 2018; de Sainte Agathe et al., 2019; Blomqvist et al., 2019). The future of galaxy surveys is promising, with planned experiments that will soon start observing as DESI, Euclid and SKA, which will survey the largest volumes ever, pushing the envelope of observational cosmology (DESI Collaboration et al., 2016a; Amendola et al., 2018; Square Kilometre Array Cosmology Science Working Group et al., 2018). Finally, weak lensing experiments also study the Large Scale Structure (LSS), directly inferring the matter distribution thanks to galaxy shear, rather than using the distribution of galaxies or other brilliant sources. Cosmic shear was measured at large scales and exploited for cosmology for the first time by the CFHTLens collaboration (Heymans et al., 2012; Erben et al., 2013; Kilbinger et al., 2013), followed by KiDS (Hildebrandt et al., 2017) and DES (Troxel et al., 2018).

All these kinds of experiments target different physical phenomena, so their measurements are sensitive to different parameter combinations of a given cosmological model. Some parameters present degeneracies: an ensemble of values for a given set of parameters predicting the very same targeted cosmological observable. This is one of the reasons why having several independent cosmological probes is a great advantage for cosmology. Individually, each experiment cannot break their own parameter degeneracies, but thanks to the combination of various kinds of experiment, these degeneracies can be broken. This boosts the precision of the parameter inference in a joint analysis. Moreover, if two experiments reach consistent conclusions, the obtained results are confirmed and more robust. Each experiment is sensitive to its own observational systematic errors and its theoretical framework rely on a series of assumptions, which, if incorrect, may lead to theoretical systematic errors. Therefore, given that the systematic errors of an experiment are usually independent from those of other experiments, combining several experiments provides also a test for possible unnacounted-for systematics.

All this effort has confirmed (and fostered) theoretical research, greatly increasing our understanding of many physical processes and the Universe as a whole, from its very beginning in the inflationary stages, to the present and the accelerated expansion. All this has been embedded in a concordance model of cosmology, which reproduces the observations almost perfectly. Nonetheless, there is a difference between modeling and understanding, and there are still many unanswered questions regarding the true nature of the evolution and composition of the Universe. Some of these will be discussed in this dissertation, which collects part of my research, focused on pushing the limits of the standard cosmological model and its assumptions, regarding also existing tensions between experiments. This way, under the umbrella of agnosticism, the work reported here contributes to the quest for answers to the open questions in cosmology: how was the Universe in its initial stages? What causes the accelerated expansion of the Universe? What is dark matter made of?

1.1 The standard model of cosmology: ΛCDM

Models are used to describe reality in a simpler way. While some models may be useful and faithful to reality, none is strictly true. Any model has a number of assumptions and pillars over which it is built. Finally, all models have a set of free parameters to be determined by maximizing the fidelity of the reproduction of the observations.

Building upon the postulates of special relativity (the laws of physics are the same in all inertial reference frames, where the speed of light in vacuum, c, is always constant and has the same value), cosmology assumes the so-called cosmological principle, which states that there is no preferred location in the Universe. This means that, at sufficiently large scales, the Universe is homogeneous and isotropic.

Another pillar of modern cosmology is General Relativity (GR) as a correct description of gravity at any scale. Nonetheless, this is not a blind assumption or axiom, given the great success of GR in every test performed to date at scales up to the size of the Solar System. In addition, GR successfully describes observations of strong gravity processes, such as the gravitational waves detected so far by the LIGO and Virgo collaborations (Abbott et al., 2016b,a, 2017a,c,b), even the extremely well measured neutron star merger together with its electromagnetic counterpart (Abbott et al., 2017a,b), which has ruled out several modified gravity theories thank to the precise measurement of the speed of the gravitational waves (see e.g., Ezquiaga & Zumalacárregui (2017)). Besides, the recent Event Horizon Telescope observations are also consistent with GR (Event Horizon Telescope Collaboration et al., 2019). Applying the cosmological principle to Einstein's Equations, the Friedman-Lemaitre-Robertson-Walker metric is obtained. The line element, $\mathrm{d}s$, given by this metric in spherical coordinates is:

$$\mathrm{d}s^2 = -c^2\mathrm{d}t^2 + a^2(t)\left(\frac{\mathrm{d}r^2}{1-\kappa r^2} + r^2\mathrm{d}\theta^2 + r^2\sin^2\mathrm{d}\phi^2\right), \tag{1.1}$$

where t denotes time, r, θ and ϕ are the spherical spatial coordinates, and κ describes the curvature of the spatial section of the Universe ($\kappa = 1,\ 0,\ -1$ for a closed, flat and open Universe, respectively). This metric introduces the scale factor a describing how the spatial sector of the metric evolves with time. Then, the time evolution of a describes the expansion history of the Universe. Using this metric, and assuming that all kind of matter or radiation behaves as a perfect fluid with energy density ρ and pressure p, one can obtain the Friedman equations:

$$H^2(a) = \left(\frac{\dot{a}}{a}\right)^2 = \frac{8\pi G}{3}\rho - \frac{\kappa}{a^2} + \frac{\Lambda}{3}; \qquad \frac{\ddot{a}}{a} = -\frac{4\pi G}{3}\left(\rho + 3p\right) + \frac{\Lambda}{3}, \tag{1.2}$$

where a dot is the time derivative operator, H is the Hubble parameter, G is the gravitational constant, and Λ is the cosmological constant, who was initially introduced by Einstein to obtain a static Universe.

For a null cosmological constant, the critical density of the Universe, ρ_c, can be defined as the energy-density for which the spatial sector of the Universe is flat. In turn, the energy density of matter or radiation can be normalized by ρ_c, obtaining the density parameters. Extrapolating also this definition to the curvature and the cosmological constant, we obtain:

$$\begin{aligned} \rho_c(a) &= \frac{3H^2(a)}{8\pi G}; \qquad & \Omega_i(a) &= \frac{\rho_i(a)}{\rho_c(a)}; \\ \Omega_\kappa(a) &= \frac{-k}{H^2(a)}; \qquad & \Omega_\Lambda &= \frac{\Lambda}{3H^2(a)}, \end{aligned} \tag{1.3}$$

where the subscript "i" denotes matter, radiation, or any individual specie belonging to one of them, and $\sum \Omega_i(a) + \Omega_\kappa(a) + \Omega_\Lambda(a) = 1$ by definition.

Although a fundamental assumption of cosmology, the cosmological principle can be tested, too. For instance, galaxy surveys and CMB observations show evidence of the Universe being very close to isotropic at scales beyond 100 Mpc (Hajian & Souradeep, 2003; Planck Collaboration et al., 2016b; Sugiyama et al., 2018; Marinoni et al., 2012). On the other hand, homogeneity can be tested observing certain types of galaxies, whose stellar population evolution is assumed to be known, at different times (Heavens et al., 2011; Hoyle et al., 2013) or studying directly the homogeneity of galaxy number counts (Gonçalves et al., 2018). Moreover, both isotropy and homogeneity can be even tested at the same time (Jimenez et al., 2019a).

We can probe the Universe at different times because observing further away is equivalent to observing earlier in time, given the finite speed of light. However, determining the distance to a brilliant source is highly non trivial, since there is no way to directly measure when the detected radiation was emitted. In 1929, Edwin Hubble detected that the measured spectral emission from distant cepheids (variable stars whose period and intrinsic luminosity are related, so that they can be used as standard candles) located in all directions was shifted to lower frequencies. This was an evidence of them moving away from Earth. This shift, known as redshift, is related to the emitted and observed frequencies ($z + 1 = \nu_{\mathrm{em}}/\nu_{\mathrm{obs}}$). Hubble's measurement was the first evidence that the Universe was not static, but was expanding at a rate given by the Hubble constant H_0. Moreover, since this redshift is produced by the expansion of the Universe, it is directly related with the scale factor: $a = 1/(1 + z)$.

Having evidence that the Universe is expanding means that Einstein's value for Λ cannot be the correct. The trivial case, $\Lambda = 0$, corresponds to $\ddot{a} < 0$, which means a decelerating expansion of the Universe. This was the paradigm until the late 1990s, when the acceleration of the expansion of the Universe was detected for the first time by two independent teams thanks to SNeIa observations (Riess et al., 1998; Perlmutter et al., 1999). SNeIa, being standard candles, provide a direct measurement of the accelerated expansion, since they enable relative distance measurements. Likewise, standard rulers, such as BAO, also yield relative distance and Hubble parameter measurements, hence they also allow to directly probe the expansion history of the Universe, as predicted by Seo & Eisenstein (2003) and shown by the first BAO detections by Eisenstein et al. (2005) and Cole et al. (2005). On the other hand, indirect measurements of the accelerated expansion of the Universe can be extracted from CMB observations (see e.g., Planck Collaboration et al. (2018, 2016a) for the latest results) and cross-correlations of galaxy clustering and CMB, through the Integrated Sachs-Wolfe effect (Giannantonio et al., 2008; Ho et al., 2008; Giannantonio et al., 2014).

The only way to model an accelerated expansion is to introducing a new component with negative pressure, i.e., with a negative equation of state parameter w at late times (where w relates the density and pressure of a perfect fluid: $p = w\rho$). This fluid was called dark energy. Taking into account that non-relativistic matter is pressureless, that $w_r = 1/3$ for radiation and relativist matter, and that the efficient equation of state for the curvature energy density is $-1/3$, one can rewrite the Hubble parameter by joining Equations (1.2) and (1.3). Assuming a general equation of state parameter for dark energy:

$$\begin{aligned} H^2(z) = H_0^2 \Big[& \Omega_M \left(1+z\right)^3 + \Omega_r \left(1+z\right)^4 + \Omega_\kappa \left(1+z\right)^2 + \\ & + \Omega_X \exp\left\{ 3 \int_0^z \frac{1+w(z)}{1+z} \mathrm{d}z \right\} \Big], \end{aligned} \tag{1.4}$$

where Ω_M, Ω_r, Ω_κ and Ω_X are the density parameters of all non-relativistic matter, all relativistic matter and radiation, curvature and dark energy at $z = 0$, respectively. Nonetheless, state-of-the-art observations favor the simplest model of dark energy, in which the cosmic acceleration is described by the same cosmological constant introduced in Equation (1.2), which has $w = -1$ (hence, dark energy energy-density is constant). Moreover, CMB and BAO measurements joint analyses are consistent with a flat spatial sector (Planck Collaboration et al., 2018; Alam et al., 2017b). Equation (1.4) shows that at different times (specified by z), the expansion of the Universe is dominated by a specific kind of component, which defines the domination eras. For instance, the redshift range for which $\Omega_M(z) \sim 1$ is called matter domination epoch, and so on.

Another pillar of modern cosmology relates to the nature of matter. There is plenty of evidence, ranging from galaxy dynamics to gravitational lensing and CMB anisotropies, among others, that most of the matter of the Universe is not made of baryons. The only observed interaction of this component of matter, so-called dark matter, is gravitational. However, one of the preferred candidates of dark matter to date also involves weak interactions.

Most of the cosmological probes, especially LSS and CMB, only need to assume whether this dark matter is relativistic (hot), non-relativistic (cold), or has an intermediate mass such as it is relativistic at early times and becomes non-relativistic in the radiation dominated era (warm). While cold dark matter clusters in a bottom-up hierarchy, hot dark matter clusters before at the largest scales to form smaller structures later, i.e., it follows a top-down hierarchical structure formation. On the other hand, since relativistic particles free stream out of overdensities smearing them, warm dark matter produces a cutoff in the growth of structures at small scales. This non-negligible free streaming length entails a smoothing of massive halo cores (increasing core radii and lowering its density), a reduction of the characteristic density of low mass halos, and an overall reduction of the abundance of low mass halos, which in turn delays ionization. Massive neutrinos have a similar effect, although smaller in comparison due to its low abundance. Thanks to this rich phenomenology, cold dark matter is very favored by LSS observations, ruling out hot dark matter and strongly constraining warm dark (Lopez-Honorez et al., 2017; Iršič et al., 2017).

The standard model of cosmology and its main alternatives assume that in the very early Universe there were scalar primordial curvature perturbations produced by a period of exponential expansion denominated as inflation. In the simplest slow-roll inflation, these scalar perturbations follow a Gaussian distribution, with an almost scale-independent power spectrum given by:

$$P_0(k) = A_s \left(\frac{k}{k_0}\right)^{\mathrm{n_s}-1}, \tag{1.5}$$

where A_s is the amplitude of the power spectrum of scalar curvature perturbations at a pivot scale k_0, and n_s is the spectral index. Inflation is expected to generate tensor perturbations, too. However, their amplitude could be vanishingly small, and they have not been detected yet.

Primordial perturbations grow under gravitational forces as the Universe evolves. Eventually, perturbations collaps and may host galaxies and clusters of galaxies. This growth is described by a set of coupled differential equations (Einstein-Boltzmann equations) which involve the evolution of the density perturbations of every kind of fluid interacting among them, accounting for the expansion of the Universe. Therefore, the expansion history and the growth of perturbations are connected, a relation which in GR is fully determined (as first noticed by Starobinsky (1998)).

Using the Einstein-Boltzmann equations, transfer functions, $T(k, z)$, can be derived, such as $\delta_i(k, z) = T_i(k, z)\delta_0(k)$, where δ_i is the overdensity of the i fluid, and δ_0 denotes the primordial perturbations. This formalism is based on linear perturbation theory, so it breaks down in scales where non-linear gravitational collapse dominates the evolution of overdensities. This way, in the linear regime, the total power matter spectrum, P_m, is given by:

$$P_m(k, z) = \left(\sum_i T_i(k, z)\right)^2 P_0(k), \tag{1.6}$$

where the sum is over all matter and radiation species.

The standard cosmological model builds upon all these pillars and encodes the simplest accurate description of the Universe. This model is called Λ-Cold Dark Matter (ΛCDM), since it considers that dark matter is cold and that the cosmic acceleration is well described by a cosmological constant, Λ. Furthermore, it uses GR to model gravity and assumes the cosmological principle. It also considers massive neutrinos, taking the measured lower limit of the sum of neutrino masses, 0.06 eV, as a fiducial value.

ΛCDM is a very powerful model, which can reproduce a plethora of cosmological probes with only six free parameters: the abundance of baryons and cold dark matter, which can be parametrized with the density parameters Ω_b, and $\Omega_{\rm cdm}$, respectively; the Hubble constant, H_0; the spectral index of the primordial power spectrum, n_s; the amplitude of primordial power spectrum of the scalar perturbations at the pivot scale, A_s; and the optical depth due to reionization, $\tau_{\rm reio}$. Yet, in light of state-of-the-art observations, ΛCDM is not a completely satisfactory model both from a phenomenological and theoretical point of view.

1.2 Observational discrepancies assuming ΛCDM

From the phenomenological point of view, we can test the consistency between different experiments and cosmological probes. If ΛCDM is an accurate description of the Universe, all results from every observation or experiment must coincide within the statistical uncertainties, if the analyses are free of non-accounted for systematic errors. Therefore, discrepancies between different data sets might be a smoking gun for failures or limitations in the model. This would motivate the inclusion of new physics in the cosmological model, or the relaxation of some of the assumptions discussed in Section 1.1.

As the observations improve, there has been claims of inconsistencies between data sets. Some have disappeared after revisiting the data analysis or increasing the statistics, such as the case of the optical depth to reionization between WMAP and Planck (Planck Collaboration et al., 2016d), the matter content and amplitude of the power spectrum between Planck CMB power spectrum and Sunyaev-Zeldovic galaxy cluster number counts (Douspis et al., 2019), or between the expansion history measured by the BAO obtained from galaxy number counts and from the Lyman-α forest (de Sainte Agathe et al., 2019; Blomqvist et al., 2019), among others. However, since a few years ago, there are some persistent tensions when ΛCDM is assumed.

Among them, the largest discrepancy is between the local, direct measurement of H_0 from SH0ES collaboration (Riess et al., 2011; Riess et al., 2016) and the inferred value from Planck observations assuming ΛCDM. Note that the physics and the analyses behind both measurements are completely different. On one hand, SH0ES directly measures the expansion rate of the Universe today (i.e., H_0), building a distance ladder using coincident geometric and relative distance indicators. For instance, parallaxes are used to calibrate nearby cepheids as standard candles, which in turn are used to calibrate distances to more distant SNeIa. This way, absolute distances up to $\gtrsim 100$ Mpc can be precisely measured. The distance ladder provides a determination of H_0 independent on cosmology. However, it does depend on astrophysics, mainly regarding the homogeneity and standardization of distance calibrators. On the other hand, Planck probes the Universe at $z \sim 1000$ and fits a six-parameter cosmological model (in the case of ΛCDM), extrapolating its measurements to the present Universe to infer local quantities such as H_0. This makes the H_0 value inferred from CMB observations extremely dependent on the cosmological model. Fortunately, other observations, such as BAO, help to constrain the Universe at low redshift, which makes the parameter inference from a joint analysis more robust. Rather than disappearing with time, independent analyses and better observations, this tension is growing and has recently surpassed the 4σ level (Riess et al., 2019).

Although the largest discrepancy on H_0 involves SH0ES and Planck collaborations, there are other probes to measure H_0 s. Some examples include strong lensing time delays (Suyu et al., 2017; Bonvin et al., 2017), BAO combined with a determination of Ω_b assuming standard Big Bang Nucleosynthesis (Aubourg et al., 2015; Addison et al., 2017), gravitational waves with electromagnetic counterparts used as standard sirens (Abbott et al., 2017), and cosmic clocks (Jimenez & Loeb, 2002; Moresco et al., 2016). A comprehensive list of measurements of H_0 can be found in Bernal & Peacock (2018). Surprisingly, the results seem to be clustered in two different groups: observations probing physics depending on the early Universe favor $H_0 \sim$ 68 km/s/Mpc (e.g., CMB anisotropies, BAO+Ω_b from Big Bang Nucleosynthesis), while strictly low redshift probes favor $H_0 \sim 73$ km/s/Mpc (e.g., distance ladder, strong lensing time delays). Apparently, the cosmic clocks are the only exception to this trend. Therefore, this discrepancy might be also interpreted as a tension between the early and the late Universe within ΛCDM.

Another recurrent discrepancy, although smaller, is related with the growth of structures. As discussed above, in a GR framework, the expansion history fully determines the growth of structures. Therefore, CMB observations are also used to infer the amplitude of perturbations at low redshift, parametrized with σ_8 (the root mean square of the overdensities within 8 h^{-1}Mpc). On the other hand, weak lensing experiments yield strong constraints on the parameter combination $\sigma_8\Omega_M^{0.5}$ (Kilbinger et al., 2013; Hildebrandt et al., 2017; Troxel et al., 2018). While there are mild tensions between different weak lensing experiments, there is a $\sim 2\sigma$ discrepancy between the values inferred by Planck and weak lensing experiments. Although the tension on $\sigma_8\Omega_M^{0.5}$ is smaller than that on H_0, the fact that weak lensing measurements involve only low redshift physics supports the hypothesis of a potential discrepancy between high and low redshift observations.

There have been attempts to reconcile the H_0 and $\sigma_8\Omega_M^{0.5}$ tensions at the same time with deviations from ΛCDM, although none of them has obtained satisfactory results to date. In most cases, when one tension is relieved, the other becomes worse. Some examples are more massive neutrinos (Planck Collaboration et al., 2018), interactions between dark matter and neutrinos (Di Valentino et al., 2018), or self-interacting neutrinos with a delayed onset of their free streaming (Kreisch et al., 2019).

1.3 Theoretical open questions of ΛCDM

Even if ΛCDM perfectly reproduced all possible observations, hence providing a perfect description of the Universe, this model is still a phenomenological model, especially regarding two of the largest unknowns: the nature of dark energy and dark matter.

1.3.1 Dark energy

The detected accelerated expansion of the Universe at late times is well described by a cosmological constant in the Einstein Equations. While vacuum energy would be the straightforward explanation for the negative pressure that triggers the accelerated expansion, the cosmological constant measured value corresponds to a density parameter $\Omega_\Lambda \approx 0.65 - 0.7$, which is extremely small compared with the predictions of quantum field theory.

Nonetheless, a cosmological constant might be a simplification of a more elaborated physical picture. In Einstein Equations it is also possible to model the accelerated expansion introducing extra fields to the energy momentum tensor or modifying the Einstein tensor, efficiently modeling dynamical dark energy or modifying GR, respectively. One of the attractive points of the former is that the extra field could be related with inflation and then connect the two epochs of the Universe with accelerated expansion in a single concept.

On the other hand, GR has been directly tested with superb precision at scales smaller than the Solar System and it is completely consistent with the gravitational waves detected so far and the most precise observation of a black hole. However, there is no direct evidence beyond these scales and phenomena. Beyond these regimes, GR is extrapolated. Therefore, what seems like an accelerated expansion if GR is assumed, might be a hint of gravity deviating from the GR description. State-of-the-art observations of both CMB and LSS have not found any deviation from GR yet (Planck Collaboration et al., 2018). But, generally, modified gravity theories change also the clustering and induce a non-zero anisotropic stress. Therefore, LSS probes should add complementary information to discriminate between modifications of GR and dynamical dark energy, especially when combining galaxy clustering and gravitational lensing (Pullen et al., 2015; Singh et al., 2019; Alam et al., 2017a).

1.3.2 Dark matter

ΛCDM models dark matter as a pressureless fluid (i.e., cold, non-relativistic) which only interacts with gravity, but does not assume anything else about its nature. For example, in N-body simulations, dark matter is usually modeled as collisionless particles. In any case, this description lacks information about the microscopic nature of dark matter. This is why there is an on going worldwide experimental effort to pursue dark matter detection and probe the dark matter nature.

In general, there are three strategies to identify particle dark matter: direct detection, which aims to detect interactions between dark matter and baryonic detectors; indirect detection, which looks for baryonic products of dark matter-dark matter processes (i.e., annihilations or decays); and detection in particle colliders, attempting to generate dark matter particles as product of collisions between standard model particles.

During the last decades, the preferred dark matter candidate has been the Weakly Interactive Massive Particles, or WIMPs, that are connected to the standard model particles through gravity and weak interactions. However, while experiments increase their sensitivity, WIMPs have yet to be detected, with increasingly stronger upper limits on the scattering cross-section between dark matter and baryonic detectors, in the case of direct detection, or annihilation cross-sections or decaying lifetimes, in the case of indirect detection. This lack of detection of WIMPs has shifted the attention to other dark matter particle candidates, such as, for example, axion-like particles (whose experimental stage is less mature at this point).

However, dark matter does not need to be necessarily a particle. The only observational evidence of dark matter is at galactic scales and above, so dark matter could also be composed of compact objects. Compact objects would behave in a completely different way at very small scales, but beyond a certain scale, the cold-matter fluid description is equally valid. In this family of candidates, Primordial Black Holes (PBHs) have drawn special attention.

PBHs form in the collapse of large density peaks in the very early Universe, mainly in the radiation dominated epoch. The concept of PBH was introduced in the sixties (Zel'dovich & Novikov, 1967) and soon after was suggested as a dark matter candidate (Chapline, 1975). However, increasingly stringent constraints (Alcock et al., 1998; Flynn et al., 1996; Carr & Sakellariadou, 1999; Wilkinson et al., 2001) gave way to particle dark matter theories. Nevertheless, the gravitational wave detections by LIGO+VIRGO collaborations from binary black hole mergers (Abbott et al. (2016b) and subsequent detections) have brought back the focus on the possibility that PBHs make up a significant fraction of the dark matter (Bird et al., 2016; Sasaki et al., 2016).

The abundance of PBHs is usually parametrized by the ratio between the density parameters of PBHs and the whole of dark matter: $f_{\rm PBH} = \Omega_{\rm PBH}/\Omega_{\rm dm}$. The possible PBH masses range spans over several order of magnitudes, and therefore PBHs as dark matter involve an wide variety of phenomena. The physical processes that allow to constrain $f_{\rm PBH}$ or eventually detect PBHs include: Hawkings evaporation, gravitational lensing, radiation due to gas accretion, dynamical effects and gravitational waves, among others.

1. INTRODUCTION

The renewed interest on PBHs as dark matter has motivated a reassessment of most of the observational constraints on $f_{\rm PBH}$. For example, Ali-Haïmoud & Kamionkowski (2017) rederived CMB constraints from the CMB, accounting for Compton drag, CMB cooling and ionization cooling, as well as using a more precise estimate of the relative velocities between baryons and PBHs. This new model predicts smaller PBH accretion rates, what significantly weakens the constraints found previously (Ricotti et al., 2008). Another example are the constraints coming from ultra-faint dwarf galaxies, whose stellar system were thought to expand in the presence of massive PBHs due to dynamical heating (Brandt, 2016). However, this reasoning ignores that too massive PBHs (or an astrophysical intermediate mass black holes) would stabilize the system and avoid its expansion (Silk, 2017a). This makes these constraints much less robust, especially the one coming from Eridanus II (one of the strongest constraints of this kind), since there is evidence of a massive compact object at its center (Li et al., 2017). One last enlightening example involves the constraints from femtolensing of gamma ray bursts. This constraint (Barnacka et al., 2012) ignored that gamma ray bursts are not suitable for femtolensing surveys due to their large sizes, hence these results are incorrect and the constraints completely vanish (Katz et al., 2018).

Therefore, these revisions have changed considerably the picture regarding the constraints on PBHs as dark matter candidate. Currently, there are two strong limits on the possible masses for a significant $f_{\rm PBH}$ with a somewhat narrow mass distribution. If the PBHs were light enough ($M_{\rm PBH} \lesssim 10^{-16} M_\odot$, where $M_{\rm PBH}$ and $M_\odot$ are the PBH mass and the solar mass, respectively), Hawkings evaporation would have left a significant background emission at high energies that has not been detected. In turn, in the large mass end, there are strong limits on the PBH mass due to accretion (the accretion rate scales as $M_{\rm PBH}^2$). CMB anisotropies provide strong constraints on the PBH abundance for masses $M_{\rm PBH} \gtrsim 10^3 - 10^4 M_\odot$ (Ali-Haïmoud & Kamionkowski, 2017).

While the renovated interest on PBH was initially focused on $M_{\rm PBH} \sim 30 M_\odot$ (mostly to match gravitational wave detections), new constraints, from SNeIa lensing (Zumalacárregui & Seljak, 2018a), and inferred from the expected PBH merger rate (Ali-Haïmoud et al., 2017), seem to disfavor PBHs as a significant fraction of the dark matter in this mass range. On the other hand, as a result of the revision of older constraints, there are now two mass ranges where $f_{\rm PBH} \sim 1$ is completely unconstrained: $10^{-16} M_\odot \lesssim M_{\rm PBH} \lesssim 10^{-14} M_\odot$, and $10^{-13} M_\odot \lesssim M_{\rm PBH} \lesssim 10^{-10} M_\odot$. These two mass ranges are separated by the constraints coming from the observed distribution of white dwarfs: PBHs would disrupt white dwarfs as they pass through, producing the ignition of a thermonuclear runaway which would lead to a supernovae explosion, as pointed out by Graham et al. (2015)). Stronger constraints coming from microlensing studies (Niikura et al., 2017, 2019; Alcock et al., 1998) limit the abundance of PBHs at $M \gtrsim 10^{-10} M_\odot$.

In any case, even if a significant fraction of dark matter made up by PBHs was to be ruled out by coming observations, the detection of PBHs would be extremely informative. Since PBHs would only form if very high density peaks were present in the primordial Universe, they are intimately related with the primordial power spectrum at very small scales. Precisely, constraints on PBHs and eventual detections involve one of the few observational probes of the primordial Universe (Josan et al., 2009; Bugaev & Klimai, 2009). In addition to this, a small fraction of very massive PBHs might make up for the intermediate massive black holes that might be present at the center of dwarf galaxies (Silk, 2017b).

Moreover, PBHs might be the solution to another open problem in astrophysics. Supermassive black holes are the nuclei of most galaxies, but there are observations pointing to these black holes being too massive at too high redshift ($\sim 10^9 M_\odot$ at $z \sim 7$) (Fan et al., 2001; Wu et al., 2015; Mortlock et al., 2011; Bañados et al., 2018). Supermassive black holes could be the evolution of population III stars remnants, formed at $z \sim 20$ with $M \sim 100 M_\odot$. However, these stars would need continuous supercritical accretion in order to grow fast enough (Madau & Rees, 2001; Inayoshi et al., 2016). This possibility is unlikely because the abundance of quasars with supercritical accretion at high redshifts is very constrained (Salvaterra et al., 2012). On the other hand, intermediate mass black holes of masses around $10^3 - 10^6 M_\odot$ (referred to as seeds in this context) would suffice to seed the supermassive black holes. These seeds might be formed due to the gravitational collapse of pristine gas clouds which do not fragment forming ordinary stars, so that all the mass directly collapses in a single black hole. These seeds are called direct collapse black holes, and form around $z \sim 15$ with $M \sim 10^5 - 10^6 M_\odot$ (Bromm & Loeb, 2003; Volonteri et al., 2008; Agarwal et al., 2014). Although direct collapse black holes could perfectly be the origin of the most massive supermassive black holes at early times, the conditions to trigger their formation are very special, and it is unlikely that they could explain the general population of supermassive black holes (Dijkstra et al., 2014; Latif et al., 2015). Nonetheless, if the high mass tail of the distribution of PBHs reaches $\sim 10^3 - 10^4 M_\odot$, PBHs could become the seeds of supermassive black holes, even with an extremely small $f_{\rm PBH} \sim 10^{-8} - 10^{-6}$. This turns them into a valid candidate.

1.4 Objectives and structure of the thesis

This doctoral thesis collects some of my research in the form of the corresponding publications, as well as on going research. The main objective of this research is to study some of what in my view are the existing loose ends of ΛCDM. Specifically the work presented is mostly focused on the discrepancy of H_0 between high and low redshift observables, the role of PBHs as candidates for dark matter or seeds of the supermassive black holes, and the future strategies to probe deviations from ΛCDM observing the LSS with intensity mapping experiments and radio-continuum galaxy surveys.

This thesis is organized as follows. In Chapter 2, the tension on H_0 is exhaustively studied, seeking for possible explanations either in the late or early Universe, using both model-independent approaches and analyses that consider the existence of possible unnacounted-for systematics. This Chapter includes the publications Bernal et al. (2016b); Verde et al. (2017) and Bernal & Peacock (2018). Chapter 3 is focused on PBHs and their role as dark matter or as seeds of the supermassive black holes. Consequences in the remaining cosmological parameters and strategies to test these hypotheses are explored; the articles Bernal et al. (2017, 2018) are included. In Chapter 4 the potential of radio-continuum galaxy surveys is discussed, focusing on the gains of probing the largest accessible scales. In addition, the use of intensity mapping observations for cosmology is studied, exploiting that this kind of experiments can observe redshifts in which LSS has neither been measured yet nor are accesible by galaxy surveys. This Chapter includes the published article Bernal et al. (2019) and two manuscripts currently under collaboration review (Bernal et al., 2019a,b). Finally, Chapter 5 summarizes the conclusions and the relevance of the work presented in this thesis, as well as future prospects and possible paths to continue this research.

In addition to the published work collected in thesis, further research co-authored by me can be found in Bernal et al. (2016a); DESI Collaboration et al. (2016a,b); Bellomo et al. (2018); Kalus et al. (2019a); D'Eramo et al. (2018) and Square Kilometre Array Cosmology Science Working Group et al. (2018).

2. Tensions in the Expansion history of the Universe

This Chapter contains the research reported in Bernal et al. (2016b), Verde et al. (2017) and Bernal & Peacock (2018). These publications are related with the existing tension between the inferred value of H_0 using CMB observations by the Planck satellite assuming ΛCDM and the direct measurement from the SH0ES collaboration, derived using the distance ladder.

In Bernal et al. (2016b) three avenues to study this tension are discussed: modifying the physics in the early cosmology without changing the late cosmology; varying the late time expansion history assuming standard high redshift physics; and a completely model-independent reconstruction of the cosmic expansion at low redshift without any assumption about the early-times physics. This work, done in collaboration with Licia Verde and Adam G. Riess, was published in the Journal of Cosmology and Astroparticle Physics (JCAP) in October 2016.

In Verde et al. (2017), the two anchors of the cosmic distance ladder (H_0 and the sound horizon at radiation drag, $r_{\rm s}$, for the direct and inverse cosmic distance ladder, respectively) are measured in a model independent way using different combinations of data sets from low redshift observations. Moreover, the low redshift standard ruler is defined as $r_{\rm s}^h$, and constrained. Using only BAO and SNeIa measurements, the low redshift standard ruler is measured with a $\sim 2\%$ error. This work, written in collaboration with Licia Verde, Alan F. Heavens and Raul Jimenez, was published in the Monthly Notices of the Royal Astronomical Society (MNRAS) in January 2017.

In Bernal & Peacock (2018), a flexible methodology is introduced: `BACCUS` (BAyesian Conservative Constraints and Unkown Systematics). This formalism allows to carry out joint analyses of different data sets to infer the parameters of a model in a conservative way, no matter the level of discrepancy between the data. It uses parameters which model the effect of unknown systematics and then marginalize over them. After describing the methodology, this framework is applied to all low redshift observations constraining H_0 to obtain conservative constraints on it. This research, performed in collaboration with John A. Peacock, was published in the Journal of Cosmology and Astroparticle Physics on July 2018.

Journal of Cosmology and Astroparticle Physics
An IOP and SISSA journal

The trouble with H_0

José Luis Bernal,[a,b] **Licia Verde**[a,c,d,e,f] **and Adam G. Riess**[g,h]

[a]ICC, University of Barcelona, IEEC-UB,
Martí i Franquès, 1, E08028 Barcelona, Spain
[b]Dept. de Física Quàntica i Astrofísica, Universitat de Barcelona,
Martí i Franquès 1, E08028 Barcelona, Spain
[c]ICREA, Pg. Lluís Companys 23, 08010 Barcelona, Spain
[d]Radcliffe Institute for Advanced Study, Harvard University,
MA 02138, U.S.A.
[f]Institute for Theory and Computation, Harvard-Smithsonian Center for Astrophysics,
60 Garden Street, Cambridge, MA 02138, U.S.A.
[e]Institute of Theoretical Astrophysics, University of Oslo,
0315, Oslo, Norway
[g]Department of Physics and Astronomy, Johns Hopkins University,
Baltimore, MD 21218, U.S.A.
[h]Space Telescope Science Institute,
3700 San Martin Drive, Baltimore, MD 21218, U.S.A.

E-mail: joseluis.bernal@icc.ub.edu, liciaverde@icc.ub.edu, ariess@stsci.edu

Received July 20, 2016
Revised September 29, 2016
Accepted September 29, 2016
Published October 11, 2016

Abstract. We perform a comprehensive cosmological study of the H_0 tension between the direct local measurement and the model-dependent value inferred from the Cosmic Microwave Background. With the recent measurement of H_0 this tension has raised to more than $3\,\sigma$. We consider changes in the early time physics without modifying the late time cosmology. We also reconstruct the late time expansion history in a model independent way with minimal assumptions using distance measurements from Baryon Acoustic Oscillations and Type Ia Supernovae, finding that at $z < 0.6$ the recovered shape of the expansion history is less than 5% different than that of a standard ΛCDM model. These probes also provide a model insensitive constraint on the low-redshift standard ruler, measuring directly the combination $r_\mathrm{s}h$ where $H_0 = h \times 100$ Mpc^{-1}km/s and r_s is the sound horizon at radiation drag (the standard ruler), traditionally constrained by CMB observations. Thus r_s and H_0 provide absolute scales for distance measurements (anchors) at opposite ends of the observable Universe. We calibrate the cosmic distance ladder and obtain a model-independent determination of the standard ruler for acoustic scale, r_s. The tension in H_0 reflects a mismatch between our determination of r_s and its standard, CMB-inferred value. Without including high-ℓ Planck

JCAP10(2016)019

doi:10.1088/1475-7516/2016/10/019

CMB polarization data (i.e., only considering the “recommended baseline” low-ℓ polarisation and temperature and the high ℓ temperature data), a modification of the early-time physics to include a component of dark radiation with an effective number of species around 0.4 would reconcile the CMB-inferred constraints, and the local H_0 and standard ruler determinations. The inclusion of the “preliminary” high-ℓ Planck CMB polarisation data disfavours this solution.

Keywords: cosmological parameters from CMBR, cosmological parameters from LSS, dark energy theory

ArXiv ePrint: 1607.05617

Contents

1 Introduction

In the last few years, the determination of cosmological parameters has reached astonishing and unprecedented precision. Within the standard Λ - Cold Dark Matter (ΛCDM) cosmological model some parameters are constrained at or below the percent level. This model assumes a spatially flat cosmology and matter content dominated by cold dark matter but with total matter energy density dominated by a cosmological constant, which drives a late time accelerated expansion. Such precision has been driven by a major observational effort. This is especially true in the case of Cosmic Microwave Background (CMB) experiments, where WMAP [1, 2] and Planck [3] have played a key role, but also in the measurements of Baryon Acoustic Oscillations (BAO) [4, 5], where the evolution of the cosmic distance scale is now measured with a $\sim 1\%$ uncertainty.

The Planck Collaboration 2015 [3] presents the strongest constraints so far in key parameters, such as geometry, the predicted Hubble constant, H_0, and the sound horizon at radiation drag epoch, r_s. These last two quantities provide an absolute scale for distance measurements at opposite ends of the observable Universe (see e.g., [6, 7]), which makes them essential to build the distance ladder and model the expansion history of the Universe. However, they are *indirect* measurements and as such they are model-dependent. Whereas the H_0 constraint assumes an expansion history model (which heavily relies on late time physics assumptions such as the details of late-time cosmic acceleration, or equivalently, the properties of dark energy), r_s is a derived parameter which relies on early time physics (such as the density and equation of state parameters of the different species in the early universe).

This is why having model-independent, direct measurements of these same quantities is of utmost importance. In the absence of significant systematic errors, if the standard cosmological model is the correct model, indirect (model-dependent) and direct (model-independent) constraints on these parameters should agree. If they are significantly inconsistent, this will provide evidence of physics beyond the standard model (or unaccounted systematic errors).

Direct measurements of H_0 rely on the ability to measure absolute distances to > 100 Mpc, usually through the use of coincident geometric and relative distance indicators. H_0 can be interpreted as the normalization of the Hubble parameter, $H(z)$, which describes the expansion rate of the Universe as function of redshift. Previous constraints on H_0 (i.e. [8]) are consistent with the final results from the WMAP mission, but are in 2-2.5σ tensions with Planck when ΛCDM model is assumed [9–11]. The low value of H_0 found, within the ΛCDM model, by the Planck Collaboration since its first data release [12], and confirmed by the latest data release [3], has attracted a lot of attention. Re-analyses of the direct measurements of H_0 have been performed ([13] including the recalibration of distances of [14]); physics beyond the standard model has been advocated to alleviate the tension, especially higher number of effective relativistic species, dynamical dark energy and non-zero curvature [7, 15–19].

In some of these model extensions, by allowing the extra parameter to vary, tension is reduced but this is mainly due to weaker constraints on H_0 (because of the increased number of model parameters), rather than an actual shift in the central value. In many cases, non-standard values of the extra parameter appear disfavoured by other data sets.

Recent improvements in the process of measuring H_0 (an increase in the number of SNeIa calibrated by Cepheids from 8 to 19, new parallax measurements, stronger constraints on the Hubble flow and a refined computation of distance to NGC4258 from maser data) have made possible a 2.4% measurement of H_0: $H_0 = 73.24 \pm 1.74$ Mpc^{-1}km/s [20]. This new measurement increases the tension with respect to the latest Planck-inferred value [21] to $\sim 3.4\sigma$. This calibration of H_0 has been successfully tested with recent Gaia DR1 parallax measurements of cepheids in [22].

Time-delay cosmography measurements of quasars which pass through strong lenses is another way to set independent constraints on H_0. Effort in this direction is represented by the H0LiCOW project [23]. Using three strong lenses, they find $H_0 = 71.9^{+2.4}_{-3.0}$ Mpc^{-1}km/s, within flat ΛCDM with free matter and energy density [24]. Fixing $\Omega_M = 0.32$ (motivated by the Planck results [3]), yields a value $H_0 = 72.8 \pm 2.4$ Mpc^{-1}km/s. These results are in 1.7σ and 2.5σ tension with respect to the most-recent CMB inferred value, while are perfectly consistent with the local measurement of [20].

In addition, in [25], it is shown that the value of H_0 depends strongly on the CMB multipole range analysed. Analysing only temperature power spectrum, tension of 2.3σ between the H_0 from $\ell < 1000$ and from $\ell \geq 1000$ is found, the former being consistent with the direct measurement of [20]. However, ref. [26] finds that the shifts in the cosmological parameters values inferred from low versus high multipoles are not highly improbable in a ΛCDM model (consistent with the expectations within a 10%). These shifts appear because when considering only multipoles $\ell < 800$ (approximately the range explored by WMAP) the cosmological parameters are more strongly affected by the well known $\ell < 10$ power deficit.

Explanation for this tension in H_0 includes internal inconsistencies in Planck data systematics in the local determination of H_0 or physics beyond the standard model. These recent results clearly motivate a detailed study of possible extensions of the ΛCDM model and an inspection of the current cosmological data sets, checking for inconsistencies.

In figure 1, we summarize the current constraints on H_0 tied to the CMB and low-redshift measurements. We show results from the public posterior samples provided by the Planck Collaboration 2015 [3], WMAP9 [1] (analysed with the same assumptions of Planck),[1] the results of the work of Addison et al. [25] and the quasar time-delay cosmography measurements of H_0 [24], along with the local measurement of [20]. CMB constraints are shown for two models: a standard flat ΛCDM and a model where the effective number of

---

[1] The values of r_s in WMAP's public posterior samples were computed using the approximation of [27], which differs from the values computed by current Boltzmann codes and used in Planck's analysis by several percent, as pointed in the appendix B of ref. [28]. As WMAP's data have been re-analysed by the Planck Collaboration, the values reported here are all computed with the same definition.

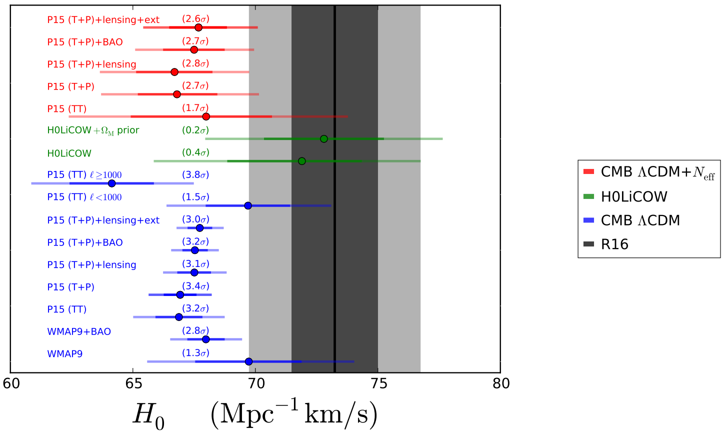

Figure 1. Marginalised 68% and 95% constraints on H_0 from different analysis of CMB data, obtained from Planck Collaboration 2015 public chains [3], WMAP9 [1] (analysed with the same assumptions than Planck) and the results of the work of Addison et al. [25] and Bonvin et al. [24]. We show the constraints obtained in a ΛCDM context in blue, ΛCDM+$N_{\rm eff}$ in red, quasar time-delay cosmography results (taken from H0LiCOW project [24], for a ΛCDM model, with and without relying on a CMB prior for $\Omega_{\rm M}$) in green and the constraints of the independent direct measurement of [20] in black. We report in parenthesis the tension with respect to the direct measurement.

relativistic species $N_{\rm eff}$ is varied in addition to the standard ΛCDM parameters. Of all the popular ΛCDM model extensions, this is the most promising one to reduce the tension. Assuming ΛCDM, the CMB-inferred H_0 is consistent with the local measurement only when $\ell < 1000$ are considered (the work of Addison et al. and WMAP9). However when BAO measurements are added to WMAP9 data, the tension reappears, but at a lower level (2.8σ).

On the other hand, $r_{\rm s}$ is the standard ruler which calibrates the distance scale measurements of BAO. Since BAO measure $D_V/r_{\rm s}$ (or $D_A/r_{\rm s}$ and $Hr_{\rm s}$ in the anisotropic analysis) the only way to constrain $r_{\rm s}$ without making assumptions about the early universe physics is combining the BAO measurement with other probes of the expansion rate (such as H_0, cosmic clocks [29] or gravitational lensing time delays [23]). When no cosmological model is assumed, H_0 and $r_{\rm s}$ are understood as anchors of the cosmic distance ladder and the inverse cosmic distance ladder, respectively. As BAO measurements always depends on the product $H_0r_{\rm s}$ (see Equations (5.1), (5.2) and (5.3)), when the Universe expansion history is probed by BAO, the two anchors are related by $H_0r_{\rm s}$ = constant. This was illustrated in [30] and more recently in [31], where only weak assumptions are made on the shape of $H(z)$, and in [6], where the normal and inverse distance ladder are studied in the context of ΛCDM and typical extensions.

While the model-independent measurement of $r_{\rm s}$ [30] is consistent with Planck, the model-dependent value of [6] is in 2σ tension with it. Both of these measurements use $H_0 \approx 73.0 \pm 2.4 \mathrm{Mpc}^{-1}\mathrm{km/s}$, so, this modest tension is expected to increase with the new constraint on H_0.

In this paper we quantify the tension in H_0 and explore how it could be resolved – without invoking systematic errors in the measurements– by studying separately changes in the early time physics and in the late time physics

We follow three avenues. Firstly, we allow the early cosmology (probed mostly by the CMB) to deviate from the standard ΛCDM assumptions, leaving unaltered the late cosmology (e.g., the expansion history at redshift below $z \sim 1000$ is given by the ΛCDM model). Secondly, we allow for changes in the late time cosmology, in particular in the expansion history at $z \leq 1.3$, assuming standard early cosmology (i.e., physics is standard until recombination, but the expansion history at late time is allowed to be non-standard). Finally, we reconstruct in a model-independent way, the late-time expansion history without making any assumption about the early-time physics, besides assuming that the BAO scale corresponds to a standard ruler (with unknown length). By combining BAO with SNeIa and H_0 measurements we are able to measure the standard ruler in a model-independent way. Comparison with the Planck-derived determination of the sound horizon at radiation drag allows us to assess the consistency of the two measurements within the assumed cosmological model.

In section 2 we present the data sets used in this work and in section 3 we describe the methodology. We explore modifications of early-time physics from the standard ΛCDM (leaving unaltered the late-time ones) in section 4 while changes in the late-time cosmology are explored in section 5. Here we present the findings both assuming standard early-time physics and in a way that is independent from it. Finally we summarize the conclusions of this work in section 6.

2 Data

The observational data we consider are: measurements of the Cosmic Microwave Background (CMB), Baryon Acoustic Oscillations (BAO), Type Ia Supernovae (SNeIa) and direct measurements of the Hubble constant H_0.

We consider the full Planck 2015 temperature (TT), polarization (EE) and the cross correlation of temperature and polarization (TE) angular data [3], corresponding to the following likelihoods: *Planck* high ℓ ($30 \leq \ell \leq 2508$) TTTEEE for TT (high ℓ TT), EE and TE (high ℓ TEEE) and the *Planck* lowℓ for TT, EE, TE and BB (lowP, $2 \leq \ell \leq 29$). The Planck team [3, 32] identifies the lowP + high ℓ TT as the "recommended baseline" dataset and the high ℓ polarisation (high ℓ TEEE) as "preliminary", because of evidence of low level systematics ($\sim (\mu K)^2$ in $\ell(\ell+1)C_\ell$). While the level of systematic contamination does not appear to affect parameter estimation, we nevertheless present results both excluding and including the high ℓ polarisation data. In addition, we use the lensing reconstruction signal for the range $40 \leq L \leq 400$, which we refer to as CMB lensing. For some models we use the publicly available posterior samples (i.e., public chains) provided by the Planck collaboration: ΛCDM, ΛCDM+$N_{\rm eff}$ (a base ΛCDM model with an extra parameter for the effective number of neutrino species) and ΛCDM $+Y_P^{\rm BBN}$ (a base ΛCDM model with an extra parameter for the primordial Helium abundance). In addition, we use the analysis of WMAP9 data with the same assumptions of Planck, which is publicly available along with the rest of Planck data. We also use the results of Addison et al. [25], where the Planck's temperature power spectrum is analysed in two separate multipole ranges: $\ell < 1000$ and $\ell \geq 1000$.

We use constraints on BAO from the following galaxy surveys: Six Degree Field Galaxy Survey (6dF) [33], the Main Galaxy Sample of Data Release 7 of Sloan Digital Sky Survey (SDSS-MGS) [34], the LOWZ and CMASS galaxy samples of the Baryon Oscillation Spectroscopic Survey (BOSS-LOWZ and BOSS-CMASS, respectively) [5], and the reanalysed measurements of WiggleZ [35]. These measurements, and their corresponding effective redshift $z_{\rm eff}$, are summarized in table 1. Note that for BOSS-CMASS there is an isotropic

Survey	$z_{\rm eff}$	Parameter	Measurement
6dF [33]	0.106	$r_{\rm s}/D_V$	0.327 ± 0.015
SDSS-MGS [34]	0.15	$D_V/r_{\rm s}$	4.47 ± 0.16
BOSS-LOWZ [5]	0.32	$D_V/r_{\rm s}$	8.59 ± 0.15
WiggleZ [35]	0.44	$D_V/r_{\rm s}$	11.6 ± 0.6
BOSS-CMASS [5]	0.57	$D_V/r_{\rm s}$	13.79 ± 0.14
BOSS-CMASS [5]	0.57	$D_A/r_{\rm s}$	9.52 ± 0.14
BOSS-CMASS [5]	0.57	$Hr_{\rm s}$	14750 ± 540
WiggleZ [35]	0.6	$D_V/r_{\rm s}$	15.0 ± 0.7
WiggleZ [35]	0.73	$D_V/r_{\rm s}$	16.9 ± 0.6

Table 1. BAO data measurements included in our analysis, specifying the survey that obtained each measurement and the corresponding effective redshift $z_{\rm eff}$. In the case where we change the late time cosmology, we use the isotropic measurements. We take into account the correlation between the anisotropic measurements of BOSS-CMASS and among the values from WiggleZ.

measurement ($D_V/r_{\rm s}$) and an anisotropic measurement ($D_A/r_{\rm s}$, $Hr_{\rm s}$), which, of course, we never combine. When we use the anisotropic values from BOSS-CMASS in section 4, we take into account that they are correlated (their correlation coefficient is 0.55). We use the covariance matrix for the measurements of WiggleZ as indicated in ref. [35]. We consider that the measurements of BOSS-CMASS and WiggleZ are independent, although the regions covered by both surveys overlap. We can do so because this overlap includes a small fraction of the BOSS-CMASS sample and the correlation is very small too (always below 4%) [5, 36], hence the constraints which come from both surveys are fairly independent. The BOSS collaboration also provides a BAO measurement at $z \sim 2.5$ obtained from Lymanα forest observed in Quasars spectra. We do not include this measurement because, as it will be clear later, our approach relies on having BAO and SNeIa data covering roughly the same redshift range. Considering an extra BAO point at high redshift would have increased the number of parameters needed to describe the expansion history without improving constraints in any of the quantities we are interested in.

The publicly available Planck 2015 posterior sampling uses a slightly different BAO data set (see ref. [3] for details). However the small difference in the data set does not drive any significant effect in the parameter constraints.

For SNeIa cosmological observations, we use the SDSS-II/SNLS3 Joint Light-curve Analysis (JLA) data compilation [37]. This catalog contains 740 spectroscopically confirmed SNeIa obtained from low redshift samples ($z < 0.1$), all three seasons of the Sky Digital Sky Survey II (SDSS-II) ($0.05 < z < 0.4$) and the three years of the SuperNovae Legacy Survey (SNLS) ($0.2 < z < 1$) together with nine additional SNeIa at high redshift from HST ($0.8 < z < 1.3$). We use the compressed form of the JLA likelihood (appendix E of ref. [37]).

Finally, we use the distance recalibrated direct measurement of H_0 from [20], which is $H_0 = 73.24 \pm 1.74$ Mpc^{-1}km/s.

3 Methods

We use the public Boltzmann code CLASS [38, 39] and the Monte Carlo public code Monte Python [40] to analyse the CMB data sets discussed in section 2 when for the selected model there are no posterior samples officially provided by the Planck collaboration. We modify the codes to include the parametrized extra dark radiation, $\Delta N_{\rm eff}$ and the effective parameters to describe its behaviour, $c_{\rm s}^2$ and $c_{\rm vis}^2$ (section 4) additional parameters to the Planck "base" model.[2] We adopt uniform priors for all the parameters, except for $\Delta N_{\rm eff}$, for which we sample $\Delta N_{\rm eff}^2$ (see section 4). We only set a lower limit in the sampling range for A_s, n_s, τ and $\Delta N_{\rm eff}$ (0.0 in all cases but for τ, which is 0.04). The prior in τ has virtually no effect on the reported constraints and is justified by observations of the Gunn-Peterson effect, see e.g., ref. [41]. Our sampling method of choice when CMB data are involved is the Metropolis Hastings algorithm; we run sixteen Monte Carlo Markov Chains (MCMC) for each ensemble of data sets until the fundamental parameters reach a convergence parameter $R - 1 < 0.03$, according to the Gelman-Rubin criterion [42].

When interpreting the low redshift probes of the expansion history (see section 5), we use a different methodology. We aim to reconstruct $H(z)$ (the main observable related with the expansion of the Universe) in the most model-independent way possible, but still requiring a smooth expansion history. For this reason the Hubble function is expressed as piece-wise natural cubic splines in the redshift range $0 \leq z \leq 1.3$. We specify the spline function $H^{\rm recon}(z)$ by the values it takes at N "knots" in redshift. These values uniquely define the piecewise cubic spline once we ask for continuity of $H^{\rm recon}(z)$ and its first and second derivatives at the knots, and two boundary conditions. We require the second derivative to vanish at the exterior knots. Thus, our free parameters are the values of $H^{\rm recon}(z_{\rm knot})$, where $z_{\rm knot}$ are the redshifts correspondent to the "knots". We also consider cases in which we vary the sound horizon at radiation drag and the curvature of the Universe (via $\Omega_{\rm k}$). The location of the knots is arbitrary and we place them at $z = [0, 0.2, 0.57, 0.8, 1.3]$ to match the BAO data constraining power and encompass the SNeIa redshift range. When SNeIa are not included, we limit the fit of $H^{\rm recon}(z)$ to the range $0 \leq z \leq 0.8$ (and vary one less parameter).

We set uniform priors for all the parameters, with limits which are never explored by the MCMC. We use the public `emcee` code [43], which implements the Affine Invariant Markov Ensemble sampler as sampling method [44] to fit the splines to the cosmological measurements discussed in the previous section. To obtain the likelihood of each position in the parameter space, we integrate the correspondent $H^{\rm recon}(z)$ to compute $D_V(z)$ and luminosity distance $D_L(z)$ and calculate the χ^2 for BAO and SNeIa, respectively. In addition, we fit $H^{\rm recon}(z=0)$ to the direct measurement of H_0. We run 500 walkers for 10000 steps each and remove the first 400 steps from each walker (as burn-in phase), as this interval corresponds to several autocorrelation times.

In section 5.1, we quantify the tension between the different joint constraints on the plane H_0-$r_{\rm s}$ following [10]. This method is based on the evidence ratio of the product of the distributions with respect to the –ideal , and ad hoc– case when the maxima of the posteriors coincide (maintaining shape and size).

Then, if we call P_A to the posterior of the experiment A and $\mathcal{E}$ to the 'unnormalized' evidence, and with a bar we refer to the shifted case,

$$\mathcal{T} = \frac{\bar{\mathcal{E}}\,|_{\max A = \max B}}{\mathcal{E}} = \frac{\int \bar{P}_A \bar{P}_B dx}{\int P_A P_B dx}. \tag{3.1}$$

$\mathcal{T}$ is the degree of tension and can be interpreted in the modified Jeffrey's scale. The odds for the null hypothesis (i.e. both posteriors are fully consistent) are $1 : \mathcal{T}$.

---

[2] The Planck "base" model is a flat, power law power spectrum ΛCDM model with three neutrino species, with total mass 0.06eV).

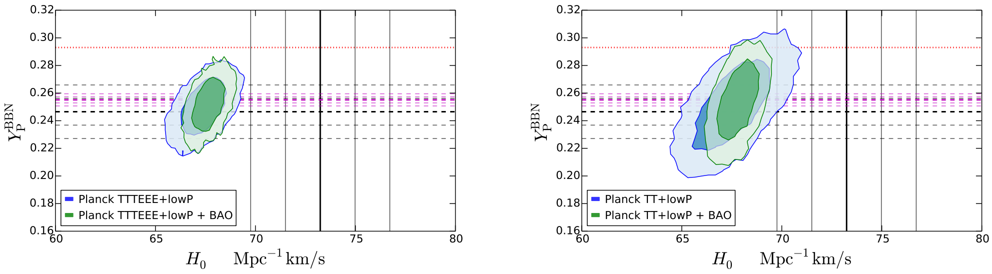

Figure 2. 68% and 95% confidence joint constraints in the H_0-Y_P^{BBN} parameter space for Planck 2015 using temperature and polarization power spectra (left) and without include high ℓ polarization data (right). The vertical bands correspond to the local H_0 measurement [20]. The horizontal black dashed lines correspond to the measurement (mean and 1 and 2 σ) of the primordial abundance of [45], and in magenta of [46], both from chemical abundances in metal-poor HII regions. The red dotted horizontal line is the 2 σ upper limit of the recent measurement of initial Solar helium abundance of [47].

4 Modifying early Universe physics: effect on H_0 and r_s

It is well known that there are two promising ways to alter early cosmology so that the tension between CMB-inferred value and measured value of H_0 is reduced. These are changing the early time expansion history and changing the details of recombination.

Changes in the details of nucleosynthesis can be captured by changes in the primordial Helium mass fraction, parametrised by Y_P^{BBN}. In the standard analyses, since the process of standard big bang nucleosynthesis (BBN) can be accurately modelled and gives a predicted relation between Y_P^{BBN}, the photon-baryon ratio, and the expansion rate, the value of Y_P^{BBN} is computed consistently with BBN for every model sampled, but one can also relax any BBN prior and let Y_P^{BBN} vary freely, which has an influence on the recombination history and affects CMB anisotropies mainly through the redshift of last scattering and the diffusion damping scale. The effect of this extra degree of freedom on the inferred value of H_0 can be seen in figure 2 (obtained using the publicly released Planck team's MCMC), the local H_0 measurement [20], and the measurements (mean and 1 and 2 σ) of the primordial abundance of [45] and [46] (which is less conservative) from chemical abundances in metal-poor HII regions and the conservative 95% upper limit of the measured initial Solar helium abundance of [47].

Even varying Y_P^{BBN} without a BBN prior, the joint H_0-Y_P^{BBN} constraints are in a $\sim 2.7\sigma$ disagreement (when using lowP and high ℓ TTTEEE) with the new measurement of H_0 [20]. If high ℓ polarization data is not included, the tension is reduced because of the larger error bars. However, the constraints from Planck are not in agreement with both H_0 and primordial abundance measurements at the same time, even considering the more conservative measurement of [45].

Changes on the early time expansion history are usually enclosed in the parameter $N_{\rm eff}$: the effective number of relativistic species. For three standard neutrinos $N_{\rm eff} = 3.046$,[3] [48]. In fact light neutrinos are relativistic at decoupling time and they behave like radiation: changing $N_{\rm eff}$ changes the composition of the energy density, changing therefore the early

---

[3] The number of (active) neutrinos species is 3, the small correction accounts for the fact that the neutrino decoupling epoch was immediately followed by e^+e^- annihilation.

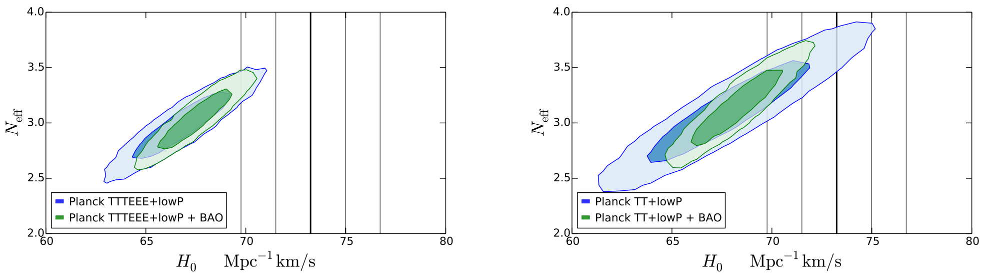

Figure 3. Confidence regions (68% and 95%) of the joint constraints in the H_0-$N_{\rm eff}$ parameter space for Planck 2015 data (blue) and Planck 2015 + BAO data (green) using full temperature and polarization power spectra (left) and without including high ℓ polarization data (right). Here all species behave like neutrinos when perturbations are concerned. The vertical bands correspond to the local H_0 measurement [20].

expansion history. This has been called "dark radiation" but it can mimic several other physical effects see e.g., [49–60]. For example a model such as the one proposed in [51] of a thermalized massless boson, has a $\Delta N_{\rm eff}$ between $\sim$ 0.57 and 0.39 depending on the decoupling temperature [3].

If we define $\Delta N_{\rm eff}$ as $N_{\rm eff} - 3.04$, it is well known that a $\Delta N_{\rm eff} > 0$ would increase the CMB-inferred H_0 value, bringing it closer to the locally measured one. This can be appreciated in figure 3, where we show the results of Planck 2015 for a model where $N_{\rm eff}$ is an additional free parameter and the extra radiation behaves like neutrinos. In the H_0-$N_{\rm eff}$ parameter space we show the joint 68% and 95% confidence regions for Planck 2015 data (blue) and Planck 2015 + BAO data (green) obtained from the Planck team's public chains, both using polarization and temperature power spectra (left) or just temperature power spectrum and lowP (right). The vertical bands correspond to the local H_0 measurement [20].

A high value of $N_{\rm eff}$ ($\Delta N_{\rm eff} \sim 0.4$) would alleviate the tension in H_0 and still be allowed by the Planck lowP and high ℓ temperature power spectra and BAO data as pointed out in [20]. The "preliminary" high ℓ polarization data, disfavours such large $\Delta N_{\rm eff}$ (at $\sim 2\sigma$ level), as polarization constrains strongly the effective number of relativistic species.

This is however not the full story. State-of-the-art CMB data have enough statistical power to measure not just the effect of this $N_{\rm eff}$ on the expansion history but also on the perturbations. Neutrino density/pressure perturbations, bulk velocity and anisotropic stress are additional sources for the gravitational potential via the Einstein equations (see e.g., [61–63]). The effect on the perturbations is described by the effective parameters sound speed and viscosity c_s^2, $c_{\rm vis}^2$ [64–67]. Neutrinos have $\{c_s^2, c_{\rm vis}^2\} = \{1/3, 1/3\}$, but other values describe other physics, for example a perfect relativistic fluid will have $\{1/3, 0\}$ and a scalar field oscillating in a quartic potential $\{1, 0\}$. Different values of c_s^2 and $c_{\rm vis}^2$ would describe other dark radiation candidates. This parametrisation is considered flexible enough for providing a good approximation to several alternatives to the standard case of free-streaming particles e.g., [68, 69].

Recent analyses have shown that if all $N_{\rm eff}$ species have the same effective parameters c_s^2, $c_{\rm vis}^2$, Planck data constraints are tight [3, 70]: $c_s^2 = 0.3240 \pm 0.0060$, $c_{\rm vis}^2 = 0.327 \pm 0.037$ (with fixed $N_{\rm eff} = 3.046$; Planck 2015). Moreover, the $N_{\rm eff}$ constraints are not significantly affected compared to the standard case: $N_{\rm eff} = 3.22^{+0.32}_{-0.37}$ ([70]) against $N_{\rm eff} = 3.13 \pm 0.31$

	$N_{\rm eff}$	c_s^2	$c_{\rm vis}^2$	H_0
lowP+TTTEEE	2.96 ± 0.23	0.324 ± 0.006	0.33 ± 0.04	67.2 ± 1.9
lowP +TTTEEE+ lensing	2.91 ± 0.21	0.325 ± 0.006	0.33 ± 0.04	67.0 ± 1.8
lowP +TTTEEE+lensing+BAO	2.94 ± 0.18	0.325 ± 0.006	0.33 ± 0.04	67.2 ± 1.3

Table 2. Marginalised mean and 68% confidence level errors for the parameters of interest for the different combinations of data.

(Planck 2015) at 68% confidence level, both using CMB temperature data and CMB lensing. We update the results of [70] by using Planck 2015 power spectra (lowP + high ℓ TTTEEE) instead of Planck 2013. Results can be seen in table 2. Using state-of-the-art observations, the constraints on are even tighter than in [70] and are driven by the high ℓ polarisation data. As the polarisation analysis is "preliminary" these results should be considered preliminary too. In all the cases studied, there is no significant shift in the central value of H_0. There is no evidence for the main component of the relativistic species behaving differently from a standard neutrino, and this extension does not alleviate the tension in H_0 significantly (tension is reduced only because extending the model results in a slightly larger uncertainty in H_0).

The fact that when leaving c_s^2, $c_{\rm vis}^2$ as free parameters in the analysis one recovers tight constraints consistent with $\{1/3, 1/3\}$ and $N_{\rm eff} = 3.04$ is a good confirmation of the existence of a cosmic neutrino background. However, this does not exclude the possibility of the existence of extra relativistic species (i.e., dark radiation) with different behaviour than neutrinos. Their presence could be masked in the analysis by the dominant component, the cosmic neutrino background. Thus next, we shall assume that there are three neutrino families in the Universe (i.e., that the 3.04 effective species have $\{c_s^2, c_{\rm vis}^2\}$=$\{1/3, 1/3\}$) and that any extra dark radiation $\Delta N_{\rm eff}$ component has free effective sound and viscosity parameters. We have modified the publicly available CLASS code [38, 39] to implement this. In figure 4 we show the qualitative effects on the CMB power spectra of the parameters describing this extra dark radiation component.

Given that for $\Delta N_{\rm eff} \sim 0$ there is almost no difference in the likelihood for different values of c_s^2 and $c_{\rm vis}^2$, the MCMC tend to be stuck in that zone of the parameter space.[4] To prevent it, we sample $\Delta N_{\rm eff}^2$ instead. We find that, once 3.046 standard neutrinos are fixed, the presence of extra relativistic species, even giving freedom to the behaviour of their perturbations, is not favoured by the data. The constraints on $c_{\rm vis}$, c_s are very weak because of the strong upper limit on $\Delta N_{\rm eff}$. The results are summarized in table 3, with the upper limits of $\Delta N_{\rm eff}$ at 95% of confidence level. We also report the values for the $\Omega_{\rm M} - \sigma_8$ combination, as this is very similar to what galaxy clusters or weak gravitational lensing constrain. While $\Delta N_{\rm eff}$ and σ_8 are slightly correlated (an increase of 0.5 in $\Delta N_{\rm eff}$ increases σ_8 by 0.03) the constraint on the $\Omega_{\rm M} - \sigma_8$ combination do not depend on the limits on $\Delta N_{\rm eff}$. The joint constraints on $\Delta N_{\rm eff}$ and H_0 are shown in figure 5.

Should the low-level systematic present in the polarisation data be found to be subdominant in the published error-budget, this finding implies that there is not much room for an extra component in the early universe whose density scales with the expansion like radiation but whose perturbations have the freedom to behave like a perfect fluid, a neutrino,

---

[4] For the parameters $c_{\rm vis}^2$ and c_s^2 we limit the sampling to the range $[0.0, 1.1]$. That is because values higher than one are not physical and this way we also optimize the performance of the analysis, since we do not explore the parameter space where these values are allowed to be very large in the region close to $\Delta N_{\rm eff} = 0$.

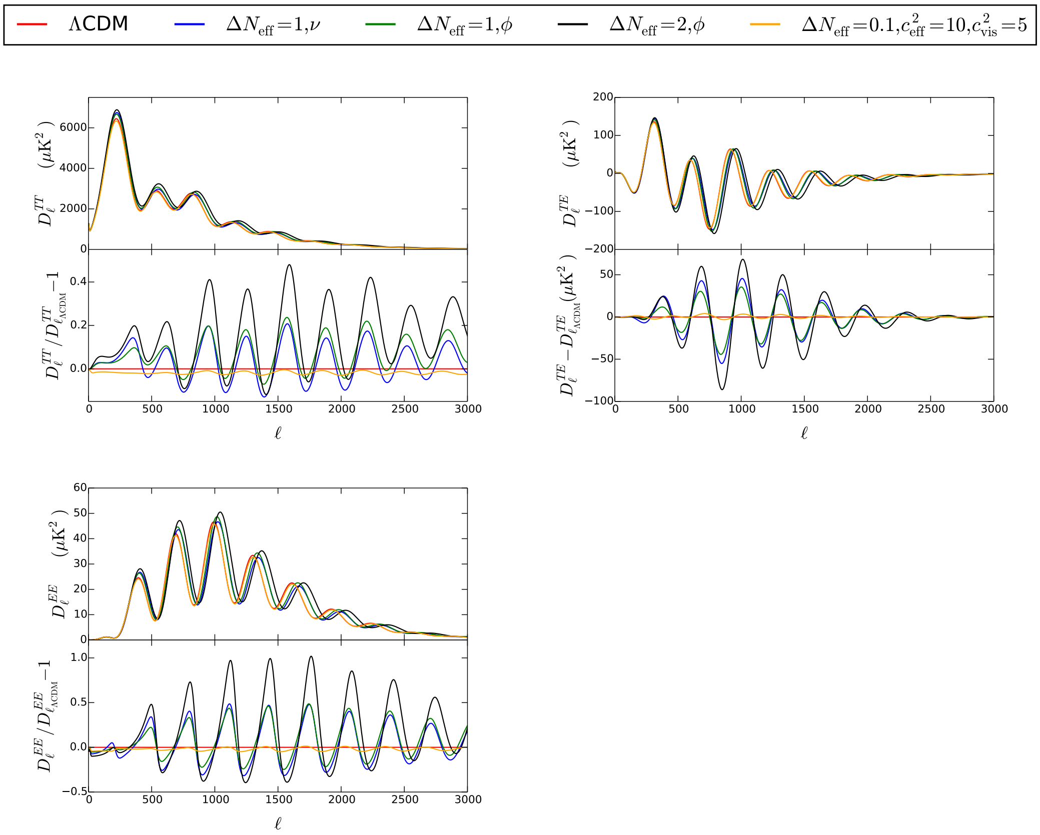

Figure 4. CMB temperature (*left*), temperature and polarization cross correlation (*right*) and polarization (*bottom*) power spectra predictions for ΛCDM (red) and the following extensions: one more neutrino (blue), one scalar field (green), two scalar fields (black) and a illustrative case with extreme (non physical) values of c_s^2 and $c_{\rm vis}^2$ with $\Delta N_{\rm eff} = 0.1$ (orange).

	$\Delta N_{\rm eff}$	c_s^2	$c_{\rm vis}^2$	H_0	$(\Omega_{\rm M}/0.3)^{0.5}\,\sigma_8$
lowP+ TTTEEE	< 0.36	$0.25^{+0.07}_{-0.15}$	$0.12^{+0.58}_{-0.11}$	$68.9^{+1.1}_{-0.9}$	$0.85^{+0.02}_{-0.02}$
lowP+ TTTEEE+CMB lensing	< 0.34	$0.24^{+0.10}_{-0.13}$	0.49 ± 0.33	$68.9^{+1.2}_{-0.9}$	$0.83^{+0.02}_{-0.01}$
lowP+ TTTEEE+CMB lensing+BAO	< 0.28	$0.26^{+0.09}_{-0.16}$	$0.28^{+0.45}_{-0.26}$	$68.7^{+0.6}_{-0.7}$	$0.84^{+0.01}_{-0.02}$
lowP + TT	< 0.76	$0.25^{+0.08}_{-0.10}$	$0.84^{+0.20}_{-0.51}$	$70.6^{+2.6}_{-2.0}$	$0.84^{+0.03}_{-0.04}$
lowP+ TT+CMB lensing	< 0.77	$0.27^{+0.07}_{-0.11}$	$0.81^{+0.19}_{-0.50}$	$71.3^{+1.9}_{-2.2}$	$0.82^{+0.02}_{-0.01}$
lowP+ TT+CMB lensing+BAO	< 0.44	$0.29^{+0.20}_{-0.16}$	$0.9^{+0.1}_{-0.7}$	$69.0^{+0.9}_{-0.8}$	$0.84^{+0.01}_{-0.02}$

Table 3. Marginalised constraints for the parameters of interest for the different combinations of data. We report the the upper limit for $\Delta N_{\rm eff}$ (95% confidence level) and the highest posterior density intervals for the rest of the parameters.

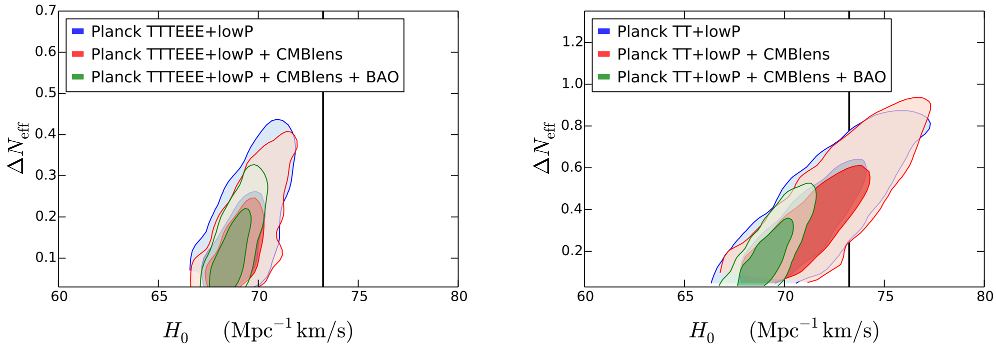

Figure 5. Marginalized 68% and 95% confidence level constraints in the $\Delta N_{\rm eff}$-H_0 plane. *Left*: Planck data including full temperature and polarization power spectra. *Right*: excluding high ℓ polarisation. We report results using Planck 2015 power spectra (blue), adding CMB lensing (red) and adding also BAO (green). The vertical black bands correspond to the local H_0 measurement [20]. Note the change in the scale of the y axis in each plot.

a scalar field or anything in between. This offers a useful confirmation of one of the key standard assumptions on which the standard cosmological model is built. Also in this more general model, of the CMB data, it is the high-ℓ polarisation what disfavor high values of H_0. On the other hand, the freedom on the nature of the extra relativistic species produces a small shift in H_0 towards higher values and, when high ℓ polarization data of the CMB are not included, our constraints are fully compatible with the direct measurement (right panel of figure 5). However, when BAO data are included, the constraint on $\Delta N_{\rm eff}$ is tighter, because the degeneracy with $\Omega_{\rm M}$.

5 Changing late-time cosmology

The CMB is sensitive to both late and early cosmology. When fitting the CMB power spectrum simultaneous assumptions about the early and late cosmology must be made, with the implication that the physics of both epochs are entwined in the resulting constraints. Then, it is difficult to determine what physics beyond ΛCDM would be the responsible of possible deviations from the model. Exploring non-standard late cosmology evolution, possibly in a minimally-parametric or model independent way is in general complicated if CMB constraints are to be included. There is however a way to analyse CMB data so that it is sensitive only to early cosmology as shown in [71–73]: the resulting constraints do not depend on late-time physics and can therefore be included when analysing late-time data in a model-independent way. The latest CMB Planck data were analysed in this way in [74], where a variety of models of the early Universe are studied. Here we use their results – obtained assuming standard early-time physics (i.e. a flat Universe composed of baryons, radiation, standard neutrinos, cold dark matter and dark energy in the form of cosmological constant from deep in the radiation era down to recombination)– in the form of a constraint on the sound horizon at radiation drag: $r_{\rm s}^{\rm early} = 147.00 \pm 0.34$ Mpc.

To reconstruct $H(z)$, we use BAO and SNeIa data along with the measured value of H_0 and $r_s^{\rm early}$. The only assumptions made are that the expansion history of the Universe is smooth and continuous, that the spatial section of the Universe is flat, that SNeIa form an homogeneous group such as they can be used as standard candles and that the sound horizon at radiation drag, r_s, is a standard ruler which calibrates the cosmic distance scale given by BAO observations ([6, 30, 31]). We also consider the case in which the assumption about the geometry of the Universe is relaxed. With this minimal assumptions, H_0 and r_s are treated only as the calibration of the cosmic distance ladder and they are related by $H_0 r_\mathrm{s} = \mathrm{constant}$.

Without any assumption about the geometry of the Universe, the comoving distance χ is related to the Hubble parameter by

$$\chi(z) = \frac{c}{H_0\sqrt{|\Omega_\mathrm{k}|}} \mathcal{S}_\mathrm{k}\left(\sqrt{|\Omega_\mathrm{k}|} H_0 \int_0^z \frac{dz'}{H(z')}\right), \tag{5.1}$$

where $\mathcal{S}_\mathrm{k}(x) = \sinh(x)$, x or $\sin(x)$ for $\Omega_\mathrm{k} > 0$, $= 0$ or < 0, respectively. Then, the angular diameter distance and the luminosity distance are

$$D_A(z) = \frac{\chi(z)}{(1+z)}, \qquad D_l(z) = (1+z)\chi(z). \tag{5.2}$$

BAO observations provide measurements of D_V, which is related to $H(z)$ by

$$D_V(z) = \left[cz\,(1+z)^2 D_A(z)^2 H(z)^{-1}\right]^{1/3} = \left[cz\left(\int_0^z \frac{c dz'}{H(z')}\right)^2 H(z)^{-1}\right]^{1/3}, \tag{5.3}$$

where the last identity is true only when flatness is assumed. While it is customary to parametrise dark energy properties via the equation of state parameter $w(z)$, it should be evident that the observable quantity is $H(z)$. Afterwards, to convert $H(z)$ into $w(z)$ a model for dark energy must be assumed as well as a value for Ω_m:

$$H(z) = (1+z)^{3/2}\sqrt{\Omega_m + \Omega_\mathrm{DE}\exp\left[3\int_0^z \frac{w(z')}{1+z'}dz'\right]}, \tag{5.4}$$

here Ω_DE is the density parameter for the dark energy and flatness is assumed.

For our model-independent reconstruction of the late-time expansion history where the Hubble parameter is expressed in piece-wise natural cubic splines, $H(z)$ is specified by the values it takes at N "knots" in redshift; $N = 4$ for BAO only analysis and $N = 5$ when SNeIA are included. This parametrisation allows for smooth and relatively generic expansion histories. As indicated in [37] for the compressed data set of supernovae, we allow an offset in the absolute magnitude compared with the standard value, ΔM, treated as a free (nuisance) parameter.

We summarize the results of our analysis (mean and 68% confidence intervals) in table 4. In the following figures (figures 6–8) we show the best fit of our reconstruction of $H(z)$ (black line), the 68% confidence region obtained by plotting the curves corresponding to 500 points of the chain randomly selected from the 68% with highest likelihood (red) and the Hubble parameter corresponding to the ΛCDM prediction using the best fit values of Planck 2015 with lensing [3] (blue). The dashed blue line is the ΛCDM prediction using $H_0 = 73.0$ Mpc^{-1}km/s instead of the Planck 2015 inferred value. In the plots, data are shown in green and the predictions of the observables using $H^\mathrm{recon}(z)$ in black (bestfit) and red (68% region). In this case we show ratios with respect ΛCDM prediction for clarity. The vertical grey lines mark the position of the "knots".

Data sets	$H(z=0)$	$H(z=0.2)$	$H(z=0.57)$	$H(z=0.8)$	$H(z=1.3)$	r_s	ΔM
H_0+BAO+$r_\mathrm{s}^\mathrm{early}$	72.3 ± 1.7	72.9 ± 1.9	96.4 ± 2.5	102.5 ± 14.0	–	–	–
H_0+SN	73.2 ± 1.8	81.0 ± 2.5	99.3 ± 4.4	107.0 ± 9.0	161.9 ± 73.1	–	0.10 ± 0.06
H_0+BAO +$r_\mathrm{s}^\mathrm{early}$+SN	69.4 ± 1.0	75.5 ± 1.2	94.0 ± 1.8	101.2 ± 6.2	150.1 ± 62.9	–	-0.03 ± 0.03
H_0+BAO(*)+SN	73.1 ± 1.8	80.6 ± 2.4	101.5 ± 3.8	109.3 ± 7.6	143.7 ± 59.7	136.8 ± 4.0	0.10 ± 0.06
H_0+BAO+$r_\mathrm{s}^\mathrm{early}$+SN(∘)	$69.6^{+1.1}_{-1.3}$	75.6 ± 1.2	94.0 ± 4.1	101.1 ± 11.2	147.1 ± 89.3	–	-0.03 ± 0.04
H_0+BAO(*)+SN(∘)	$73.4^{+1.5}_{-2.0}$	83.0 ± 3.0	111.9 ± 8.9	130.0 ± 17.8	237.9 ± 123.4	133.0 ± 4.7	0.10 ± 0.06
BAO+$r_\mathrm{s}^\mathrm{early}$+SN(∘)	$66.3^{+1.7}_{-1.7}$	75.1 ± 1.1	101.2 ± 5.7	118.1 ± 13.9	215.9 ± 112.0	–	-0.11 ± 0.05

Table 4. Marginalized mean and 68% confidence regions for the parameters included in the reconstruction for each of the combinations of data sets we consider. When reporting asymmetric errors, we report the highest posterior density value for H_0. The last column corresponds to ΔM, the offset in the absolute magnitude compared with the standard value. We report it here to show that the supernovae absolute magnitude is not significantly shifted away from its value determined internally by external the data. the "*" symbol indicate that no CMB-derived r_s prior is used. The symbol "∘" indicates that Ω_k is left as a free parameter.

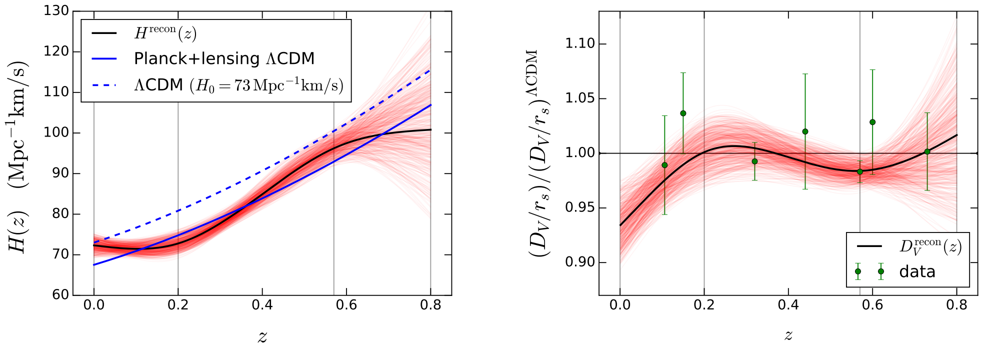

Figure 6. *Left*: results of the reconstruction of $H(z)$ using the direct measurement of H_0 of [20] and the BAO data set. *Right*: BAO data included in the reconstruction. We plot $(D_V/r_\mathrm{s})r_\mathrm{s}^\mathrm{early}$ data points and the D_V obtained with the corresponding $H^\mathrm{recon}(z)$.

Figure 6 shows the reconstruction of $H^\mathrm{recon}(z)$ and $D_V(z)$ for the analysis of BAO and H_0 [20] data with the $r_\mathrm{s}^\mathrm{early}$ prior. While in a ΛCDM model $H(z)$ is monotonically increasing with redshift, here $H^\mathrm{recon}(z)$ is almost constant in the range $0 < z < 0.2$ to match the local H_0 determination to the distance measurements which are "anchored" by $r_\mathrm{s}^\mathrm{early}$, predicting a sharper acceleration at low redshift. Given that the lowest redshift sampled by the BAO data is $z = 0.106$, H_0 is determined mostly by the direct measurement of [20]. Using the formalism described in section 3, we can quantify the significance of this feature with respect to the Planck 2015 ΛCDM $H(z)$ distribution. We consider various redshifts ($z = 0$, 0.2 and 0.57 which we select to coincide with the knots) yielding a multivariate distribution. With this choice the odds of obtaining the same results are 1:49. Although the results would be different depending on the chosen redshifts, we consider that this choice is representative and the results will not vary qualitatively with another reasonable choice. This applies for all the cases studied here.

In figure 7 we show the results for the reconstruction of $H(z)$ using SNeIa and H_0. We show $H^\mathrm{recon}(z)$ and the distance modulus. The redshift sampling of SNIa data is much

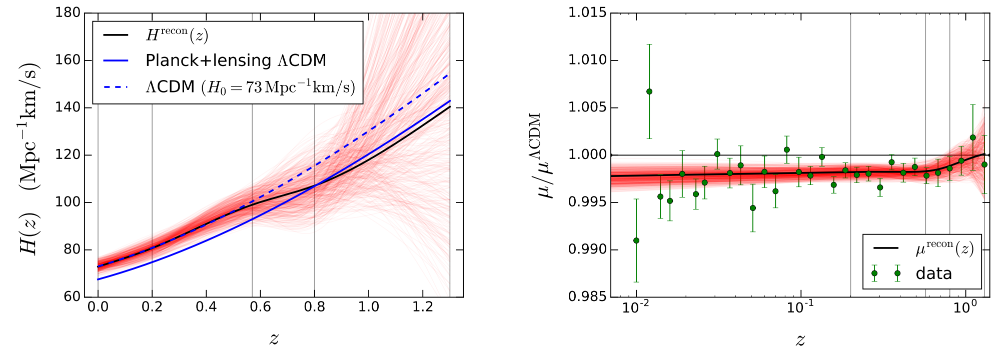

Figure 7. *Left*: results of the reconstruction of $H(z)$ using the direct measurement of H_0 of [20] and the SNeIa data set. *Right*: SNeIa data included in the reconstruction (green). We plot the distance modulus, μ, obtained with the corresponding $H^{\rm recon}(z)$. The plotted errorbars correspond to the square root of the diagonal of the covariance matrix (we account correctly for the actual correlation among bins in the analysis).

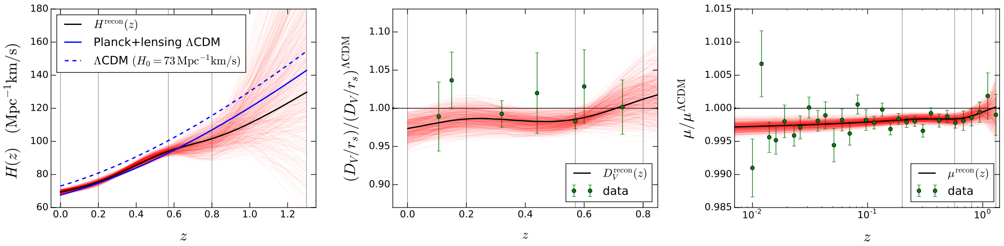

Figure 8. *Left*: results of the reconstruction of $H(z)$ using the direct measurement of H_0 of [20], BAO and SNeIa data set with a CMB-derived $r_{\rm s}$ prior. *Middle and right*: observational data included in the reconstruction (green), as in the previous cases, and the prediction using the corresponding $H^{\rm recon}(z)$.

denser than BAO: this constrains the shape of $H^{\rm recon}(z)$, but not the normalisation (as the analysis marginalises over the supernovae absolute magnitude) which is anchored at $H_0 \sim 73$ Mpc^{-1}km/s by the H_0 measurement. The reconstructed shape is very close to the ΛCDM until the data sampling is sparser ($z \gtrsim 0.6$) and errors grow. The odds of SNeIa reconstructed $H(z)$ shape compared to the one obtained using only BAO, H_0 and $r_{\rm s}^{\rm early}$ are 1:52.

Finally, when using the combination H_0, SNeIa and BAO with our $r_{\rm s}^{\rm early}$ prior (figure 8), SNeIa observations constrain the shape of $H^{\rm recon}(z)$ but the normalization tries to fit H_0 and BAO (via $r_{\rm s}^{\rm early}$) at the same time. The H_0 measurement has a 2.4% error, but the $r_{\rm s}^{\rm early}$ determination a 0.23% error: the statistical power of the BAO normalisation shifts the recovered $H^{\rm recon}(z = 0)$ to lower values compared to the local determination (and closer to the Planck-inferred value under a ΛCDM model). Remarkably, given the freedom that the cubic splines have, our reconstruction of $H(z)$ is close to the ΛCDM prediction. In this case, the odds compared to the shape obtained using only BAO, $r_{\rm s}^{\rm early}$ and H_0 are 1:6, as this is an intermediate solution between the standard ΛCDM shape with low H_0 and the wiggly reconstruction obtained above.

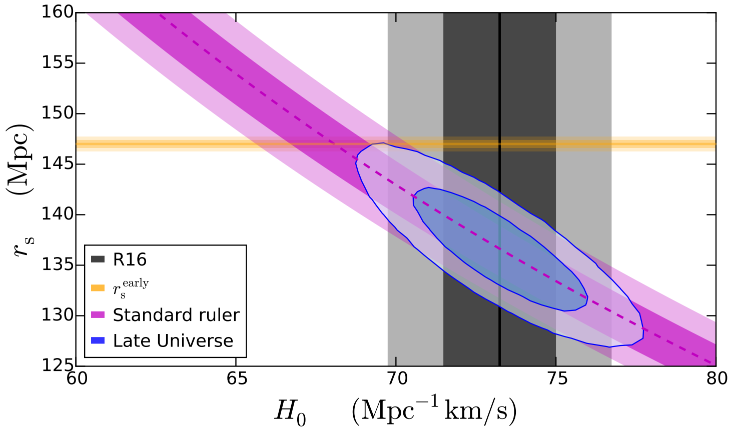

Figure 9. Without an absolute distance scale, such as an H_0 determination, the low redshift standard ruler measurement constrains the combination $r_s h$, and thus $r_s H_0$ which appears as a (purple) band. This measurement does not include the prior on $r_s^{\rm early}$. The local H_0 measurement (gray) can be used to break the degeneracy (yielding the blue confidence regions).

To summarise, when using the local H_0 measurement and BAO data normalised to the CMB-derived $r_s^{\rm early}$ under standard early Universe assumptions, the reconstruction indicates a sharp increase in the cosmic acceleration rate ($H(z)$ ∼constant) at $z < 0.2$, where the BAO data have little statistical power. A dark energy equation of state parameter $w < -1$ (or dropping recently below -1) would fit the bill. However, when including SNeIa the shape of the expansion history is constrained not to deviate significantly from that of ΛCDM (at $z < 0.6$ where there are many data points) and thus only the normalisation can adjust, taking a value intermediate between the low and high redshift "anchors", as $H_0 r_s \approx$ constant. Thus a phantom dark energy is not favoured by the data. Below we will show that relaxing the flatness assumption does not change the results qualitatively.

5.1 Reconstruction independent from the early-time physics

To remove the dependence on the early Universe assumptions introduced by the high redshift BAO anchor, we now treat r_s as a free parameter in our analysis without including the prior of the early Universe of $r_s^{\rm early}$. We consider the data set combination H_0, BAO(*) and SNeIa (hereafter the "*" symbol indicate that no CMB-derived $r_s^{\rm early}$ prior is used).

This is illustrated in figure 9. The low redshift standard ruler measurement constrains the combination $r_s h$ which is reported here as a band in the H_0-r_s plane, constraining $H_0 r_s =$ constant. This constraint only relies on the BAO yielding a standard ruler (of unknown length), on SNe being standard candles (of unknown luminosity), on spatial flatness and on a smooth expansion history. The local H_0 measurement or the early-time r_s "anchors" can be used to break the degeneracy. The r_s measurement relies on early-time physics assumptions (i.e. the value of $N_{\rm eff}$, $Y_{\rm P}^{\rm BBN}$, recombination physics, epoch of matter-radiation equality etc.). The H_0 measurement relies on local calibrators of the cosmic distance ladder.

The constraints on our parameters are reported in table 4 and the reconstruction results are shown in figure 10, using the same conventions as in previous plots. Once we free the

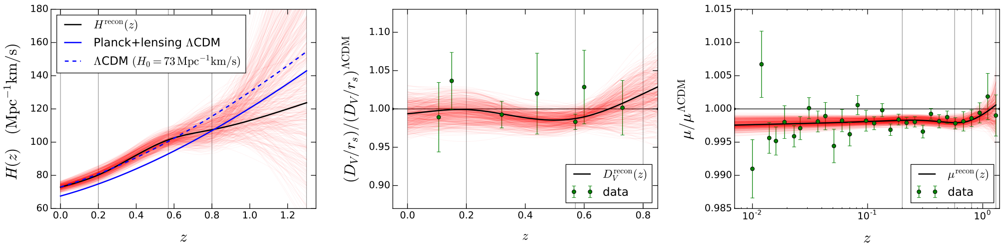

Figure 10. *Left*: reconstructed of $H(z)$ using the direct measurement of H_0 of [20], BAO(*) and SNeIa data set and letting $r_{\rm s}$ vary as a free parameter. *Middle and right*: observational data included in the reconstruction (green), as in previous cases, and the prediction using the corresponding $H^{\rm recon}(z)$.

CMB-anchor of BAO (no $r_{\rm s}$ prior) the reconstruction is similar to that with only SNeIa: $H^{\rm recon}(z)$ is very similar to the ΛCDM prediction (with $H_0 \sim 73\ {\rm Mpc}^{-1}{\rm km/s}$). $H^{\rm recon}(z=0)$ is in $\sim 2.9\sigma$ tension with the value obtained by Planck 2015 [3], which assumes ΛCDM. This procedure yields a model-independent estimate of $r_{\rm s} = 136.7 \pm 4.1$ Mpc; remarkably, with an error small enough to raise a tension of 2.6σ with Planck 2015-derived value assuming ΛCDM, and 2.5σ if we compare with $r_{\rm s}^{\rm early}$ of [74]. This tension in $r_{\rm s}$ between the model independent measurement and the CMB-inferred value is entirely due to the tension in H_0, via the relation $H_0 r_{\rm s} = {\rm constant}$. As in previous cases, this data combination disfavours a recent sharp acceleration given by the shape of $H^{\rm recon}(z)$ using H_0 and BAO, with odds of 1:65.

It is interesting to note that the reconstructed *shape* of $H^{\rm recon}(z)$ is constrained to be very close to the ΛCDM-predicted shape. This is illustrated in figure 11 for the combination SNeIa, BAO(*) and H_0: the maximal deviations at $z < 0.6$, where the data have most of their statistical power, are at the 5% level.

For completeness, in figure 12, we show different CMB constraints on $r_{\rm s}$ compared with our measurement (black bands). Only when $N_{\rm eff}$ is free and only Planck temperature and lowP data are used, the constraint is modestly consistent ($\sim 2\sigma$). In the other cases, the tension is significant, except for the analysis of Planck 2015 temperature power spectrum limited to $\ell \geq 1000$ [25]. However, as discussed by these authors, most of the parameters obtained using only this ℓ range are in tension with Planck 2015 $\ell < 1000$ and WMAP9 constraints.[5]

It is illustrative to show the joint constraints for H_0 and $r_{\rm s}$, which we do in figure 13. The vertical band is the local H_0 measurement and the blue contours are the constraints obtained in this work. As said before, H_0 and $r_{\rm s}$ are related by $H_0 r_{\rm s} \approx {\rm constant}$ and they are perfectly anticorrelated in our measurement. Here the perfect degeneracy is lifted by the measurement of H_0. In the same way, if the prior $r_{\rm s}^{\rm early}$ is included instead H_0 from [20], the constraint on H_0 will be approximately[6] $H_0^{\rm m} r_{\rm s}^{\rm m}/r_{\rm s}^{\rm early} \sim 68\ {\rm Mpc}^{-1}{\rm km/s}$, with the superscript m meaning "measured", recovering a value of H_0 close to the Planck-inferred value.

We also show the results of Planck using temperature and polarization power spectra (left) and only temperature power spectrum and lowP (right) for a ΛCDM model (red) and

---

[5] Note that the tensions in each case (in parenthesis in figure 12) are very similar in most of the cases although by eye it may not be obviously apparent. This is because the error on the low redshift determination is much larger and dominates the comparison.

[6] This relation is not exact because the prior $r_{\rm s}^{\rm early}$ is applied at various redshift and in combination with the BAO measurements.

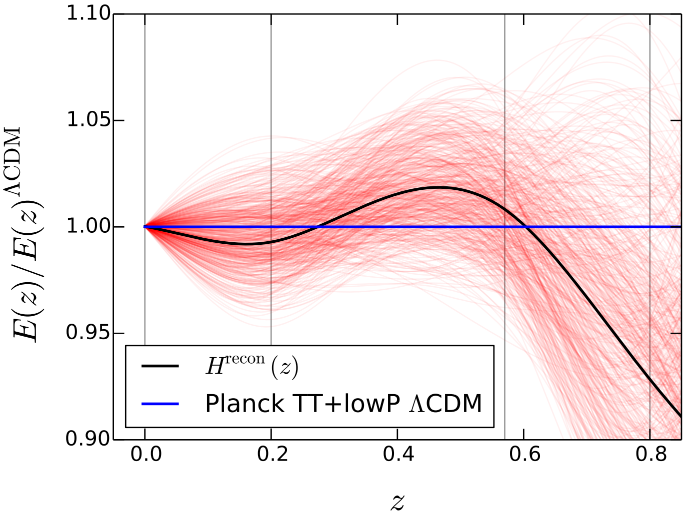

Figure 11. Reconstructed shape of the expansion history $E(z) = H(z)/H_0$, normalised to a standard ΛCDM expansion (with Planck-inferred density parameters), each with its corresponding value of H_0. At $z < 0.6$ where the data have most statistical power, maximal deviations are at the 5% level.

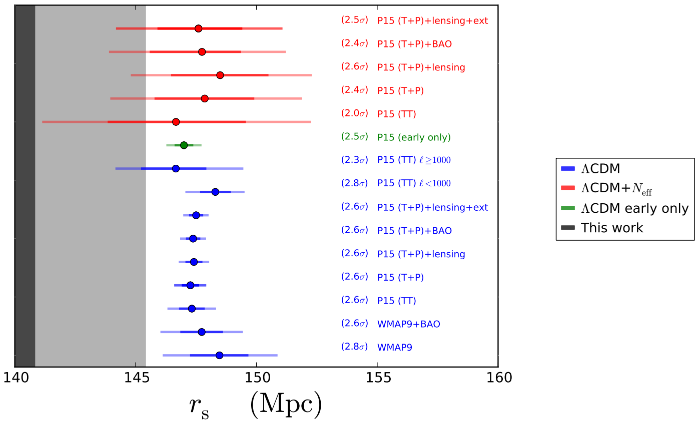

Figure 12. Marginalised 68% and 95% constraints on r_s for different analysis of CMB data, obtained from Planck Collaboration 2015 public chains [3], WMAP9 [1] (analysed with the same assumptions than Planck) and the results of the work of [25] (TT, $\ell > 1000$ and $\ell < 1000$) and [74] (early only). We show the constraints obtained in a ΛCDM context in blue, ΛCDM+N_eff in red, the constraints obtained by analysing the CMB without any assumption of late universe physics (taken from [74]) in green. The result from this work is shown as a gray band.

	$\log \mathcal{T}$	Odds	Jeffrey's modified scale	Gaussian tension
Planck ΛCDM (T+P)	4.75	0.0086 (1:116)	strong	3.7
Planck ΛCDM (TT)	4.31	0.013 (1:76)	strong	3.5
Planck ΛCDM+$N_{\rm eff}$ (T+P)	3.55	0.029 (1:34)	strong	3.1
Planck ΛCDM+$N_{\rm eff}$ (TT)	2.02	0.13 (1:8)	positive	2.1
WMAP ΛCDM	3.59	0.027 (1:37)	strong	3.1

Table 5. Two dimensional tension between the low redshift joint constraints on $H_0 - r_{\rm s}$ and a set of CMB-derived constraints. See section 3 for details.

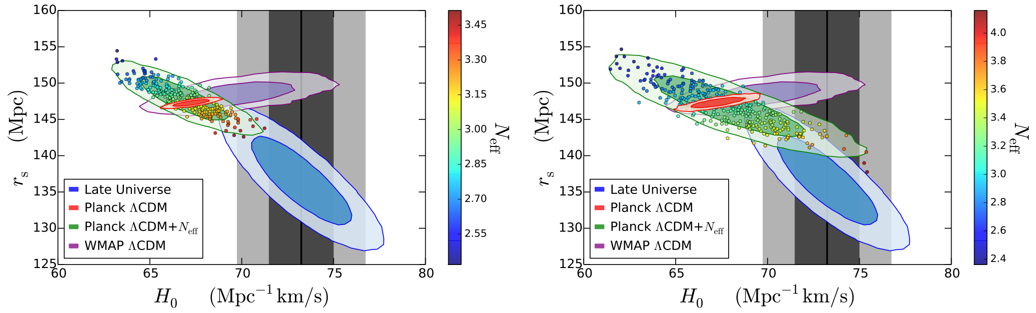

Figure 13. Marginalized constraints in the H_0-$r_{\rm s}$ plane (68% and 95% regions) for the cases discussed in the text. Planck data includes high ℓ polarization in the left panel and does not in the right one. Color-coded are the corresponding values of $N_{\rm eff}$ in the case of ΛCDM+$N_{\rm eff}$.

a model which varies $N_{\rm eff}$ (green); and of WMAP9 for a ΛCDM model (analysed in the same way as Planck, purple). It is possible to appreciate how, as CMB experiments derive constraints assuming a model, the correlation is different and it depends strongly on the adopted model (i.e ΛCDM vs. ΛCDM+$N_{\rm eff}$).

In table 5, we report the tension in the H_0-$r_{\rm s}$ plane between our measurement and CMB experiments for different models (computed as explained in section 3), expressed as $\log \mathcal{T}$, the odds of full consistency and the tensions in terms of number of σ (computed assuming gaussianity). Only for a model with extra dark radiation and discarding Planck's high ℓ polarisation data the two constraints are in acceptable agreement (i.e., the tension is not considered strong). From figure 13 it is possible to appreciate that within ΛCDM, excluding polarisation data makes the CMB-derived H_0 value more consistent with the local H_0, but mainly because of an increase of the error bars; however including or excluding polarisation data does not alter significantly the $r_{\rm s}$ determination. To make the local H_0 determination, the low-redshift estimate of the combination $r_{\rm s}h$ and the CMB $r_{\rm s}$ determination fully consistent with each other, $r_{\rm s}$ should be significantly lowered. Among the ΛCDM extensions we explored, the only one that achieves this is allowing $N_{\rm eff} \sim 3.4$.

Finally, we also explore the case where the curvature of the Universe is not fixed to $\Omega_{\rm k} = 0$.In this case, $\Omega_{\rm k}$ remains largely unconstrained, and still broadly consistent with zero. There is no significant shift in the rest of parameters, but the error bars are larger. The constraints are summarized in the bottom rows of table 4. Given the freedom of our expansion history reconstruction, to obtain useful constraints on $\Omega_{\rm k}$ more data would be needed (see for example, [30, 31] where curvature constraints are reported). In the near future, anisotropic measurements of the BAO feature from on-going and forthcoming surveys could also be used.

6 Discussion and conclusions

The standard ΛCDM model with only a handful of parameters, provides an excellent description of a host of cosmological observations with remarkably few exceptions. The most notable and persistent one is the local determination of the Hubble constant H_0, which, with the recent improvement by [20], presents a $\sim 3\sigma$ tension with respect to the value inferred by the Planck Collaboration (assuming ΛCDM). The CMB is mostly sensitive to early-Universe physics, and the CMB-inferred H_0 measurement thus depends on assumptions about both early time and late-time physics. A related quantity that the CMB can measure in a way that does not depend on late-time physics is the sound horizon at radiation drag, $r_{\rm s}$. This measurement however is still model-dependent in that it relies on standard assumptions about early-time physics. On the other hand the local measurement of H_0 is model-independent as it does not depend on cosmological assumptions. As this work was nearing completion, new quasar time-delay cosmography data became available [24]. Within the ΛCDM model these provide an H_0 constraint centered around 72 Mpc^{-1}km/s, with a 4% error and thus shows reduced tension.

The two parameters $r_{\rm s}$ and H_0 are strictly related when we consider also BAO observations. Expansion history probes such as BAO and SNIa can provide a model-independent estimate of the low-redshift standard ruler, constraining directly the combination $r_{\rm s}h$ (with $H_0 = h \times 100\ \mathrm{Mpc}^{-1}\mathrm{km/s}$). Thus $r_{\rm s}$ and H_0 provide absolute scales for distance measurements (anchors) at opposite ends of the observable Universe. In the absence of systematic errors in the measurements, if the standard cosmological model is the correct model, indirect (model-dependent) and direct (model-independent) constraints on these parameters should agree. The tension could thus provide evidence of physics beyond the standard model (or unaccounted systematic errors).

We have performed a complete cosmological study of the current tension between the inferred value of H_0 from the latest CMB data (as provided by the Planck satellite) [3] and its direct measurement, with the recent update from [20]. This reflects into a tension between cosmological model-dependent and model-independent constraints on $r_{\rm s}$.

We first have explored models for deviations from the standard ΛCDM in the early-Universe physics. When including CMB data alone (or in combination with geometric measurements that do not rely on the H_0 anchor such as BAO) we find no evidence for deviations from the standard ΛCDM model and in particular no evidence for extra effective relativistic species beyond three active neutrinos. This conclusion is unchanged if we allow additional freedom in the behaviour of the perturbations, both in all relativistic species or only in the additional ones.

Therefore we put limits on the possible presence of a Universe component whose mean energy scales like radiation with the Universe expansion but which perturbations could behave like radiation, a perfect fluid, a scalar field or anything else in between. On the other hand the value for the Hubble constant inferred by these analyses and other promising modifications of early-time physics, is always significantly lower than the local measurement of [20]. Should the low-level systematics present in the high ℓ “preliminary” Planck polarisation data be found to be non-negligible, the TEEE data should not be included in the analysis. In this case, including only the “recommended” baseline of low ℓ temperature and polarisation data and only temperature for high ℓ, the tight limits relax and the tension disappears for a cosmological model with extra dark radiation corresponding to $\Delta N_{\rm eff} \sim 0.4$. However the tension appears (but at an acceptable level) again when BAO data is included. The constraints on the effective parameters which describe the behaviour of the extra radiation in terms of perturbations are too weak to discriminate among the different candidates.

Another possible way to reconcile the CMB-derived H_0 value and the local measurement is to allow deviations from the standard late-time expansion history of the Universe. Rather than invoking specific models we have reconstructed the expansion history in a model-independent, minimally parametric way. Our method to reconstruct $H(z)$ does not rely on any model and only require minimal assumptions. These are: SNeIa form a homogeneous group and can be used as standard candles, $r_{\rm s}$ is a standard ruler for BAO corresponding to the sound horizon at radiation drag, the expansion history is smooth and continuous and the Universe is spatially flat. When only using BAO, and the H_0 measurement with an early Universe $r_{\rm s}$ prior, the reconstructed $H(z)$ shows a sharp increase in acceleration at low redshift, such as that provided by a phantom equation of state parameter for dark energy. However when SNeIa are included, the shape of $H(z)$ cannot deviate significantly from that of a ΛCDM, disfavouring therefore the phantom dark energy solution. When the CMB $r_{\rm s}$ prior is removed, this procedure yields a model-independent determination of $r_{\rm s}$ (and the expansion history) without any assumption on the early Universe. The $r_{\rm s}$ value so obtained is significantly lower than that obtained from the CMB assuming standard early-time physics (2.6σ tension). When we relax the assumption about the flatness of the Universe, the curvature remains largely unconstrained and the error on the other parameters grow slightly. We do not find significant shifts in the rest of the parameters.

Of course this hinges on identifying the BAO standard ruler with the sound horizon at radiation drag. Several processes have been proposed that could displace the BAO feature, the most important being non-linearities, bias e.g., [75, 76] and non-zero baryon-dark matter relative velocity [77–79]. These effects however have been found to be below current errors [80–82] and below the 1% level. It is therefore hard to imagine how these effects could introduce the $5-7\%$ shift required to solve the tension.

In summary, because the shape of the expansion history is tightly constrained by current data, in a model-independent way, the H_0 tension can be restated as a mis-match in the normalisation of the cosmic distance ladder between the two anchors: H_0 at low redshift and $r_{\rm s}$ at high redshift. In the absence of systematic errors, especially in the high ℓ CMB polarisation data and/or in the local H_0 measurement, the mismatch suggest reconsidering the standard assumptions about early-time physics. Should the "preliminary" high ℓ CMB polarisation data be found to be affected by significant systematics and excluded from the analysis, the mismatch could be resolved by allowing an extra component behaving like dark radiation at the background level with a $\Delta N_{\rm eff} \sim 0.4$. Other new physics in the early Universe that reduce the CMB-inferred sound horizon at radiation drag by ~ 10 Mpc (6%) would have the same effect.

Acknowledgments

We thank Graeme Addison, Alan Heavens and Antonio J. Cuesta for valuable discussion during the development of this study, which helped to improve this work. JLB is supported by the Spanish MINECO under grant BES-2015-071307, co-funded by the ESF. Funding for this work was partially provided by the Spanish MINECO under projects AYA2014-58747-P and MDM-2014- 0369 of ICCUB (Unidad de Excelencia Maria de Maeztu). JLB acknowledges hospitality of Radcliffe Institute for Advanced Study, Harvard University.

Based on observations obtained with Planck (http://www.esa.int/Planck), an ESA science mission with instruments and contributions directly funded by ESA Member States, NASA, and Canada.

Funding for SDSS-III has been provided by the Alfred P. Sloan Foundation, the Participating Institutions, the National Science Foundation, and the U.S. Department of Energy Office of Science. The SDSS-III web site is http://www.sdss3.org/.

SDSS-III is managed by the Astrophysical Research Consortium for the Participating Institutions of the SDSS-III Collaboration including the University of Arizona, the Brazilian Participation Group, Brookhaven National Laboratory, Carnegie Mellon University, University of Florida, the French Participation Group, the German Participation Group, Harvard University, the Instituto de Astrofisica de Canarias, the Michigan State/Notre Dame/JINA Participation Group, Johns Hopkins University, Lawrence Berkeley National Laboratory, Max Planck Institute for Astrophysics, Max Planck Institute for Extraterrestrial Physics, New Mexico State University, New York University, Ohio State University, Pennsylvania State University, University of Portsmouth, Princeton University, the Spanish Participation Group, University of Tokyo, University of Utah, Vanderbilt University, University of Virginia, University of Washington, and Yale University.

References

[1] WMAP collaboration, G. Hinshaw et al., *Nine-Year Wilkinson Microwave Anisotropy Probe (WMAP) Observations: Cosmological Parameter Results*, *Astrophys. J. Suppl.* **208** (2013) 19 [`arXiv:1212.5226`] [inSPIRE].

[2] WMAP collaboration, C.L. Bennett et al., *Nine-Year Wilkinson Microwave Anisotropy Probe (WMAP) Observations: Final Maps and Results*, *Astrophys. J. Suppl.* **208** (2013) 20 [`arXiv:1212.5225`] [inSPIRE].

[3] Planck collaboration, P.A.R. Ade et al., *Planck 2015 results. XIII. Cosmological parameters*, *Astron. Astrophys.* **594** (2016) A13 [`arXiv:1502.01589`] [inSPIRE].

[4] BOSS collaboration, L. Anderson et al., *The clustering of galaxies in the SDSS-III Baryon Oscillation Spectroscopic Survey: baryon acoustic oscillations in the Data Releases 10 and 11 Galaxy samples*, *Mon. Not. Roy. Astron. Soc.* **441** (2014) 24 [`arXiv:1312.4877`] [inSPIRE].

[5] A.J. Cuesta et al., *The clustering of galaxies in the SDSS-III Baryon Oscillation Spectroscopic Survey: Baryon Acoustic Oscillations in the correlation function of LOWZ and CMASS galaxies in Data Release 12*, *Mon. Not. Roy. Astron. Soc.* **457** (2016) 1770 [`arXiv:1509.06371`] [inSPIRE].

[6] A.J. Cuesta, L. Verde, A. Riess and R. Jimenez, *Calibrating the cosmic distance scale ladder: the role of the sound horizon scale and the local expansion rate as distance anchors*, *Mon. Not. Roy. Astron. Soc.* **448** (2015) 3463 [`arXiv:1411.1094`] [inSPIRE].

[7] É.e.a. Aubourg et al., *Cosmological implications of baryon acoustic oscillation measurements*, *Phys. Rev.* **D 92** (2015) 123516 [`arXiv:1411.1074`] [inSPIRE].

[8] A.G. Riess, L. Macri, S. Casertano, H. Lampeitl, H.C. Ferguson, A.V. Filippenko et al., *A 3% Solution: Determination of the Hubble Constant with the Hubble Space Telescope and Wide Field Camera 3*, *Astrophys. J.* **730** (2011) 119 [*Erratum ibid.* **732** (2011) 129] [`arXiv:1103.2976`] [inSPIRE].

[9] V. Marra, L. Amendola, I. Sawicki and W. Valkenburg, *Cosmic variance and the measurement of the local Hubble parameter*, *Phys. Rev. Lett.* **110** (2013) 241305 [`arXiv:1303.3121`] [INSPIRE].

[10] L. Verde, P. Protopapas and R. Jimenez, *Planck and the local Universe: Quantifying the tension*, *Phys. Dark Univ.* **2** (2013) 166 [`arXiv:1306.6766`] [INSPIRE].

[11] C.L. Bennett, D. Larson, J.L. Weiland and G. Hinshaw, *The 1% Concordance Hubble Constant*, *Astrophys. J.* **794** (2014) 135 [`arXiv:1406.1718`] [INSPIRE].

[12] PLANCK collaboration, P.A.R. Ade et al., *Planck 2013 results. XVI. Cosmological parameters*, *Astron. Astrophys.* **571** (2014) A16 [`arXiv:1303.5076`] [INSPIRE].

[13] G. Efstathiou, *H0 Revisited*, *Mon. Not. Roy. Astron. Soc.* **440** (2014) 1138 [`arXiv:1311.3461`] [INSPIRE].

[14] E.M.L. Humphreys, M.J. Reid, J.M. Moran, L.J. Greenhill and A.L. Argon, *Toward a New Geometric Distance to the Active Galaxy NGC 4258. III. Final Results and the Hubble Constant*, *Astrophys. J.* **775** (2013) 13 [`arXiv:1307.6031`] [INSPIRE].

[15] M. Wyman, D.H. Rudd, R.A. Vanderveld and W. Hu, *Neutrinos Help Reconcile Planck Measurements with the Local Universe*, *Phys. Rev. Lett.* **112** (2014) 051302 [`arXiv:1307.7715`] [INSPIRE].

[16] C. Dvorkin, M. Wyman, D.H. Rudd and W. Hu, *Neutrinos help reconcile Planck measurements with both the early and local Universe*, *Phys. Rev.* **D 90** (2014) 083503 [`arXiv:1403.8049`] [INSPIRE].

[17] B. Leistedt, H.V. Peiris and L. Verde, *No new cosmological concordance with massive sterile neutrinos*, *Phys. Rev. Lett.* **113** (2014) 041301 [`arXiv:1404.5950`] [INSPIRE].

[18] PLANCK collaboration, P.A.R. Ade et al., *Planck 2015 results. XIV. Dark energy and modified gravity*, `arXiv:1502.01590` [INSPIRE].

[19] E. Di Valentino, A. Melchiorri and J. Silk, *Reconciling Planck with the local value of H_0 in extended parameter space*, *Phys. Lett.* **B 761** (2016) 242 [`arXiv:1606.00634`] [INSPIRE].

[20] A.G. Riess et al., *A 2.4% Determination of the Local Value of the Hubble Constant*, *Astrophys. J.* **826** (2016) 56 [`arXiv:1604.01424`] [INSPIRE].

[21] PLANCK collaboration, N. Aghanim et al., *Planck intermediate results. XLVI. Reduction of large-scale systematic effects in HFI polarization maps and estimation of the reionization optical depth*, `arXiv:1605.02985` [INSPIRE].

[22] S. Casertano, A.G. Riess, B. Bucciarelli and M.G. Lattanzi, *A test of Gaia Data Release 1 parallaxes: implications for the local distance scale*, `arXiv:1609.05175`.

[23] S.H. Suyu et al., *H0LiCOW I. H0 Lenses in COSMOGRAIL's Wellspring: Program Overview*, `arXiv:1607.00017` [INSPIRE].

[24] V. Bonvin et al., *H0LiCOW V. New COSMOGRAIL time delays of HE0435-1223: H_0 to 3.8% precision from strong lensing in a flat ΛCDM model*, `arXiv:1607.01790` [INSPIRE].

[25] G.E. Addison, Y. Huang, D.J. Watts, C.L. Bennett, M. Halpern, G. Hinshaw et al., *Quantifying discordance in the 2015 Planck CMB spectrum*, *Astrophys. J.* **818** (2016) 132 [`arXiv:1511.00055`] [INSPIRE].

[26] PLANCK collaboration, N. Aghanim et al., *Planck 2016 intermediate results. LI. Features in the cosmic microwave background temperature power spectrum and shifts in cosmological parameters*, `arXiv:1608.02487` [INSPIRE].

[27] D.J. Eisenstein and W. Hu, *Baryonic features in the matter transfer function*, *Astrophys. J.* **496** (1998) 605 [`astro-ph/9709112`] [INSPIRE].

[28] J. Hamann, S. Hannestad, J. Lesgourgues, C. Rampf and Y.Y.Y. Wong, *Cosmological parameters from large scale structure - geometric versus shape information*, *JCAP* **07** (2010) 022 [`arXiv:1003.3999`] [INSPIRE].

[29] R. Jimenez and A. Loeb, *Constraining cosmological parameters based on relative galaxy ages*, *Astrophys. J.* **573** (2002) 37 [`astro-ph/0106145`] [INSPIRE].

[30] A. Heavens, R. Jimenez and L. Verde, *Standard rulers, candles and clocks from the low-redshift Universe*, *Phys. Rev. Lett.* **113** (2014) 241302 [`arXiv:1409.6217`] [INSPIRE].

[31] L. Verde, J.L. Bernal, A.F. Heavens and R. Jimenez, *The length of the low-redshift standard ruler*, `arXiv:1607.05297` [INSPIRE].

[32] Planck collaboration, N. Aghanim et al., *Planck 2015 results. XI. CMB power spectra, likelihoods and robustness of parameters*, *Astron. Astrophys.* **594** (2015) A11 [`arXiv:1507.02704`] [INSPIRE].

[33] F. Beutler et al., *The 6dF Galaxy Survey: baryon acoustic oscillations and the local Hubble constant*, *Mon. Not. Roy. Astron. Soc.* **416** (2011) 3017 [`arXiv:1106.3366`] [INSPIRE].

[34] A.J. Ross, L. Samushia, C. Howlett, W.J. Percival, A. Burden and M. Manera, *The clustering of the SDSS DR7 main Galaxy sample — I. A 4 per cent distance measure at $z = 0.15$*, *Mon. Not. Roy. Astron. Soc.* **449** (2015) 835 [`arXiv:1409.3242`] [INSPIRE].

[35] E.A. Kazin et al., *The WiggleZ Dark Energy Survey: improved distance measurements to $z = 1$ with reconstruction of the baryonic acoustic feature*, *Mon. Not. Roy. Astron. Soc.* **441** (2014) 3524 [`arXiv:1401.0358`] [INSPIRE].

[36] F. Beutler, C. Blake, J. Koda, F. Marín, H.-J. Seo, A.J. Cuesta et al., *The BOSS-WiggleZ overlap region — I. Baryon acoustic oscillations*, *Mon. Not. Roy. Astron. Soc.* **455** (2016) 3230 [`arXiv:1506.03900`] [INSPIRE].

[37] SDSS collaboration, M. Betoule et al., *Improved cosmological constraints from a joint analysis of the SDSS-II and SNLS supernova samples*, *Astron. Astrophys.* **568** (2014) A22 [`arXiv:1401.4064`] [INSPIRE].

[38] J. Lesgourgues, *The Cosmic Linear Anisotropy Solving System (CLASS) I: Overview*, `arXiv:1104.2932` [INSPIRE].

[39] D. Blas, J. Lesgourgues and T. Tram, *The Cosmic Linear Anisotropy Solving System (CLASS) II: Approximation schemes*, *JCAP* **07** (2011) 034 [`arXiv:1104.2933`] [INSPIRE].

[40] B. Audren, J. Lesgourgues, K. Benabed and S. Prunet, *Conservative Constraints on Early Cosmology: an illustration of the Monte Python cosmological parameter inference code*, *JCAP* **02** (2013) 001 [`arXiv:1210.7183`] [INSPIRE].

[41] J. Caruana, A.J. Bunker, S.M. Wilkins, E.R. Stanway, S. Lorenzoni, M.J. Jarvis et al., *Spectroscopy of $z \sim 7$ candidate galaxies: Using Lyman α to constrain the neutral fraction of hydrogen in the high-redshift universe*, *Mon. Not. Roy. Astron. Soc.* **443** (2014) 2831 [`arXiv:1311.0057`] [INSPIRE].

[42] A. Gelman and D. Rubin, *Inference from iterative simulation using multiple sequences*, *Stat. Sci.* **7** (1992) 457 [http://www.stat.columbia.edu/~gelman/research/published/itsim.pdf].

[43] D. Foreman-Mackey, D.W. Hogg, D. Lang and J. Goodman, *emcee: The MCMC Hammer*, *Publ. Astron. Soc. Pac.* **125** (2013) 306 [`arXiv:1202.3665`] [INSPIRE].

[44] J. Goodman and J. Weare, *Ensemble samplers with affine invariance*, *Comm. App. Math. Comp.* **5** (2010) 65.

[45] E. Aver, K.A. Olive, R.L. Porter and E.D. Skillman, *The primordial helium abundance from updated emissivities*, *JCAP* **11** (2013) 017 [`arXiv:1309.0047`] [INSPIRE].

[46] Y.I. Izotov, T.X. Thuan and N.G. Guseva, *A new determination of the primordial He abundance using the He I λ10830 Åemission line: cosmological implications*, Mon. Not. Roy. Astron. Soc. **445** (2014) 778 [arXiv:1408.6953] [INSPIRE].

[47] A. Serenelli and S. Basu, *Determining the initial helium abundance of the Sun*, Astrophys. J. **719** (2010) 865 [arXiv:1006.0244] [INSPIRE].

[48] G. Mangano, G. Miele, S. Pastor, T. Pinto, O. Pisanti and P.D. Serpico, *Relic neutrino decoupling including flavor oscillations*, Nucl. Phys. **B 729** (2005) 221 [hep-ph/0506164] [INSPIRE].

[49] L. Ackerman, M.R. Buckley, S.M. Carroll and M. Kamionkowski, *Dark Matter and Dark Radiation*, Phys. Rev. **D 79** (2009) 023519 [arXiv:0810.5126] [INSPIRE].

[50] K.N. Abazajian et al., *Light Sterile Neutrinos: A White Paper*, arXiv:1204.5379 [INSPIRE].

[51] S. Weinberg, *Goldstone Bosons as Fractional Cosmic Neutrinos*, Phys. Rev. Lett. **110** (2013) 241301 [arXiv:1305.1971] [INSPIRE].

[52] C. Kelso, S. Profumo and F.S. Queiroz, *Non-thermal WIMPs as "Dark Radiation" in Light of ATACAMA, SPT, WMAP9 and Planck*, Phys. Rev. **D 88** (2013) 023511 [arXiv:1304.5243] [INSPIRE].

[53] J. Mastache and A. de la Macorra, *Extra relativistic degrees of freedom without extra particles using Planck data*, Phys. Rev. **D 88** (2013) 043506 [arXiv:1303.7038] [INSPIRE].

[54] P. Di Bari, S.F. King and A. Merle, *Dark Radiation or Warm Dark Matter from long lived particle decays in the light of Planck*, Phys. Lett. **B 724** (2013) 77 [arXiv:1303.6267] [INSPIRE].

[55] M. Archidiacono, E. Giusarma, S. Hannestad and O. Mena, *Cosmic dark radiation and neutrinos*, Adv. High Energy Phys. **2013** (2013) 191047 [arXiv:1307.0637] [INSPIRE].

[56] C. Boehm, M.J. Dolan and C. McCabe, *Increasing Neff with particles in thermal equilibrium with neutrinos*, JCAP **12** (2012) 027 [arXiv:1207.0497] [INSPIRE].

[57] J. Hasenkamp and J. Kersten, *Dark radiation from particle decay: cosmological constraints and opportunities*, JCAP **08** (2013) 024 [arXiv:1212.4160] [INSPIRE].

[58] L.A. Anchordoqui, H. Goldberg, X. Huang and B.J. Vlcek, *Reconciling BICEP2 and Planck results with right-handed Dirac neutrinos in the fundamental representation of grand unified* E_6, JCAP **06** (2014) 042 [arXiv:1404.1825] [INSPIRE].

[59] A. Solaguren-Beascoa and M.C. Gonzalez-Garcia, *Dark Radiation Confronting LHC in Z' Models*, Phys. Lett. **B 719** (2013) 121 [arXiv:1210.6350] [INSPIRE].

[60] M.C. Gonzalez-Garcia, V. Niro and J. Salvado, *Dark Radiation and Decaying Matter*, JHEP **04** (2013) 052 [arXiv:1212.1472] [INSPIRE].

[61] S. Bashinsky and U. Seljak, *Neutrino perturbations in CMB anisotropy and matter clustering*, Phys. Rev. **D 69** (2004) 083002 [astro-ph/0310198] [INSPIRE].

[62] Z. Hou, R. Keisler, L. Knox, M. Millea and C. Reichardt, *How Massless Neutrinos Affect the Cosmic Microwave Background Damping Tail*, Phys. Rev. **D 87** (2013) 083008 [arXiv:1104.2333] [INSPIRE].

[63] J. Lesgourgues, G. Mangano, G. Miele and S. Pastor, *Neutrino cosmology*, Cambridge University Press, Cambridge (2013).

[64] W. Hu, D.J. Eisenstein, M. Tegmark and M.J. White, *Observationally determining the properties of dark matter*, Phys. Rev. **D 59** (1999) 023512 [astro-ph/9806362] [INSPIRE].

[65] W. Hu, *Structure formation with generalized dark matter*, Astrophys. J. **506** (1998) 485 [astro-ph/9801234] [INSPIRE].

[66] R. Trotta and A. Melchiorri, *Indication for primordial anisotropies in the neutrino background from WMAP and SDSS*, *Phys. Rev. Lett.* **95** (2005) 011305 [`astro-ph/0412066`] [INSPIRE].

[67] T.L. Smith, S. Das and O. Zahn, *Constraints on neutrino and dark radiation interactions using cosmological observations*, *Phys. Rev.* **D 85** (2012) 023001 [`arXiv:1105.3246`] [INSPIRE].

[68] F.-Y. Cyr-Racine and K. Sigurdson, *Limits on Neutrino-Neutrino Scattering in the Early Universe*, *Phys. Rev.* **D 90** (2014) 123533 [`arXiv:1306.1536`] [INSPIRE].

[69] I.M. Oldengott, C. Rampf and Y.Y.Y. Wong, *Boltzmann hierarchy for interacting neutrinos I: formalism*, *JCAP* **04** (2015) 016 [`arXiv:1409.1577`] [INSPIRE].

[70] B. Audren et al., *Robustness of cosmic neutrino background detection in the cosmic microwave background*, *JCAP* **03** (2015) 036 [`arXiv:1412.5948`] [INSPIRE].

[71] M. Vonlanthen, S. Rasanen and R. Durrer, *Model-independent cosmological constraints from the CMB*, *JCAP* **08** (2010) 023 [`arXiv:1003.0810`] [INSPIRE].

[72] B. Audren, *Separate Constraints on Early and Late Cosmology*, *Mon. Not. Roy. Astron. Soc.* **444** (2014) 827 [`arXiv:1312.5696`] [INSPIRE].

[73] B. Audren, J. Lesgourgues, K. Benabed and S. Prunet, *Conservative Constraints on Early Cosmology: an illustration of the Monte Python cosmological parameter inference code*, *JCAP* **02** (2013) 001 [`arXiv:1210.7183`] [INSPIRE].

[74] E. Bellini et al., *Early Cosmology Constrained*, in preparation.

[75] R.E. Angulo, S.D.M. White, V. Springel and B. Henriques, *Galaxy formation on the largest scales: the impact of astrophysics on the baryonic acoustic oscillation peak*, *Mon. Not. Roy. Astron. Soc.* **442** (2014) 2131 [`arXiv:1311.7100`] [INSPIRE].

[76] Y. Rasera, P.-S. Corasaniti, J.-M. Alimi, V. Bouillot, V. Reverdy and I. Balmès, *Cosmic variance limited Baryon Acoustic Oscillations from the DEUS-FUR ΛCDM simulation*, *Mon. Not. Roy. Astron. Soc.* **440** (2014) 1420 [`arXiv:1311.5662`] [INSPIRE].

[77] D. Tseliakhovich and C. Hirata, *Relative velocity of dark matter and baryonic fluids and the formation of the first structures*, *Phys. Rev.* **D 82** (2010) 083520 [`arXiv:1005.2416`] [INSPIRE].

[78] N. Dalal, U.-L. Pen and U. Seljak, *Large-scale BAO signatures of the smallest galaxies*, *JCAP* **11** (2010) 007 [`arXiv:1009.4704`] [INSPIRE].

[79] Z. Slepian and D. Eisenstein, *On the signature of the baryon-dark matter relative velocity in the two and three-point galaxy correlation functions*, *Mon. Not. Roy. Astron. Soc.* **448** (2015) 9 [`arXiv:1411.4052`] [INSPIRE].

[80] N. Padmanabhan and M. White, *Calibrating the Baryon Oscillation Ruler for Matter and Halos*, *Phys. Rev.* **D 80** (2009) 063508 [`arXiv:0906.1198`] [INSPIRE].

[81] J. Blazek, J.E. McEwen and C.M. Hirata, *Streaming velocities and the baryon-acoustic oscillation scale*, *Phys. Rev. Lett.* **116** (2016) 121303 [`arXiv:1510.03554`] [INSPIRE].

[82] Z. Slepian et al., *Constraining the Baryon-Dark Matter Relative Velocity with the Large-Scale 3-Point Correlation Function of the SDSS BOSS DR12 CMASS Galaxies*, `arXiv:1607.06098` [INSPIRE].

Monthly Notices
of the
ROYAL ASTRONOMICAL SOCIETY

MNRAS **467,** 731–736 (2017)
Advance Access publication 2017 January 17

doi:10.1093/mnras/stx116

The length of the low-redshift standard ruler

Licia Verde,[1,2,3,4,5] José Luis Bernal,[1,6] Alan F. Heavens[7] and Raul Jimenez[1,2,3,4][⋆]

[1] *ICC, Instituto de Ciencias del Cosmos, Universitat de Barcelona, IEEC-UB, Martí i Franquès 1, E-08028 Barcelona, Spain*
[2] *ICREA, Pg. Llus Companys 23, E-08010 Barcelona, Spain*
[3] *Radcliffe Institute for Advanced Study, Harvard University, MA 02138, USA*
[4] *Institute for Theory and Computation, Harvard–Smithsonian Center for Astrophysics, 60 Garden Street, Cambridge, MA 02138, USA*
[5] *Institute of Theoretical Astrophysics, University of Oslo, 0315 Oslo, Norway*
[6] *Departamento de Física Quàntica i Astrofísica, Universitat de Barcelona, Martí i Franquès 1, E-08028 Barcelona, Spain*
[7] *Imperial Centre for Inference and Cosmology, Imperial College, Blackett Laboratory, Prince Consort Road, London SW7 2AZ, UK*

Accepted 2017 January 13. Received 2017 January 10; in original form 2016 July 20

ABSTRACT

Assuming the existence of standard rulers, standard candles and standard clocks, requiring only the cosmological principle, a metric theory of gravity, a smooth expansion history and using state-of-the-art observations, we determine the length of the ‘low-redshift standard ruler’. The data we use are a compilation of recent baryon acoustic oscillation data (relying on the standard ruler), Type Ia supernovae (as standard candles), ages of early-type galaxies (as standard clocks) and local determinations of the Hubble constant (as a local anchor of the cosmic distance scale). In a standard Λ cold dark matter cosmology, the ‘low-redshift standard ruler’ coincides with the sound horizon at radiation drag, which can also be determined – in a model dependent way – from cosmic microwave background observations. However, in general, the two quantities need not coincide. We obtain constraints on the length of the low-redshift standard ruler: $r_\mathrm{s}^h = 101.0 \pm 2.3\,h^{-1}$ Mpc, when using only Type Ia supernovae and baryon acoustic oscillations, and $r_\mathrm{s} = 150.0 \pm 4.7$ Mpc when using clocks to set the Hubble normalization, while $r_\mathrm{s} = 141.0 \pm 5.5$ Mpc when using the local Hubble constant determination (using both yields $r_\mathrm{s} = 143.9 \pm 3.1$ Mpc). The low-redshift determination of the standard ruler has an error, which is competitive with the model-dependent determination from cosmic microwave background measurements made with the *Planck* satellite, which assumes that it is the sound horizon at the end of baryon drag.

Key words: supernovae: general – cosmology: distance scale – large-scale structure of the Universe.

1 INTRODUCTION

We build on the idea presented in Sutherland (2012) and Heavens, Jimenez & Verde (2014) that relatively low redshift measurements of the cosmic expansion history $H(z)$ can be used, in combination with measurements of the baryon acoustic oscillation (BAO) feature, to determine the length of a standard ruler in a model-independent way. Type Ia supernovae are standard(izable) candles yielding a luminosity–distance–redshift relation. The BAO feature is probably the best-understood standard ruler in the Universe. However, it has the drawback that the comoving length of the ruler, the sound horizon at radiation drag r_s, is usually calibrated at $z > 1000$ relying on cosmic microwave background (CMB) observations and theoretical assumptions. Without knowing the length of the ruler or the brightness of the candles or the Hubble parameter, these probes can give only relative measurements of the expansion history. The quantities r_s and H_0 provide absolute scales for distance measurements (anchors) at the opposite ends of the observable Universe. But while the CMB r_s determination depends on several assumptions (standard gravity, standard radiation content, negligible isocurvature perturbations, standard scaling of matter and radiation components, negligible early dark energy, etc.), local determinations of the expansion rate are cosmology-independent. Alternatively, standard clocks (Jimenez & Loeb 2002) can be used, representing objects whose age is determined by established physics, and whose formation time is sufficiently early that scatter amongst formation times is negligible in the present cosmological context. Standard clocks provide (absolute) measurements of $H(z)$.

Even relative measurements of the expansion history, from observations of Type Ia supernovae, in combination with measurements of the BAO feature, can yield a constraint on the low-redshift standard ruler, r_s^h, which is the ruler length in units of h^{-1} Mpc. An *absolute* distance scale can be provided by adding a constraint on h

---

[⋆] E-mail: rauljimenez@g.harvard.edu

Published by Oxford University Press on behalf of the Royal Astronomical Society

such as that provided by H_0 or clocks, in which case observations of the BAO feature can be used to determine the absolute length of the low-redshift standard ruler, r_s, in units of Mpc. The importance of this scale is that it is a key theoretical prediction of cosmological models, depending on the sound speed and expansion rate of the Universe at early times, before matter and radiation decouple. However, the low-redshift standard ruler is a direct measurement, which will survive even if the standard cosmological model and standard assumptions about early-time physics do not. Since the analysis of Heavens et al. (2014), new BAO, H_0 and cosmic clock data have become available, with improved statistics, which we consider here.

2 DATA AND METHODOLOGY

The latest H_0 determination is provided by the SH0ES program, reaching a 2.4 per cent precision, $H_0^{\rm SH0ES} = 73.24 \pm 1.74\ {\rm km\,s^{-1}\,Mpc^{-1}}$ (Riess et al. 2016). A Gaussian likelihood is assumed.

The Type Ia supernovae data are the compilation of Betoule et al. (2014), binned into 31 redshift intervals between 0 and 1.3, equally spaced in $\log{(1+z)}$ to yield the distance modulus as a function of redshift. The covariance matrix is supplied for the binned data. The binning, in conjunction with the central limit theorem, motivates the use of a Gaussian likelihood. The data are given as measurements of the distance modulus

$$\mu(z) \equiv m - M = 25 + 5\log_{10} D_{\rm L}(z), \tag{1}$$

where m is the apparent magnitude, M is a fiducial absolute magnitude, $M \simeq -19.3$, and $D_{\rm L}$ is the luminosity distance.

Constraints on the BAO are from the following galaxy surveys: Six Degree Field Galaxy Survey (Beutler et al. 2011), the LOWZ and CMASS galaxy samples of the Baryon Oscillation Spectroscopic Survey (BOSS-LOWZ and BOSS-CMASS, respectively; Cuesta et al. 2016, we use the isotropic measurement) and the reanalysed measurements of WiggleZ (Blake et al. 2011) by Kazin et al. (2014). While we take into account the correlation among the WiggleZ measurements, we neglect the correlation between WiggleZ and CMASS. This is motivated by the fact that the WiggleZ-CMASS overlap includes a small fraction of the BOSS-CMASS sample and the correlation is very small, always below 4 per cent (Beutler et al. 2016; Cuesta et al. 2016). BAO data provide measurements of the dilation scale normalized by the standard ruler length, D_V/r_s, where

$$D_V(z) \equiv \left[(1+z)^2 D_{\rm A}^2(z)\frac{cz}{H(z)}\right]^{1/3}. \tag{2}$$

If r_s is interpreted as the sound horizon at radiation drag, $r_{\rm d}(z_{\rm d})$, then

$$r_{\rm d}(z_{\rm d}) = \int_{z_d}^{\infty} \frac{c_{\rm s}(z)}{H(z)}{\rm d}z, \tag{3}$$

where $c_{\rm s}(z)$ is the sound speed.

Strictly speaking, the measurement of the BAO scale relies on correcting small non-linear shifts and sharpening the feature with the so-called reconstruction procedure (e.g. Noh, White & Padmanabhan 2009; Padmanabhan, White & Cohn 2009). This procedure is somewhat model-dependent (assumes Newtonian gravity), but the effect is small compared with current error bars.

For the standard clocks, we use galaxy ages determined from the analysis of stellar populations of old elliptical galaxies. We assume that the formation time was at a sufficiently high redshift that variations in formation time of stars within each galaxy and among galaxies are negligible. Differential ages, Δt, then provide estimates of the inverse Hubble parameter as $1/H(z) = {\rm d}t/{\rm d}z(1+z)$ and ${\rm d}t/{\rm d}z \simeq \Delta t/\Delta z$ for suitable redshift intervals Δz. We use the measurements of $H(z)$ obtained by Moresco et al. (2016), who extend the previously available compilation to include both a fine sampling at $0.38 < z < 0.48$ exploiting the unprecedented statistics provided by the BOSS Data Release 9 and the redshift range up to $z \sim 2$.

As in Heavens et al. (2014), we parametrize the expansion history by an inverse Hubble parameter, $\mathbf{h}^{-1}(z) \equiv 100\ {\rm km\,s^{-1}\,Mpc^{-1}}/H(z)$, which is specified at $N = 7$ values (nodes) equally spaced between $z = 0$ and 1.97; we linearly interpolate $\mathbf{h}^{-1}(z)$ in between. Since the maximum redshift probed by supernovae data is smaller than that probed by clocks, when clocks are not included, $N = 5$, and the maximum redshift value considered is $z = 1.3$. This implicitly assumes a smooth expansion history.

Assuming the cosmological principle of homogeneity and isotropy (and thus an FRW metric), the curvature of the Universe ($k = \{1, 0, -1\}$) and $H(z)$ completely specify the metric and the geometric observables considered here: luminosity distance $D_{\rm L}$ and the dilation scale D_V through the angular diameter distance $D_{\rm A}$. The curvature radius of the Universe is kR_0 (for $k = \pm 1$) and infinity for $k = 0$, where R_0 denotes the present value of the scalefactor, and the curvature is $\kappa = c/(R_0 H_0)$. If we wish to further assume General Relativity (GR), the curvature density parameter is given by $\Omega_k = k[c/(R_0H_0)]^2 = k\kappa^2$ with c the speed of light.[1]

As it is customary for supernovae, we allow an absolute magnitude offset ΔM: We are assuming the existence of a standard candle, but not its luminosity. Similarly, for the BAO measurements, we assume that there is a standard ruler, which is normally interpreted as the sound horizon at radiation drag, but for the purposes here, it is simply a ruler.

The parameters are therefore $(r_{\rm s}^h, \Omega_k, \Delta M, \mathbf{h}^{-1}(0), \mathbf{h}^{-1}(z_1), \ldots, \mathbf{h}^{-1}(z_N))$. Uniform priors are assumed for all parameters. The parameter space is explored through standard Markov chain Monte Carlo (MCMC) methods.

In Section 3.1, we compare this parametrization with a prior on $H(z)$ in five knots, r_s and a spline interpolation. We also compare results for different sampling techniques: Metropolis Hastings (Hastings 1970) and Affine Invariant sampler (Goodman & Weare 2010).

3 RESULTS

In Table 1, we report the mean and 68 per cent credible regions for the recovered quantities for various combinations of the data: CSBH indicating clocks, supernovae, BAOs and local H_0, respectively. The posterior distributions are very symmetric (unless otherwise stated) and very close to Gaussian, and for this reason, herein we report symmetric error bars. However, the posterior distribution of the curvature parameter is highly non-Gaussian, except when both clocks and supernovae data are considered or in the SB case; the curvature is poorly constrained otherwise; hence, in these cases we

---

[1] In fact recall that

$$r(z) = \frac{c}{R_0 H_0}\int_0^z \frac{{\rm d}z'}{E(z')} \equiv \frac{c}{R_0 H_0}\tilde{r}(z), \tag{4}$$

where $E(z) \equiv H(z)/H_0$ and $H(z) = a^{-1}{\rm d}a/{\rm d}t$.

$$D_{\rm A}(z) = (1+z)^{-1}\frac{c}{H_0\kappa}S_k(\kappa\tilde{r}), \tag{5}$$

where $S_k(r) = \sin r$, r, $\sinh r$ for $k = 1, 0, -1$, respectively. For any metric theory of gravity, the angular diameter distance and luminosity distance are related by $D_{\rm L} = (1+z)^2 D_{\rm A}$.

Table 1. Posterior mean and standard deviation for the model parameters. In the first column, the abbreviation of the data set combination is reported: C = clocks, B = BAO, S = supernovae and H = H_0 measurement. The curvature radius of the Universe R_0 is constrained, independently of GR, but we report it in terms of the GR-specific curvature density parameter Ω_k. The curvature distribution in some cases is highly non-Gaussian; therefore, we also report in parentheses the maximum of the posterior and the 68 per cent highest posterior density interval. When supernovae are not included, ΔM is not a parameter (hence the 'N/A' table entry).

Data	$r_s^h(h^{-1}\,\mathrm{Mpc})$	$r_\mathrm{s}(\mathrm{Mpc})$	H_0	ΔM	$\Omega_k = k(c/H_0R_0)^2$
SBH	$102.0 \pm 2.5\ \left(^{+2.2}_{-2.8}\right)$	140.8 ± 4.9	72.8 ± 1.8	0.079 ± 0.083	$-0.49 \pm 0.64\ \left(-0.99^{+0.86}_{-0.26}\right)$
BH	107.2 ± 7.2	147 ± 10	73.0 ± 1.8	N/A	Unconstrained
SB	101.0 ± 2.3	Unconstrained	Unconstrained	Unconstrained	0.07 ± 0.61
CB	103.9 ± 5.6	149.5 ± 4.3	69.6 ± 4.2	N/A	Unconstrained
CSB	100.5 ± 1.9	150.0 ± 4.7	67.0 ± 2.5	-0.090 ± 0.079	0.36 ± 0.41
CBH	107.2 ± 3.4	148.0 ± 3.9	72.5 ± 1.7	N/A	Unconstrained
CSBH	102.3 ± 1.8	143.9 ± 3.1	71.1 ± 1.5	0.028 ± 0.047	$-0.03 \pm 0.31\ \left(-0.08^{+0.32}_{-0.28}\right)$
SBH	100.7 ± 1.8	138.5 ± 4.3	72.8 ± 1.8	0.083 ± 0.061	Flat
BH	107.1 ± 7.2	147 ± 10	73.0 ± 1.8	N/A	Flat
SB	101.2 ± 1.8	Unconstrained	Unconstrained	Unconstrained	Flat
CB	103.7 ± 5.5	149.8 ± 4.2	69.2 ± 4.0	N/A	Flat
CSB	101.4 ± 1.7	148.3 ± 4.3	68.5 ± 2.1	-0.047 ± 0.064	Flat
CBH	107.4 ± 3.4	148.0 ± 3.6	72.6 ± 1.7	N/A	Flat
CSBH	102.3 ± 1.6	143.9 ± 3.1	71.1 ± 1.4	0.026 ± 0.043	Flat

also report the maximum of the posterior and the 68 per cent highest posterior density interval.

The results of Table 1 indicate the following:

(1) There is only a mild dependence of the low-redshift standard ruler determination on curvature. Imposing flatness slightly reduces the error bars, and has no effect when all data sets are considered. Only in the case of SBH does imposing flatness induce a change of $\sim 1\sigma$ in the low-redshift standard ruler towards lower values.

(2) The recovered H_0 estimates cluster around two values: $h \equiv \mathbf{h}(z=0) \sim 0.73$ obtained when the local H_0^{SH0ES} is used (as expected); and $h \sim 0.68$ when clocks are used, and 0.71 when both are used.

(3) These two values for H_0 correspond to the low versus high Hubble constant obtained, respectively, from the *Planck* CMB analysis assuming a Λcolddarkmatter(ΛCDM) model and the local measurement based on cepheids and local supernovae (Riess et al. 2016). A more detailed discussion and extended analysis can be found in Bernal, Verde & Riess (2016, hereafter BVR).

(4) The H_0 value obtained by the CSB combination has an error bar of 3.7 per cent, to be compared with a 2.4 per cent error for H_0^{SH0ES} and a 3.8 per cent error for H0LiCOW (Bonvin et al. 2016). These two measurements are in agreement at the 2σ level with the CSB value.

(5) Supernovae and cosmic clocks data are needed to constrain the curvature. The curvature distribution is highly non-Gaussian, unless these data sets are considered.

(6) Without H_0^{SH0ES}, r_s tends to be $\sim$149 Mpc, as expected, and H_0^{SH0ES} pulls the recovered r_s downwards.

(7) Depending on how extensive the data set considered is, the error on r_s^h varies between 7 per cent (for BH) to 1.8 per cent (CSBH), and the error on r_s varies between 7 per cent (for BH) to 2.1 per cent (CSBH).

(8) While r_s^h is better determined than r_s, the recovered value across different data sets is more consistent for r_s.

(9) r_s^h is determined at the 2 per cent level with only BAOs and supernovae. In this case, the curvature distribution is remarkably more symmetric than for the SBH case.

Fig. 1 offers visual comparisons of the r_s^h and r_s measurements, for the flat case and marginalizing over curvature. The CSB combination yields an r_s value fully consistent with the *Planck* mission CMB inferred one, while the SBH determination yields lower values, which are still consistent in the non-flat case but become an $\sim 2\sigma$ tension (with respect to the *Planck* value for the ΛCDM model) when flatness is imposed.

Fig. 2 shows the envelope enclosing 95 per cent of the reconstructed $H(z)$ for two representative data set combinations. The odd shape of the envelope is due to the fact that the linear interpolation is being performed in $1/H$, while the quantity plotted is $H(z)$. Symbols represent the best-fitting $H(z)$ of each redshift. The highest redshift nodes are poorly constrained and therefore not shown. Also for the CSBH case, the joint distribution of the $\mathbf{h}^{-1}(z_n)$ values for the last two redshift nodes shows a structure indicating a high degree of interdependence between the two quantities. This does not affect the determination of the standard ruler, as there is no correlation between r_s or r_s^h and $\mathbf{h}^{-1}(z_n)$ for $n \geq 4$.

3.1 Robustness to prior assumptions

To assess the dependence on the prior assumptions, we compare our findings with the results and the approach of BVR. In that work, a similar reconstruction of the late time expansion history is performed in the context of the study of the tension between the (direct) local H_0 determination and its CMB-inferred value within the ΛCDM model. However, they use a different parametrization and sampling method: $H(z)$ and r_s are the free parameters, and $H(z)$ values are interpolated using natural cubic splines, instead of r_s^h, $\mathbf{h}^{-1}(z)$ and linear interpolation as done here. They also use an Affine Invariant sampler [implemented in the public code EMCEE (Foreman-Mackey et al. 2013)] instead of Metropolis Hastings. BVR do not include cosmic clocks, so we concentrate on the SBH data combination for this test. The number of nodes is the same ($N = 5$), although their location is different. We isolate each of the methodological differences to study their effect in the final results.

As supernovae data impose very strong constraints on the shape of $H(z)$, the resulting expansion history does not depend on the

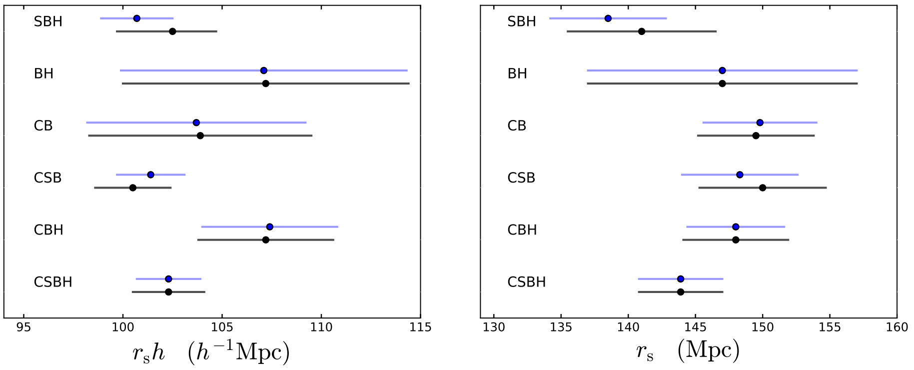

Figure 1. At a glance: comparison of central values and 1σ errors on the r_s^h (left-hand panel) and r_s (right-hand panel) measurements for flat geometry (blue) and marginalizing over the curvature (black). Note the change of the scale in the x-axis in each figure.

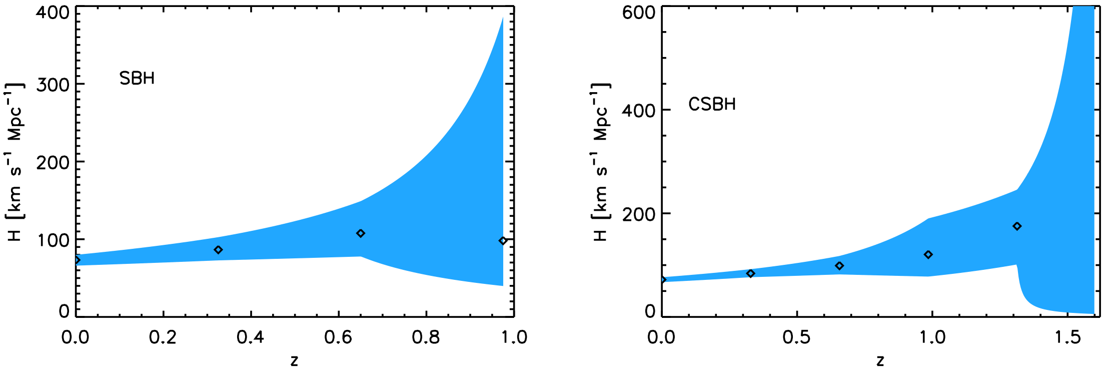

Figure 2. Reconstructed expansion history $H(z)$ (95 per cent confidence envelop) for two representative data set combinations: SBH (left-hand panel) CSBH (right-hand panel). The last redshift nodes (one on the left-hand side, two on the right-hand side) are not shown as there $H(z)$ is poorly constrained. The jagged shape of the envelop is due to the linear interpolation being performed in $1/H$, while the quantity plotted is $H(z)$. Symbols represent the best-fitting values for the reconstruction.

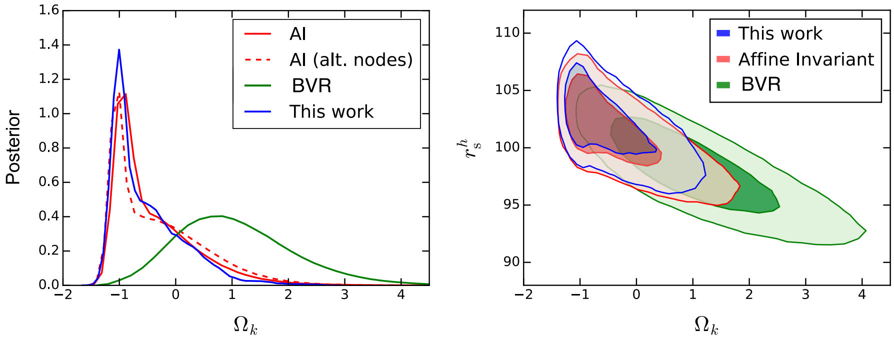

Figure 3. Effects of prior assumptions and the MCMC sampling method. We show the comparison of the posterior distributions of Ω_k (left-hand panel) and in the Ω_k–r_s^h plane (right-hand panel) obtained from the same data (SBH) with different methodologies: this work (blue), using an Affine Invariant sampler instead of Metropolis Hastings (red) with two choices for the redshift sampling, the one from this work (solid) and the other from BVR (dashed), and the approach of BVR (green), which uses an Affine Invariant sampler, r_s and $H(z_i)$ as variables and a spline interpolation of $H(z)$.

interpolation method, even taking into account that the splines allow much more freedom than the linear interpolation. Also, the location of the knots does not have any significant effect in the final fit of the reconstruction. It does, however, have a mild effect on the curvature, which is the parameter most weakly constrained.

In Fig. 3, we show the posterior distribution of Ω_k (left-hand panel) and the joint distribution in the Ω_k–r_s^h plane (right-hand panel) for the different cases compared in this section. The distributions are marginalized over all other parameters. We refer as 'Affine Invariant' to the case when the only change with respect to this work is the MCMC sampler. The figure also quantifies the effect of a different choice of redshift sampling (nodes). Unlike in our parametrization, using r_s and $H(z)$ as free parameters makes the distribution of Ω_k

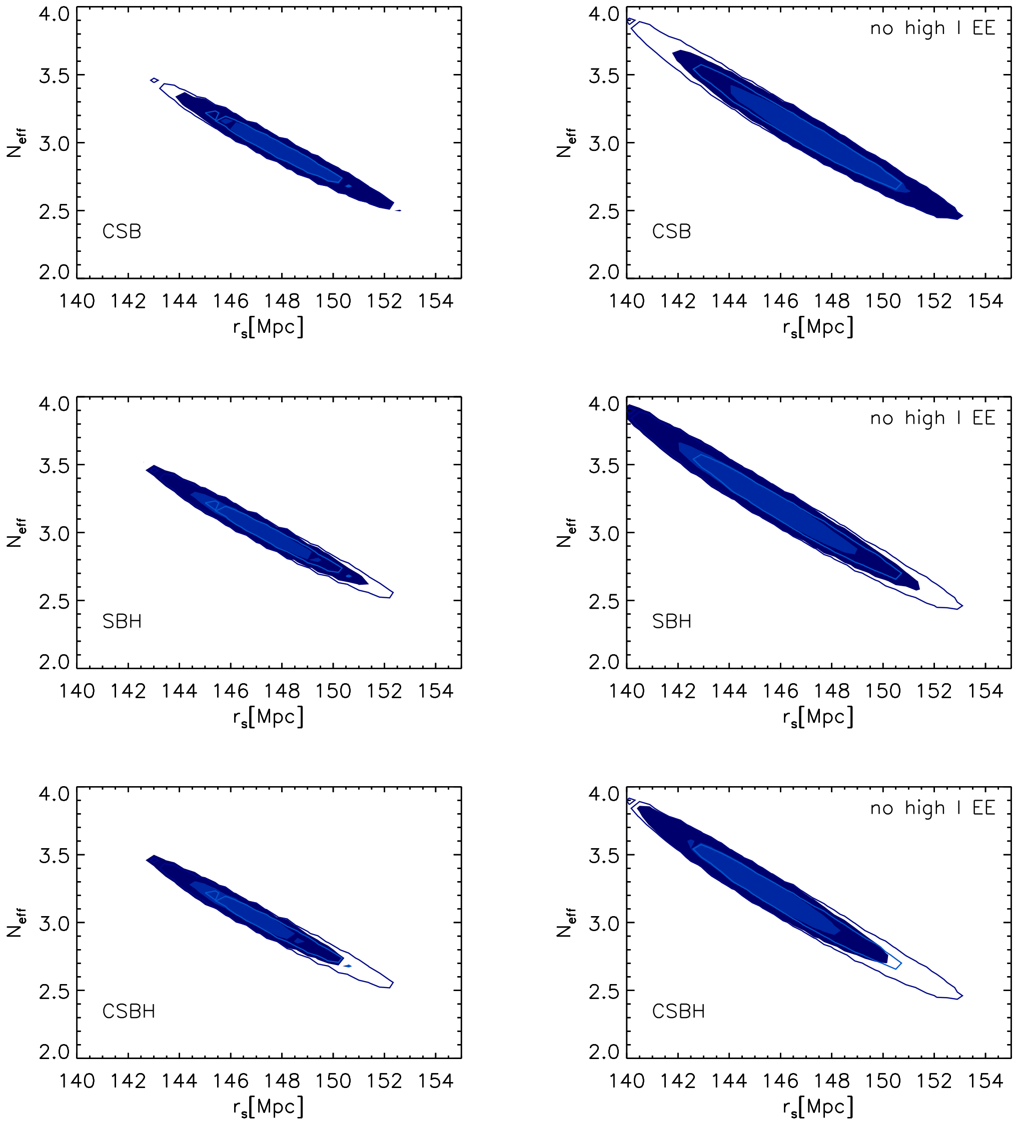

Figure 4. Effect of combining the low-redshift standard ruler measurement (interpreted as the sound horizon at radiation drag) with *Planck* CMB observations. The transparent contours show the joint $r_{\rm s}$ versus $N_{\rm eff}$ 68 per cent and 95 per cent marginalized confidence regions obtained from the posterior sample provided by the *Planck* CMB mission. On the left-hand side, all temperature and polarization data are used, whereas on the right-hand side, high-ℓ polarization data are not included. The filled contours result from importance sampling this with our CSB measurement (top row), SBH (middle row) and CSBH (bottom row).

Gaussian, but centred around higher values and with larger error bars.

As $r_{\rm s}$ and Ω_k are anticorrelated (and Ω_k and H_0 are independent), differences in the posterior of Ω_k result in different determinations of the low-redshift standard ruler. The values of $r_{\rm s}$ and $r_{\rm s}^h$ obtained in this work (for the non-flat case) are $\sim 1\sigma$ higher than in BVR. Once flatness is imposed, the discrepancies between the two sampling algorithms and prior choices disappear.

It is important to point out that the dependence of the posterior on the prior choice and the MCMC sampling method appears only when the parameters are weakly constrained. This is the case when using only BAOs, supernovae and H_0 (SBH) and not imposing flatness. Both cosmic clocks and supernovae data are needed to obtain a Gaussian posterior distribution for the curvature: In these cases (CSBH and CSB), the dependence on the prior assumptions and the sampler becomes unimportant. The dependence on prior is negligible also for the SBH data set combination when flatness is imposed.

4 DISCUSSION AND CONCLUSIONS

This model-independent determination of the low-redshift standard ruler can be interpreted as the sound horizon at the baryon drag and thus compared with (model-dependent) CMB determinations. This comparison can be used to limit the scope of new physics that may alter the early expansion rate and sound speed. This is investigated in detail, for example, in Bernal et al. (2016). Here, we only compare our constraints with those obtained by the Planck team with the

Planck 2015 data release, using publicly available posterior samples (Planck Collaboration XIII 2015). The direct measurement of the ruler is in good agreement with the CMB-derived one for all models considered by the Planck team and especially the standard ΛCDM model. In all cases, the CMB-inferred error bars are, understandably, much smaller, with one notable exception: the model where the effective number of neutrino species is free (Heavens et al. 2014). The effect of combining our measurement with the CMB one is illustrated in Fig. 4. Transparent contours are the (joint) 68 per cent and 95 per cent confidence regions for CMB data alone, including (excluding) high-ℓ polarization data on the left-hand (right-hand) panel. The filled contours result from importance sampling this with our SBH, CSB or CSBH measurement, which reduces the errors significantly. When $H_0^{\rm SH0ES}$ is included, the error on $N_{\rm eff}$ is reduced by suppressing the posterior for low $N_{\rm eff}$ values. A similar trend was found by Riess et al. (2016) and by BVR.

Note that even without an estimate of h, the combination of BAO and supernovae data already constrains the low-redshift standard ruler scale $r_{\rm s}^h$ at the 2 per cent level, $r_{\rm s}^h = 101.0 \pm 2.3$ Mpc h^{-1}.

Looking ahead, improvements on the low-redshift standard ruler measurement may arise from the next generation of BAO surveys. For example, if in the CSB (or CSBH) combination we substitute the current BAO measurements with forecasted constraints achievable with a survey with the specifications of DESI (Levi et al. 2013), errors without imposing flatness will reduce as follows. The error on $r_{\rm s}^h$ will go from 1.9 per cent to 1.3 per cent (1.8 per cent to 1.1 per cent), the error on $r_{\rm s}$ from 3.2 per cent to 2.8 per cent (2.2 per cent to 1.9 per cent), the error on H_0 from 3.7 per cent to 3.4 per cent (2.1 per cent to 2 per cent) and the error on Ω_k from ±0.41 to ±0.28 (±0.31 to ±0.22). For the SB combination, we find an error on $r_{\rm s}^h$ of 1.5 per cent, and 1.3 per cent with flatness imposed. Given the dramatic improvement in the precision of expansion history constraints provided by the next generation of BAO surveys, these forecasts indicate that we are entering a regime where the error on $r_{\rm s}^h$ is dominated by the supernovae errors and the error on $r_{\rm s}$ is dominated by that on the normalization of the expansion history h, and therefore directly or indirectly on H_0. Improvement on the local H_0 determination towards a goal of ∼1 per cent error budget may be provided by, for example, gravitational lensing time delays (Suyu et al. 2016) and by further improvements of the classic distance ladder approach (Riess et al. 2016).

ACKNOWLEDGEMENTS

LV and JLB thank A. Riess for discussions. RJ and LV acknowledge support from Mineco grants AYA2014-58747-P and MDM-2014-0369 of ICCUB (Unidad de Excelencia Maria de Maeztu), and a visiting scientist grant from the Royal Society. JLB is supported by the Spanish MINECO under grant BES-2015-071307, co-funded by the ESF. JLB and AFH acknowledge the hospitality of the Radcliffe Institute for Advanced Study, Harvard University. AFH, RJ and LV acknowledge the Imperial College for support under the CosmoCLASSIC collaboration.

Based on observations obtained with *Planck* (http://www.esa.int/Planck), an ESA science mission with instruments and contributions directly funded by ESA Member States, NASA and Canada.

Funding for SDSS-III has been provided by the Alfred P. Sloan Foundation, the Participating Institutions, the National Science Foundation, and the US Department of Energy Office of Science. The SDSS-III web site is http://www.sdss3.org/.

SDSS-III is managed by the Astrophysical Research Consortium for the Participating Institutions of the SDSS-III Collaboration including the University of Arizona, the Brazilian Participation Group, Brookhaven National Laboratory, Carnegie Mellon University, University of Florida, the French Participation Group, the German Participation Group, Harvard University, the Instituto de Astrofisica de Canarias, the Michigan State/Notre Dame/JINA Participation Group, Johns Hopkins University, Lawrence Berkeley National Laboratory, Max Planck Institute for Astrophysics, Max Planck Institute for Extraterrestrial Physics, New Mexico State University, New York University, Ohio State University, Pennsylvania State University, University of Portsmouth, Princeton University, the Spanish Participation Group, University of Tokyo, University of Utah, Vanderbilt University, University of Virginia, University of Washington and Yale University.

REFERENCES

Bernal J. L., Verde L., Riess A. G., 2016, JCAP, 10, 019, (BVR)
Betoule M. et al., 2014, A&A, 568, A22
Beutler F. et al., 2011, MNRAS, 416, 3017
Beutler F., Blake C., Koda J., Marín F. A., Seo H.-J., Cuesta A. J., Schneider D. P., 2016, MNRAS, 455, 3230
Blake C. et al., 2011, MNRAS, 418, 1707
Bonvin V. et al., 2016, MNRAS, 465, 4914
Cuesta A. J. et al., 2016, MNRAS, 457, 1770
Foreman-Mackey D., Hogg D. W., Lang D., Goodman J., 2013, PASP, 125, 306
Goodman J., Weare J., 2010, Comm. App. Math. Comp., 5, 65
Hastings W. K., 1970, Biometrika, 57, 97
Heavens A., Jimenez R., Verde L., 2014, Phys. Rev. Lett., 113, 241302
Jimenez R., Loeb A., 2002, ApJ, 573, 37
Kazin E. A. et al., 2014, MNRAS, 441, 3524
Levi M. et al., 2013, preprint (arXiv:1308.0847)
Moresco M. et al., 2016, J. Cosmol. Astropart. Phys., 5, 014
Noh Y., White M., Padmanabhan N., 2009, Phys. Rev. D, 80, 123501
Padmanabhan N., White M., Cohn J. D., 2009, Phys. Rev. D, 79, 063523
Planck Collaboration XIII, 2015, A&A, 594, A13
Riess A. G. et al., 2016, AJ, 826, 56
Sutherland W., 2012, MNRAS, 426, 1280
Suyu S. H. et al., 2016, MNRAS, preprint (arXiv:1607.00017)

This paper has been typeset from a TEX/LATEX file prepared by the author.

Journal of Cosmology and Astroparticle Physics
An IOP and SISSA journal

Conservative cosmology: combining data with allowance for unknown systematics

José Luis Bernal[a,b] **and John A. Peacock**[c]

[a]ICC, University of Barcelona, IEEC-UB,
Martí i Franquès, 1, E08028, Barcelona, Spain
[b]Dept. de Física Quàntica i Astrofísica, Universitat de Barcelona,
Martí i Franquès 1, E08028 Barcelona, Spain
[c]Institute for Astronomy, University of Edinburgh, Royal Observatory,
Blackford Hill, Edinburgh, EH9 3HJ, U.K.

E-mail: joseluis.bernal@icc.ub.edu, jap@roe.ac.uk

Received March 14, 2018
Accepted June 20, 2018
Published July 2, 2018

Abstract. When combining data sets to perform parameter inference, the results will be unreliable if there are unknown systematics in data or models. Here we introduce a flexible methodology, `BACCUS`: BAyesian Conservative Constraints and Unknown Systematics, which deals in a conservative way with the problem of data combination, for any degree of tension between experiments. We introduce parameters that describe a bias in each model parameter for each class of experiments. A conservative posterior for the model parameters is then obtained by marginalization both over these unknown shifts and over the width of their prior. We contrast this approach with an existing method in which each individual likelihood is scaled, comparing the performance of each approach and their combination in application to some idealized models. Using only these rescaling is not a suitable approach for the current observational situation, in which internal null tests of the errors are passed, and yet different experiments prefer models that are in poor agreement. The possible existence of large shift systematics cannot be constrained with a small number of data sets, leading to extended tails on the conservative posterior distributions. We illustrate our method with the case of the H_0 tension between results from the cosmic distance ladder and physical measurements that rely on the standard cosmological model.

Keywords: cosmological parameters from CMBR, cosmological parameters from LSS, dark energy experiments

ArXiv ePrint: 1803.04470

https://doi.org/10.1088/1475-7516/2018/07/002

Contents

1 Introduction

For two decades or more, the standard Λ-Cold Dark Matter (ΛCDM) cosmological model has succeeded astonishingly well in matching new astronomical observations, and its parameters are precisely constrained (e.g. [1–3]). However, more recent work has persistently revealed tensions between high and low redshift observables. In the case of the Hubble constant, H_0, the best direct measurement using cepheids and supernovae type Ia [4] is in 3.4σ tension with the value inferred assuming ΛCDM using Planck observations [1]. Planck and weak lensing surveys both measure the normalization of density fluctuations via the combination $\Omega_m^{0.5}\sigma_8$, and their estimates were claimed to be in 2.3σ tension by the KiDS collaboration [5] — although recent results from DES are less discrepant [6]. These inconsistencies are not currently definitive (e.g. [7]), but they raise the concern that something could be missing in our current cosmological understanding. It could be that the ΛCDM model needs extending, but it could also be that the existing experimental results suffer from unaccounted-for systematics or underestimated errors.

When inconsistent data are combined naively, it is well understood that the results risk being inaccurate and that formal errors may be unrealistically small. For this reason, much emphasis is placed on tests that can be used to assess the consistency between two data sets (e.g. [8–10]). We refer the interested reader to [11, 12] for more methodologies but also for a comprehensive comparison between different measures of discordance. Another approach is the posterior predictive distribution, which is the sampling distribution for new data given existing data and a model, as used in e.g., [13]. However, these methods are not really helpful in cases of mild tension, where a subjective binary decision is required as to whether or not a genuine inconsistency exists.

Unknown systematics can be modelled as the combination of two distinct types. Type 1 systematics affect the random scatter in the measurements (and therefore the size of the errors in a parameterised model), but do not change the maximum-posterior values for the parameters of the model. In contrast, type 2 systematics offset the best-fitting parameters without altering the random errors; they are completely equivalent to shifts in the parameters of the model without modifying the shape of the posterior of each parameter. While the former are commonly detectable through internal evidence, the latter are more dangerous and they can only reveal themselves when independent experiments are compared. Much of our discussion will focus on this class of systematic. With a detailed understanding of a given experiment, one could do better than this simple classification; but here we are trying to capture 'unknown unknowns' that have evaded the existing modelling of systematics, and so the focus must be on the general character of these additional systematics.

Taking all this into account, there is a need for a general conservative approach to the combination of data. This method should allow for possible unknown systematics of both kinds and it should permit the combination of data sets in tension with an agnostic perspective. Such a method will inevitably yield uncertainties in the inferred parameters that are larger than in the conventional approach, but having realistic uncertainties is important if we are to establish any credible claims for the detection of new physics.

The desired method can be built using a hierarchical approach. Hierarchical schemes have been used widely in cosmology, e.g. to model in more detail the dependence of the parameters on each measurement in the case of H_0 and the cosmic distance ladder [14], or the cosmic shear power spectrum [15]. While the extra parameters often model physical quantities, our application simply requires empirical nuisance parameters. The introduction of extra parameters to deal with data combination was first introduced in the pioneering discussion of [16]. A more general formulation was provided by [17] and refined in [18] (H02 hereinafter). This work assigns a free weight to each data set, rescaling the logarithm of each individual likelihood (which is equivalent to rescaling the errors of each experiment if the likelihood is Gaussian), in order to achieve an overall reduced χ^2 close to unity. The H02 method yields meaningful constraints when combining data sets affected by type 1 errors, and it detects the presence of the errors by comparing the relative evidences of the conventional combination of data and their approach. However, this method is not appropriate for obtaining reliable constraints in the presence of type 2 systematics, where we might find several experiments that all have reduced χ^2 values of unity, but with respect to different best-fitting models. H02 do not make our distinction between different types of systematics, but in fact they do show an example where one of the data sets has a systematic type 2 shift (see figures 3 & 4 of H02). Although their method does detect the presence of the systematic, we do not feel that it gives a satisfactory posterior in this case, for reasons discussed below in section 3.2.

Here we present a method called `BACCUS`,[1] BAyesian Conservative Constraints and Unknown Systematics, which is designed to deal with systematics of both types. Rather than weighting each data set, the optimal way to account for type 2 systematics is to consider the possibility that the parameters preferred by each experiment are offset from the true values. Therefore, extra parameters shift the model parameters when computing each individual likelihood, and marginalized posteriors of the model parameters will account for the possible existence of systematics in a consistent way. Moreover, studying the marginalized posteriors of these new parameters can reveal which experiments are most strongly affected by systematics.

This paper is structured as follows. In section 2, we introduce our method and its key underlying assumptions. In section 3, we consider a number of illustrative examples of data sets constructed to exhibit both concordance and discordance, contrasting the results

---

[1] A python package implementing is publicly available in https://github.com/jl-bernal/BACCUS.

from our approach with those of H02. We then apply our method to a genuine cosmological problem, the tension in H_0, in section 4. Finally, a summary and some general discussion of the results can be found in section 5. We use the Monte Carlo sampler `emcee` [19] in all the cases where Monte Carlo Markov Chains are employed.

2 Overview of assumptions and methodology

We begin by listing the key assumptions that underlie our statistical approach to the problem of unknown systematics. Firstly, we will group all codependent experiments in different *classes*, and consider each of them independent from the others. For example, observations performed with the same telescope or analyzed employing the same pipeline or model assumptions will be considered in the same class, since all the really dangerous systematics would be in common. Then, our fundamental assumption regarding systematics will be that a experiment belonging to each of these classes is equally likely to commit an error of a given magnitude, and that these errors will be randomly and independently drawn from some prior distribution. Attempts have been made to allow for dependence between data sets when introducing scaling parameters as in H02 (see [20]). We believe that a similar extension of our approach should be possible, but we will not pursue this complication here.

With this preamble, we can now present the formalism to be used. Consider a model M, parameterised by a set of model parameters, $\boldsymbol{\theta}$ (we will refer to $M(\boldsymbol{\theta})$ as $\boldsymbol{\theta}$ for simplicity), which are to be constrained by several data sets, $\mathbf{D}$. The corresponding posterior, $\mathcal{P}\left(\boldsymbol{\theta}|\mathbf{D}\right)$, and the likelihood, $\mathcal{P}\left(\mathbf{D}|\boldsymbol{\theta}\right)$, are related by the Bayes theorem:

$$\mathcal{P}\left(\boldsymbol{\theta}|\mathbf{D}\right) = \frac{\mathcal{P}\left(\boldsymbol{\theta}\right)\mathcal{P}\left(\mathbf{D}|\boldsymbol{\theta}\right)}{\mathcal{P}\left(\mathbf{D}\right)}, \tag{2.1}$$

where $P(\boldsymbol{\theta})$ is the prior. We will consider flat priors in what follows and concentrate on the likelihood, unless otherwise stated. For parameter inference, we can drop the normalization without loss of generality.

We can account for the presence of the two types of systematics in the data by introducing new parameters. For type 2 systematics, the best fit values of the parameters for each experiment, $\tilde{\boldsymbol{\theta}}_i$, may be offset from the true value by some amount. We introduce a shift parameter, $\Delta^i_{\theta_j}$, for each parameter θ_j and class i of experiments. For type 1 systematics, we follow H02 and introduce a rescaling parameter α_i which weights the logarithm of the likelihood of each class of experiments; if the likelihood is Gaussian, this is equivalent to rescaling each individual χ^2 and therefore the covariance. Considering n_i data points for the class of experiments i, the likelihood is now:

$$\mathcal{P}(\boldsymbol{\theta}, \boldsymbol{\alpha}, \{\boldsymbol{\Delta_\theta}\}|\mathbf{D}) \propto \prod_i \alpha_i^{n_i/2} \exp\left[-\frac{\alpha_i}{2}\left(\chi^2_{\mathrm{bf},i} + \Delta\chi^2_i(\boldsymbol{\theta} + \boldsymbol{\Delta}^i_{\boldsymbol{\theta}} - \tilde{\boldsymbol{\theta}}_i)\right)\right], \tag{2.2}$$

where χ^2_{bf} is the minimum χ^2, corresponding to the best-fit value of $\boldsymbol{\theta}$, $\tilde{\boldsymbol{\theta}}$. Here, we use the notation $\{\boldsymbol{\Delta_\theta}\}$ to indicate the vector of shift parameters for each parameter of the model. There is a different vector of this sort for every class of experiments, indexed by i.

For rescaling parameters, H02 argue that the prior should be taken as:

$$\mathcal{P}(\alpha_i) = \exp[-\alpha_i] \tag{2.3}$$

so that the mean value of α_i over the prior is unity, i.e. experiments estimate the size of their random errors correctly on average. One might quarrel with this and suspect that underestimation of errors could be more common, but we will retain the H02 choice; this does not affect the results significantly. In realistic cases where the number of degrees of freedom is large and null tests are passed so that $\chi^2_{\mathrm{bf},i} \simeq n$, the scope for rescaling the errors will be small and α_i will be forced to be close to unity. For the prior on shift parameters, we choose a zero-mean Gaussian with a different unknown standard deviation determined by σ_{θ^j}, corresponding to each parameter θ_j and common to all classes of experiments. Furthermore, it is easy to imagine systematics that might shift several parameters in a correlated way, so that the prior on the shifts should involve a full covariance matrix, $\boldsymbol{\Sigma}_\Delta$, containing the variances, $\sigma^2_{\theta^j}$, in the diagonal and off-diagonal terms obtained with the correlations ρ_{j_1,j_2} for each pair of shifts ($\Sigma_{j_1,j_2} = \rho_{j_1,j_2}\sigma_{\theta^{j_1}}\sigma_{\theta^{j_2}}$). Thus the assumed prior on the shifts is:

$$\mathcal{P}(\{\boldsymbol{\Delta_\theta}\}|\boldsymbol{\sigma}_\theta, \boldsymbol{\rho}) \propto \prod_i^N |\boldsymbol{\Sigma}_\Delta|^{-1/2} \exp\left[-\frac{1}{2}\boldsymbol{\Delta}_\theta^{i\,\mathrm{T}}\boldsymbol{\Sigma}_\Delta^{-1}\boldsymbol{\Delta}_\theta^i\right]. \tag{2.4}$$

We now need to specify the hyperpriors for the covariance matrix of the shifts, $\boldsymbol{\Sigma}_\Delta$. Our philosophy here is to seek an uninformative hyperprior: it is safer to allow the data to limit the degree of possible systematic shifts, rather than imposing a constraining prior that risks forcing the shifts to be unrealistically small.

Different options of priors for covariance matrices are discussed by e.g. [21]. In order to ensure independence among variances and correlations, we use a separation strategy, applying different priors to variances and correlations (e.g. [22]). A covariance matrix can be expressed as $\boldsymbol{\Sigma} = \boldsymbol{SRS}$, with $\boldsymbol{S}$ being a diagonal matrix with $S_{jj} = \sigma_{\theta^j}$ and $\boldsymbol{R}$, the correlation matrix, with $R_{ii} = 1$ and $R_{ij} = \rho_{ij}$. As hyperprior for each of the covariances we choose a lognormal distribution ($\log\sigma = N(b,\xi)$, where $N(b,\xi)$ is a Gaussian distribution in $\log\sigma$ with mean value b and variance ξ). In the case of the correlation matrix, we use the LKJ distribution [23] as hyperprior, which depends only on the parameter η: for $\eta = 1$, it is an uniform prior over all correlation matrices of a given order; for $\eta > 1$, lower absolute correlations are favoured (and vice versa for $\eta < 1$). The parameters b, ξ and η can be chosen to suit the needs of the specific problem. We prefer to be as agnostic as possible, so we will choose $\eta = 1$ and b and ξ such as the hyperprior of each covariance is broad enough to not force the shifts to be small.

The final posterior can be marginalized over all added parameters, leaving the conservative distribution of the model parameters $\boldsymbol{\theta}$, that is the main aim of this work. This immediately provides a striking insight: a single experiment gives no information whatsoever. It is only when we have several experiments that the possibility of large $\boldsymbol{\sigma_\theta}$ starts to become constrained (so that the $\{\boldsymbol{\Delta_\theta}\}$ cannot be too large). In the case of consistent data, as the shifts are drawn from a Gaussian distribution, only small shifts are favoured (as the individual likelihoods would not overlap otherwise). If, on the other hand, only two data sets are available and there is a tension between them regarding some parameter θ_j, the prior width σ_{θ^j} could be of the order of such tension, but much larger values will be disfavoured.

However, an alternative would be to obtain the marginalized posteriors of $\{\boldsymbol{\Delta_\theta}\}$. This tells us the likely range of shifts that each data set needs for each parameter, so that unusually discrepant experiments can be identified by the system. As we will see in examples below, this automatically results in their contribution to the final posterior being downweighted. If one class of experiments has shifts that are far beyond all others, this might give an objective reason to repeat the analysis without it, but generally we prefer not to take this approach: judging whether an offset is significant enough to merit exclusion is a somewhat arbitrary decision, and is complicated in a multidimensional parameter space. Our formalism automatically downweights data sets as their degree of inconsistency grows, and this seems sufficient.

3 Application to illustrative examples

3.1 Shift parameters in the one-parameter Gaussian case

In order to exhibit all the features of our method more clearly, we first apply the formalism to the simple model in which there is only one parameter ($\boldsymbol{\theta} = a$) and the probability density functions (PDFs) of a for the N individual experiments are Gaussian. In this case, we can rewrite Equation 2.2 as:

$$\mathcal{P}(a, \boldsymbol{\alpha}, \boldsymbol{\Delta}_a, \sigma_a|\mathbf{D}) \propto \prod_i^N \alpha_i^{n_i/2} \exp\left[-\frac{1}{2}\alpha_i \left(\chi^2_{i,\mathrm{bf}} + \Delta\chi^2_i(a+\Delta^i_a)\right)\right]. \tag{3.1}$$

We apply the prior for rescaling parameters (Equation 2.3) and marginalize over each α_i to obtain the marginalized posterior for a single class of experiments:

$$\mathcal{P}_i(a, \Delta^i_a, \sigma_a|D_i) \propto \left(\Delta\chi^2_i(a+\Delta^i_a)+2\right)^{-(n_i/2+1)}. \tag{3.2}$$

For large n_i, $\chi^2_i + 2 \simeq \chi^2_i$, and the right hand side of Equation 3.2 is proportional to $\exp[-(\Delta\chi^2_i/2)(n_i/\chi^2_{i,\mathrm{bf}})]$, which in effect instructs us to rescale parameter uncertainties according to $(\chi^2_{\nu,i})^{1/2}$, where $\chi^2_{\nu,i}$ is the reduced χ^2_i for the class of experiments i. But it can be assumed that experiments will pursue internal null tests to the point where $\chi^2_\nu \simeq 1$; thus in practice rescaling parameters can do little to erase tensions.

Assuming hereafter that experimenters will achieve $\chi_\nu = 1$ exactly, we can now focus on the novel feature of our approach, which is the introduction of shift parameters. Then, the posterior can be written as

$$\mathcal{P}(a, \boldsymbol{\Delta}_a, \sigma_a|\mathbf{D}) \propto \prod_i^N \sigma_a^{-1} \exp\left[-\frac{1}{2}\sum_{k=1}^{n_i}\left(\frac{\left(y^k_i(a+\Delta^i_a)-D^k_i\right)^2}{\sigma^{k\,2}_i}\right) + \frac{\Delta^{i\,2}_a}{2\sigma^2_a}\right], \tag{3.3}$$

where $y^k_i(x)$ is the theoretical prediction to fit to the measurement D^k_i of the class of experiments i, with error σ^k_i. Note that the width of the prior for the shifts, σ_a, is the same for all data sets, by assumption. Marginalizing over the shifts, then the posterior of each class of experiments is:

$$\mathcal{P}_i(a, \sigma_a|\mathbf{D}) \propto \prod_{k=1}^{n_i}(\sigma^{k\,2}_i + \sigma^2_a)^{-1/2} \exp\left[-\frac{1}{2}\frac{\left(y^k_i(a)-D^k_i\right)^2}{\left(\sigma^{k\,2}_i+\sigma^2_a\right)^2}\right]. \tag{3.4}$$

Therefore, our method applied to a model with only one parameter and Gaussian likelihoods reduces to the convolution of the original posteriors with a Gaussian of width σ_a.

Finally, we need to marginalize over σ_a. Consider for example a hyperprior wide enough to be approximated as uniform in σ_a, and suppose that all the N data sets agree on $\tilde{a}_i = 0$

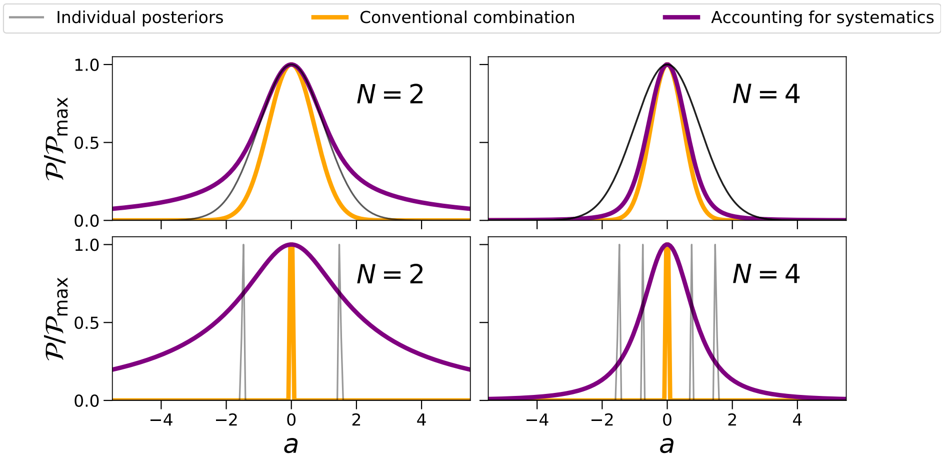

Figure 1. Comparison of the results obtained using shift parameters and the conventional approach to combining data sets in a model with only one parameter, a, and N data sets whose individual posteriors are Gaussians. We show individual posteriors in black, the posteriors obtained with the conventional approach in orange and the posterior obtained with our approach, in purple. The dependence of the posterior on the number of data sets for the exactly consistent case is shown in the top panels, while strongly inconsistent cases are shown in the bottom panels.

and all the errors, $\sigma_i^k = \sigma_i$, are identical. Then we can derive the marginalized posterior in the limit of small and large a:

$$\mathcal{P}(a|\mathbf{D}) \propto \begin{cases} 1 - \exp\left[\dfrac{(N-1)a^2}{2\sigma_i^2}\right], & \text{for } a \ll 1 \\ a^{1-N}, & \text{for } a \gg 1 \end{cases} \tag{3.5}$$

For values of a close to $\tilde{a}_i$ the posterior presents a Gaussian core, whose width is $\sigma_i/\sqrt{N-1}$, in contrast with the conventional $\sigma_i/\sqrt{N}$ from averaging compatible data. For values of a very far from $\tilde{a}_i$, the posterior has non-Gaussian power-law tails. For $N = 2$ these are so severe that the distribution cannot be normalized, so in fact three measurements is the minimum requirement to obtain well-defined posteriors. As will be discussed in section 5, one can avoid such divergence by choosing harder priors on Δ_a^i or σ_a, but we prefer to be as agnostic as possible. Nonetheless, these 'fat tails' on the posterior are less of an issue as N increases. These two aspects of compatible data can be appreciated in the top panels of figure 1. The message here is relatively optimistic: provided we have a number of compatible data sets, the conservative posterior is not greatly different from the conventional one.

Alternatively, we can consider an example of strongly incompatible data. Let the N data sets have negligible σ_i and suppose the corresponding $\tilde{a}_i$ are disposed symmetrically about $a = 0$ with spacing ϵ, e.g. $\tilde{a} = (-\epsilon, 0, +\epsilon)$ for $N = 3$. This gives a marginalized posterior that depends on N. For example, the tails follow a power law: $\mathcal{P}(a|\mathbf{D}) \propto (1 + 4a^2/\epsilon^2)^{-1/2}$ for $N = 2$, $\mathcal{P}\ (a|\mathbf{D}) \propto (1 + 3a^2/2\epsilon^2)^{-1}$ for $N = 3$, etc., with an asymptotic dependence of $(a/\epsilon)^{1-N}$ for $N \gg 1$. So, as in the previous case, the posterior cannot be normalized if $N = 2$, but it rapidly tends to a Gaussian for large N. This case is shown in the bottom panels of figure 1. The appearance of these extended tails on the posterior is a characteristic result of our method, and seems inevitable if one is unwilling in advance to limit the size of

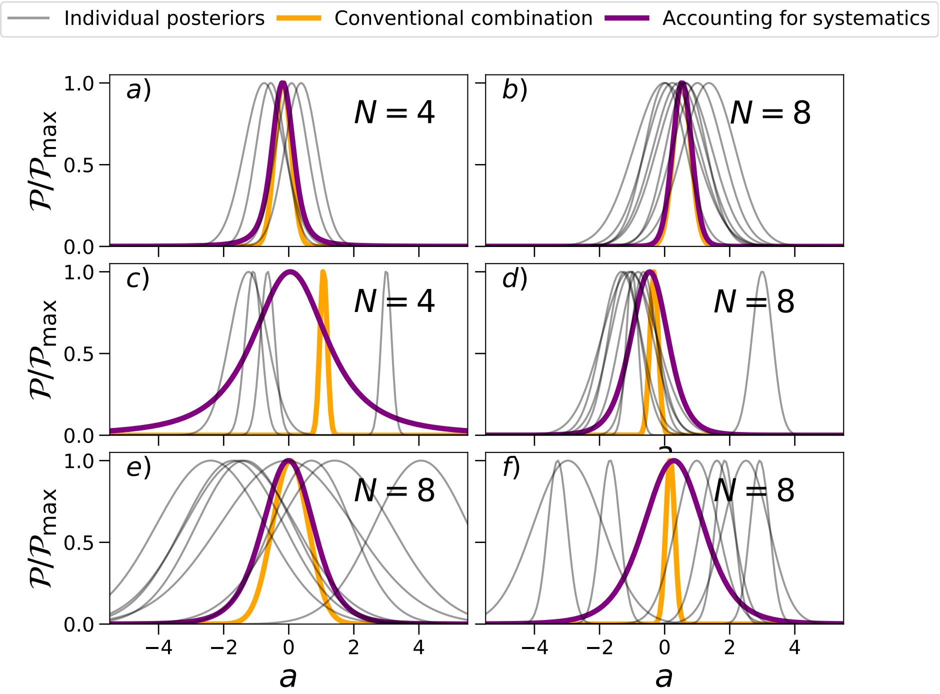

Figure 2. The same as figure 1, but considering cases in which all the data sets are consistent (panels a and b), only one is discrepant with the rest (panels c and d), eight data sets with scatter larger than the errors (panel e) and eight data sets with random values of the best fit and errors (panel f).

possible shift systematics. The power-law form depends in detail on the hyperprior, but if we altered this by some power of σ_a, the result would be a different power-law form for the 'fat tails' still with the generic non-Gaussinianity.

We also show in figure 2 some more realistic examples, starting with mock consistent data that are drawn from a Gaussian using the assumed errors (rather than $\tilde{a} = 0$), but then forcing one or more of these measurements to be discrepant. As with the simple $\tilde{a} = 0$ example, we see that the results for several consistent data sets approach the conventional analysis for larger N (panels a and b). But when there is a single discrepant data set, the posterior is much broader than in the conventional case (panel c). Nevertheless, as the number of consistent data sets increases, the posterior shrinks to the point where it is only modestly broader than the conventional distribution, and where the single outlying measurement is clearly identified as discrepant (panel d). Thus our prior on the shifts, in which all measurements are assumed equally likely to be in error, does not prevent the identification of a case where there is a single rogue measurement. However, these examples do emphasize the desirability of having as many distinct classes of measurement as possible, even though this may mean resorting to measurements where the individual uncertainties are larger. Additional coarse information can play an important role in limiting the tails on the posterior, especially in cases where there are discordant data sets (see panel d). Finally, we also show examples where the scatter of the individual best-fit is larger than the individual uncertainties of the data sets, so the size of the shifts are larger and our posterior is broader than the one obtained with conventional approach (panel *e*), and a case with several inconsistent measurements (with best-fit and errors distributed randomly), for which our posterior is centred close to 0 with a width set by the empirical distribution of the data (panel *f*).

3.2 Contrasting shift and rescaling parameters

If we ignore the constraints on α_i and consider only the relative likelihoods (with width of the distribution determined by σ_i), then there is an illuminating parallel between the effects of rescaling and shift parameters. Compare Equation 3.4, where all α have been already marginalized over ($\mathcal{P}_1$), with H02's method ($\mathcal{P}_2$):

$$\mathcal{P}_1 \propto \prod_i (\sigma_a^2 + \sigma_i^2)^{-1/2} \exp\left[-\frac{1}{2}\sum_i \frac{(a-\tilde{a}_i)^2}{\sigma_a^2+\sigma_i^2}\right] ;$$

$$\mathcal{P}_2 \propto \prod_i \alpha_i^{1/2}\sigma_i^{-1} \exp\left[-\frac{1}{2}\sum_i \frac{\alpha_i(a-\tilde{a}_i)^2}{\sigma_i^2}\right] , \tag{3.6}$$

these two expressions are clearly the same if $\alpha_i = \left(1+\sigma_a^2/\sigma_i^2\right)^{-1}$. However, there is a critical difference: while there is an α_i for each class of experiments, we only consider a single σ_a, which participates in the prior for all the shift parameters of all classes of experiments.

On the other hand, if different $\sigma_{\theta j}$ for each data sets were to be used, this would be equivalent to a double use of rescaling parameters. Furthermore, in the case of having several experiments with inconsistent results, the posterior using only rescaling parameters would be a multimodal distribution peaked at the points corresponding to the individual posteriors, as seen in figures 3 & 4 of H02. We feel that this is not a satisfactory outcome: it seems dangerously optimistic to believe that one out of a flawed set of experiments can be perfect when there is evidence that the majority of experiments are incorrect. Our aim should be to set conservative constraints, in which all experiments have to demonstrate empirically that they are *not* flawed (i.e. 'guilty until proved innocent').

3.3 Examples with multiple parameters

The approach to models with multiple parameters differs conceptually from the one-parameter case: there are several families of shifts, $\{\boldsymbol{\Delta}_\theta\}$, with their corresponding covariance matrix. A convenient simple illustration is provided by the example chosen by H02: consider data sets sampled from different straight lines. Thus, the model under consideration is $y = mx + c$, where y & x are the information given by the data and m & c are the parameters to constrain.

We consider three different straight lines for which we sample the data, D_i: $\{D_1\}$ and $\{D_2\} \equiv \{m = c = 1\}$; $\{D_3\} \equiv \{m = 0, c = 1.5\}$; and $\{D_4\} \equiv \{m = c = 0.7\}$. For all D_i, we consider three independent data sets (so $N = 6$ when combining i.e., D_1 and D_2) and assume $\sigma_y = 0.1$ for every data point. We combine $\{D_1\}$ with $\{D_2\}$ in figure 3, with $\{D_3\}$ in figure 4, and with $\{D_4\}$ in figure 5. Note the change of scale in each panel. In all cases, we study four situations corresponding to the combination of: all data sets with 50 or 5 points and errors correctly estimated or underestimated by a factor 5 (only in data sets from $\{D_2\}$, $\{D_3\}$ or $\{D_4\}$). We use lognormal priors with $b = -2$ and $\xi = 16$ both for σ_m and σ_c, and a LKJ distribution with $\eta = 1$ as the shifts hyperprior. We show the individual posteriors of each data set in black; the results using the conventional approach in

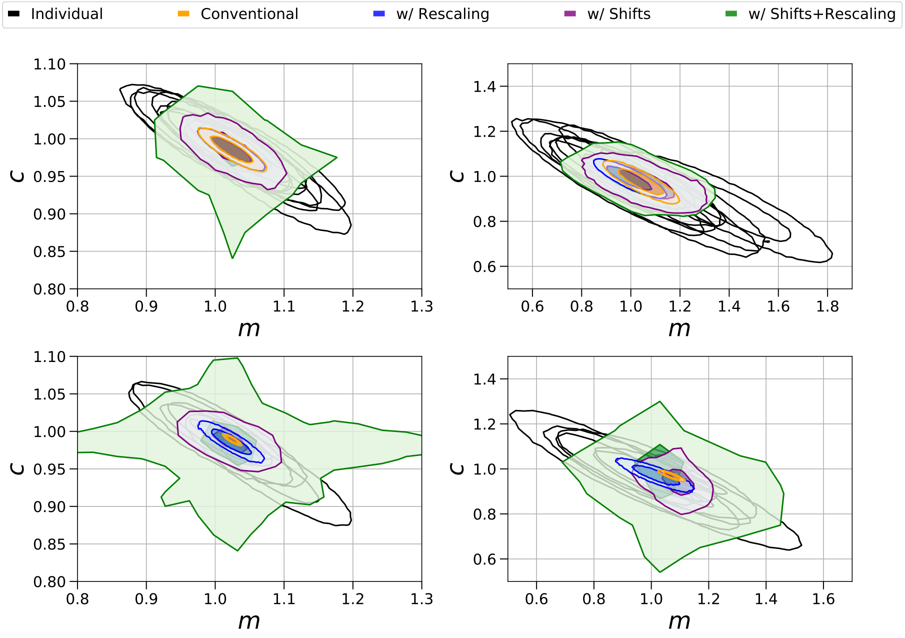

Figure 3. Constraints for six data sets sampled from a straight line with slope $m = 1$ and intercept $c = 1$ ($\{D_1\}$ and $\{D_2\}$). We show the individual posteriors in black and the results from using the conventional approach in orange, using rescaling parameters, in blue, using shift parameters, in purple, and using both in green. Top left: all data sets have 50 points. Top right: all data sets have 5 points. Bottom panels: as in the top panels, but the errors of $\{D_2\}$ are underestimated a factor 5.

orange; the constraints using only rescaling parameters in blue; using only shift parameters in purple; and using both in green. The occasional noisy shape of the latter is due to the numerical complexity of sampling the parameter space using rescaling and shifts. Generally, in this case the uncertainties are somewhat larger than in the case of using only shifts, except when individual errors are poorly estimated and the credible regions are much larger. This is because rescaling parameters gain a large weight in the analysis in order to recover a sensible $\chi^2_{\nu,i}$, which permits shifts that are too large for the corresponding prior (given that the corresponding likelihood is downweighted by small values of α_i). This can be seen comparing green and purple contours in the bottom panels of figures 3, 4 & 5.

As can be seen in figure 3, if the data sets are consistent and the errors are correctly estimated (top left panel), rescaling parameters have rather little effect on the final posterior. This supports our argument in Equation 3.2 and below. On the other hand, when errors are underestimated (bottom left panel), the recovered posterior is similar to the one in which the errors are correctly estimated. When the data sets contain smaller number of points (right panels) the results are qualitatively similar.

As expected, rescaling parameters yield conservative constraints accounting for type 1 systematics, but it is not a good choice if the data sets are not consistent. As shown in figures 4 & 5, the posterior for this case is multimodal, implying that the true values for the parameters are equally likely to correspond to one of the reported sets of values and ruling out values in between experiments, as foreshadowed in the previous section. Moreover, when the

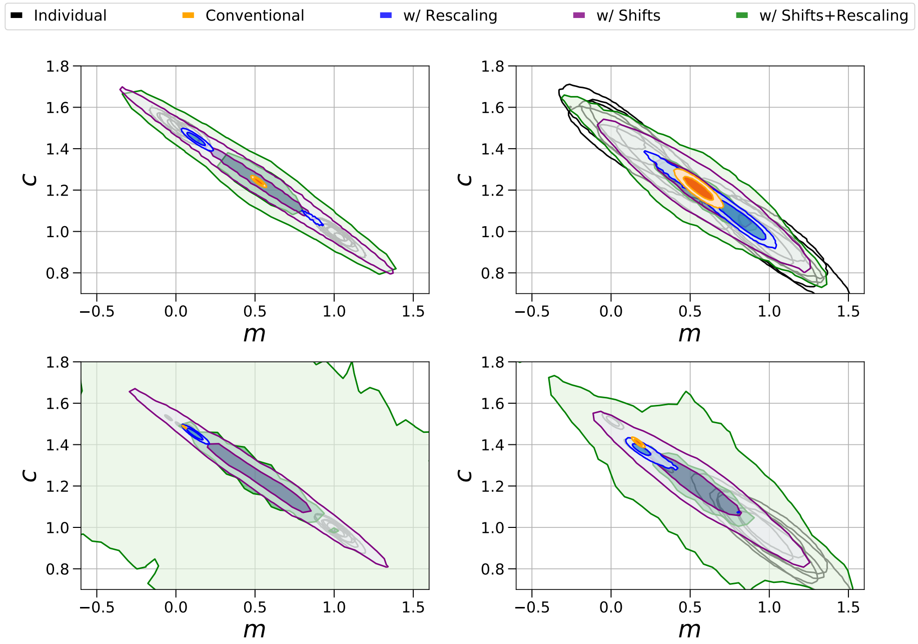

Figure 4. As figure 3 but using $\{D_3\}$ (with slope $m = 0$ and intercept $c = 1.5$) instead of $\{D_2\}$.

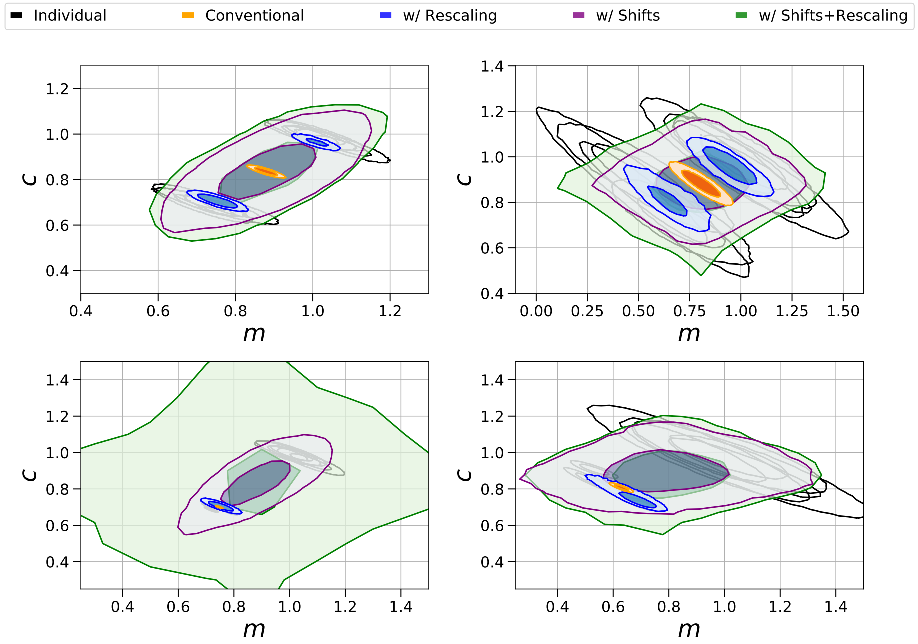

Figure 5. As figure 3 but using $\{D_4\}$ (with slope $m = 0.7$ and intercept $c = 0.7$) instead of $\{D_2\}$.

data sets are inconsistent and the errors of some of them underestimated, the constraints tend to favour only the values corresponding to such data sets (although with larger uncertainties than the conventional approach). Therefore, although rescaling parameters help to diagnose if any data set is suffering from both types of systematics, they cannot be used to obtain meaningful constraints if type 2 systematics are present.

On the other hand, using shift parameters gives constraints with larger uncertainties, allowing values between the results of the individual data sets and accepting the possibility that experiments might be polluted by unaccounted-for type 2 systematics (as it is the case in figures 4 & 5). Surprisingly, they also provide correct conservative constraints when only type 1 systematics are present, with results similar to those obtained using only rescaling parameters (see, e.g., the bottom left panel of figure 3).

4 Applications to cosmology: H_0

In order to illustrate how our method performs in a problem of real interest, we apply it to the tensions in H_0. This tension has been studied from different perspectives in the literature. One of the options is to perform an independent analysis of the measurements to check for systematics in a concrete constraint, e.g., by including rescaling parameters to consider type 1 systematics in each measurement used to constrain H_0 [24] or using a hierarchical analysis to model in more detail all the probability distribution functions [14]. Another possibility is to consider that this tension is a hint of new physics, rather than a product of unaccounted-for systematics, and therefore explore if other cosmological models ease it or if model independent approaches result in constraints that differ from the expectations of ΛCDM (see [25] and references therein).

Here we propose a third way. We consider all the existing independent constraints of H_0 from low redshift observations and apply `BACCUS` to combine them and obtain a conservative joint constraint of H_0, accounting for any possible scale or shift systematic in each class of experiments (grouped as described in section 4.1). We use only low redshift observations in order to have a consensus conservative constraint to confront with early Universe constraints from CMB observations. We assume a ΛCDM background expansion and use the cosmic distance ladder as in [26–28].

4.1 Data and modelling

In this section we describe the data included in the analysis. As discussed in section 3.1, the size of the uncertainties using `BACCUS` are smaller for a larger number of classes of experiments, even if the individual errors are larger. Therefore, we include all independent constraints on H_0 from low redshift observations available, independent of the size of their error bars. In principle, we should use the exact posterior reported by each experiment, but these are not always easily available. Therefore, we use the reported 68% credible limits in the case of the direct measurements of H_0, assuming a Gaussian likelihood. The resulting error in the tails of the posterior is one form of systematic, which `BACCUS` should be able to absorb. The different classes of experiments are grouped as described below:

- *Direct measurements using the distance ladder.* We include as different classes of experiments direct measurements that use different standard candles or distance anchors. These are: the three independent measurements used in Riess et al. 2016 (see table 6 in [4]), the relation between the integrated Hβ line luminosity and the velocity dispersion of the ionized gas in HII galaxies and giant HII regions [29], megamasers [30–32] and the H_0 value measured by the Cosmic Flows project [33]. Finally, we use the direct measurement coming from the standard siren [34] from the neutron star merger whose gravitational wave was detected by VIRGO and LIGO collaborations [35] and whose electromagnetic counterpart was also detected by several telescopes [36]. We do not include the measurement using the Tip of the Red Giant Branch from [37] because such analysis uses anchors and measurements included in the analysis of Riess et al. (2016) [4].

- *Baryon Acoustic Oscillations (BAO).* Assuming an underlying expansion history, BAO measurements constrain the low redshift standard ruler, $r_{\rm s}h$ (see e.g. [28]), where $r_{\rm s}$ is the sound horizon at radiation drag and $h = H_0/100$. Measurements of the primordial deuterium abundance can be used to break this degeneracy [38, 39], given that they can be used to infer the physical density of baryons, $\Omega_b h^2$ [40]. We use BAO measurements from the following galaxy surveys: Six Degree Field Galaxy Survey (6dF) [41], the Main Galaxy Sample of Data Release 7 of Sloan Digital Sky Survey (SDSS-MGS) [42], the galaxy sample of Baryon Oscillation Spectroscopic Survey Data Release 12 (BOSS DR12) [2], the Lyman-α forest autocorrelation from BOSS DR12 [43] and their cross correlation with quasars [44], the reanalysed measurements of WiggleZ [45], and the measurement using quasars at $z = 1.52$ [46]. We use anisotropic measurements when available (including their covariance) and account for the covariance between the different redshift bins within the same survey when needed. We consider BOSS DR12 and WiggleZ measurements as independent because the overlap of both surveys is very small, hence their correlation (always below 4%) can be neglected [47, 48]. For our analysis, we consider observations of different surveys or tracers (i.e., the autocorrelation of the Lyman-α forest and its cross correlation with quasars are subject to different systematics) as different classes of experiments.

- *Time delay distances.* Using the time delays from the different images of strong lensed quasars it is possible to obtain a good constraint on H_0 by using the time delay distance if an expansion history is assumed. We use the three measurements of the H0LiCOW project [49] as a single class of experiment

- *Cosmic clocks.* Differential ages of old elliptical galaxies provide estimate of the inverse of the Hubble parameter, $H(z)^{-1}$ [51]. We use a compilation of cosmic clocks measurements including the measurement of [52], which extends the prior compilation to include both a fine sampling at $0.38 < z < 0.48$ using BOSS Data Release 9, and the redshift range up to $z \sim 2$. As all cosmic clock measurements have been obtained from the same group using similar analyses, we consider the whole compilation as a single class of experiment.

- *Supernovae Type Ia.* As we want to focus mostly on H_0, we use the Joint Light curve Analysis (JLA) of Supernovae Type Ia [3] as a single class of experiment to constrain the unnormalized expansion history $E(z) = H(z)/H_0$, hence tighter constraints on the matter density parameter, Ω_M, are obtained.

We do not consider the assumption of a ΛCDM-like expansion history (which connects BAO, time delay distances, cosmic clocks and supernovae) as a source of systematic errors which couples different class of experiments (since it affects each observable in a different way). Therefore, we can neglect any correlation among these four probes. In order to interpret the above experiments, we need a model that contains three free parameters: H_0, $\Omega_c h^2$, and $\Omega_b h^2$. $\Omega_b h^2$ will only be constrained by a prior coming from [40] and, together with $\Omega_c h^2$ and H_0, allows us to compute $r_{\rm s}$ and break the degeneracy between H_0 and $r_{\rm s}$ in BAO measurements. As we focus on H_0 and variations in $\Omega_b h^2$ do not affect $E(z)$ significantly, we do not apply any shift to $\Omega_b h^2$. We compute a grid of values of $100 \times r_{\rm s} h$ for different values of H_0, $\Omega_c h^2$ and $\Omega_b h^2$ using the public Boltzmann code CLASS [53, 54] before running the analysis and interpolate the values at each step of the MCMC to obtain $r_{\rm s}$ in a rapid manner.[2]

4.2 Results

In this section we show the results using `BACCUS` when addressing the tension in H_0. We compare them with the results obtained using the conventional approach and the methodology introduced in H02. First, we consider marginalized measurements of H_0. Ideally, we would apply `BACCUS` to Riess et al. 2016 and Planck measurements. However, as stated in section 2, this method can not be applied to only two measurements. Thus, we use the independent and much broader measurement coming from the neutron star merger [34] in order to constrain the tails of the final posterior. These results can be found in figure 6. Even with the inclusion of a third measurement, the tails of the posterior when shift parameters are added are still too large and therefore the conservative constraints are very week (due to the low number of experiments included). On the other hand, adding only rescaling parameters results in a bimodal distribution. In order to obtain relevant conservative constraints, more observations need to be included in the analysis.

As the next step, we perform an analysis with more data and compare the results of the different methodologies to the combination of the data listed in table 1, as recently used in [55]. Since marginalized constraints in clear tension are combined, this is a case where `BACCUS` is clearly necessary. We use the lognormal hyperprior with $b = -2$ and $\xi = 16$ for the hyperprior of variance of the shifts in both cases.

The results of this comparison can be found in figure 7 and table 1, where we report the marginalized highest posterior density values and 68% (95% in parenthesis) credible limits and the individual measurements used. As expected, the results using `BACCUS` peak among the individual best fits and have larger uncertainties than using the conventional approach. However, comparing with the individual constraints, the result seems more sensible. There is a small difference between the combined result reported in [55] and our result using the conventional approach due to using different samplers.

We now apply our method to the data described in section 4.1 to obtain conservative limits on H_0 using all the available independent low redshift observations. Regarding the introduction of shift parameters, we consider two cases. In the first case (shown in figure 8) we only use them on H_0, $\boldsymbol{\Delta}_H$. On the other hand, in the second case (shown in figure 9) we also use them on $\Omega_c h^2$, $\boldsymbol{\Delta}_\Omega$. In both cases, rescaling parameters are applied to every class of experiments and we use the same parameters as in the previous case for the hyperprior for σ_H and a lognormal distribution with $b = -4$ and $\xi = 9$ as the hyperprior for σ_Ω. We use $\eta = 1$ for the LKJ hyperprior of the correlation. Marginalized credible limits from both cases can be found in table 2.

As there is no inconsistency in Ω_M among the experiments (given that most of the constraints are very weak) the only effect of including $\boldsymbol{\Delta}_\Omega$ in the marginalized constraints in Ω_M is to broaden the posteriors. In contrast, including $\boldsymbol{\Delta}_H$ shifts the peak of the H_0

---

[2] We make a grid for $100 \times r_{\rm s} h$ in order to minimize the error in the interpolation ($\lesssim 0.1\%$). This grid is available upon request.

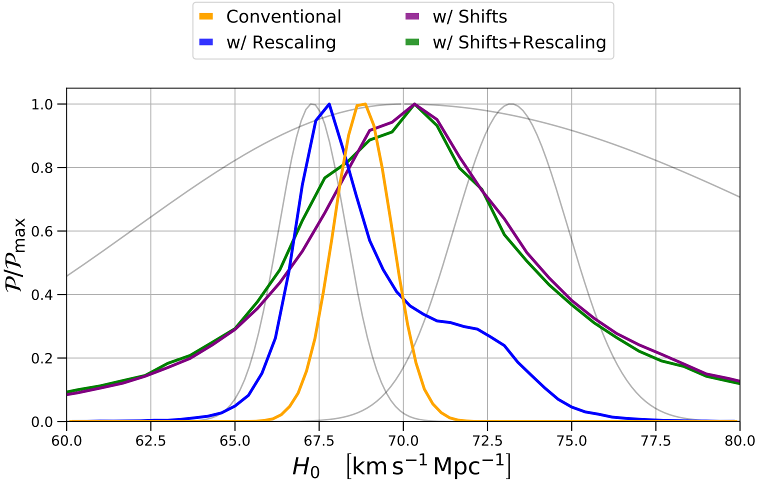

Figure 6. Marginalized H_0 posterior distributions obtained from the combination of marginalized H_0 constraints from the local measurement of Riess et al. 2016, Planck and the neutron star merger. We show results with the standard approach (orange), with only rescaling (blue), with only shifts (purple) and with both rescaling and shifts (green).

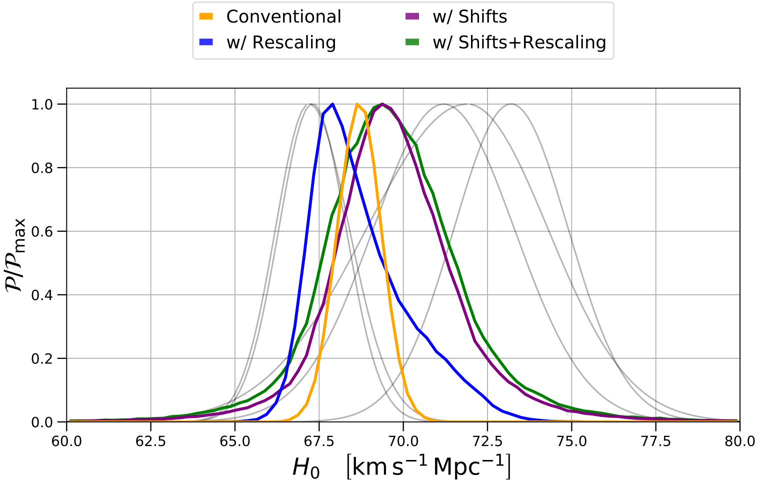

Figure 7. Marginalized H_0 posterior distributions obtained from the combination of marginalized H_0 constraints from the experiments listed in table 1. We show results with the standard approach (orange), with only rescaling (blue), with only shifts (purple) and with both rescaling and shifts (green).

marginalized posterior. While the tightest individual constraints correspond to low values of H_0 (BAO and cosmic clocks), `BACCUS` favours slightly larger values than the conventional approach (which stays in the middle of the tension, as expected). These effects are larger when we include $\mathbf{\Delta}_\Omega$, given that there is more freedom in the parameter space. On the other hand, as BAO and cosmic clocks are the largest data sets, the analysis with only rescaling parameters prefers a lower H_0. Nonetheless, as the constraints weaken when introducing shifts and rescaling, all these modifications are not of great statistical significance.

	Experiment/Approach	H_0 ($\mathrm{km\,s^{-1}Mpc^{-1}}$)
Individual Measurements	DES [55]	$67.2^{+1.2}_{-1.0}$
	Planck [1]	67.3 ± 1.0
	SPTpol [56]	71.2 ± 2.1
	H0LiCOW [49]	$71.9^{+2.4}_{-3.0}$
	Riess et al. 2016 [4]	73.2 ± 1.7
This work	Conventional combination	$68.7 \pm 0.6(\pm 1.2)$
	Rescaling param.	$67.8^{+1.8}_{-0.6}(^{+4.1}_{-1.3})$
	Shift param.	$69.5^{+1.7}_{-1.4}(^{+4.7}_{-3.4})$
	Shift + rescaling param.	$69.4^{+2.1}_{-1.4}(^{+4.9}_{-3.8})$

Table 1. Individual marginalized constraints on H_0 combined to evaluate the performance of our method in a real one dimensional problem. In the bottom part, we report highest posterior density values and 68% (95% in parenthesis) credible limits obtained combining the individual measurement using different kind of parameters.

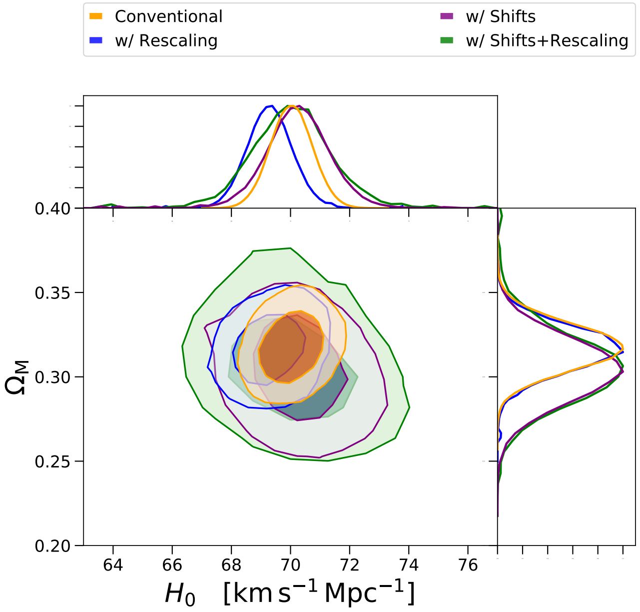

Figure 8. 68% and 95% credible level marginalized constraints on the H_0-Ω_M plane using different methods. We show results with the standard approach (orange), with only rescaling parameters (blue), with only shift parameters (purple) and with both rescaling and shifts (green). Shifts are applied only to H_0.

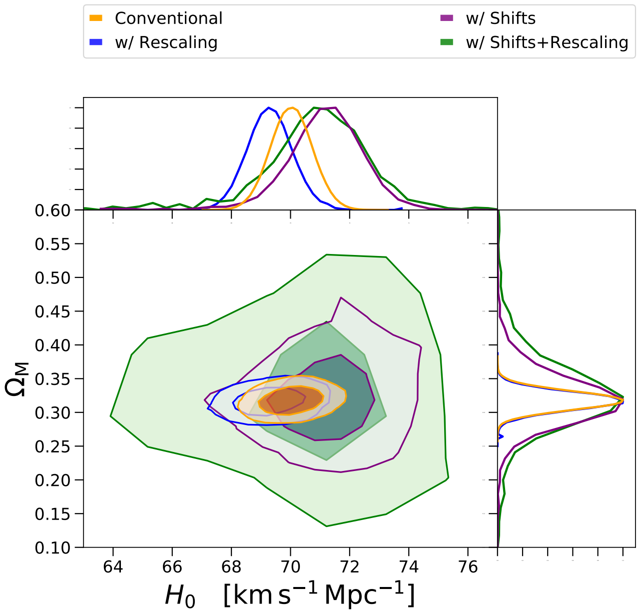

Figure 9. Same as figure 8 but in this case the shifts are applied to both H_0 and $\Omega_c h^2$. Note the change of scale in the vertical axis.

Approach	H_0 (km s^{-1}Mpc^{-1})	Ω_M
Conventional combination	$70.15^{+0.5}_{-0.6}(^{+1.3}_{-1.4})$	$0.32 \pm 0.01(\pm 0.03)$
Rescaling param.	$69.4 \pm 0.7(\pm 1.5)$	$0.32 \pm 0.01(\pm 0.03)$
Shift param. (only H_0)	$70.6^{+0.8}_{-1.1}(^{+1.9}_{-2.3})$	$0.31 \pm -0.02(\pm 0.04)$
Shift (only H_0) + rescaling param.	$70.5^{+0.9}_{-1.3}(^{+2.6}_{-3.1})$	$0.31 \pm -0.02(^{+0.04}_{-0.05})$
Shift param. (H_0 & Ω_M)	$71.7^{+0.8}_{-1.2}(^{+2.0}_{-2.8})$	$0.33 \pm 0.04(^{+0.09}_{-0.07})$
Shift (H_0 & Ω_M) + rescaling param.	$71.0^{+1.8}_{-0.9}(^{+3.6}_{-5.4})$	$0.33^{+0.02}_{-0.04}(^{+0.12}_{-0.14})$

Table 2. Highest posterior density values and 68% (95% in parenthesis) credible level marginalized constraints of H_0 and Ω_M obtained using the data and methodology described in section 4.1.

When including only $\boldsymbol{\Delta}_H$, there is an effect on both the constraints on H_0 and also on Ω_M (both slightly shifting the maximum and broadening the errors), due to the small correlation between the two parameters. The behaviour of the marginalized constraints on H_0 is similar to the one discussed above. However, when both $\boldsymbol{\Delta}_H$ and $\boldsymbol{\Delta}_\Omega$ are included, the constraints are much weaker than in the previous case. Including shifts for $\Omega_c h^2$ also increases the uncertainties in the marginalized constraints on H_0. Nonetheless, it is important to bear in mind that the data used in this analysis constrain H_0 much better than they do Ω_M, even using the conventional approach. Finally, note that in this case the constraints including both shift and rescaling parameters and those using only shifts are not very different (in contrast to the cases showed in figures 3, 4 & 5), since here the type 1 systematic errors are well accounted for and individual $\chi^2_\nu \simeq 1$.

Regarding the ability of `BACCUS` to spot which data set is more likely to be affected by systematics, there is not a clear answer for this specific problem. This is because more independent data is needed in order to discriminate between different classes of experiments, given the inconsistencies within the data sets listed in section 4.1.

5 Summary and discussion

In this paper, we have considered the increasingly common issue of statistical tensions in the results of cosmological experiments: small inconsistencies in estimated parameters that are of marginal significance, but which are too large for comfort. In this case, we face the statistical question of how to combine data sets that are in tension, in order to obtain parameter constraints that are robust. If there are 'unknown unknowns' in the data or the theory, then the standard analysis of the combined constraints on model parameters may not be reliable — which in turn risks erroneous claims of new physics in a distinct way. This is indeed a statistical issue that is not confined to cosmology: similar challenges arise elsewhere in astrophysics (e.g. [57]), and analogous challenges can be encountered in particle physics experiments.

In response to this situation, we have introduced `BACCUS`, a method for combining data for parameter inference in a conservative and agnostic way that allows consistently for the possible presence of unknown systematics in the data sets. It deals not only with systematics arising from incorrect estimation of the magnitude of random measurement errors (already considered by Hobson et al. 2002; H02), but also with those systematics whose effect is such that the inferred model parameters are biased with respect to the true values. The latter are the truly dangerous systematics, since they cannot be detected by any internal null test of a single experiment. In order to account for such effects, we introduce 'shift' parameters, $\{\boldsymbol{\Delta}_{\boldsymbol{\theta}}\}$, which offset the best-fitting model parameters for each set of data independent from the rest. The magnitude of such offsets can be constrained by inspecting the degree of agreement between different data sets, and conservative posteriors on parameters can be inferred by marginalizing over the offsets.

Our approach is democratic and also pessimistic: we assume that all experiments are equally likely to suffer from shift systematics of similar magnitude, independent of their quoted statistical precision, and we are reluctant to set an upper limit to the size of possible systematics. Crucially, therefore, the prior for the shifts should take no account of the size of the reported random errors, since shift systematics by definition cannot be diagnosed internally to an experiment, however precise it may be. In practice, we assume that the shifts have a Gaussian distribution, with a prior characterised by some unknown covariance matrix. We adopt a separation strategy to address the hyperprior for this covariance, using the LKJ distribution for the correlations and independent lognormal distributions for the standard deviations. We recommend agnostic wide hyperpriors, preferring to see explicitly how data can rein in the possibility of arbitrarily large systematics.

For each data set, the shift parameters are assumed to be drawn independently from the same prior. But this assumption is not valid when considering independent experiments that use the same technique, since they may well all suffer from systematics that are common to that method. Therefore data should first be combined into different *classes* of experiments before applying our method. In practice, however, a single experiment may use a number of methods that are substantially independent (e.g. the use of lensing correlations and angular clustering by DES). In that case, our approach can be similarly applied to obtain conservative constraints and assess internal consistency of the various sub-methods.

Because it is common for joint posterior distributions to display approximate degeneracies between some parameters, a systematic that affects one parameter may induce an important shift in others. For example, in figure 8 the probability density function of $\Omega_{\rm M}$ changes due to $\boldsymbol{\Delta}_H$. For complicated posteriors, it is therefore better in principle to use our approach at the level of the analysis of the data (where all the model parameters are varied), rather than constructing marginalized constraints on a single parameter of interest and only then considering systematics.

These assumptions could be varied: in some cases there could be enough evidence to consider certain experiments more reliable than others, so that the prior for the shifts will not be universal. But recalling the discussion in 3.1 concerning the use of different shift priors for each data sets, a way to proceed might be to rescale $\sigma_{\theta j}$ only for certain data sets (those more trusted), but then to use the same prior for all data sets after rescaling. If we consider the data sets $D_{i'}$ to be more reliable than the rest, the final prior should be

$$\mathcal{P}(\boldsymbol{\Delta}_a|\sigma_a) \propto \frac{1}{\sigma_a^{N-1}} \exp\left[-\frac{1}{2}\sum_{i\neq i'}^{N}(\Delta_a^i/\sigma_a)^2\right] \frac{1}{\sigma_a/\beta} \exp\left[-\frac{1}{2}(\Delta_a^{i'}/(\sigma_a/\beta))^2\right], \tag{5.1}$$

where we consider the case with only one parameter a for clarity and β is a constant > 1.

Another possibility is to weaken the assumption that arbitrarily bad shift systematics are possible. One can achieve this either by imposing explicit limits so that the shifts never take values beyond the chosen bound, or by altering the prior on the shift parameters, making it narrower. Although the methodology is sufficiently flexible to accommodate such customizations, we have preferred to keep the assumptions as few and simple as possible. As we have seen, large shifts are automatically disfavoured as the number of concordant data sets rises, and this seems a better way to achieve the outcome.

It is also possible to ascertain if a single experiment is affected by atypically large shifts, by inspecting the marginalized posteriors for the shifts applicable to each dataset. A straightforward option now is to compute the relative Bayesian evidence between the models with and without shifts, telling us how strongly we need to include them, as done in H02. But this procedure needs care: consider a model with many parameters but only one, θ_j, strongly affected by type 2 systematics. In that case, the evidence ratio will favour the model without shifts, those not affecting θ_j are not necessary. Therefore, the ideal procedure is to check the evidence ratio between models with different sets of families of shifts, although this is computationally demanding.

After applying our method to some simple example models and comparing it with the scaling of reported errors as advocated by H02, we have applied it to a real case in cosmology: the tension in H_0. In general, H_0 values obtained in this way are larger than either those from the conventional approach, or the combination using the approach of H02. However, as our conservative uncertainties are larger there is no tension when compared with the CMB value inferred assuming ΛCDM. We have focused on the application to parameter inference by shifting the model parameters for each data set. However, it is also possible to apply the same approach to each individual measurement of a data set, in the manner that rescaling parameters were used by [24].

We may expect that the issues explored here will continue to generate debate in the future. Next-generation surveys will witness improvements of an order of magnitude in precision, yielding statistical errors that are smaller than currently known systematics. Great efforts will be invested in refining methods for treating these known problems, but the smaller the statistical errors become, the more we risk falling victim to unknown systematics. In the analysis presented here, we have shown how allowance can be made for these, in order to yield error bounds on model parameters that are conservative. We can hardly claim our method to be perfect: there is always the possibility of global errors in basic assumptions that will be in common between apparently independent methods. Even so, we have shown that realistic credibility intervals can be much broader than the formal ones derived using standard methods. But we would not want to end with a too pessimistic conclusion: the degradation of precision need not be substantial provided we have a number of independent methods, and provided they are in good concordance. As we have seen, a conservative treatment will nevertheless leave us with extended tails to the posterior, so there is an important role to be played by pursuing a number of independent techniques of lower formal precision. In this way, we can obtain the best of both worlds: the accuracy of the best experiments, and reassurance that these have not been rendered unreliable by unknown unknowns.

Finally, a possible criticism of our approach is that an arms-length meta-analysis is no substitute for the hard work of becoming deeply embedded in a given experiment to the point where all systematics are understood and rooted out. We would not dispute this, and do not wish our approach to be seen as encouraging lower standards of internal statistical rigour; at best, it is a mean of taking stock of existing results before planning the next steps. But we believe our analysis is useful in indicating how the community can succeed in its efforts.

Acknowledgments

We thank Licia Verde and Charles Jenkins for useful discussion during the development of this work, and Alan Heavens, Andrew Liddle, & Mike Hobson for comments which help to improve this manuscript. Funding for this work was partially provided by the Spanish MINECO under projects AYA2014-58747-P AEI/FEDER UE and MDM-2014-0369 of ICCUB (Unidad de Excelencia Maria de Maeztu). JLB is supported by the Spanish MINECO under grant BES-2015-071307, co-funded by the ESF. JLB thanks the Royal Observatory Edinburgh at the University of Edinburgh for hospitality. JAP is supported by the European Research Council, under grant no. 670193 (the COSFORM project).

References

[1] Planck collaboration, P.A.R. Ade et al., *Planck 2015 results. XIII. Cosmological parameters*, *Astron. Astrophys.* **594** (2016) A13 [`arXiv:1502.01589`] [inSPIRE].

[2] BOSS collaboration, S. Alam et al., *The clustering of galaxies in the completed SDSS-III Baryon Oscillation Spectroscopic Survey: cosmological analysis of the DR12 galaxy sample*, *Mon. Not. Roy. Astron. Soc.* **470** (2017) 2617 [`arXiv:1607.03155`] [inSPIRE].

[3] SDSS collaboration, M. Betoule et al., *Improved cosmological constraints from a joint analysis of the SDSS-II and SNLS supernova samples*, *Astron. Astrophys.* **568** (2014) A22 [`arXiv:1401.4064`] [inSPIRE].

[4] A.G. Riess et al., *A* 2.4% *determination of the local value of the Hubble constant*, *Astrophys. J.* **826** (2016) 56 [`arXiv:1604.01424`] [inSPIRE].

[5] H. Hildebrandt et al., *KiDS-450: cosmological parameter constraints from tomographic weak gravitational lensing*, *Mon. Not. Roy. Astron. Soc.* **465** (2017) 1454 [`arXiv:1606.05338`] [INSPIRE].

[6] DES collaboration, T.M.C. Abbott et al., *Dark energy survey year 1 results: cosmological constraints from galaxy clustering and weak lensing*, `arXiv:1708.01530` [INSPIRE].

[7] A. Heavens et al., *No evidence for extensions to the standard cosmological model*, *Phys. Rev. Lett.* **119** (2017) 101301 [`arXiv:1704.03467`] [INSPIRE].

[8] P. Marshall, N. Rajguru and A. Slosar, *Bayesian evidence as a tool for comparing datasets*, *Phys. Rev.* **D 73** (2006) 067302 [`astro-ph/0412535`] [INSPIRE].

[9] L. Verde, P. Protopapas and R. Jimenez, *Planck and the local Universe: quantifying the tension*, *Phys. Dark Univ.* **2** (2013) 166 [`arXiv:1306.6766`] [INSPIRE].

[10] S. Seehars et al., *Information gains from Cosmic Microwave Background experiments*, *Phys. Rev.* **D 90** (2014) 023533 [`arXiv:1402.3593`] [INSPIRE].

[11] T. Charnock, R.A. Battye and A. Moss, *Planck data versus large scale structure*, *Phys. Rev.* **D 95** (2017) 123535 [`arXiv:1703.05959`] [INSPIRE].

[12] W. Lin and M. Ishak, *Cosmological discordances: A new measure, marginalization effects and application to geometry versus growth current data sets*, *Phys. Rev.* **D 96** (2017) 023532 [`arXiv:1705.05303`] [INSPIRE].

[13] S.M. Feeney et al., *Prospects for resolving the Hubble constant tension with standard sirens*, `arXiv:1802.03404` [INSPIRE].

[14] S.M. Feeney, D.J. Mortlock and N. Dalmasso, *Clarifying the Hubble constant tension with a Bayesian hierarchical model of the local distance ladder*, *Mon. Not. Roy. Astron. Soc.* **476** (2018) 3861 [`arXiv:1707.00007`] [INSPIRE].

[15] J. Alsing, A.F. Heavens and A.H. Jaffe, *Cosmological parameters, shear maps and power spectra from CFHTLenS using Bayesian hierarchical inference*, *Mon. Not. Roy. Astron. Soc.* **466** (2017) 3272 [`arXiv:1607.00008`] [INSPIRE].

[16] W.H. Press, *Understanding data better with Bayesian and global statistical methods*, in *Conference on Some Unsolved Problems in Astrophysics Princeton, New Jersey, April 27-29, 1995*, 1996, `astro-ph/9604126` [INSPIRE].

[17] O. Lahav et al., *Bayesian 'hyper-parameters' approach to joint estimation: the Hubble constant from CMB measurements*, *Mon. Not. Roy. Astron. Soc.* **315** (2000) L45 [`astro-ph/9912105`].

[18] M.P. Hobson, S.L. Bridle and O. Lahav, *Combining cosmological data sets: hyperparameters and Bayesian evidence*, *Mon. Not. Roy. Astron. Soc.* **335** (2002) 377 [`astro-ph/0203259`].

[19] D. Foreman-Mackey, D.W. Hogg, D. Lang and J. Goodman, *emcee: the MCMC hammer*, *Publ. Astron. Soc. Pac.* **125** (2013) 306 [`arXiv:1202.3665`] [INSPIRE].

[20] Y.-Z. Ma and A. Berndsen, *How to combine correlated data sets — A Bayesian hyperparameter matrix method*, *Computing* **5** (2014) 45 [`arXiv:1309.3271`] [INSPIRE].

[21] I. Alvarez, J. Niemi and M. Simpson, *Bayesian inference for a covariance matrix*, *Ann. Conf. Appl. Stat. Agric.* **26** (2014) 71 [`arXiv:1408.4050`].

[22] J. Barnard, R. McCulloch and X.L. Meng, *Modeling covariance matrices in terms of standard deviations and correlations, with application to shrinkage*, *Stat. Sinica* **10** (2000) 1281.

[23] D. Lewandowski, D. Kurowicka and H. Joe, *Generating random correlation matrices based on vines and extended onion method*, *J. Multiv. Anal.* **100** (2009) 1989.

[24] W. Cardona, M. Kunz and V. Pettorino, *Determining H_0 with Bayesian hyper-parameters*, *JCAP* **03** (2017) 056 [`arXiv:1611.06088`] [INSPIRE].

[25] J.L. Bernal, L. Verde and A.G. Riess, *The trouble with H_0*, *JCAP* **10** (2016) 019 [arXiv:1607.05617] [INSPIRE].

[26] A. Heavens, R. Jimenez and L. Verde, *Standard rulers, candles and clocks from the low-redshift Universe*, *Phys. Rev. Lett.* **113** (2014) 241302 [arXiv:1409.6217] [INSPIRE].

[27] A.J. Cuesta, L. Verde, A. Riess and R. Jimenez, *Calibrating the cosmic distance scale ladder: the role of the sound horizon scale and the local expansion rate as distance anchors*, *Mon. Not. Roy. Astron. Soc.* **448** (2015) 3463 [arXiv:1411.1094] [INSPIRE].

[28] L. Verde, J.L. Bernal, A.F. Heavens and R. Jimenez, *The length of the low-redshift standard ruler*, *Mon. Not. Roy. Astron. Soc.* **467** (2017) 731 [arXiv:1607.05297] [INSPIRE].

[29] D. Fernández Arenas et al., *An independent determination of the local Hubble constant*, *Mon. Not. Roy. Astron. Soc.* **474** (2018) 1250 [arXiv:1710.05951] [INSPIRE].

[30] M.J. Reid et al., *The megamaser cosmology project: IV. A direct measurement of the Hubble constant from UGC 3789*, *Astrophys. J.* **767** (2013) 154 [arXiv:1207.7292] [INSPIRE].

[31] C.Y. Kuo et al., *The Megamaser Cosmology Project. VI. Observations of NGC 6323*, *Astrophys. J.* **800** (2015) 26 [arXiv:1411.5106] [INSPIRE].

[32] F. Gao et al., *The Megamaser Cosmology Project VIII. A geometric distance to NGC 5765b*, *Astrophys. J.* **817** (2016) 128 [arXiv:1511.08311] [INSPIRE].

[33] R.B. Tully, H.M. Courtois and J.G. Sorce, *Cosmicflows-3*, *Astron. J.* **152** (2016) 50 [arXiv:1605.01765] [INSPIRE].

[34] LIGO Scientific, VINROUGE, Las Cumbres Observatory, DES, DLT40, Virgo, 1M2H, Dark Energy Camera GW-E, MASTER collaboration, B.P. Abbott et al., *A gravitational-wave standard siren measurement of the Hubble constant*, *Nature* **551** (2017) 85 [arXiv:1710.05835] [INSPIRE].

[35] Virgo, LIGO Scientific collaboration, B. Abbott et al., *GW170817: Observation of Gravitational Waves from a Binary Neutron Star Inspiral*, *Phys. Rev. Lett.* **119** (2017) 161101 [arXiv:1710.05832] [INSPIRE].

[36] GROND, SALT Group, OzGrav, DFN, INTEGRAL, Virgo, Insight-Hxmt, MAXI Team, Fermi-LAT, J-GEM, RATIR, IceCube, CAASTRO, LWA, ePESSTO, GRAWITA, RIMAS, SKA South Africa/MeerKAT, H.E.S.S., 1M2H Team, IKI-GW Follow-up, Fermi GBM, Pi of Sky, DWF (Deeper Wider Faster Program), Dark Energy Survey, MASTER, AstroSat Cadmium Zinc Telluride Imager Team, Swift, Pierre Auger, ASKAP, VINROUGE, JAGWAR, Chandra Team at McGill University, TTU-NRAO, GROWTH, AGILE Team, MWA, ATCA, AST3, TOROS, Pan-STARRS, NuSTAR, ATLAS Telescopes, BOOTES, CaltechNRAO, LIGO Scientific, High Time Resolution Universe Survey, Nordic Optical Telescope, Las Cumbres Observatory Group, TZAC Consortium, LOFAR, IPN, DLT40, Texas Tech University, HAWC, ANTARES, KU, Dark Energy Camera GW-EM, CALET, Euro VLBI Team, ALMA collaboration, B.P. Abbott et al., *Multi-messenger observations of a binary neutron star merger*, *Astrophys. J.* **848** (2017) L12 [arXiv:1710.05833] [INSPIRE].

[37] I.S. Jang and M.G. Lee, *The tip of the red giant branch distances to typa Ia Supernova Host Galaxies. V. NGC 3021, NGC 3370 and NGC 1309 and the Value of the Hubble Constant*, *Astrophys. J.* **836** (2017) 74 [arXiv:1702.01118] [INSPIRE].

[38] G.E. Addison, G. Hinshaw and M. Halpern, *Cosmological constraints from baryon acoustic oscillations and clustering of large-scale structure*, *Mon. Not. Roy. Astron. Soc.* **436** (2013) 1674 [arXiv:1304.6984] [INSPIRE].

[39] É. Aubourg et al., *Cosmological implications of baryon acoustic oscillation measurements*, *Phys. Rev.* **D 92** (2015) 123516 [arXiv:1411.1074] [INSPIRE].

[40] R.J. Cooke, M. Pettini and C.C. Steidel, *One percent determination of the primordial deuterium abundance*, *Astrophys. J.* **855** (2018) 102 [arXiv:1710.11129] [INSPIRE].

[41] F. Beutler et al., *The 6dF Galaxy Survey: baryon acoustic oscillations and the local Hubble constant*, *Mon. Not. Roy. Astron. Soc.* **416** (2011) 3017 [arXiv:1106.3366].

[42] A.J. Ross, L. Samushia, C. Howlett, W.J. Percival, A. Burden and M. Manera, *The clustering of the SDSS DR7 main Galaxy sample — I. A 4 per cent distance measure at* $z = 0.15$, *Mon. Not. Roy. Astron. Soc.* **449** (2015) 835 [arXiv:1409.3242] [INSPIRE].

[43] J.E. Bautista et al., *Measurement of baryon acoustic oscillation correlations at* $z = 2.3$ *with SDSS DR12 Ly*α*-forests*, *Astron. Astrophys.* **603** (2017) A12 [arXiv:1702.00176] [INSPIRE].

[44] H. du Mas des Bourboux et al., *Baryon acoustic oscillations from the complete SDSS-III Ly*α*-quasar cross-correlation function at* $z = 2.4$, *Astron. Astrophys.* **608** (2017) A130 [arXiv:1708.02225] [INSPIRE].

[45] E.A. Kazin et al., *The WiggleZ dark energy survey: improved distance measurements to* $z = 1$ *with reconstruction of the baryonic acoustic feature*, *Mon. Not. Roy. Astron. Soc.* **441** (2014) 3524 [arXiv:1401.0358] [INSPIRE].

[46] M. Ata et al., *The clustering of the SDSS-IV extended Baryon Oscillation Spectroscopic Survey DR14 quasar sample: first measurement of baryon acoustic oscillations between redshift* 0.8 *and* 2.2, *Mon. Not. Roy. Astron. Soc.* **473** (2018) 4773 [arXiv:1705.06373] [INSPIRE].

[47] F. Beutler et al., *The BOSS-WiggleZ overlap region — I. Baryon acoustic oscillations*, *Mon. Not. Roy. Astron. Soc.* **455** (2016) 3230 [arXiv:1506.03900] [INSPIRE].

[48] A.J. Cuesta et al., *The clustering of galaxies in the SDSS-III Baryon Oscillation Spectroscopic Survey: Baryon Acoustic Oscillations in the correlation function of LOWZ and CMASS galaxies in Data Release 12*, *Mon. Not. Roy. Astron. Soc.* **457** (2016) 1770 [arXiv:1509.06371] [INSPIRE].

[49] V. Bonvin et al., *H0LiCOW V. New COSMOGRAIL time delays of HE0435-1223:* H_0 *to* 3.8 *per cent precision from strong lensing in a flat* Λ*CDM model*, *Mon. Not. Roy. Astron. Soc.* **465** (2017) 4914 [arXiv:1607.01790] [INSPIRE].

[50] J. Vega-Ferrero, J.M. Diego, V. Miranda and G.M. Bernstein, *The Hubble constant from SN Refsdal*, *Astrophys. J.* **853** (2018) L31 [arXiv:1712.05800] [INSPIRE].

[51] R. Jimenez and A. Loeb, *Constraining cosmological parameters based on relative galaxy ages*, *Astrophys. J.* **573** (2002) 37 [astro-ph/0106145] [INSPIRE].

[52] M. Moresco et al., *A 6% measurement of the Hubble parameter at* $z \sim 0.45$*: direct evidence of the epoch of cosmic re-acceleration*, *JCAP* **05** (2016) 014 [arXiv:1601.01701] [INSPIRE].

[53] J. Lesgourgues, *The Cosmic Linear Anisotropy Solving System (CLASS) I: overview*, arXiv:1104.2932 [INSPIRE].

[54] D. Blas, J. Lesgourgues and T. Tram, *The Cosmic Linear Anisotropy Solving System (CLASS) II: approximation schemes*, *JCAP* **07** (2011) 034 [arXiv:1104.2933] [INSPIRE].

[55] DES collaboration, T.M.C. Abbott et al., *Dark energy survey year 1 results: a precise H0 measurement from DES Y1, BAO and D/H Data*, arXiv:1711.00403 [INSPIRE].

[56] SPT collaboration, J.W. Henning et al., *Measurements of the temperature and E-mode polarization of the CMB from 500 square degrees of SPTpol data*, *Astrophys. J.* **852** (2018) 97 [arXiv:1707.09353] [INSPIRE].

[57] H. Lee et al., *Accounting for calibration uncertainties in X-ray analysis: effective areas in spectral fitting*, *Astrophys. J.* **731** (2011) 126 [arXiv:1102.4610] [INSPIRE].

3. Primordial black holes as seeds of super massive black holes or candidates for dark matter

This Chapter, focused on different roles of PBHs in open questions in cosmology and astrophysics, includes the publications Bernal et al. (2018) and Bernal et al. (2017).

In Bernal et al. (2018), the possibility of PBHs being the seeds of the supermassive black holes is considered, and a strategy to probe this hypothesis is proposed. Any black hole, unless it is primordial, forms after the first stars are formed, at the earliest. Therefore, if any signature from massive black holes is detected before any star could have formed, they must be primordial. Following this logic, this work models the contribution to 21 cm intensity mapping signal from the dark ages ($30 \gtrsim z \gtrsim 200$) of a population of PBHs with the abundance and masses needed to match supermassive black holes observed at lower redshift. Then, the total angular 21 cm intensity mapping power spectrum is computed as function of redshift, and PBH mass, abundance and radiative efficiency. We account for the first time for the substructure and angular dependence of the PBH contribution. Finally, the detectability with SKA and futuristic radio arrays in the far side of the Moon is estimated. This work, done in collaboration with Alvise Raccanelli, Licia Verde and Joseph Silk was published in the Journal of Cosmology and Astroparticle Physics (JCAP) in May 2018. Another way to unequivocally identify a detected black hole as primordial, rather than astrophysical, is if its mass is $< 1M_{\odot}$. Since this work was focused on the possibility of PBHs being the seeds of supermassive black holes, the identification of lighter PBHs was left for future research.

In turn, in Bernal et al. (2017) we study the hypothesis of PBHs of masses $10\ M_{\odot} \lesssim\ M_{\rm PBH} \lesssim\ 10^4 M_{\odot}$ being a significant fraction of dark matter. PBHs in this mass range affect the CMB anisotropies due to the radiation emitted as they accrete gas. Starting from this effect, this work explores the degeneracies between the abundance of PBHs and the rest of cosmological parameters, also for cosmologies beyond ΛCDM. Besides, CMB constraints on the PBH abundance considering PBH extended mass distributions are computed for the first time, both explicitly and validating the approach proposed in Bellomo et al. (2018). This work, carried out in collaboration with Nicola Bellomo, Alvise Raccanelli and Licia Verde, was published in the Journal of Cosmology and Astroparticle Physics in October 2017.

Journal of Cosmology and Astroparticle Physics
An IOP and SISSA journal

Signatures of primordial black holes as seeds of supermassive black holes

José Luis Bernal,[a,b] **Alvise Raccanelli,**[a] **Licia Verde**[a,c]
and Joseph Silk[d,e,f]

[a]Institut de Ciències del Cosmos (ICCUB), Universitat de Barcelona (IEEC-UB),
Martí Franquès 1, E08028 Barcelona, Spain
[b]Dept. de Física Quàntica i Astrofísica, Universitat de Barcelona,
Martí i Franquès 1, E08028 Barcelona, Spain
[c]ICREA, Pg. Lluís Companys 23, 08010 Barcelona, Spain
[d]Department of Physics and Astronomy, Johns Hopkins University,
3400 N. Charles St., Baltimore, MD 21218, Maryland, U.S.A.
[e]Institut d'Astrophysique de Paris, UMR 7095, CNRS, UPMC Univ. Paris VI,
98 bis Boulevard Arago, 75014 Paris, France
[f]BIPAC, Department of Physics, University of Oxford,
Keble Road, Oxford OX1 3RH, U.K.
E-mail: joseluis.bernal@icc.ub.edu, alvise@icc.ub.edu, liciaverde@icc.ub.edu,
joseph.silk@physics.ox.ac.uk

Received December 15, 2017
Accepted April 3, 2018
Published May 4, 2018

JCAP05(2018)017

Abstract. It is broadly accepted that Supermassive Black Holes (SMBHs) are located in the centers of most massive galaxies, although there is still no convincing scenario for the origin of their massive seeds. It has been suggested that primordial black holes (PBHs) of masses $\gtrsim 10^2 M_\odot$ may provide such seeds, which would grow to become SMBHs. We suggest an observational test to constrain this hypothesis: gas accretion around PBHs during the cosmic dark ages powers the emission of high energy photons which would modify the spin temperature as measured by 21cm Intensity Mapping (IM) observations. We model and compute their contribution to the standard sky-averaged signal and power spectrum of 21cm IM, accounting for its substructure and angular dependence for the first time. If PBHs exist, the sky-averaged 21cm IM signal in absorption would be higher, while we expect an increase in the power spectrum for $\ell \gtrsim 10^2 - 10^3$. We also forecast PBH detectability and measurement errors in the abundance and Eddington ratios for different fiducial parameter configurations for various future experiments, ranging from SKA to a futuristic radio array on the dark side of the Moon. While the SKA could provide a detection, only a more ambitious experiment would provide accurate measurements.

Keywords: massive black holes, primordial black holes

ArXiv ePrint: 1712.01311

https://doi.org/10.1088/1475-7516/2018/05/017

Contents

1 Introduction

The idea that density fluctuations can provide the seeds for galaxy formation via gravitational instability and leave detectable traces in the Cosmic Microwave Background (CMB) [1, 2] introduced the concept that the graininess in the Universe would be the seeds around which galaxies form [3]. Now we know that Supermassive Black Holes (SMBHs) inhabit the centers of most galaxies (see [4] for a review). Observations of quasars at $z \sim 6-7$ indicate that, even at these early times, there were SMBHs with masses of several $10^9 M_\odot$ [5–8]. The existence of a population of Intermediate Mass Black Holes (IMBH) of masses around $10^2 - 10^6 M_\odot$ at $z \sim 20 - 15$ would suffice [9] to seed them. The possible detection of a $\sim 10^5 M_\odot$ black hole in the Milky Way close to its center [10, 11] may provide evidence for such a relic and support the argument that Intermediate Mass Black Holes are the seeds of SMBHs. Besides, IMBHs may inhabit the center of dwarf galaxies (e.g., [12] and references therein).

The optimal conditions in the relevant parameter space of the mass of the black hole and the gas density around it, that lead to fast growth of the black hole, were studied in [13, 14]. This happens if the combined effects of the angular momentum and radiation pressure are ineffective in stopping the stream of gas flowing from large scales towards the black hole. They find that this condition is fulfilled for $M \gtrsim 10^4 - 10^5\ M_\odot$ (where M stands for the mass of the seed) and large gas densities, for which the growth of massive seeds up to SMBHs is feasible. Even so, there is a limit on the maximum mass that the black hole can reach in an isolated halo, which depends on the total mass of the host halo and on the radiative efficiency of the accretion [15]. For smaller masses, the accretion is very inefficient, but fast enough growth can be achieved via mergers.

However, the origin and formation mechanism of the massive seeds are still uncertain (see [16, 17] for a review). There are two main scenarios proposed to explain their origin: supercritical growth from stellar mass black holes formed from Population III stars and directly formed massive seeds at lower redshift. There are more exotic scenarios, such as IMBHs formed by a subdominant component of the dark matter being dissipative [18].

According to the first hypothesis, the seeds of SMBHs are remnants of Population III stars, formed with masses of tens of solar masses at $z \gtrsim 20$, which grow due to gas accretion and mergers [19–21]. However, in order to reach masses such as those observed at $z \sim 6-7$ [22–24], the accretion needs to be supercritical over extended periods of time. Moreover, SMBH seeds growth is probably depressed due to the shallow gravitational potentials existing at those redshifts and the radiation pressure of the black hole emission. Indeed the recently discovered IMBHs in dwarfs are anorexic: apparently undermassive compared to the $M_{BH} - \sigma$ scaling relation [25, 26]. Besides, cosmic X-ray background observations impose constraints on the growth of SMBHs, constraining the abundance of quasars with supercritical accretion [27] as well as of the abundance of miniquasars at high redshift [28]. Therefore, this scenario alone is very unlikely to account for the present abundance of SMBHs.

On the other hand, SMBH seeds might also be formed due to the collapse of gas clouds which do not fragment or form ordinary stars, but directly form a massive black hole ($M \sim 10^5 - 10^6 M_\odot$) at lower redshifts ($z \lesssim 15$) [29–36]. This kind of seed is called a Direct Collapse Black Hole (DCBH). DCBHs may be realized if a metal-poor cloud is irradiated by non-ionizing ultraviolet light from nearby star-forming galaxies, which photodissociate molecular hydrogen and therefore prevent star formation. Hence, the gas can only cool via Lyman-α emission, which leads to a quasi-isothermal contraction without fragmentation until the gravitational collapse and the formation of an IMBH (see e.g. [37]). Conveniently, the DCBH radiation is very efficient in preventing the formation of H_2. Therefore, a DCBH may trigger the formation of other DCBHs in a slowly-collapsing gas cloud more efficiently than galaxies [38].

Moreover, DCBHs are a good candidate for explaining the large-scale power spectrum of the Near Infrared Background and its cross correlation with the cosmic X-ray background [39]. As DCBHs have a characteristic observational imprint [40], it can be possible to identify these seeds in deep multi-wavelength surveys [41]. Two promising candidates, whose infrared spectra require an exceptionally high star formation rate, were found at high redshift, with a predicted mass higher than $10^5 M_\odot$ [41]. These candidates are likely to be formed by direct collapse.

Nonetheless, the exact conditions and the probability of obtaining DCBHs are still uncertain; recent theoretical studies suggest that this mechanism might explain the abundance of the most luminous quasars at $z \sim 6-7$, but not the general population of SMBHs [42–44].

In summary, neither of these two scenarios individually provide an entirely convincing explanation for the origin of the seeds of SMBHs. However, massive seeds could have been formed much earlier. This third possibility (see [45–50] and references therein), much less explored in the literature, considers Primordial Black Holes (PBHs) as the seeds which will grow to become SMBHs. If PBHs are formed with large enough masses, there is no need for supercritical accretion, as is the case for Population III stars.

The idea of the existence of PBHs [51] has recently regained popularity after they were suggested to be the progenitors (and to make up a sizeable fraction of the dark matter, see e.g. [52]) of the stellar mass black holes ($\sim 30 M_\odot$) detected by LIGO+VIRGO Collaboration [53].

Since then, a number of possible tests of the model have been performed with available data. They cover all of the theoretically allowed range, from the smallest masses constrained by black holes evaporation [54], to e.g. microlensing of stars [55, 56], to larger masses, constrained by e.g. X-ray and radio emission [57], wide-binaries disruption [58], and accretion effects [59–61]. More innovative tests that can be performed in the future have also been suggested, including using quantum gravity effects [62], the lensing of fast radio bursts [63], the cross-correlation of gravitational waves with galaxy maps [64–66], eccentricity of the binary orbits [67], the black hole mass function [68], the gravitational wave mass spectrum [69], merger rates [70] and the stochastic gravitational wave background [71–74].

The mass range required for PBHs to be the seeds of SMBHs is $\gtrsim 10^2 M_\odot$. In this range, the PBH abundance, $f_{\rm PBH} = \Omega_{\rm PBH}/\Omega_{\rm CDM}$, is strongly constrained by e.g., CMB observations [59, 61], Ultra-Faint Dwarf Galaxies [75] and wide binaries [58]. However, most of these constraints have been derived in the context of a model in which PBHs comprise most of the dark matter, and they assume a delta function in their mass distribution (see [76] for updated constraints allowing for a wide mass distribution); if, on the other hand, PBHs of these masses are only required to be the seeds of SMBHs and not a substantial part of the dark matter, the high-mass tail of the PBH mass distribution can have a very small $f_{\rm PBH}$, satisfying all observational constraints.

Different scenarios for the SMBH seeds have different observational signatures. In this paper, we focus on their imprints on 21 cm Intensity Mapping (IM). The term 'IM' is sometimes dropped in the literature related to the emission from neutral hydrogen at large redshifts, in contrast with the studies of the emission lines from galaxies. However, we maintain it for the sake of clarity.21 cm IM observations represent a promising future tool for cosmology (for a recent review, see [77]). In particular, observations of spin temperature maps in the dark ages provide a direct window into the matter density fluctuations free of complications such as galaxy bias and most astrophysical processes. It can be thought of as a series of CMB-like screens, and therefore, besides the auto-correlation signal, one can also consider the ISW effect [78] and lensing of 21 cm IM maps [79], including the possibility of performing tomographic analyses. It has recently been shown that 21 cm IM observations will give very powerful constraints on e.g., primordial non-gaussianity [80], inflationary models [81–83], scattering between dark matter and baryons [84], statistical isotropy [85] and annihilating and decaying dark matter [86, 87].

21 cm IM will also be very powerful for setting observational constraints on PBHs. Using the power spectrum originating from Poisson fluctuations, the authors of [88] forecast constraints on $f_{\rm PBH}$ based on future observations with SKA in the mass range $M \gtrsim 10^{-2} M_\odot$. The abundance of PBHs of much lighter masses can be constrained by looking for the effects of Hawking evaporation on the Inter Galactic Medium (IGM) via 21 cm IM of the dark ages [89]. Minihalos have been also studied as interesting 21 cm emitters between reionization and the dark ages [90], although they are hard to differentiate from the standard diffuse signal emanating from the IGM [91].

The 21 cm IM sky-averaged signal can be also used to discriminate between the two main scenarios for the origin of SMBH seeds. Seeds formed from remnants of Popularion III stars dominate X-ray heating of the IGM and cause a rise in the 21 cm brightness temperature at $z \gtrsim 20$. An absence of such a signature might be due to the seeds being formed later, which would favor the DCBH scenario [92]. However, such a signature could originate not only via seeds formed from Population III star remnants but also by PBHs. Besides, at these redshifts, the 21 cm IM signal is affected by a large number of astrophysical uncertainties and its dependence on redshift changes considerably with different assumptions [93, 94], making it difficult to identify the signal coming from the SMBH seeds.

Here we study the scenario in which PBHs are the seeds of SMBHs. In order to avoid the astrophysical uncertainties mentioned above, we concentrate on the dark ages ($z \gtrsim 30$). The detection of a signal corresponding to the predictions reported in this work would be an indication that massive miniquasars were already present in the dark ages and the most likely explanation would be that these black holes are primordial, hence the most straightforward candidate to be the seeds of SMBHs. In the standard scenario, during the so-called dark ages, the cosmic time previous to the formation of the first stars, there is no astrophysical feedback which contaminates the 21 cm IM signal and haloes are still not formed, so observations are free from galaxy bias and non-linearities in the clustering. Hence, the main uncertainties are only coming from the PBH sector. However, other exotic energy injections, such as that sourced in dark matter annihilation, might also heat up the IGM [86, 87]. Nonetheless, we expect such signature to be distinguishable from the one of PBHs. A more quantitative evaluation of this issue will be presented elsewhere.

We assume that the dark ages end at $z \sim 30$ (as it is standard convention), although in some scenarios star formation may start at earlier times and heat the IGM, hence changing both the sky-averaged and power spectrum of 21 cm IM (see e.g. [93, 94]). In such cases, the uncertainties in the standard signal at $z \sim 30$ would be larger and the identification of deviations as signatures of the presence of PBHs, more difficult.

We model the signature of massive PBHs, with abundances required to explain the current SMBH population in the 21 cm IM signal. We compute 2-point statistics of the fluctuations accounting explicitly for the temperature profiles around the PBHs in a comprehensive way, for the first time. We improve upon the work of [83, 88, 90, 91] as we consider the scale-dependence of the PBH contribution to the spectrum (and not only a rescaling of the amplitude of the standard 21 cm IM signal or only the Poisson component).

After characterizing the PBH contribution to the standard signal, we forecast the detectability with future experiments, ranging from the Square Kilometre Array (SKA, [95]) to a futuristic radio array on the dark side of the moon [96], which we refer to as the "Lunar Radio Array" (LRA).

This paper is structured as follows. First, we review the standard 21 cm IM sky-averaged signal and power spectrum coming from the IGM in the dark ages, as well as the instrumental noise, in section 2. The effects of PBHs in the IGM and the spin temperature are characterized in section 3. Afterwards, the contribution to the 21 cm IM signal is modelled in section 4 and section 5 for the sky-averaged signal and the power spectrum, respectively. Finally, forecasts for different future experiments are presented in section 6. Discussions and conclusions can be found in section 7. Throughout this paper, we assume the best fit values of the Planck 2015 TTTEEE+lowP power spectra [97] for the cosmological parameters.

2 Standard signal

We begin by reviewing the modelling of the standard 21 cm IM signal, i.e., without including the PBH contribution.

2.1 Sky-averaged signal

The optical depth of the IGM in the hyperfine transition is [98]

$$\tau = \frac{3c^3\hbar A_{10} x_H n_H}{16 k_B T_s \nu_0^2} \, \frac{1}{H(z) + (1+z)\partial_r v_r}, \tag{2.1}$$

where c is the speed of light, $\nu_0 = 1420.4$ MHz is the rest-frame frequency of the hyperfine transition, $A_{10} = 2.85 \times 10^{-15}$ s^{-1} is the Einstein spontaneous emission rate coefficient for this transition, T_s is the spin temperature of the gas, $H(z)$ is the Hubble parameter, $n_H = 8.6 \times 10^{-6} \Omega_b h^2 (1+z)^3$ cm^{-3} is the hydrogen comoving number density [97], x_H is the neutral fraction of hydrogen, k_B is the Boltzmann constant and $\partial_r v_r$ is the comoving gradient of the peculiar velocity along the Line of Sight (LoS). We define $T_{21}^{\rm obs}$ as the observed differential brightness temperature between the 21 cm emission and the CMB:

$$\begin{aligned} T_{21}^{\rm obs} &= \frac{T_s(z) - T_{\rm CMB}(z)}{1+z} \left(1 - e^{-\tau}\right) \;\; \approx \\ &\approx (27 {\rm mK})(1+\delta_b) x_H \left(1 - \frac{T_{CMB}}{T_s}\right) \left(\frac{\Omega_b h^2}{0.023}\right) \times \left(\frac{1+z}{10} \, \frac{0.15}{\Omega_m h^2}\right)^{0.5} \frac{1}{1 + (1+z) \frac{\partial_r v_r}{H(z)}}, \end{aligned} \tag{2.2}$$

where δ_b is the local baryon overdensity, $h = H_0/100$ is the reduced Hubble constant and Ω_m and Ω_b are the matter and baryon density parameters, respectively. Therefore, the sky-averaged 21 cm IM signal, $\bar{T}_{21}$, can be obtained from eq. (2.2) by setting $\delta_b = 0$ and $\partial_r v_r = 0$. We will mostly refer to the observed brightness temperature rather than to the local one, $T_{21}^{\rm loc} = T_{21}^{\rm obs}(1+z)$, throughout the paper, so we drop the superscript "obs" for simplicity.

Assuming that the background radiation includes only CMB photons, the spin temperature can be expressed as [99]:

$$T_s = \frac{T_\star + T_{CMB}(z) + y_k T_k(z) + y_\alpha T_\alpha}{1 + y_k + y_\alpha} \tag{2.3}$$

where $T_\star = 0.068K$ is the temperature correspondent to the 21 cm transitions, T_k is the mean kinetic temperature of the IGM and y_k and y_α are the kinetic and Lyman-α coupling terms, respectively. We set $T_\alpha \approx T_k$, since it is a very good approximation when the medium is optically thick to Lyman-α photons [100], as in the case of study. The kinetic coupling term is due to the increase in the kinetic temperature by X-ray photon collisions with the gas:

$$y_k = \frac{T_\star}{A_{10} T_k} (C_H + C_e + C_p), \tag{2.4}$$

where C_i are the de-excitation rates due to neutral hydrogen, electrons and protons, respectively . We use the fitting formulas of [101]:

$$C_H = 3.1 \times 10^{-11} n_H(z) T_k^{0.357} \exp(-32/T_k) \; {\rm s}^{-1}, \tag{2.5}$$

$$C_e = n_e \gamma_e = n_H(z)(1 - x_H(z,r)) \gamma_e \; {\rm s}^{-1}, \tag{2.6}$$

$$C_p = 3.2 x_H(z,r) C_H, \tag{2.7}$$

where the number densities are in cm^{-3} and $\log(\gamma_e/{\rm cm}^3/{\rm s}) = -9.607 + 0.5 \log T_k \; \exp(-(\log T_k)^{4.5}/1800)$ if $T_k \leq 10^4$ K, otherwise, $\gamma_e = \gamma_e(T_k = 10^4)$.

The coupling with the Lyman-α photons is described by the Wouthusyen-Field effect [99]. It depends on Lyman-α photons intensity, $\tilde{J}_0$, given by:

$$\tilde{J}_0 = \frac{\phi_\alpha c}{4\pi H(z)\nu_\alpha} n_H x_H \int_{E_0}^{\infty} \sigma(E)\mathcal{N}(E)dE \tag{2.8}$$

where ν_α is the frequency of the Lyman-α transition, ϕ_α is the fraction of the absorbed energy that goes into kinetic excitation of Lyman-α, $\mathcal{N}$ is the number of photons per unit area per unit time and σ is the absorption cross-section. We use the parametrization of [102], given by $\phi_\alpha = 0.48\left(1 - x_e^{0.27}\right)^{1.52}$. Finally, the coupling term can be expressed as:

$$y_\alpha = \frac{16\pi^2 T_\star e^2 f_{12} \tilde{J}_0}{27 A_{10} T_k m_e c} \tag{2.9}$$

where $f_{12} = 0.416$ is the oscillator strength of the Lyman-α oscillator.

2.2 Fluctuations

The optical depth and the spin temperature of a hydrogen cloud depend on its density and velocity divergence. Small anisotropies in these two quantities create fluctuations in T_{21}. The 21 cm IM fluctuations power spectrum in the dark ages was computed in [103], and in [104] including the local velocity term. At the precision level we need in this work, given the uncertainties and assumptions in the modeling of the PBH contribution (see section 3, section 4 and section 5), it suffices to limit our computations to linear order. We follow the formalism developed in [105], which includes the effects due to supersonic relative velocities between baryons and dark matter [106]. This effect has been shown to help the formation of DCBHs at large redshifts [107], but it does not play a major role in the population of SMBHs at $z \sim 6$ [108]. We refer the interested reader to [109, 110] for a more detailed description of the 21 cm IM fluctuations, extending the formalism to higher order and including fluctuations in other quantities, such as the ionized fraction.

Let us define $\delta_v \equiv -(1+z)\,\partial_r v_r/H(z)$. Then, at linear order, the fluctuations in the 21 cm IM signal can be expressed as:

$$\delta T_{21}(\mathbf{x}) = \ \alpha(z)\ \delta_b(\mathbf{x}) + \ \bar{T}_{21}(z)\ \delta_v(\mathbf{x}), \tag{2.10}$$

where $\alpha(z) = \mathrm{d}T_{21}/\mathrm{d}\ \delta_b$, including gas temperature fluctuations. The observed δT_{21} in a direction $\hat{n}$ on the sky and at a certain frequency ν is given by

$$\delta T_{21}(\hat{n},\ \nu) = \int_0^\infty dx W_\nu(x)\ \delta T_{21}(x, \hat{n})\,, \tag{2.11}$$

where $W_\nu(x)$ is the window function selecting the information at a certain frequency band centered in ν and x is the comoving distance along the LoS. This $W_\nu(x)$ is a narrow function peaked at $x(z)$ which depends on the experiment. Here we assume a Gaussian function of width $\Delta\nu$. In Fourier space, assuming that the baryons have caught up the dark matter and $\delta_b \propto (1+z)^{-1}$, $\delta_v(\mathbf{k}, z) = \mu^2 \delta_b(\mathbf{k}, z)$ at linear order, with $\mu = (\hat{k}\ \cdot\ \hat{n})$. We can, therefore, define the transfer function of δT_{21} as:

$$\mathcal{T}_\ell(k,\nu) = \int_0^\infty dx W_\nu(x)\ \left[\bar{T}_{21}(z) J_\ell(kx) + \ \alpha(z) j_\ell(kx)\ \right], \tag{2.12}$$

where j_ℓ is the spherical Bessel function with index ℓ, and we have defined $J_\ell(kx) \equiv -\,\partial^2 j_\ell(kx)/(\partial kx)^2$, which can be written in terms of j_ℓ, and $j_{\ell\pm2}$[1] [104]. Given this, we can easily compute the 21 cm IM angular power spectrum at a certain frequency ν as:

$$C_\ell(\nu) = \frac{2}{\pi}\int_0^\infty k^2 dk P_m(k)\mathcal{T}_\ell^2(k,\nu)\,, \tag{2.13}$$

where $P_m(k)$ is the (isotropic) matter power spectrum. For computational efficiency, we will employ the flat-sky approximation [111] (for a pedagogical treatment, see e.g. [112, 113]) for $\ell \geq 10^3$.

2.3 Instrumental noise

Although in the cosmic-variance limit the only source of noise is the variance arising by having a limited number of measurements of the power spectrum C_ℓ, when considering an interferometer looking at the dark ages at a given frequency ν, there is an additional noise power spectrum [114–117]:

$$\ell^2 C_\ell^N = \frac{(2\pi)^3 T_{\rm sys}^2(\nu)}{\Delta\nu\;\; t_o f_{\rm cover}^2}\left(\frac{\ell}{\ell_{\rm cover}(\nu)}\right)^2, \tag{2.14}$$

where t_o is the total time of observation, $\ell_{\rm cover}(\nu) \equiv 2\pi D_{\rm base}/\lambda(\nu)$ is the maximum multipole observable, $D_{\rm base}$ being the largest baseline of the interferometer, $f_{\rm cover}$ is the fraction of such baseline covered with antennas, and the amplitude $T_{\rm sys}$ is the system temperature, which we assume to be the synchrotron temperature of the observed sky:

$$T_{\rm sys}(\nu) = 295\,\left(\frac{\nu}{150\quad{\rm MHz}}\right)^{-2.62}\;{\rm K} \tag{2.15}$$

found from extrapolating to lower frequencies the results of ref. [118].

Therefore, the final uncertainty in the measurement of the C_ℓ at the required multipole ℓ is:

$$\sigma_{C_\ell} = \sqrt{\frac{2\left(C_\ell + C_\ell^N\right)^2}{f_{\rm sky}\,(2\ell+1)}}, \tag{2.16}$$

where $f_{\rm sky}$ is the fraction of the sky observed by the experiment.

3 Effects of PBHs on the 21cm IM signal

The presence of PBHs affect the gas spin temperature: the PBH accretion triggers the emission of high-energy photons which heat and ionize the gas around the PBH. In this work, we present for the first time a computation of the 2-point statistics of the fluctuations accounting for the whole scale-dependence of the temperature profiles around the PBHs, focusing on linear perturbations in the dark ages.

An accreting PBH builds up a classical Bondi profile (i.e., $r^{-3/2}$) around it. However, overdensities during the dark ages are still small and haloes are not formed yet. Therefore, as a first approach, we consider that there is no density profile in the gas around the PBH nor velocity inhomogeneities ($\delta_b(r) = 0$ and $\partial_r v_r = 0$, respectively). Regarding the interaction between radiation and gas, we neglect radiative transfer effects (and limit ourselves to

---

[1] $J_\ell(y) = \frac{-\ell(\ell-1)}{4\ell^2-1}j_{\ell-2}(y) + \frac{2\ell^2+2\ell-1}{4\ell^2+4\ell-3}j_\ell(y) + \frac{-(\ell+2)(\ell+1)}{(2\ell+1)(2\ell+3)}j_{\ell+2}$.

integrate over the frequency, as in eq. (3.8)). Although these two effects might be relevant in some parameter configurations, they are competing: the former tends to reduce the volume affected by the PBH radiation, while radiative transfer increases the mean free path of high energy photons, hence increasing the distance to which X-rays can propagate and so the region heated by the PBH. While a more careful treatment will be needed, especially for comparison with observations and to assess their effective relative importance, here, for this initial exploration and signal-to-noise estimate, we assume that they compensate.

We assume that all processes are in equilibrium, given that their timescales are much smaller than the Hubble timescale. The steady-state approximation is very precise for masses $M \lesssim 3 \times 10^4 M_\odot$ [119], but it breaks down for larger masses. Therefore, we limit our exploration to $M \leq 10^4 M_\odot$. To explore a suitable mass range we consider three representative cases: $M = 10^4 M_\odot$, $10^3 M_\odot$ and $10^2 M_\odot$. Given the slow growth of the PBHs at $z \gtrsim 30$, we assume that the PBH mass at different redshifts is the same when we perform a tomography analysis. Finally, we consider for simplicity that all PBHs have the same mass. This is an unrealistic scenario, but constraints for monochromatic mass distributions can be translated to any extended mass distribution using e.g., the methods proposed in [76, 120].

We explain below the formalism we use to compute the temperature profiles around a PBH and show intermediate plots and results. Exact numerical calculations accounting for the time dependence can be found in [121].

3.1 Emission and neutral hydrogen fraction ($x_H(r)$)

IMBH emission is usually modelled by the combination of three components: a "multicolour disk black body spectrum" at low energies, a power-law spectrum from a surrounding "hot corona" at high energies and a small contribution from the reflected light from the corona by the gas around it. The contribution to the total emission due to the reflected radiation is small, but the light emitted by the disk produces a rather hard spectrum peaking at ~ 1 KeV, as shown in e.g., [39, 122] and references therein.

As the emission at low energies does not heat the gas around the PBH efficiently and sources at $z > 22$ contribute only little to the Near Infrared Background [39], we assume that gas accretion around the PBH powers only X-ray emission. Moreover we assume, as commonly done, that the emission is spherically symmetric. Therefore, a bubble with 21 cm IM signal different from the sky-averaged value is formed around the PBH. Finally, we can safely assume that PBHs of the masses we consider do not affect cosmic reionization [123].

Following [124], we assume that PBH accretion powers a miniquasar with a spherically symmetric power-law X-ray flux (limited to an energy range between 0.2 and 100 KeV). The difference between the heating of the gas by hard sources and those with a power-law spectrum may be significant (see e.g., [125, 126]). However, we show in the appendix A that the differences in the final angular power spectrum between a power-law spectrum and other more realistic choices (such as a piece-wise power-law [127] or including the emission from the disk as in [39]) are not significant with respect to the uncertainties in key parameters of the PBH population, i.e. their abundance, mass or Eddington ratio of the emission, as discussed below. Of course, in a refined application that goes beyond an initial feasibility analysis such as this paper, all these affects must be correctly modelled. Then, the spectrum of the photon emission, $F(E)$, is given by:

$$F(E) = \mathcal{A}(M\lambda)\, E^{-1} \mathrm{s}^{-1}, \tag{3.1}$$

where $\mathcal{A}$ is a normalization factor chosen to have a luminosity $L = \lambda L_{\rm Edd}$, where λ is the Eddington ratio and $L_{\rm Edd}$ is the Eddington luminosity:

$$\mathcal{A}(M\lambda) = \frac{\lambda L_{\rm Edd}(M)}{\int_{E_{\rm range}} E^{-1}dE}\ \text{keV/s}, \tag{3.2}$$

$$L_{\rm Edd}(M) = 8.614 \times 10^{46}(M/M_\odot)\ \text{keV/s}. \tag{3.3}$$

Combining eq. (3.2) and eq. (3.3), it is easy to notice that λ and M are degenerate when computing the emission of the PBH, since $\mathcal{A} \propto \lambda M \equiv \mathcal{M}$. As explained below, relevant quantities, as x_H or T_{21}, only depend on the redshift and the intensity of the emission. Therefore, in order to illustrate how these quantities depend on both λ and M, we will show them in terms of $\mathcal{M}$.

The spectrum of eq. (3.1) translates into number of photons per unit area per unit time at a comoving distance r from the source:

$$\mathcal{N}(E,r) = e^{-\tau(E,r)}\frac{\mathcal{A}(\mathcal{M})E^{-1}}{4\pi r^2}\ \text{cm}^{-2}\text{s}^{-1}\,, \tag{3.4}$$

where

$$\tau(E,r) = \int_0^r n_H(z)x_H(r)\sigma(E)dr. \tag{3.5}$$

We use the fitting formula of [128] to compute the absorption cross section taking into account the contribution from helium and hydrogen atoms:

$$\sigma(E) = 4.25\times 10^{-21}\left(\frac{E}{0.25\text{keV}}\right)^{-p}\ \text{cm}^2, \tag{3.6}$$

with $p = 2.65$ if $E < 0.25\,$keV and $p = 3.30$ if $E > 0.25\,$keV. The emitted photons ionize the surrounding gas at a rate per hydrogen atom, Γ, as a function of the comoving distance r, given by:

$$\Gamma(r) = \int_{E_0}^{\infty} \sigma(E)\mathcal{N}(E,r)(1+\frac{E}{E_0}\phi(E,x_e))\frac{dE}{E}\,, \tag{3.7}$$

where $x_e(r)$=$(1 - x_H(r))$ is the ionized fraction, and the term $\frac{E}{E_0}\phi(E,x_e)$ is introduced to take into account secondary ionizations. We apply the fitting formulas from [28] and [102] for $E \leq 0.5$ KeV and $E > 0.5$ KeV, respectively.

Therefore, the neutral fraction is determined by the equilibrium between ionization and recombination rates:

$$\alpha_H n_H^2(z)(1-x_H(r))^2 = \Gamma(r)x_H(r)n_H(z), \tag{3.8}$$

where $\alpha_H = 2.6\times 10^{-13}T_4^{-0.85}$ cm^3/s is the recombination cross-section to the second excited atomic level, with $T_4 = T_k/10^4$ K. For this computation, we assume $T_4 = 1$ (as in [124]).

The neutral fraction radial profile, $x_H(r)$, is shown in figure 1 for different redshifts and values of $\mathcal{M}$. With increasing redshift, the hydrogen density increases; in a given volume at fixed photon flux, there are more atoms to ionize, hence the size of the ionized region decreases.

On the other hand, for increasing masses or Eddington ratios (i.e., larger $\mathcal{M}$), as the PBH emission is more intense, the ionized region becomes larger.

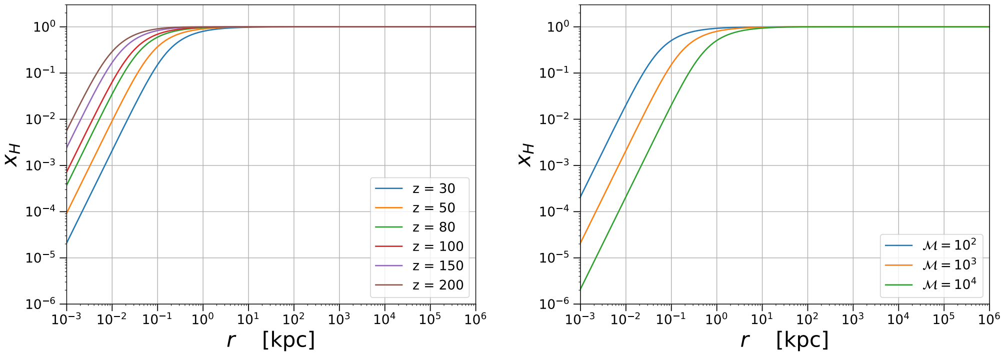

Figure 1. Neutral hydrogen fraction profile x_H for a PBH with $\mathcal{M} = 100$ at various redshifts *(left)* and for a PBH with various $\mathcal{M}$ values at $z = 30$ *(right)*.

3.2 Kinetic temperature

In addition to being ionized, the gas around the PBH is heated by the photons emitted by the miniquasar and cooled by the interaction with the CMB and the expansion of the Universe. The miniquasar heating affects the kinetic temperature, hence T_k varies with the distance to the PBH. The heating rate per unit volume per unit time at a given comoving distance r from the source is:

$$\mathcal{H}_{\text{PBH}} = f(x_e(r))n_H(z)x_H(r)\int_{E_0}^{\infty} \sigma(E)\mathcal{N}(E,r)dE, \tag{3.9}$$

where $f(x_e(r))$ is the fraction of the photon energy absorbed through collisional excitations. We use an extrapolation of the fitting formula of [102]: $f = 0.9771(1-(1-x_e^{0.2663})^{1.3163})$. As this fitting formula does not work well for a low-ionization medium (in reality f never goes to 0), we consider a floor $f = 0.15$ when $x_e \leq 10^{-4}$ [121].

Since the gas is exposed to Compton cooling by CMB photons, the heating rate per unit volume per unit time due to Compton processes is:

$$\mathcal{H}_{\text{Compton}} = \frac{32\pi^5 \ \sigma_T c k_B^5 n_e(z,r) T_{CMB}^4(z)}{15(hc)^3 m_e c^2} \times (T_{CMB}(z) - T_k(r)), \tag{3.10}$$

where $n_e(z,r) = n_H(z)x_e(r)$ is the number density of electrons. On the other hand, the adiabatic expansion cooling per unit volume per unit time is $\mathcal{H}_{\text{exp}} = -3H(z)k_B T_k(r)n_H(z)(2-x_H(r))$. Then, in equilibrium, $\sum \mathcal{H}_i = 0$.

Here, we do not consider Compton heating due to the emitted photons, because it is efficient only very close to the source [121]. Nonetheless, at those distances the hydrogen is totally ionized, so there is no signal in 21 cm IM and the results do not change. Moreover, those scales are far beyond the reach of 21 cm IM power spectrum resolution.

At large distances from the source, the gas is not affected by the PBH emission and its temperature is only determined by the adiabatic cooling due to the expansion of the Universe (there are no free electrons to scatter via Compton). Therefore, we need to set a contour condition by which $T_k(r \to \infty) = T_k^0$, the mean kinetic temperature of the IGM (without PBHs, which we take from the output of HyRec [129, 130]). We include this condition in our

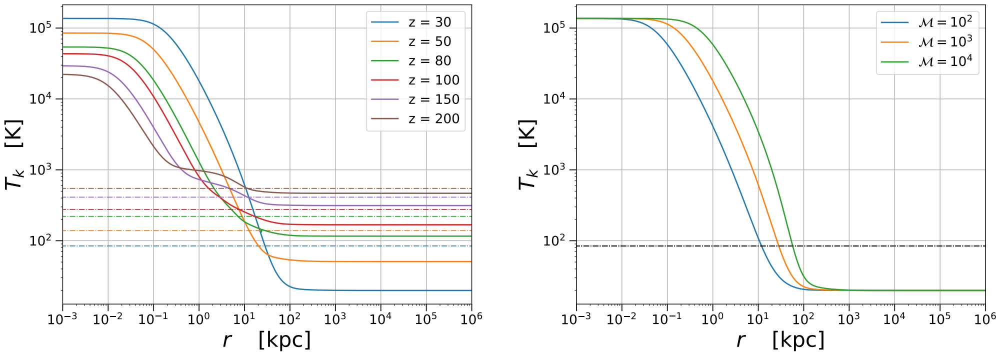

Figure 2. Kinetic temperature profile T_k for a PBH with $\mathcal{M} = 100$ at various redshifts *(left)* and for a PBH with various values of $\mathcal{M}$ at $z = 30$ *(right)*. The CMB temperature is shown in dot-dashed line for reference for each redshift in the upper panel and for $z = 30$ in the lower.

computation of T_k by a adding $T_k^0 x_H(r)$ to the obtained T_k. We will remove this contribution when computing T_{21} of an isolated PBH.

We show gas temperature profiles as function of the comoving distance to the PBH in figure 2 for different redshifts and values of $\mathcal{M}$. At large distances from the PBH, $T_k = T_k^0$, hence the gas temperature is lower at lower redshifts. In the inner regions, the heating due to the emission of the PBH is coupled only to the neutral hydrogen, but, as the number of photons decays exponentially with the distance, this heating is more efficient close to the PBH. In these regions, PBH heating dominates over Compton and adiabatic cooling, so T_k needs to be high to reach equilibrium. If Compton heating due to the emitted photons were considered, T_k at distances tending to 0 would be much higher. However, as stated before, this would not change the signal in 21 cm IM because the hydrogen is totally ionized in those regions. At intermediate distances, PBH heating loses efficiency and T_k drops even below $T_{\rm CMB}$ until it reaches T_k^0.

3.3 Spin temperature and differential brightness temperature

Once we have computed the ionization fraction and gas temperature profiles ($x_H(r)$ and $T_k(r)$), obtaining the spin and differential brightness temperature is straightforward using eq. (2.3) and eq. (2.2), respectively. T_s may be driven whether by the collisional coupling or via the Wouthusyen-Field effect, whose weight is encoded in the coupling terms y_k and y_α in eq. (2.3), respectively. We show radial profiles of y_k and y_α in figure 3 and figure 4, respectively, which make evident that T_s is driven by collisional coupling in all the cases of study.

Spin temperature profiles can be seen in figure 5. T_s behaves qualitatively similar to T_k until $T_k \approx T_s < T_{\rm CMB}$, where spin temperature coupling with CMB photons dominates and T_s rises until $T_s \approx T_{\rm CMB}$, as can be seen in figure 3.

So far, we have applied the boundary condition that all quantities must match the standard values (i.e., without PBHs) when the distance to the PBH is large enough (e.g., $T_k(r \to \infty) = T_k^0$). Nonetheless, we are interested on the isolated signal in 21 cm IM of a single PBH. Therefore, we subtract the contribution added due to the boundary condition

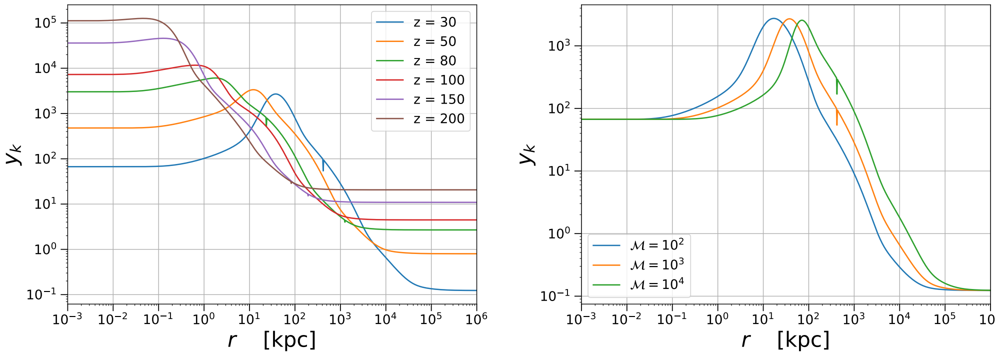

Figure 3. Radial profile of the kinetic coupling term y_k of the spin temperature for a PBH with $\mathcal{M} = 100$ at various redshifts *(left)* and for a PBH with various values of $\mathcal{M}$ at $z = 30$ *(right)*.

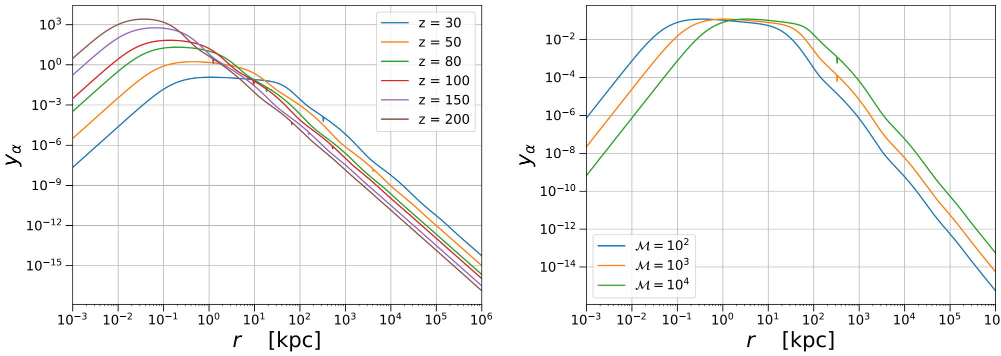

Figure 4. Radial profile of the coupling term of the spin temperature with photons due to the Wouthusyen-Field y_α of the spin temperature for a PBH with $\mathcal{M} = 100$ at various redshifts *(left)* and for a PBH with various values of $\mathcal{M}$ at $z = 30$ *(right)*.

in the same way that it was added before:

$$T_{21}(r) \ \rightarrow T_{21}(r) - T_{21}^0 x_H(r), \tag{3.11}$$

where T_{21}^0 is the sky-averaged T_{21} without PBHs.

The $T_{21}(r)$ profile shown in figure 6 can be explained as follows. In the inner part, $T_{21} = 0$ because all of the gas is ionized. The region with $T_{21} > 0$ corresponds to the region where $T_k > T_{\rm CMB}$ and x_H starts to grow; then, when T_k drops because the PBH heating at those distances is less efficient, T_{21} drops to negative values. Finally, T_{21} rises again due to the collisional and Lyman-α coupling of the photons to the source with the gas becomes totally inefficient and $T_s \rightarrow T_s^0$ so $T_{21} \rightarrow T_{21}^0$. Given that the PBH signal is isolated, at these distances, $T_{21} = 0$.

In order to compute the fluctuations of T_{21}, we need to compute also α profiles as a function of distance to the PBH, for which we follow the analytic expressions of [109]. Such profiles can be seen in figure 7.

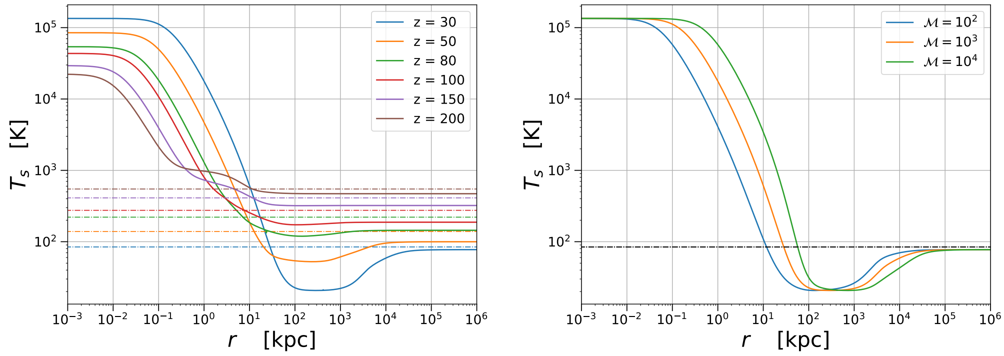

Figure 5. Spin temperature profile T_s for a PBH with $\mathcal{M} = 100$ at various redshifts *(left)* and for a PBH with various values of $\mathcal{M}$ at $z = 30$ *(right)*. The CMB temperature is shown as a dot-dashed line for reference for each redshift in the upper panel and for $z = 30$ in the lower.

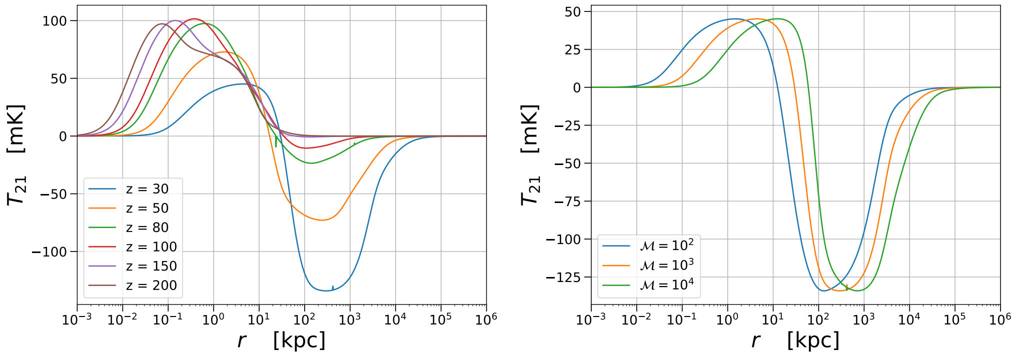

Figure 6. Differential brightness temperature profile T_{21} for a PBH with $\mathcal{M} = 100$ at various redshifts *(left)* and for a PBH with various values of $\mathcal{M}$ at $z = 30$ *(right)*.

4 Contribution to the sky-averaged signal of 21 cm IM

Considerations about the minimum seed masses required [9, 13], number of galaxies in the universe hosting SMBH [131], uncertainties on the accretion mechanisms, and CMB observations constraints on the maximum allowed dark matter fraction in PBH [59], lead us to consider a range of $10^{-8} < \Omega_{\rm PBH} < 10^{-6}$ [123].

Key parameters of the model are largely unknown: SMBHs abundance and Eddington ratio (which is a proxy for the radiative efficiency) and mass. We consider here some representative values.

In addition to considering that all PBHs have the same mass, we also consider that all of them have the same Eddington ratio. This is an idealized case, since each kind of SMBH population (e.g. not active, type 1, type 2 and so on) has a different distribution of Eddington ratio (see e.g. [132–134]). It is customary to consider that SMBHs are active if $\lambda \gtrsim 10^{-4}$, although this is an arbitrary limit, given that the Eddington ratio distribution is broad, and extends towards $\lambda < 10^4$, as pointed by observations [135–137].

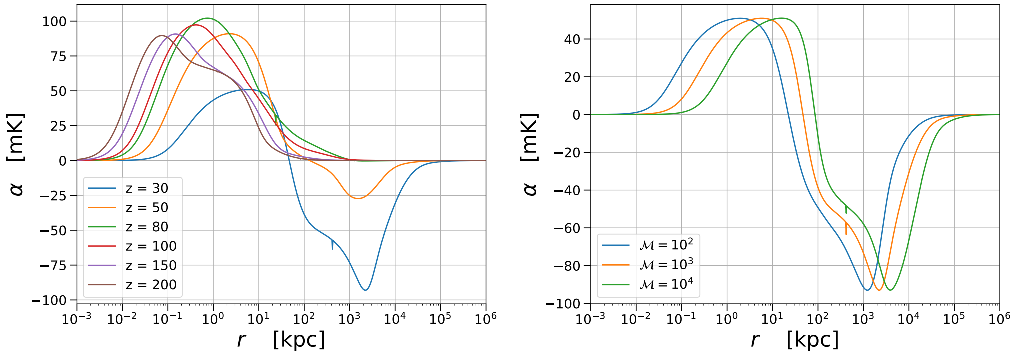

Figure 7. α profile for a PBH with $\mathcal{M} = 100$ at various redshifts *(left)* and for a PBH with various values of $\mathcal{M}$ at $z = 30$ *(right)*.

In any case, a characteristic value of the Eddington ratio is also largely unconstrained. Observational studies of X-ray selected SMBHs (which of course implies a selection bias favouring the most active luminous SMBHs) suggest large values of the Eddington ratio, i.e. $\lambda \sim 0.1$. Nonetheless, one can consider that all SMBHs are active (not only those with $\lambda \gtrsim 10^{-4}$) and then, λ can take values $\ll 10^{-4}$ [138]. Moreover, in [59], the evolution of PBH accretion under the most conservative assumptions was studied in a cosmological context assuming spherical accretion, finding much lower and mass dependent Eddington ratios. Besides, we assume for simplicity a duty cycle of unity, so the Eddington ratio would be smaller to match more realistic cases with lower duty cycles but higher luminosity.

Taking all this into account, we prefer to consider different parameter configurations to account for different possibilities spanning a wide range in the parameter space. We consider all the possible combinations of three masses (10^2, 10^3 and 10^4 $M_\odot$) and three abundances ($\Omega_{\rm PBH} = 10^{-8}$, 10^{-7} and 10^{-6}). We also consider two possible scenarios with different choices of λ for each combination of M and $\Omega_{\rm PBH}$: one with large Eddington ratio ($\lambda \sim 0.1$ for astrophysical considerations) and another with small λ (see [59]). If a disk is formed and the accretion is not spherical, values of λ above this lower limit, but still below the astrophysical one, are expected [60]. Following, [59], as the change of λ with redshift for $z \lesssim 200$ is small, we consider it constant and we take $\lambda = 10^{-4}$ for $M = 10^4 M_\odot$, $\lambda = 10^{-7}$ for $M = 10^3 M_\odot$ and $\lambda = 10^{-10}$ for $M = 10^2 M_\odot$.

If we assume that there are PBHs present in the dark ages, their signal is superimposed to the standard one coming from the IGM and temperature fluctuations. We consider that the gas "bubble" around the PBH extends until the distance where $|T_{21}| < \Delta T$, which we set $\Delta T = 1$ mK. This distance corresponds to the point in which T_{21} (figure 6) becomes flat, and refer to it as $r_{\rm lim}$.

The differential flux per unit frequency received from the bubble can be expressed in terms of the differential brightness temperature as:

$$\delta\, \mathcal{F}_\nu = \frac{2\, \nu_{\rm rec}^2}{c^2} k_b T_{21} \Delta\Omega_{\rm bubble}, \tag{4.1}$$

where $\Delta\Omega_{\rm bubble} = A/\chi^2(z)$, being $A = \pi r_{\rm lim}^2$ the comoving cross section of the bubble, and $\chi(z)$, the comoving distance to us. Furthermore, the line-integrated differential flux, δF, can be obtained multiplying the differential flux evaluated in the desired frequency, ν', by a redshift effective line width, $\Delta\nu_{\rm eff} = (\mathcal{F}(\nu)d\nu\ )/\mathcal{F}(\nu')$. For an optically thin cloud, $\Delta\nu_{\rm eff}$ can be approximated by:

$$\Delta\nu_{\rm eff} = \frac{\nu'}{(1+z)}\sqrt{\frac{2k_BT_k}{m_Hc^2}}. \tag{4.2}$$

As both our gas and differential brightness temperature have radial profiles, we use an effective surface average defined as:

$$\tilde{T}_{21} = \frac{2\pi}{A}\int_0^{r_{\rm lim}} T_{21}(r')\Delta\nu_{\rm eff}(r')r'dr'. \tag{4.3}$$

The comoving number density of PBHs is:

$$n_{\rm PBH}(\Omega_{\rm PBH}, M) = 1.256\times 10^{-2}\ \times\left(\frac{\Omega_{\rm PBH}}{10^{-9}}\right)\left(\frac{M}{10^4M_\odot}\right)^{-1}{\rm Mpc}^{-3}. \tag{4.4}$$

As was discussed in the previous section, λ and M are degenerate when considering the signal of an individual PBH. However, when considering the entire population, as the comoving number density of PBHs (eq.(4.4)) only depends on $\Omega_{\rm PBH}$ and M, this degeneracy is broken. The average contribution of all the bubbles around the PBHs population to the differential flux per unit frequency is

$$\langle\delta\mathcal{F}_\nu\rangle = \frac{\Delta z\Delta\Omega_{\rm beam}}{\Delta\ \nu}\frac{d^2V}{d\Omega dz}\delta F n_{\rm PBH}. \tag{4.5}$$

Finally, taking into account that $\Delta\nu/\Delta z =\ \nu_0/(1+z)^2$ and defining the beam-averaged effective differential brightness temperature, $\langle T_{21}\rangle$, using $\langle\ \delta\mathcal{F}_\nu\rangle =\ 2\ \nu_{\rm rec}^2k_b\langle T_{21}\rangle\Delta\Omega_{\rm beam}/c^2$, we obtain [90]:

$$\langle T_{21}\rangle = \frac{(1+z)^2}{\nu_0}\frac{c}{H(z)}n_{\rm PBH}\tilde{T}_{21}A. \tag{4.6}$$

We show the evolution of the sky-averaged signal with redshift in figure 8 for different cases with $\lambda = 0.1$. As can be seen, the contribution to the standard signal is positive (detected in emission) for $z \gtrsim 130$ (for which $T_{21} > 0$ at any distance, figure 6), and negative (detected in absorption) for lower z. However, the contribution is only appreciable for $z \lesssim 50$. For the same values of $\mathcal{M}$, the PBH contribution is larger for larger $n_{\rm PBH}$, which is reasonable. On the other hand, for the same number density, the contribution is larger for larger intensity of the emission (i.e. larger $\mathcal{M}$). Therefore, the contribution of PBHs to the standard sky-averaged signal in the cases where λ takes much smaller values will be negligible unless the number density is really high.

5 Contribution to the angular power spectrum of 21 cm IM

In this section, we introduce how we compute the angular power spectrum of 21 cm IM, accounting for the first time for the emission of PBHs, the temperature profiles around them, and thus the full scale dependence of their contribution to the 21cm IM signal. As reference, note that the corresponding scale for the multipole ℓ at redshift z fulfills approximately $k\chi(z) = \ell$ (using the Limber approximation); therefore, at $z = 30$, $\ell = 10^3$ corresponds to $k \sim 0.09$ Mpc^{-1} in a ΛCDM cosmology with the best fit parameters of Planck.

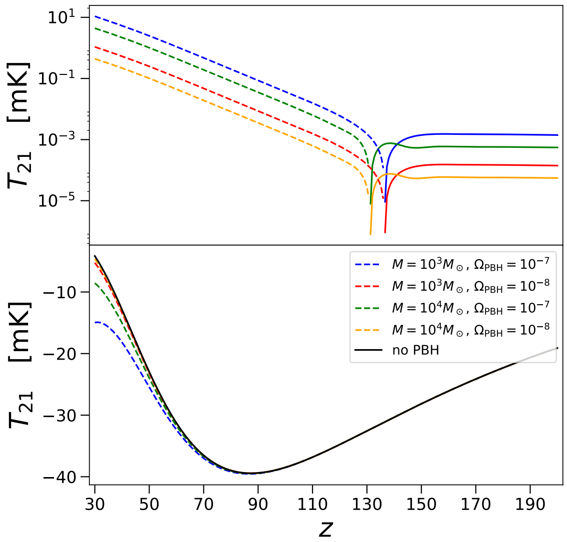

Figure 8. Sky-averaged differential brightness temperature as a function of redshift. *Top panel*: isolated contribution of PBHs assuming different masses and abundances (positive values are shown as solid lines while negative, in dashed lines). *Bottom panel*: total signal.

The modelling of the PBH signal in the fluctuations of T_{21} is similar to that of the Sunyaev-Zel'dovich effect fluctuations from clusters of galaxies [139] or 21 cm IM from mini-haloes before reionization [91]. In all these cases, there are extended sources tracing the peaks of the matter density field. In analogy, we use the halo model [140] to characterize the T_{21} power spectrum during the dark ages in the presence of PBHs. A review of the formalism of the halo model can be found in [141]. Given that we only consider a monochromatic PBH population, all the integrals in mass that appear in the halo model formalism, which are of the type $\int_{M_{\rm min}}^{M_{\rm max}} dM' n_{\rm PBH}(M')\mathcal{G}(M')$, where $\mathcal{G}$ is a general function, simplify to $n_{\rm PBH}(M)\mathcal{G}(M)$.

In the halo model, the power spectrum is the sum of two components: the correlation between points within the same halo or bubble is described by the 'one-halo' term, while the correlation between points in separate halos/bubbles is encoded in the 'two-halo' term. Hence $P_{\rm PBH}(k) = P^{\rm 1h}_{\rm PBH} + P^{\rm 2h}_{\rm PBH}$. In the same way, one can express the angular power spectrum in multipole coefficients as $C_\ell^{\rm PBH} = C_\ell^{\rm PBH(1h)} + C_\ell^{\rm PBH(2h)}$.

We build on eq. (2.11) to obtain the observed fluctuations of the 21 cm temperature fluctuations originated due only to the presence of PBHs in a direction $\hat{n}$ and in a frequency ν:

$$\delta T^{\ell}_{21,\rm PBH}(\hat{n},\ \nu) = \int_0^\infty dx \left[W_\nu(x)\ \alpha_{\rm PBH}(r)\ \delta_b(\mathbf{r}) + T_{21,\rm PBH}(r)\ \delta_v(\mathbf{r})\right], \tag{5.1}$$

where $T_{21}(r)$ and $\alpha(r)$ are the quantities obtained in section 3, $r = \sqrt{x^2 + R^2}$ is the comoving distance to the center of the PBH and $R = \chi(z)/\ell$ is the comoving transverse distance to the center of the PBH. By using $R = \chi(z)/\ell$, we assume a plane parallel approximation. This is justified because for low ℓ (where the plane parallel approximation breaks down), $r \gg r_{\rm lim}$, hence $\delta T_{21,\mathrm{PBH}}(r) = 0$. Once we have computed $\delta T^{\ell}_{21,\mathrm{PBH}}$, we obtain the transfer function for the 21 cm IM fluctuations due to PBHs, $\mathcal{T}_\ell^{\mathrm{PBH}}$, as in eq. (2.12).

As the standard contribution in the linear regime without the PBHs comes from a continuum where there are no haloes, we consider that the one-halo term of the standard contribution vanishes. Therefore, we obtain the total angular power spectrum as the sum of the one-halo and two-halo terms, expressed as:

$$C_\ell^{\mathrm{PBH(1h)}} = \frac{2}{\pi} n_{\mathrm{PBH}} \int_0^\infty dk k^2 \, \left(\mathcal{T}_\ell^{\mathrm{PBH}}\right)^2, \tag{5.2}$$

$$C_\ell^{\mathrm{PBH(2h)}} = \frac{2}{\pi} \int_0^\infty dk k^2 \, \left(\mathcal{T}_\ell + n_{\mathrm{PBH}} b \mathcal{T}_\ell^{\mathrm{PBH}}\right)^2 P_m(k), \tag{5.3}$$

where we assume that PBHs are completely correlated with the dark matter distribution and b is a scale-independent bias. This is motivated by the following consideration. If PBHs are the seeds of the SMBHs, they are located at the centers of the potential wells so galaxies will form around them. We take the bias factor to be approximately the mean value of the galaxy bias. In explicit calculations we assume $b = 1.25$.

Given that the formation of a PBH is a rare event and PBHs spatial distribution is discrete, there is a Poissonian fluctuation in the number density of PBHs. Therefore, in addition to the standard matter power spectrum appearing in eq. (5.3), there is a Poissonian power spectrum contribution. These fluctuations behave like isocurvature modes, as the formation of compact objects at small scales does not affect immediately the curvature at large scales [142]. The primordial power spectrum that describes them is:

$$P^0_{\mathrm{PBH}} = \frac{{f_{\mathrm{PBH}}}^2}{n_{\mathrm{PBH}}}. \tag{5.4}$$

The isocurvature behaviour is enclosed in the transfer function of isocurvature modes, which is scale-independent ($T_{\mathrm{iso}} = \frac{3}{2}(1+z_{\mathrm{eq}})$, where z_{eq} is the redshift of matter-radiation equality, $1 + z_{\mathrm{eq}} \approx 3400$). Therefore, the power spectrum generated by the Poisson fluctuations is:

$$P_{\mathrm{Poisson}}(z) = \left(T_{\mathrm{iso}} D(z)\right)^2 P^0_{\mathrm{PBH}} = \frac{9}{4}(1+z_{\mathrm{eq}})^2 D^2(z) \frac{f^2_{\mathrm{PBH}}}{n_{\mathrm{PBH}}}, \tag{5.5}$$

where $D(z)$ is the growth factor. The mass fraction, f_{PBH}, appears because this contribution comes only from the fluctuation in number of PBHs and not all the matter. P_{Poisson} should be added to the two-halo term multiplied only by $\mathcal{T}_\ell^{\mathrm{PBH}}$. Nonetheless, given the ranges of f_{PBH} we consider, the Poisson contribution is negligible at all scales. Only in studies exploring PBHs as a sizable fraction of the dark matter, where $f_{\mathrm{PBH}} \sim 1$, it is found that the contribution of eq. (5.5) dominates at small scales. In fact, Afshordi et al. (2003) [142] and Kashilinsky (2016) [143] propose to constrain the abundance of PBHs by looking for this scale independent contribution to the power spectrum in observations of the Lyα forest and the Cosmic Infrared Background anisotropies, respectively.

Looking at eq. (5.1), eq.(5.2) and eq.(5.3) it is easy to notice that the angular power spectrum will depend only on two quantities related to PBHs: n_{PBH} and $\mathcal{T}_\ell^{\mathrm{PBH}}$ (C_ℓs also depend on other quantities not related with PBHs, such as the redshift). Therefore, although we do consider three parameters regarding PBHs, the relevant quantities are combinations of them: $\mathcal{M} = M\lambda$ and $n_{\mathrm{PBH}} \propto \Omega_{\mathrm{PBH}}/M$. The former is needed to compute the size of the bubble around the PBH (i.e., r_{lim}). Essentially, varying $\mathcal{M}$ shifts the features related with

JCAP05(2018)017

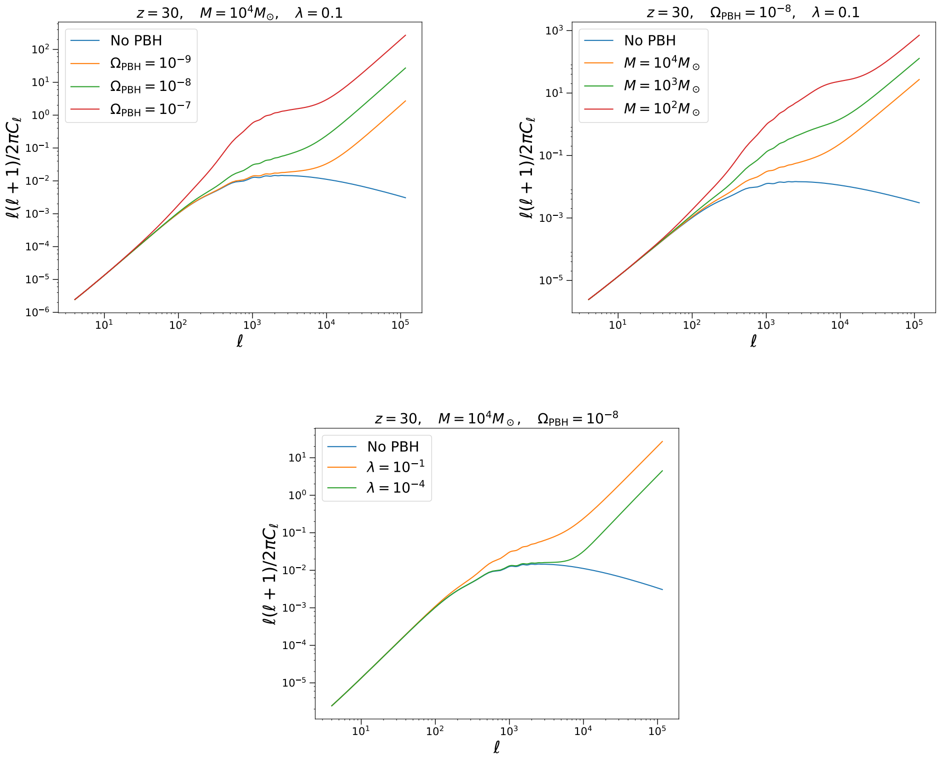

Figure 9. Angular power spectrum of the total signal in 21 cm IM at $z = 30$ varying the density parameter of PBH *(top left)*, the mass *(top right)* and the Eddington ratio *(bottom)*.

PBHs to different multipole ranges (via $\mathcal{T}_\ell^{\rm PBH}$). The latter is a rescaling of such contributions ($C_\ell^{\rm PBH(1h)} \propto n_{\rm PBH}$ and $C_\ell^{\rm PBH(2h)} \propto n_{\rm PBH}^2$). Therefore, varying $n_{\rm PBH}$ changes the amplitude of the PBH features. These two effects are relevant to determine at which scale the PBH contribution starts to dominate. Thus, there is a degeneracy among the PBH parameters:

$$C_\ell(M, \lambda, \Omega_{\rm PBH}) = C_\ell(M/\beta, \lambda\beta, \Omega_{\rm PBH}/\beta), \tag{5.6}$$

where β is an arbitrary positive constant. All these effects can be seen in figure 9. In most of the cases, the PBH effects modify the standard power spectrum at $\ell \sim 10^2 - 10^3$, with a large variation at $\ell \sim 10^5$.

As can be seen in figure 10, the PBH-induced deviation from the standard signal decreases with redshift because the size of the bubble decreases with redshift (see figure 6 and figure 7), so the multipole at which the deviation is appreciable at fixed $n_{\rm PBH}$ and $\mathcal{M}$ increases.

6 Detectability

We have characterized the imprints of massive PBHs in both the sky averaged signal and the power spectrum of 21 cm IM. The sky averaged signal requires dedicated single dipole

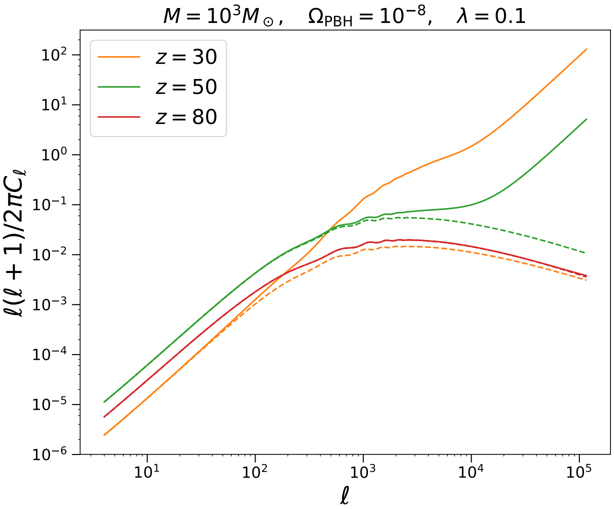

Figure 10. Angular power spectrum comparing the total signal in 21 cm IM *(solid lines)* with the case where there are no PBHs *(dashed lines)* for $M = 10^3 M_\odot$, $\Omega_{\rm PBH} = 10^{-8}$, $\lambda = 0.1$ and $\Delta\nu = 1$ MHz at different redshifts.

Spec	SKA	SKA$_{\rm Adv}$	LRA1	LRA2	LRA3
$D_{\rm base}$ (km)	6	100	30	100	300
$f_{\rm cover}$	0.02	0.2	0.1	0.5	0.75
$t_{\rm obs}$ (years)	5	10	5	5	5
$l_{\rm cover}\frac{1+z}{31}$	5790	96515	28954	96515	289547

Table 1. Instrument specifications for SKA, advanced SKA and three different realizations of the Lunar Radio Array.

experiments, such as EDGES [144], LEDA [145] or SARAS [146], to be measured. On the other hand, radio arrays as SKA aim to measure the fluctuations. As the PBH contribution on the sky-averaged signal is very small in most of the cases, we focus on the power spectrum and observations done with radio arrays.

We study the detectability of the signal and forecast constraints on massive PBH parameters assuming observations in the dark ages done with the SKA [95] and a futuristic Earth-based experiment, similar to the SKA but with much larger baseline and $f_{\rm cover}$, which we refer to as "SKA$_{\rm Adv}$". Given that the atmosphere is opaque for frequencies $\lesssim 45$ MHz, SKA will not be able to observe much further than $z \approx 30$. Then, in order to observe well beyond the end of the dark ages ($z \gtrsim 30$) it will be necessary to observe from outside the Earth's atmosphere; a good candidate as a location for such observations is provided by the Moon [147, 148]. This is why we also consider three different realizations of a futuristic radio array on the dark side of the Moon, that we call the "Lunar Radio Array" (LRA) [96]. The relevant specifications of the experiments considered can be found in table 1.

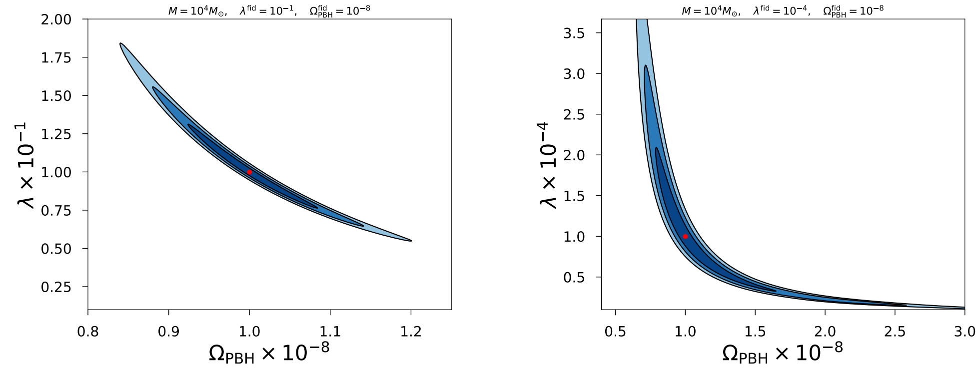

Figure 11. 1σ, 2σ and 3σ confidence level forecasted constraints in the $\Omega_{\rm PBH}$-λ plane from theoretical $\Delta\chi^2$ values for the fiducial cases of $M^{\rm fid} = 10^4 M_\odot$, $\Omega_{\rm PBH}^{\rm fid} = 10^8$ and $\lambda^{\rm fid} = 0.1$ *(left)* and $\lambda^{\rm fid} = 10^{-4}$ *(right)*, considering SKA$_{\rm Adv}$ in both cases. The fiducial case is marked with a red dot.

Because of its wide frequency coverage we consider that it will be possible to do tomography with LRA beyond $z \sim 30$. We follow the arguments introduced in [80] to determine the redshift bins that can be considered independent when observing with $\Delta\nu = 1$ MHz between $z = 30$ and $z = 200$.

First of all, we compute the $\Delta\ \chi^2$ considering SKA$_{\rm Adv}$ as a function of $\Omega_{\rm PBH}$ and λ for two fiducial cases ($M^{\rm fid} = 10^4 M_\odot$, $\Omega_{\rm PBH}^{\rm fid} = 10^8$ and $\lambda^{\rm fid} = 0.1$ (left) and $\lambda^{\rm fid} = 10^{-4}$ (right)). The 1σ, 2σ and 3σ contours are shown in figure 11 where the degeneracy among the parameters discussed in section 5 can be appreciated.

We also forecast the errors on $\Omega_{\rm PBH}$ (σ_Ω) and λ (σ_λ) using Fisher matrices for all the fiducial cases we consider. The resulting forecasts are reported in table 2. The Fisher forecasts obtained should be considered as a rough estimate, especially for low fiducial values for λ: figure 11 shows that the constant $\Delta\chi^2$ contours are not well described by ellipses, which is what the Fisher approach assumes.

The PBH signal will be barely detected by SKA, since only for extreme cases in which $n_{\rm PBH}$ is very large, the signal-to-noise ratio, S/N, for $\Omega_{\rm PBH}$ and λ is larger than unity.

As the amplitude of the power spectrum increases greatly at small scales, being able to resolve very small scales (i.e., large $D_{\rm base}$, which implies large $\ell_{\rm cover}$) will be key to detect the PBH signal and constrain the parameters. This is why the forecast uncertainties for SKA$_{\rm Adv}$ are much smaller than for SKA (and similar considerations apply to LRA3 vs. LRA1).

On the other hand, the contribution of PBHs to the power spectrum decays with redshift (figure 10), hence the S/N between the case with PBHs and the standard one decreases fast with redshift, as shown in figure 12 for the three realizations of LRA and $M = 10^3 M_\odot$, $\Omega_{\rm PBH} = 10^{-7}$ and $\lambda = 0.1$. As tomography does not add much information, $\ell_{\rm cover}$ has more impact in the final S/N. Generally, forecast errors for LRA1 are larger than for SKA$_{\rm Adv}$; however, they are smaller for LRA2 than for SKA$_{\rm Adv}$, both having the same $D_{\rm base}$. This is true always except when both $\mathcal{M}$ and $n_{\rm PBH}$ are large.

To summarize, although a detection of the PBH contribution in the dark ages might be achieved by SKA, in order to measure $\Omega_{\rm PBH}$ and λ accurately, a more ambitious experiment with a larger baseline is needed. Such measurements will be more precise if tomography is possible, for which experiments such as LRA are needed.

$M_{\rm fid}(M_\odot)$	$\lambda_{\rm fid}$	Forecasted precision
10^4	10^{-1}	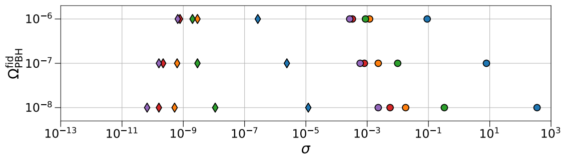
	10^{-4}	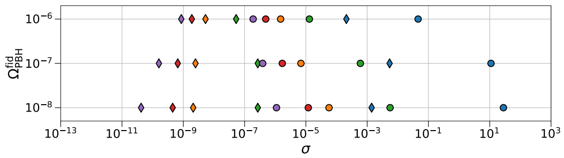
10^3	10^{-1}	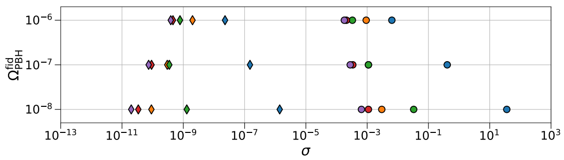
	10^{-7}	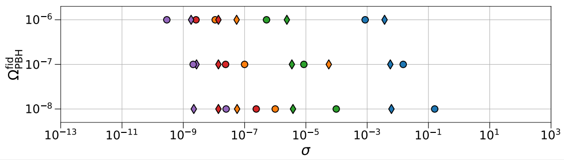
10^2	10^{-1}	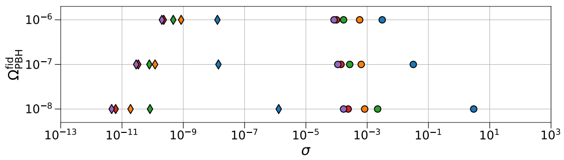
	10^{-10}	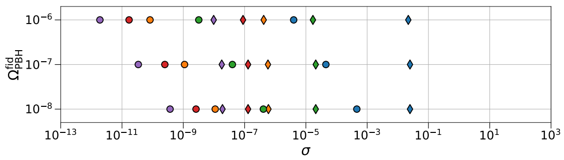

🟦 SKA 🟧 $\mathrm{SKA}_{\mathrm{Adv}}$ 🟩 LRA1 🟥 LRA2 🟪 LRA3

♦ σ_Ω ● σ_λ

Table 2. 1σ forecasted uncertainties on the abundance of PBHs, $\Omega_{\rm PBH}$, (σ_Ω) and the Eddington ration, λ (σ_λ) for different fiducial cases and experiments using Fisher matrices.

7 Discussion and conclusions

The origin and formation mechanism of SMBHs remains largely unknown. If the growth of the black holes happens only through (standard) accretion, in order to grow fast enough and reach $M \sim 10^9 M_\odot$ at $z \sim 7$ [13] (and thus match the observed quasar abundance), massive seeds of $\sim 10^4 - 10^5 M_\odot$ need to be already present in regions with large gas densities at

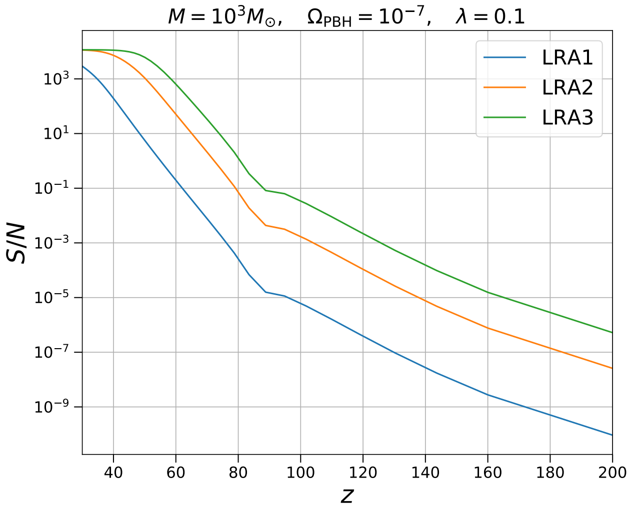

Figure 12. Evolution of the signal-to-noise ratio between the power spectrum accounting for the PBH contribution and the standard one with respect to redshift. We consider $M = 10^3 M_\odot$, $\Omega_{\rm PBH} = 10^{-7}$ and $\lambda = 0.1$, and show the results for the three realizations of the LRA.

$z \sim 20$. However, if mergers are also considered, the seeds can be lighter. Therefore, there are three candidates to be the seeds of SMBHs: remnants of Population III stars, DCBHs or intermediate mass PBHs.

In this work, we address the observational signatures that intermediate mass PBHs would have on 21 cm IM during the dark ages. We model this signal starting from the characterization of the radial profiles of T_{21} around a single PBH to compute the contribution to the standard sky-averaged signal and to the angular power spectrum, using the halo model. This is the first time that the signature of PBHs accounting for its full scale dependence is modeled in the 21 cm IM power spectrum.

The values of the abundance of SMBHs (and therefore, of the seeds needed, $\Omega_{\rm PBH}$), the radiative efficiency (i.e., the Eddington ratio, λ) and the mass of the possible seeds, M, are largely unconstrained. Therefore, we consider several parameter configurations as fiducial cases. We forecast observational errors on λ and $\Omega_{\rm PBH}$ for each fiducial case assuming future observations made with SKA, a futuristic improved SKA-like experiment, and three different realizations of a futuristic radio array on the far side of the Moon (LRA).

We find that, although we consider three parameters (M, λ and $\Omega_{\rm PBH}$), the final power spectrum is only sensitive to two combinations of them: $M\lambda = \mathcal{M}$ (i.e., horizontal shifts of the one- and two-halo terms) and $\Omega_{\rm PBH}/M \propto n_{\rm PBH}$ (i.e., changes in the amplitude of the PBH contribution to the power spectrum). As a consequence, there is a degeneracy between the parameters, which can be expressed as $C_\ell(M, \lambda, \Omega_{\rm PBH}) = C_\ell(M/\beta, \lambda\beta, \Omega_{\rm PBH}/\beta)$ (with β being an arbitrary positive constant), as can be seen in figure 11. This perfect degeneracy is expected to be partially broken with more detailed modelling.

We find that the presence of PBHs increases the sky-averaged signal of 21 cm IM in absorption at $z \lesssim 50$, but it is only appreciable when both $\mathcal{M}$ and $n_{\rm PBH}$ are large (figure 8). With respect to the angular power spectrum, we find an enhancement of the signal for

$\ell \gtrsim 10^2 - 10^3$ (figure 9), which decays with redshift (because the size of the bubble around the PBH, i.e., the gas cloud producing a signal different from the standard sky-averaged value, is smaller for larger redshift, figure 6), as shown in figure 10. Although the enhancement is large, measuring λ and $\Omega_{\rm PBH}$ will be very difficult with SKA, as the effect is large only on small scales that can be reached only with a much longer baseline. On the other hand, as the signal-to-noise ratio decays fast with redshift, tomography does not add much information.

In this paper we have concentrated on the dark ages, given that they directly probe an epoch where the seeds should be present if they are primordial (and absent otherwise). Extending the analysis to lower redshift ranges would be interesting for experiments happening on a shorter timescale, although added complications due to astrophysics and degeneracy with other signals would be involved.

Our modelling makes several assumptions and simplifications, which we recap and discuss their resulting implications here. First of all, we consider that there is no overdensity surrounding the PBH (or that the profile around it does not affect drastically the signal) and also neglect radiative transfer effects. For this initial exploration of the subject, we assume that the effects of these two assumptions compensate, since accounting for density profiles would generate smaller bubbles but larger mean free paths of X-rays (consequence of the radiative transfer) would make the bubbles larger.

To compute the contribution of PBHs to the standard signal, we model a single PBH and afterwards we use the number density of PBHs, $n_{\rm PBH} \propto \Omega_{\rm PBH}/M$, to account for the full population. Hence, our formalism breaks down for large number densities. In such scenario, bubbles around different PBHs overlap, so PBHs can not be considered as isolated anymore. Besides, PBHs contribute significantly to cosmic reionization, advancing it if their number density is too high. In this case, more accurate modelling is needed. Actually, the cases with the largest $n_{\rm PBH}$ considered here should be interpreted carefully due to the effects commented above. This caveat could also be more relevant if the actual bubbles are larger than considered here due to radiative transfer effects.

Moreover, we assume a simple power-law spectrum for the radiation emitted by the PBH accretion without modelling the full spectral energy distribution (although see appendix A) and that all processes are in equilibrium (steady-state approximation, hence we are limited to $M \leq 10^4 M_\odot$). Although the effect of supersonic relative velocities between baryons and dark matter is included in our computation of the 21 cm IM fluctuations (see section 2.2), it is not included in the modelling the heating of the IGM due to the PBH emission. Relative streaming velocities between gas and PBHs leave an imprint on T_{21} radial profiles at the corresponding baryon acoustic oscillation scales, imprinting the corresponding features in the total angular power spectrum. The interested reader can find a study of the effects of relative velocities in the 21 cm IM power spectrum in the pre-reionization era, but after the first stars formed (hence at lower redshifts that those we are focused on) in e.g., [149]. We expect a similar qualitative behaviour for the case of PBHs at larger redshifts.

Finally, we have assumed an average value for the bias between the seeds and the dark matter distribution, while in reality its value might change with redshift and the mass of the seeds. However, given that the value of the bias is strictly related to the height of the peaks in the density field, it is also directly connected to the PBH initial mass and number. In principle, given that it affects the two-halo term contribution but not the one-halo term, variations of the bias would cause a slightly different signal, but we do not expect the final result of this paper to be substantially different.

Nonetheless, the impact of these assumptions and simplifications on the final power spectrum in the scenario under study are subdominant, given the magnitude of the uncertainties due to the PBH parameters. On top of this, we assume that a comprehensive characterization of the foregrounds which affect the detectability of the signal is possible, hence they do not affect the S/N or the forecast uncertainties in the PBH parameters reported in section 6. In addition, we have considered that there is no other exotic energy injection during the dark ages and that star formation begins at $z \lesssim 30$, although this might not be the case. In such cases, the identification of a signal as the product of the IGM heating due to the PBHs would be more difficult. A comprehensive study of these effects using simulations and radiative transfer codes to account for PBH distribution, clustering, relative velocities, gas accretion, mergers, and/or extended mass distributions of the PBHs as well as an estimation of how removing the foreground wedge or an early star formation affects the detectability is left for future work.

There are previous proposals to identify the seeds of the SMBHs from their observational signatures, e.g., with the 21 cm IM sky-averaged signals at $10 \lesssim z \lesssim 30$ [92] to distinguish between black holes formed from remnants of Population III stars or DCBHs (although the signal at larger redshifts might also come from PBHs) or with spectral distortions, to ascertain if the seeds are primordial [46]. DCBHs are also one of the preferred candidates to explain the power spectrum of the Near Infrared Background and its cross correlation with the cosmic X-ray radiation, both at large scales [39]. The emerging spectrum from the DCBH environment is non-zero only in this window [123], which may be useful for identifying them with Chandra[2] or Athena.[3] Moreover, while the growth of remnants of Population III stars may remain undetectable for JWST,[4] the evolved stages of DCBHs might be identifiable [150]. However, these signatures might also have been produced by massive PBHs. We leave the study of this scenario for future work. With advanced gravitational wave detectors, such as LISA,[5] it will be possible to measure gravitational waves created in mergers of SMBHs at large redshifts, which will offer insights on the environments and history of such black holes and help to discriminate among the different candidates for being the seeds.

The advent of new experiments and corresponding observations will shed light on how SMBHs reached such huge masses and on the nature of the massive seeds needed to explain their existence. It is also possible that the three kinds of seeds discussed above coexist and give different signatures. We eagerly await observations that will open the window toward higher redshifts and will give us the opportunity to improve our understanding of some of the most extreme structures in the Universe.

Acknowledgments

We thank Andrea Ferrara for carefully reading the manuscript and for insightful comments. We also thank Ely Kovetz, Julian B. Muñoz, Yacine Ali-Haïmoud and Mark Kamionkowski for useful discussions during the development of this work and Alkistis Pourtsidou, Philip Bull and Guido d'Amico for comments on the final version of the manuscript. Funding for this work was partially provided by the Spanish MINECO under projects AYA2014-58747-P AEI/FEDER UE and MDM-2014-0369 of ICCUB (Unidad de Excelencia Maria de Maeztu). JLB is supported by the Spanish MINECO under grant BES-2015-071307, co-funded by the ESF and thanks the Royal Observatory of Edinburgh for hospitality. AR has received funding

---

[2] Chandra, http://cxc.harvard.edu.

[3] Athena, http://www.the-athena-x-ray-observatory.eu.

[4] JWST, https://www.jwst.nasa.gov.

[5] LISA, https://lisa.nasa.gov.

from the People Programme (Marie Curie Actions) of the European Union H2020 Programme under REA grant agreement number 706896 (COSMOFLAGS). LV acknowledges support of European Union's Horizon 2020 research and innovation programme ERC (BePreSySe, grant agreement 725327) and thanks the Radcliffe Institute for Advanced Study at Harvard University for hospitality.

A Dependence on the flux

In this appendix we discuss the dependence of the final T_{21} radial profile and power spectrum on the emitted spectrum assumed. We referred to the spectrum used in the main text (eq. (3.1)) as Power-Law (PL) in opposition to a Power-Law with Low Energies (PL LE) in which the energy range is extended at the low energy limit (10.4 eV $\leq E$ $\leq$ 100 keV) and a Power-Law with High Energies (PL HE) in which the energy range is extended at the high energy limit (200 eV $\leq E$ $\leq$ 300 keV). All of them have the same exponent: -1.

We also consider a more elaborated spectrum, as the one introduced by Sazonov, Ostriker & Sunyaev (2004) [127]:

$$F(E) = \mathcal{A}(\mathcal{M}) \begin{cases} E^{-1.7}, & 10.4\,\mathrm{eV} < E < 1\,\mathrm{keV}, \\ E^{-1}, & 1\ \mathrm{keV} < E < 100\,\mathrm{keV}, \\ E^{-1.6}, & 100\,\mathrm{keV} < E, \end{cases} \tag{A.1}$$

with $\mathcal{A}(\mathcal{M})$ computed as in eq. (3.2). We consider one case with a high energy cut of 100 keV (SOS LE) and another with the cut at 300 keV (SOS HE). Finally, we consider a more realistic spectrum which includes the contribution of the disk as a multicolor black body spectrum, added to a power-law with index -1 for energies larger than $\sim 3T_{\rm max}$ (where $k_B T_{\rm max} = (M/M_\odot)^{-0.25}$ KeV) and with a high energy exponential cut off at 300 KeV, modelling the emission of the hot corona. We follow [39] and normalize each contribution to the total emission to have the same luminosity. The emission from the disk can be expressed as:

$$F_{\rm MBB}(E) = \mathcal{A}_{\rm MBB}(\mathcal{M}) \int_0^{T_{\rm max}} B(E,T) \left(\frac{T}{T_{\rm max}}\right)^{-11/3} \frac{dT}{T_{\rm max}} \tag{A.2}$$

Again, we set a low energy limit at 10.4 eV.

We show the resulting $T_{21}(r)$ and C_ℓ for all the emission models explained above in figure 13 and figure 14, respectively. Although the radial profiles of T_{21} are different, the effect on the final power spectrum is small, compared with the uncertainties in the PBH parameters (i.e., $\Omega_{\rm PBH}$, M and $n_{\rm PBH}$). Moreover, as the dependence on the PBH parameters is the same for all the different emission spectra, significant changes on the forecasts reported on table 2 or on the two dimensional confidence levels shown in figure 11 are not expected.

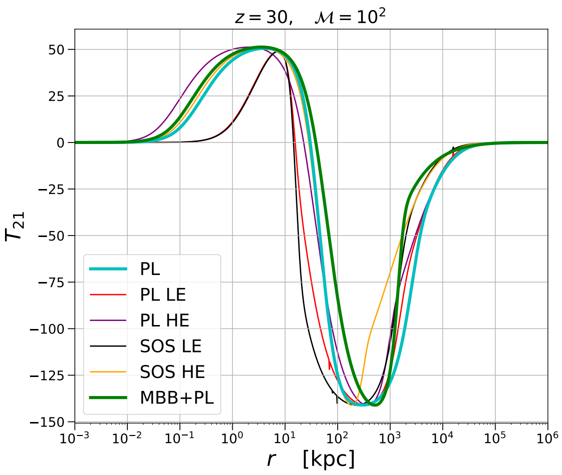

Figure 13. Differential brightness temperature profile T_{21} for a PBH with $\mathcal{M} = 100$ at $z = 30$ for different spectra for the emitted radiation.

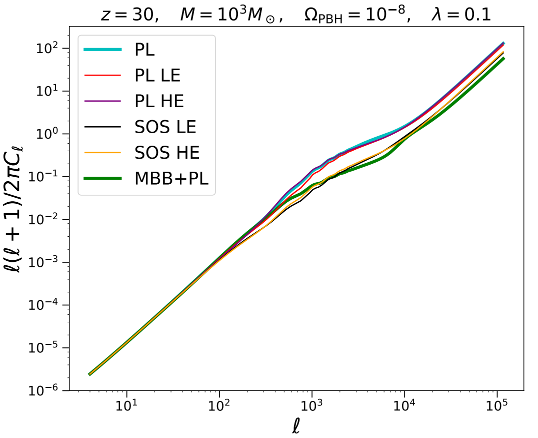

Figure 14. Angular power spectrum comparing the total signal in 21 cm IM for $M = 10^3 M_\odot$, $\Omega_{\rm PBH} = 10^{-8}$, $\lambda = 0.1$, $z = 30$ and $\Delta\nu = 1$ MHz for different spectra for the emitted radiation.

References

[1] J. Silk, *Fluctuations in the Primordial Fireball*, *Nature* **215** (1967) 1155.

[2] J. Silk, *Cosmic black body radiation and galaxy formation*, *Astrophys. J.* **151** (1968) 459 [INSPIRE].

[3] B.J. Carr and J. Silk, *Can graininess in the early universe make galaxies?*, *Astrophys. J.* **268** (1983) 1

[4] J. Kormendy and L.C. Ho, *Coevolution (Or Not) of Supermassive Black Holes and Host Galaxies*, *Ann. Rev. Astron. Astrophys.* **51** (2013) 511 [`arXiv:1304.7762`] [INSPIRE].

[5] E. Bañados et al., *An 800 million solar mass black hole in a significantly neutral universe at redshift 7.5*, *Nature* **553** (2018) 473 [`arXiv:1712.01860`] [INSPIRE].

[6] SDSS collaboration, X. Fan et al., *A Survey of $z > 5.8$ quasars in the Sloan Digital Sky Survey I: Discovery of three new quasars and the spatial density of luminous quasars at $z \sim 6$*, *Astron. J.* **122** (2001) 2833 [`astro-ph/0108063`] [INSPIRE].

[7] X.-B. Wu, F. Wang, X. Fan, W. Yi, W. Zuo, F. Bian et al., *An ultraluminous quasar with a twelve-billion-solar-mass black hole at redshift 6.30*, *Nature* **518** (2015) 512 [`arXiv:1502.07418`].

[8] D.J. Mortlock et al., *A luminous quasar at a redshift of $z = 7.085$*, *Nature* **474** (2011) 616 [`arXiv:1106.6088`] [INSPIRE].

[9] A. Smith, V. Bromm and A. Loeb, *The first supermassive black holes*, *Astron. Geophys.* **58** (2017) 3.22 [`arXiv:1703.03083`].

[10] T. Oka, R. Mizuno, K. Miura and S. Takekawa, *Signature of an Intermediate-mass Black Hole in the Central Molecular Zone of Our Galaxy*, *Astrophys. J. Lett.* **816** (2016) L7 [`arXiv:1512.04661`].

[11] T. Oka, S. Tsujimoto, Y. Iwata, M. Nomura and S. Takekawa, *Millimetre-wave Emission from an Intermediate-Mass Black Hole Candidate in the Milky Way*, *Nature Astronomy* **1** (2017) 709 [`arXiv:1707.07603`].

[12] J. Silk, *Feedback by Massive Black Holes in Gas-rich Dwarf Galaxies*, *Astrophys. J.* **839** (2017) L13 [`arXiv:1703.08553`] [INSPIRE].

[13] F. Pacucci, P. Natarajan, M. Volonteri, N. Cappelluti and C.M. Urry, *Conditions for Optimal Growth of Black Hole Seeds*, *Astrophys. J.* **850** (2017) L42 [`arXiv:1710.09375`] [INSPIRE].

[14] F. Pacucci, M. Volonteri and A. Ferrara, *The Growth Efficiency of High-Redshift Black Holes*, *Mon. Not. Roy. Astron. Soc.* **452** (2015) 1922 [`arXiv:1506.04750`] [INSPIRE].

[15] F. Pacucci, P. Natarajan and A. Ferrara, *Feedback Limits to Maximum Seed Masses of Black Holes*, *Astrophys. J.* **835** (2017) L36 [`arXiv:1701.06565`] [INSPIRE].

[16] M. Volonteri, *Formation of Supermassive Black Holes*, *Astron. Astrophys. Rev.* **18** (2010) 279 [`arXiv:1003.4404`] [INSPIRE].

[17] M.A. Latif and A. Ferrara, *Formation of supermassive black hole seeds*, *Publ. Astron. Soc. Austral.* **33** (2016) e051 [`arXiv:1605.07391`] [INSPIRE].

[18] G. D'Amico, P. Panci, A. Lupi, S. Bovino and J. Silk, *Massive Black Holes from Dissipative Dark Matter*, *Mon. Not. Roy. Astron. Soc.* **473** (2018) 328 [`arXiv:1707.03419`] [INSPIRE].

[19] P. Madau and M.J. Rees, *Massive black holes as Population III remnants*, *Astrophys. J.* **551** (2001) L27 [`astro-ph/0101223`] [INSPIRE].

[20] T. Tanaka and Z. Haiman, *The Assembly of Supermassive Black Holes at High Redshifts*, *Astrophys. J.* **696** (2009) 1798 [`arXiv:0807.4702`] [INSPIRE].

[21] Y.-X. Li et al., *Formation of $z \sim 6$ quasars from hierarchical galaxy mergers*, *Astrophys. J.* **665** (2007) 187 [`astro-ph/0608190`] [INSPIRE].

[22] P. Madau, F. Haardt and M. Dotti, *Super-Critical Growth of Massive Black Holes from Stellar-Mass Seeds*, *Astrophys. J.* **784** (2014) L38 [`arXiv:1402.6995`] [INSPIRE].

[23] A. Lupi, F. Haardt, M. Dotti, D. Fiacconi, L. Mayer and P. Madau, *Growing massive black holes through supercritical accretion of stellar-mass seeds*, *Mon. Not. Roy. Astron. Soc.* **456** (2016) 2993 [`arXiv:1512.02651`] [INSPIRE].

[24] K. Inayoshi, Z. Haiman and J.P. Ostriker, *Hyper-Eddington accretion flows on to massive black holes*, *Mon. Not. Roy. Astron. Soc.* **459** (2016) 3738 [`arXiv:1511.02116`] [INSPIRE].

[25] V.F. Baldassare, A.E. Reines, E. Gallo and J.E. Greene, *A $\sim$ 50,000 $M_\odot$ Solar Mass Black Hole in the Nucleus of RGG 118*, *Astrophys. J. Lett.* **809** (2015) L14 [`arXiv:1506.07531`].

[26] M. Mezcua, F. Civano, G. Fabbiano, T. Miyaji and S. Marchesi, *A Population of Intermediate-mass Black Holes in Dwarf Starburst Galaxies Up to Redshift=1.5*, Astrophys. J. **817** (2016) 20 [arXiv:1511.05844].

[27] R. Salvaterra, F. Haardt, M. Volonteri and A. Moretti, *Limits on the high redshift growth of massive black holes*, Astron. Astrophys. **545** (2012) L6 [arXiv:1209.1095] [INSPIRE].

[28] M. Dijkstra, Z. Haiman and A. Loeb, *A Limit from the x-ray background on the contribution of quasars to reionization*, Astrophys. J. **613** (2004) 646 [astro-ph/0403078] [INSPIRE].

[29] V. Bromm and A. Loeb, *Formation of the first supermassive black holes*, Astrophys. J. **596** (2003) 34 [astro-ph/0212400] [INSPIRE].

[30] M.C. Begelman, M. Volonteri and M.J. Rees, *Formation of supermassive black holes by direct collapse in pregalactic halos*, Mon. Not. Roy. Astron. Soc. **370** (2006) 289 [astro-ph/0602363] [INSPIRE].

[31] G. Lodato and P. Natarajan, *Supermassive black hole formation during the assembly of pre-galactic discs*, Mon. Not. Roy. Astron. Soc. **371** (2006) 1813 [astro-ph/0606159] [INSPIRE].

[32] J.-H. Choi, I. Shlosman and M.C. Begelman, *Supermassive Black Hole Formation at High Redshifts via Direct Collapse in a Cosmological Context*, Mon. Not. Roy. Astron. Soc. **450** (2015) 4411 [arXiv:1412.2761] [INSPIRE].

[33] M. Volonteri, G. Lodato and P. Natarajan, *The evolution of massive black hole seeds*, Mon. Not. Roy. Astron. Soc. **383** (2008) 1079 [arXiv:0709.0529] [INSPIRE].

[34] J.L. Johnson, D.J. Whalen, C.L. Fryer and H. Li, *The Growth of the Stellar Seeds of Supermassive Black Holes*, Astrophys. J. **750** (2012) 66 [arXiv:1112.2726] [INSPIRE].

[35] B. Agarwal, C.D. Vecchia, J.L. Johnson, S. Khochfar and J.-P. Paardekooper, *The First Billion Years project: birthplaces of direct collapse black holes*, Mon. Not. Roy. Astron. Soc. **443** (2014) 648 [arXiv:1403.5267] [INSPIRE].

[36] C. Shang, G. Bryan and Z. Haiman, *Supermassive Black Hole Formation by Direct Collapse: Keeping Protogalactic Gas H_2–Free in Dark Matter Halos with Virial Temperatures $T_{vir} > rsim 10^4$ K*, Mon. Not. Roy. Astron. Soc. **402** (2010) 1249 [arXiv:0906.4773] [INSPIRE].

[37] J. Regan, E. Visbal, J.H. Wise, Z. Haiman, P.H. Johansson and G.L. Bryan, *Rapid Formation of Massive Black Holes in close proximity to Embryonic Proto-Galaxies*, arXiv:1703.03805 [INSPIRE].

[38] B. Yue, A. Ferrara, F. Pacucci and K. Omukai, *Triggering the Formation of Direct Collapse Black Holes by Their Congeners*, Astrophys. J. **838** (2017) 111 [arXiv:1612.07885].

[39] B. Yue, A. Ferrara, R. Salvaterra, Y. Xu and X. Chen, *Infrared background signatures of the first black holes*, Mon. Not. Roy. Astron. Soc. **433** (2013) 1556 [arXiv:1305.5177] [INSPIRE].

[40] F. Pacucci and A. Ferrara, *Simulating the growth of Intermediate Mass Black Holes*, Mon. Not. Roy. Astron. Soc. **448** (2015) 104 [arXiv:1501.00989] [INSPIRE].

[41] F. Pacucci, A. Ferrara, A. Grazian, F. Fiore, E. Giallongo and S. Puccetti, *First Identification of Direct Collapse Black Hole Candidates in the Early Universe in CANDELS/GOODS-S*, Mon. Not. Roy. Astron. Soc. **459** (2016) 1432 [arXiv:1603.08522] [INSPIRE].

[42] M. Dijkstra, A. Ferrara and A. Mesinger, *Feedback-regulated supermassive black hole seed formation*, Mon. Not. Roy. Astron. Soc. **442** (2014) 2036 [arXiv:1405.6743].

[43] M.A. Latif, S. Bovino, T. Grassi, D.R.G. Schleicher and M. Spaans, *How realistic UV spectra and X-rays suppress the abundance of direct collapse black holes*, Mon. Not. Roy. Astron. Soc. **446** (2015) 3163 [arXiv:1408.3061] [INSPIRE].

[44] M. Habouzit, M. Volonteri, M. Latif, Y. Dubois and S. Peirani, *On the number density of 'direct collapse' black hole seeds*, Mon. Not. Roy. Astron. Soc. **463** (2016) 529 [arXiv:1601.00557] [INSPIRE].

[45] A. Dolgov and J. Silk, *Baryon isocurvature fluctuations at small scales and baryonic dark matter*, *Phys. Rev.* **D 47** (1993) 4244 [INSPIRE].

[46] K. Kohri, T. Nakama and T. Suyama, *Testing scenarios of primordial black holes being the seeds of supermassive black holes by ultracompact minihalos and CMB μ-distortions*, *Phys. Rev.* **D 90** (2014) 083514 [`arXiv:1405.5999`] [INSPIRE].

[47] S. Clesse and J. García-Bellido, *Massive Primordial Black Holes from Hybrid Inflation as Dark Matter and the seeds of Galaxies*, *Phys. Rev.* **D 92** (2015) 023524 [`arXiv:1501.07565`] [INSPIRE].

[48] M. Kawasaki, A. Kusenko and T.T. Yanagida, *Primordial seeds of supermassive black holes*, *Phys. Lett.* **B 711** (2012) 1 [`arXiv:1202.3848`] [INSPIRE].

[49] M. Yu. Khlopov, S.G. Rubin and A.S. Sakharov, *Primordial structure of massive black hole clusters*, *Astropart. Phys.* **23** (2005) 265 [`astro-ph/0401532`] [INSPIRE].

[50] A.D. Dolgov, M. Kawasaki and N. Kevlishvili, *Inhomogeneous baryogenesis, cosmic antimatter and dark matter*, *Nucl. Phys.* **B 807** (2009) 229 [`arXiv:0806.2986`] [INSPIRE].

[51] Y.B. Zel'dovich and I.D. Novikov, *The Hypothesis of Cores Retarded during Expansion and the Hot Cosmological Model*, *Soviet Astronomy* **10** (1967) 602.

[52] S. Bird, I. Cholis, J.B. Muñoz, Y. Ali-Haïmoud, M. Kamionkowski, E.D. Kovetz et al., *Did LIGO detect dark matter?*, *Phys. Rev. Lett.* **116** (2016) 201301 [`arXiv:1603.00464`] [INSPIRE].

[53] VIRGO, LIGO SCIENTIFIC collaborations, B.P. Abbott et al., *Observation of Gravitational Waves from a Binary Black Hole Merger*, *Phys. Rev. Lett.* **116** (2016) 061102 [`arXiv:1602.03837`] [INSPIRE].

[54] B.J. Carr, K. Kohri, Y. Sendouda and J. Yokoyama, *New cosmological constraints on primordial black holes*, *Phys. Rev.* **D 81** (2010) 104019 [`arXiv:0912.5297`] [INSPIRE].

[55] K. Griest, A.M. Cieplak and M.J. Lehner, *Experimental Limits on Primordial Black Hole Dark Matter from the First 2 yr of Kepler Data*, *Astrophys. J.* **786** (2014) 158 [`arXiv:1307.5798`] [INSPIRE].

[56] H. Niikura, M. Takada, N. Yasuda, R.H. Lupton, T. Sumi, S. More et al., *Microlensing constraints on primordial black holes with the Subaru/HSC Andromeda observation*, `arXiv:1701.02151` [INSPIRE].

[57] D. Gaggero, G. Bertone, F. Calore, R.M.T. Connors, M. Lovell, S. Markoff et al., *Searching for Primordial Black Holes in the radio and X-ray sky*, *Phys. Rev. Lett.* **118** (2017) 241101 [`arXiv:1612.00457`] [INSPIRE].

[58] D. P. Quinn, M. I. Wilkinson, M. J. Irwin, J. Marshall, A. Koch and V. Belokurov, *On the reported death of the macho era*, *Mon. Not. Roy. Astron. Soc. Lett.* **396** (2009) L11 [`arXiv:0903.1644`].

[59] Y. Ali-Haïmoud and M. Kamionkowski, *Cosmic microwave background limits on accreting primordial black holes*, *Phys. Rev.* **D 95** (2017) 043534 [`arXiv:1612.05644`] [INSPIRE].

[60] V. Poulin, P.D. Serpico, F. Calore, S. Clesse and K. Kohri, *CMB bounds on disk-accreting massive primordial black holes*, *Phys. Rev.* **D 96** (2017) 083524 [`arXiv:1707.04206`] [INSPIRE].

[61] J. Luis Bernal, N. Bellomo, A. Raccanelli and L. Verde, *Cosmological implications of Primordial Black Holes*, *JCAP* **10** (2017) 052 [`arXiv:1709.07465`] [INSPIRE].

[62] A. Raccanelli, F. Vidotto and L. Verde, *Effects of primordial black holes quantum gravity decay on galaxy clustering*, `arXiv:1708.02588` [INSPIRE].

[63] J.B. Muñoz, E.D. Kovetz, L. Dai and M. Kamionkowski, *Lensing of Fast Radio Bursts as a Probe of Compact Dark Matter*, *Phys. Rev. Lett.* **117** (2016) 091301 [`arXiv:1605.00008`] [INSPIRE].

[64] A. Raccanelli, E.D. Kovetz, S. Bird, I. Cholis and J.B. Muñoz, *Determining the progenitors of merging black-hole binaries*, *Phys. Rev.* **D 94** (2016) 023516 [`arXiv:1605.01405`] [INSPIRE].

[65] A. Raccanelli, *Gravitational wave astronomy with radio galaxy surveys*, *Mon. Not. Roy. Astron. Soc.* **469** (2017) 656 [`arXiv:1609.09377`] [INSPIRE].

[66] H. Nishikawa, E.D. Kovetz, M. Kamionkowski and J. Silk, *Primordial-black-hole mergers in dark-matter spikes*, `arXiv:1708.08449` [INSPIRE].

[67] I. Cholis, E.D. Kovetz, Y. Ali-Haïmoud, S. Bird, M. Kamionkowski, J.B. Muñoz et al., *Orbital eccentricities in primordial black hole binaries*, *Phys. Rev.* **D 94** (2016) 084013 [`arXiv:1606.07437`] [INSPIRE].

[68] E.D. Kovetz, I. Cholis, P.C. Breysse and M. Kamionkowski, *Black hole mass function from gravitational wave measurements*, *Phys. Rev.* **D 95** (2017) 103010 [`arXiv:1611.01157`] [INSPIRE].

[69] E.D. Kovetz, *Probing Primordial-Black-Hole Dark Matter with Gravitational Waves*, *Phys. Rev. Lett.* **119** (2017) 131301 [`arXiv:1705.09182`] [INSPIRE].

[70] Y. Ali-Haïmoud, E.D. Kovetz and M. Kamionkowski, *Merger rate of primordial black-hole binaries*, *Phys. Rev.* **D 96** (2017) 123523 [`arXiv:1709.06576`] [INSPIRE].

[71] V. Mandic, S. Bird and I. Cholis, *Stochastic Gravitational-Wave Background due to Primordial Binary Black Hole Mergers*, *Phys. Rev. Lett.* **117** (2016) 201102 [`arXiv:1608.06699`] [INSPIRE].

[72] I. Cholis, *On the Gravitational Wave Background from Black Hole Binaries after the First LIGO Detections*, *JCAP* **06** (2017) 037 [`arXiv:1609.03565`] [INSPIRE].

[73] T. Nakama, J. Silk and M. Kamionkowski, *Stochastic gravitational waves associated with the formation of primordial black holes*, *Phys. Rev.* **D 95** (2017) 043511 [`arXiv:1612.06264`] [INSPIRE].

[74] M. Raidal, V. Vaskonen and H. Veermäe, *Gravitational Waves from Primordial Black Hole Mergers*, *JCAP* **09** (2017) 037 [`arXiv:1707.01480`] [INSPIRE].

[75] T.D. Brandt, *Constraints on MACHO Dark Matter from Compact Stellar Systems in Ultra-Faint Dwarf Galaxies*, *Astrophys. J.* **824** (2016) L31 [`arXiv:1605.03665`] [INSPIRE].

[76] N. Bellomo, J.L. Bernal, A. Raccanelli and L. Verde, *Primordial Black Holes as Dark Matter: Converting Constraints from Monochromatic to Extended Mass Distributions*, *JCAP* **01** (2018) 004 [`arXiv:1709.07467`] [INSPIRE].

[77] E.D. Kovetz et al., *Line-Intensity Mapping: 2017 Status Report*, `arXiv:1709.09066` [INSPIRE].

[78] A. Raccanelli, E. Kovetz, L. Dai and M. Kamionkowski, *Detecting the integrated Sachs-Wolfe effect with high-redshift 21-cm surveys*, *Phys. Rev.* **D 93** (2016) 083512 [`arXiv:1502.03107`] [INSPIRE].

[79] E.D. Kovetz and M. Kamionkowski, *Galaxy-Cluster Masses via 21st-Century Measurements of Lensing of 21-cm Fluctuations*, *Phys. Rev.* **D 87** (2013) 063516 [`arXiv:1210.3041`] [INSPIRE].

[80] J.B. Muñoz, Y. Ali-Haïmoud and M. Kamionkowski, *Primordial non-Gaussianity from the bispectrum of 21-cm fluctuations in the dark ages*, *Phys. Rev.* **D 92** (2015) 083508 [`arXiv:1506.04152`] [INSPIRE].

[81] J.B. Muñoz, E.D. Kovetz, A. Raccanelli, M. Kamionkowski and J. Silk, *Towards a measurement of the spectral runnings*, *JCAP* **05** (2017) 032 [`arXiv:1611.05883`] [INSPIRE].

[82] A. Pourtsidou, *Synergistic tests of inflation*, `arXiv:1612.05138` [INSPIRE].

[83] T. Sekiguchi, T. Takahashi, H. Tashiro and S. Yokoyama, *21 cm Angular Power Spectrum from Minihalos as a Probe of Primordial Spectral Runnings*, *JCAP* **02** (2018) 053 [`arXiv:1705.00405`] [INSPIRE].

[84] J.B. Muñoz, E.D. Kovetz and Y. Ali-Haïmoud, *Heating of Baryons due to Scattering with Dark Matter During the Dark Ages*, Phys. Rev. **D 92** (2015) 083528 [arXiv:1509.00029] [INSPIRE].

[85] M. Shiraishi, J.B. Muñoz, M. Kamionkowski and A. Raccanelli, *Violation of statistical isotropy and homogeneity in the 21-cm power spectrum*, Phys. Rev. **D 93** (2016) 103506 [arXiv:1603.01206] [INSPIRE].

[86] C. Evoli, A. Mesinger and A. Ferrara, *Unveiling the nature of dark matter with high redshift 21 cm line experiments*, JCAP **11** (2014) 024 [arXiv:1408.1109] [INSPIRE].

[87] M. Valdes, C. Evoli, A. Mesinger, A. Ferrara and N. Yoshida, *The nature of dark matter from the global high redshift HI 21 cm signal*, Mon. Not. Roy. Astron. Soc. **429** (2013) 1705 [arXiv:1209.2120] [INSPIRE].

[88] J.-O. Gong and N. Kitajima, *Small-scale structure and 21cm fluctuations by primordial black holes*, JCAP **08** (2017) 017 [arXiv:1704.04132] [INSPIRE].

[89] K.J. Mack and D.H. Wesley, *Primordial black holes in the Dark Ages: Observational prospects for future 21cm surveys*, arXiv:0805.1531 [INSPIRE].

[90] I.T. Iliev, P.R. Shapiro, A. Ferrara and H. Martel, *On the direct detectability of the cosmic dark ages: 21-cm emission from minihalos*, Astrophys. J. **572** (2002) 123 [astro-ph/0202410] [INSPIRE].

[91] S. Furlanetto and S.P. Oh, *Redshifted 21 centimeter emission from minihalos before reionization*, Astrophys. J. **652** (2006) 849 [astro-ph/0604080] [INSPIRE].

[92] T.L. Tanaka, R.M. O'Leary and R. Perna, *The imprint of the cosmic supermassive black hole growth history on the 21 cm background radiation*, Mon. Not. Roy. Astron. Soc. **455** (2016) 2619 [arXiv:1509.05406] [INSPIRE].

[93] A. Cohen, A. Fialkov, R. Barkana and M. Lotem, *Charting the Parameter Space of the Global 21-cm Signal*, Mon. Not. Roy. Astron. Soc. **472** (2017) 1915 [arXiv:1609.02312] [INSPIRE].

[94] A. Cohen, A. Fialkov and R. Barkana, *Charting the Parameter Space of the 21-cm Power Spectrum*, arXiv:1709.02122 [INSPIRE].

[95] M. Santos et al., *Cosmology from a SKA HI intensity mapping survey*, PoS(AASKA14)019.

[96] J. Silk, A. Raccanelli, C.S., M.J. and E.D. Kovetz, *A White Paper on Cosmology with a Lunar Radio Array*, in preparation.

[97] PLANCK collaboration, P.A.R. Ade et al., *Planck 2015 results. XIII. Cosmological parameters*, Astron. Astrophys. **594** (2016) A13 [arXiv:1502.01589] [INSPIRE].

[98] G. B. Field, *An Attempt to Observe Neutral Hydrogen Between the Galaxies.*, Astrophys. J. **129** (1959) 525.

[99] G.B. Field, *Excitation of the Hydrogen 21-CM Line*, Proc. of the IRE **46** (1958) 240.

[100] G.B. Field, *The Time Relaxation of a Resonance-Line Profile.*, Astrophys. J. **129** (1959) 551.

[101] M. Kuhlen, P. Madau and R. Montgomery, *The spin temperature and 21cm brightness of the intergalactic medium in the pre-reionization era*, Astrophys. J. **637** (2006) L1 [astro-ph/0510814] [INSPIRE].

[102] J.M. Shull and M.E. van Steenberg, *X-ray secondary heating and ionization in quasar emission-line clouds*, Astrophys. J. **298** (1985) 268.

[103] A. Loeb and M. Zaldarriaga, *Measuring the small - scale power spectrum of cosmic density fluctuations through 21 cm tomography prior to the epoch of structure formation*, Phys. Rev. Lett. **92** (2004) 211301 [astro-ph/0312134] [INSPIRE].

[104] S. Bharadwaj and S.S. Ali, *The CMBR fluctuations from HI perturbations prior to reionization*, Mon. Not. Roy. Astron. Soc. **352** (2004) 142 [astro-ph/0401206] [INSPIRE].

[105] Y. Ali-Haïmoud, P.D. Meerburg and S. Yuan, *New light on 21 cm intensity fluctuations from the dark ages*, Phys. Rev. **D 89** (2014) 083506 [arXiv:1312.4948] [INSPIRE].

[106] D. Tseliakhovich and C. Hirata, *Relative velocity of dark matter and baryonic fluids and the formation of the first structures*, *Phys. Rev.* **D 82** (2010) 083520 [`arXiv:1005.2416`] [INSPIRE].

[107] S. Hirano, T. Hosokawa, N. Yoshida and R. Kuiper, *Supersonic Gas Streams Enhance the Formation of Massive Black Holes in the Early Universe*, *Science* **357** (2017) 1375 [`arXiv:1709.09863`] [INSPIRE].

[108] T.L. Tanaka, M. Li and Z. Haiman, *The effect of baryonic streaming motions on the formation of the first supermassive black holes*, *Mon. Not. Roy. Astron. Soc.* **435** (2013) 3559 [`arXiv:1309.2301`] [INSPIRE].

[109] A. Pillepich, C. Porciani and S. Matarrese, *The bispectrum of redshifted 21-cm fluctuations from the dark ages*, *Astrophys. J.* **662** (2007) 1 [`astro-ph/0611126`] [INSPIRE].

[110] A. Lewis and A. Challinor, *The 21cm angular-power spectrum from the dark ages*, *Phys. Rev.* **D 76** (2007) 083005 [`astro-ph/0702600`] [INSPIRE].

[111] D.N. Limber, *The Analysis of Counts of the Extragalactic Nebulae in Terms of a Fluctuating Density Field.*, *Astrophys. J.* **117** (1953) 134.

[112] W. Hu, *Weak lensing of the CMB: A harmonic approach*, *Phys. Rev.* **D 62** (2000) 043007 [`astro-ph/0001303`] [INSPIRE].

[113] M.J. White, J. Carlstrom, M. Dragovan and S.W.L. Holzapfel, *Analyzing data from DASI*, `astro-ph/9912422` [INSPIRE].

[114] A.H. Jaffe, M. Kamionkowski and L.-M. Wang, *Polarization pursuers' guide*, *Phys. Rev.* **D 61** (2000) 083501 [`astro-ph/9909281`] [INSPIRE].

[115] L. Knox and Y.-S. Song, *A Limit on the detectability of the energy scale of inflation*, *Phys. Rev. Lett.* **89** (2002) 011303 [`astro-ph/0202286`] [INSPIRE].

[116] M. Kesden, A. Cooray and M. Kamionkowski, *Separation of gravitational wave and cosmic shear contributions to cosmic microwave background polarization*, *Phys. Rev. Lett.* **89** (2002) 011304 [`astro-ph/0202434`] [INSPIRE].

[117] M. Zaldarriaga, S.R. Furlanetto and L. Hernquist, *21 Centimeter fluctuations from cosmic gas at high redshifts*, *Astrophys. J.* **608** (2004) 622 [`astro-ph/0311514`] [INSPIRE].

[118] T.J. Mozdzen, J.D. Bowman, R.A. Monsalve and A.E.E. Rogers, *Improved measurement of the spectral index of the diffuse radio background between 90 and 190 MHz*, *Mon. Not. Roy. Astron. Soc.* **464** (2017) 4995 [`arXiv:1609.08705`].

[119] M. Ricotti, *Bondi accretion in the early universe*, *Astrophys. J.* **662** (2007) 53 [`arXiv:0706.0864`] [INSPIRE].

[120] B. Carr, M. Raidal, T. Tenkanen, V. Vaskonen and H. Veermäe, *Primordial black hole constraints for extended mass functions*, *Phys. Rev.* **D 96** (2017) 023514 [`arXiv:1705.05567`] [INSPIRE].

[121] R.M. Thomas and S. Zaroubi, *Time-evolution of ionization and heating around first stars and miniqsos*, *Mon. Not. Roy. Astron. Soc.* **384** (2008) 1080 [`arXiv:0709.1657`] [INSPIRE].

[122] T. Tanaka, R. Perna and Z. Haiman, *X-ray emission from high-redshift miniquasars: self-regulating the population of massive black holes through global warming*, *Mon. Not. Roy. Astron. Soc.* **425** (2012) 2974 [`arXiv:1205.6467`] [INSPIRE].

[123] F. Pacucci, A. Ferrara, M. Volonteri and G. Dubus, *Shining in the Dark: the Spectral Evolution of the First Black Holes*, *Mon. Not. Roy. Astron. Soc.* **454** (2015) 3771 [`arXiv:1506.05299`] [INSPIRE].

[124] S. Zaroubi, R.M. Thomas, N. Sugiyama and J. Silk, *Heating of the Intergalactic Medium by Primordial Miniquasars*, *Mon. Not. Roy. Astron. Soc.* **375** (2007) 1269 [`astro-ph/0609151`] [INSPIRE].

[125] A. Fialkov, R. Barkana and E. Visbal, *The observable signature of late heating of the Universe during cosmic reionization*, *Nature* **506** (2014) 197 [`arXiv:1402.0940`] [INSPIRE].

[126] F. Pacucci, A. Mesinger, S. Mineo and A. Ferrara, *The X-ray spectra of the first galaxies: 21 cm signatures*, *Mon. Not. Roy. Astron. Soc.* **443** (2014) 678 [`arXiv:1403.6125`] [INSPIRE].

[127] S. Yu. Sazonov, J.P. Ostriker and R.A. Sunyaev, *Quasars: The Characteristic spectrum and the induced radiative heating*, *Mon. Not. Roy. Astron. Soc.* **347** (2004) 144 [`astro-ph/0305233`] [INSPIRE].

[128] A.A. Zdziarski and R. Svensson, *Absorption of X-rays and gamma rays at cosmological distances*, *Astrophys. J.* **344** (1989) 551.

[129] Y. Ali-Haimoud and C.M. Hirata, *Ultrafast effective multi-level atom method for primordial hydrogen recombination*, *Phys. Rev.* **D 82** (2010) 063521 [`arXiv:1006.1355`] [INSPIRE].

[130] Y. Ali-Haimoud and C.M. Hirata, *HyRec: A fast and highly accurate primordial hydrogen and helium recombination code*, *Phys. Rev.* **D 83** (2011) 043513 [`arXiv:1011.3758`] [INSPIRE].

[131] C.J. Conselice, A. Wilkinson, K. Duncan and A. Mortlock, *The Evolution of Galaxy Number Density at $z < 8$ and Its Implications*, *Astrophys. J.* **830** (2016) 83 [`arXiv:1607.03909`].

[132] Y. Shen and B.C. Kelly, *The Demographics of Broad-Line Quasars in the Mass-Luminosity Plane. I. Testing FWHM-Based Virial Black Hole Masses*, *Astrophys. J.* **746** (2012) 169 [`arXiv:1107.4372`] [INSPIRE].

[133] B.C. Kelly and Y. Shen, *The Demographics of Broad Line Quasars in the Mass-Luminosity Plane II. Black Hole Mass and Eddington Ratio Functions*, *Astrophys. J.* **764** (2013) 45 [`arXiv:1209.0477`] [INSPIRE].

[134] P.F. Hopkins and L. Hernquist, *Quasars Are Not Light-Bulbs: Testing Models of Quasar Lifetimes with the Observed Eddington Ratio Distribution*, *Astrophys. J.* **698** (2009) 1550 [`arXiv:0809.3789`] [INSPIRE].

[135] F. Panessa, L. Bassani, M. Cappi, M. Dadina, X. Barcons, F.J. Carrera et al., *On the X-ray, optical emission line and black hole mass properties of local Seyfert galaxies*, *Astron. Astrophys.* **455** (2006) 173 [`astro-ph/0605236`] [INSPIRE].

[136] P.F. Hopkins, R. Narayan and L. Hernquist, *How much mass do supermassive black holes eat in their old age?*, *Astrophys. J.* **643** (2006) 641 [`astro-ph/0510369`] [INSPIRE].

[137] A. Babic, L. Miller, M.J. Jarvis, T.J. Turner, D.M. Alexander and S.M. Croom, *Low accretion rates at the AGN cosmic downsizing epoch*, *Astron. Astrophys.* **474** (2007) 755 [`arXiv:0709.0786`] [INSPIRE].

[138] A. Merloni and S. Heinz, *A synthesis model for AGN evolution: supermassive black holes growth and feedback modes*, *Mon. Not. Roy. Astron. Soc.* **388** (2008) 1011 [`arXiv:0805.2499`] [INSPIRE].

[139] E. Komatsu and T. Kitayama, *Sunyaev - zel'dovich fluctuations from spatial correlations between clusters of galaxies*, *Astrophys. J.* **526** (1999) L1 [`astro-ph/9908087`] [INSPIRE].

[140] S. Cole and N. Kaiser, *Sunyaev-Zel'dovich fluctuations in the cold dark matter scenario*, *Mon. Not. Roy. Astron. Soc.* **233** (1988) 637.

[141] A. Cooray and R.K. Sheth, *Halo models of large scale structure*, *Phys. Rept.* **372** (2002) 1 [`astro-ph/0206508`] [INSPIRE].

[142] N. Afshordi, P. McDonald and D.N. Spergel, *Primordial black holes as dark matter: The Power spectrum and evaporation of early structures*, *Astrophys. J.* **594** (2003) L71 [`astro-ph/0302035`] [INSPIRE].

[143] A. Kashlinsky, *LIGO gravitational wave detection, primordial black holes and the near-IR cosmic infrared background anisotropies*, *Astrophys. J.* **823** (2016) L25 [`arXiv:1605.04023`] [INSPIRE].

[144] J.D. Bowman and A.E.E. Rogers, *A lower limit of $\Delta z > 0.06$ for the duration of the reionization epoch*, Nature **468** (2010) 796 [arXiv:1209.1117] [INSPIRE].

[145] G. Bernardi, J.T.L. Zwart, D. Price, L.J. Greenhill, A. Mesinger, J. Dowell et al., *Bayesian constraints on the global 21-cm signal from the Cosmic Dawn*, Mon. Not. Roy. Astron. Soc. **461** (2016) 2847 [arXiv:1606.06006] [INSPIRE].

[146] S. Singh et al., *SARAS 2 constraints on global 21-cm signals from the Epoch of Reionization*, arXiv:1711.11281 [INSPIRE].

[147] S. Jester and H. Falcke, *Science with a lunar low-frequency array: from the dark ages of the Universe to nearby exoplanets*, New Astron. Rev. **53** (2009) 1 [arXiv:0902.0493] [INSPIRE].

[148] J.O. Burns, T.J.W. Lazio and W. Bottke, *Astrophysics Conducted by the Lunar University Network for Astrophysics Research (LUNAR) and the Center for Lunar Origins (CLOE)*, arXiv:1209.2233 [INSPIRE].

[149] E. Visbal, R. Barkana, A. Fialkov, D. Tseliakhovich and C. Hirata, *The signature of the first stars in atomic hydrogen at redshift 20*, Nature **487** (2012) 70 [arXiv:1201.1005] [INSPIRE].

[150] P. Natarajan, F. Pacucci, A. Ferrara, B. Agarwal, A. Ricarte, E. Zackrisson et al., *Unveiling the First Black Holes With JWST:Multi-wavelength Spectral Predictions*, Astrophys. J. **838** (2017) 117 [arXiv:1610.05312] [INSPIRE].

Journal of Cosmology and Astroparticle Physics
An IOP and SISSA journal

Cosmological implications of primordial black holes

José Luis Bernal,^{a,b} **Nicola Bellomo,**^{a,b} **Alvise Raccanelli**^{a}
and Licia Verde^{a,c}

^{a}ICC, University of Barcelona, IEEC-UB,
Martí i Franquès, 1, E08028 Barcelona, Spain
^{b}Dept. de Física Quàntica i Astrofísica, Universitat de Barcelona,
Martí i Franquès 1, E08028 Barcelona, Spain
^{c}ICREA,
Pg. Lluís Companys 23, 08010 Barcelona, Spain

E-mail: joseluis.bernal@icc.ub.edu, nicola.bellomo@icc.ub.edu, alvise@icc.ub.edu, liciaverde@icc.ub.edu

Received September 28, 2017
Accepted October 18, 2017
Published October 30, 2017

Abstract. The possibility that a relevant fraction of the dark matter might be comprised of Primordial Black Holes (PBHs) has been seriously reconsidered after LIGO's detection of a $\sim 30 M_{\odot}$ binary black holes merger. Despite the strong interest in the model, there is a lack of studies on possible cosmological implications and effects on cosmological parameters inference. We investigate correlations with the other standard cosmological parameters using cosmic microwave background observations, finding significant degeneracies, especially with the tilt of the primordial power spectrum and the sound horizon at radiation drag. However, these degeneracies can be greatly reduced with the inclusion of small scale polarization data. We also explore if PBHs as dark matter in simple extensions of the standard ΛCDM cosmological model induces extra degeneracies, especially between the additional parameters and the PBH's ones. Finally, we present cosmic microwave background constraints on the fraction of dark matter in PBHs, not only for monochromatic PBH mass distributions but also for popular extended mass distributions. Our results show that extended mass distribution's constraints are tighter, but also that a considerable amount of constraining power comes from the high-ℓ polarization data. Moreover, we constrain the shape of such mass distributions in terms of the correspondent constraints on the PBH mass fraction.

Keywords: cosmological parameters from CMBR, primordial black holes

ArXiv ePrint: 1709.07465

https://doi.org/10.1088/1475-7516/2017/10/052

Contents

1 Introduction

The concept of Primordial Black Holes (PBHs) was introduced in the sixties [1], and subsequently it was suggested that they might make up the dark matter [2]. However, increasingly stringent constraints (see e.g. [3–6]) gave way to theories proposing elementary particles as dark matter. Of the latter, the most popular theory is the Weakly Interactive Massive Particles (see e.g., [7]). Nonetheless, the fact that WIMPs are still undetected while experiments are reaching the background sensitivity [8] joint with the LIGO+VIRGO collaboration's [9] first detection of gravitational waves emissions from $\sim 30 M_\odot$ binary black hole mergers, make it timely to reconsider PBHs abundance constraints (see e.g., [10–12]).

It is important to bear in mind that even without accounting for a relevant fraction of the dark matter, the existence of PBHs might be a possible solution for other astrophysical open questions. For instance, PBHs might be the progenitors of the super massive black holes located at the nuclei of galaxies (e.g., [13, 14] and references therein) or the intermediate massive black holes that could inhabit the center of dwarf galaxies (e.g., [15] and references therein).

The abundance of PBHs (and hence the fraction of the total dark matter that they constitute, $f_{\rm PBH}$) is constrained by several independent observations in a wide range of masses, with present datasets and new observables suggested for future experiments (see e.g. [16–26]). For stellar masses, existing constraints include microlensing by compact objects with masses $\lesssim 10 M_\odot$ [27–31], wide binaries disruption [32] or stellar distribution in ultra-faint dwarfs galaxies [33] at slightly larger masses. There are also constraints on $f_{\rm PBH}$ on this mass range from X-ray and radio observations of the Milky Way [34], although they depend strongly on astrophysical assumptions. In addition to astrophysical observables, the presence of PBHs has also consequences on cosmological observables such as the Cosmic Microwave Background (CMB).

The basic mechanism behind the effects that a PBH population has on the CMB is the following. PBHs accrete primordial gas in the early Universe and inject energy into the primordial plasma via radiation. Therefore, the Universe's thermal and ionization histories are affected by the presence of PBHs, leaving potentially detectable signatures in the CMB.

Given that the medium has more energy because of the PBH energy injection, recombination is delayed. This shifts the acoustic peaks and affects some physical quantities (e.g., the sound horizon at radiation drag, r_s). To summarize, the imprints are similar to those imposed by the energy injection of exotic species such as dark matter decaying into photons [35].

Recently, Ali-Haïmoud & Kamionkowski [36] (hereafter AHK) rederived constraints from CMB power spectra and spectral distortions using the recently released Planck power spectra [37], assuming spherical accretion and considering two limiting cases of ionization mechanisms (collisional ionization and photoionization). Compared to the previous analysis, AHK generalize the radiative efficiency computation accounting for Compton drag and cooling by CMB photons, as well as ionization cooling once the gas is neutral, and use a more precise estimate of the relative velocity between PBHs and baryons. All this leads to significantly smaller accretion rates and PBH luminosities than previous analyses, therefore weakening constraints with respect to previous studies [38]. These updated results leave a window open for PBHs to be the dark matter ($f_\mathrm{PBH} = 1$), precisely for masses of tens of $M_\odot$. In contrast to the standard cosmological model, Λ-Cold Dark Matter (ΛCDM), hereafter we refer to a ΛCDM model where a significant fraction of the dark matter is PBH as ΛPBH. Recently, the authors of [39] revisited CMB constraints assuming disk accretion. They find tighter constraints, which close the mentioned window and exclude the possibility that PBHs of tens of $M_\odot$ account for $f_\mathrm{PBH} \gtrsim 0.1$. This would rule out the ΛPBH model. However, both spherical accretion and disk accretion for all the PBHs are limiting cases. It is therefore reasonable to expect that a realistic scenario would be in between these (refs. [36] and [39]) limiting cases.

Most of the constraints mentioned above are derived assuming a Dirac delta function for the mass distribution (i.e., *monochromatic* distribution). While being a good approximation as a first step, this is an idealized case. Extended mass distributions (EMDs) appear naturally in formation mechanisms such as the collapse of large primordial fluctuations [40] or cosmic strings [41], or cosmological phase transitions, like bubble collisions [42], among others [43]. Besides, critical collapse [44] broadens any distribution, even if it is nearly monochromatic, making an EMD for PBHs unavoidable [45]. This effect has been studied numerically in [46–48], showing that it applies over ten orders of magnitude in density contrast (see e.g. figure 1 of [47]).

Given the wide variety of EMDs for PBHs, it is impossible to explore them all in detail in a cosmological context. The authors of [22, 23, 49] have proposed approaches to translate monochromatic constraints to EMDs; for a discussion of the advantages and limitations of these approaches see the above references and [50]. Constraints for simple EMDs have been derived exactly for microlensing observations [51].

Recent works demonstrate that it is possible to interpret very accurately the effects of a population of PBHs with an EMD in each different cosmological probe as a monochromatic population with a corresponding effective equivalent mass. The approach is physically motivated as it accounts for the underlying physics of the effects of PBHs [50]. This is the approach we follow here. We refer the reader to ref. [50] for more details and advantages compared to other approaches.

Although recently there has been a renewed effort to revisit PBHs constraints, there is still a lack of studies on PBHs cosmological implications and their possible correlations with other cosmological parameters. Given the persistent tensions that exist among some observations at high and low redshift within ΛCDM, it is worthwhile to explore the possibility that the inclusion of PBHs in the model might reconcile these tensions. Using the formalism described in AHK, we study the impact of a large PBH mass fraction on CMB-derived cosmological parameters, for the standard six parameters of ΛCDM and for common extensions to this model. We also compute constraints on $f_{\rm PBH}$ for PBHs with EMDs and test the prescriptions of [50] for the effective equivalent mass for the CMB.

This paper is structured as follows. In section 2 we introduce the observational data we use and our methodology. Results are presented in section 3: the results for monochromatic distributions are shown in section 3.1 and those for EMDs, in section 3.2. Finally, discussion and conclusions can be found in section 4.

2 Methodology and data

We use the public Boltzmann code CLASS [52, 53] using the modified version of HyRec [54, 55] introduced in AHK. This modification allows us to compute CMB power spectra accounting for effects due to a monochromatic mass distribution of PBH with mass M and fraction $f_{\rm PBH}$. We further modify this code to allow also for a variety of PBH EMDs following the prescriptions suggested in AHK.

We use the Markov Chain Monte Carlo (MCMC) public code Monte Python [56] to infer cosmological parameters using the observational data described below. We use uniform priors for $f_{\rm PBH}$ in the range $0 \leq f_{\rm PBH} \leq 1$, which is motivated by the linear dependence of the differences in the CMB power spectra on $f_{\rm PBH}$, shown in AHK. We also consider logarithmic priors finding that results do no change significantly.

We consider the full Planck 2015 temperature (TT), polarization (EE) and the cross correlation of temperature and polarization (TE) angular power spectra [37], corresponding to the following likelihoods: Planck highℓ TTTEEE (for $\ell \geq 30$), Planck lowℓ (for $2 \leq \ell \leq 29$) and the lensing power spectrum (CMB lensing). The Planck team identifies the lowℓ + highℓ TT as the recommended baseline dataset for models beyond ΛCDM and the highℓ polarization data as preliminary, because of evidence of low level systematics ($\sim \mu{\rm K}^2$ in $\ell(\ell+1)C_\ell$) [57]. While the level of systematic contamination does not appear to affect parameter estimation, we present results both excluding and including the highℓ polarization data. Hereinafter we refer to the data set of Planck highℓ TTTEEE, Planck lowℓ and CMB lensing as "Full Planck" (or *full* for short) and we refer to the Planck recommended baseline as "PlanckTT+lowP+lensing" (or *baseline*).

The approach we follow builds on AHK work and is similar in spirit. In that work, the authors use the `Plik_lite` best fit C_ℓ, a provided covariance matrix for the highℓ CMB-only TTTEEE power spectra, and a prior on the optical depth of reionization, $\tau_{\rm reio}$, from [58]. Note that such covariance matrix is computed for a ΛCDM model without the presence of PBHs, so no correlation among $f_{\rm PBH}$ and the standard cosmological parameters is considered. One difference comes from the fact that, while AHK use a Fisher matrix approach to estimate parameters constraints, we use MCMC for parameter inference. The price of being more rigorous comes at a considerable increase in the computation time of the analysis. Computing the constraints on $f_{\rm PBH}$ for all masses would take an unpractical amount of time. However, given that the dependence of the upper limits on $f_{\rm PBH}$ on $M_{\rm PBH}$ is smooth, we choose $M_{\rm PBH}$ values equally spaced in logarithmic scale and interpolate the constraints in between. With this procedure, for any $M_{\rm PBH}$ in the interval covered by the sampling, we have an estimated value for the 95% and 68% confidence limit on $f_{\rm PBH}$. This correspondence will be useful in section 3.2 and figures 7 and 8.

2.1 Accounting for EMDs

To consider the effect of an extended mass distribution (EMD), rather than exploring the whole parameter space of all possibilities, we follow the Bellomo et al. [50] prescriptions to interpret EMDs as monochromatic populations with an effective equivalent mass, $M_{\rm eq}$, which depends on both the shape of the EMD and the observable considered. Here we just briefly introduce the formalism for the CMB and refer the interested reader to ref. [50] for a full explanation.

For an EMD, we define the PBH mass fraction as:

$$\frac{df_{\rm PBH}}{dM} = f_{\rm PBH}\frac{d\Phi_{\rm PBH}}{dM}, \tag{2.1}$$

in such a way that $\frac{d\Phi_{\rm PBH}}{dM}$ is normalized to unity. We consider two popular mass distributions: a power law (PL) and a lognormal (LN). The former can be expressed as:

$$\frac{d\Phi_{\rm PBH}}{dM} = \frac{\mathcal{N}_{\rm PL}(\gamma, M_{\rm min}, M_{\rm max})}{M^{1-\gamma}}\Theta(M - M_{\rm min})\Theta(M_{\rm max} - M), \tag{2.2}$$

characterized by the exponent γ, a mass range $(M_{\rm min}, M_{\rm max})$ and a normalization factor

$$\mathcal{N}_{\rm PL}(\gamma, M_{\rm min}, M_{\rm max}) = \begin{cases} \dfrac{\gamma}{M_{\rm max}^{\gamma} - M_{\rm min}^{\gamma}}, & \gamma \neq 0, \\ \log^{-1}\left(\dfrac{M_{\rm max}}{M_{\rm min}}\right), & \gamma = 0, \end{cases} \tag{2.3}$$

where $\gamma = -\frac{2w}{1+w}$, w being the equation of state when PBHs form. If an expanding Universe is assumed ($w > -1/3$), γ spans the range $(-1, 1)$. We consider two cases of power law distribution: one with $\gamma = 0$ (corresponding to PBHs formed in matter domination epoch) and another one with $\gamma = -0.5$ (corresponding to PBHs formed in radiation dominated epoch).

Lognormal mass distributions can be expressed as:

$$\frac{d\Phi_{\rm PBH}}{dM} = \frac{1}{\sqrt{2\pi\sigma^2 M^2}} e^{-\frac{\log^2(M/\mu)}{2\sigma^2}}, \tag{2.4}$$

where μ and σ are the mean and the standard deviation of the logarithm of the mass.

In order to account for an EMD, the energy density injection rate has to be integrated over the whole mass range spanned by PBHs:

$$\dot{\rho}_{\rm inj} = \rho_{\rm dm} f_{\rm PBH} \int dM \frac{d\Phi_{\rm PBH}}{dM}\frac{\langle L(M)\rangle}{M}, \tag{2.5}$$

where $\langle L(M)\rangle$ is the velocity-averaged[1] luminosity of a PBH. Starting from the results of AHK, it is possible to estimate the mass dependence of the integrand in eq. (2.5) as:

$$\frac{\langle L\rangle}{M} \propto \frac{L}{M} \propto \frac{\dot{M}^2/L_{\rm Edd}}{M} \propto \frac{M^4\lambda^2(M)/M}{M} = M^2\lambda^2(M), \tag{2.6}$$

where L is the luminosity of an accreting black hole, $\dot{M}$ is the black hole growth rate, $L_{\rm Edd}$ is the Eddington luminosity and $\lambda(M)$ is the dimensionless accretion rate. In principle the

---

[1] Recall that the accretion rate depends, among others, on the relative velocity PBH-gas.

averaged luminosity will depend not only on the mass but also on redshift, gas temperature, free electron fraction and ionization regime. Ref. [50] assumes that these dependencies can be factored out by parametrizing the dimensionless accretion rate as $\lambda(M) = M^{\alpha/2}$, where α is a parameter tuned numerically a posteriori to minimize differences in the relevant observable quantity between the EMD case and the equivalent monochromatic case.

Therefore, the effects of an EMD on the CMB power spectra are mimicked by a monochromatic distribution of mass $M_{\rm eq}$ when:

$$f_{\rm PBH}^{\rm MMD} M_{\rm eq}^{2+\alpha} = f_{\rm PBH}^{\rm EMD} \begin{cases} \mathcal{N}_{\rm PL} \dfrac{M_{\rm max}^{\gamma+2+\alpha} - M_{\rm min}^{\gamma+2+\alpha}}{\gamma+2+\alpha}, & PL, \\ \\ \mu^{2+\alpha} e^{\frac{(2+\alpha)^2\sigma^2}{2}}, & LN. \end{cases} \tag{2.7}$$

where $f_{\rm PBH}^{\rm MMD}$ is the PBH mass fraction associated with a monochromatic distribution. In order to obtain the effective equivalent mass, we fix $f_{\rm PBH}^{\rm MMD} = f_{\rm PBH}^{\rm EMD}$. This way, the upper limit on $f_{\rm PBH}^{\rm EMD}$ is the corresponding upper limit for a monochromatic distribution with the effective equivalent mass.

As the authors of [50] indicate, there is no single choice of the parameter α in eq. (2.7) able to correctly match the time dependent energy injection of the EMDs with the monochromatic case. Since we require to select one effective value for α, the relation between the "best" value of α and the redshift range where the match is optimised depends also on the EMD. Given that Planck power spectra have the smallest error bars for $10^2 \lesssim \ell \lesssim 10^3$, we choose to select α by minimizing the differences in the CMB power spectra in that multipole range. Although we expect that different values of α do not have great impact in the performance of the method, we use $\alpha = 0.3$ for Power Law distributions, and $\alpha = 0.2$ for Lognormal distributions [50].

In principle, our effective treatment of the EMD (eq. (2.7)) and related results strictly applies only for $M < 10^4 M_\odot$. This is because AHK modelling includes a steady-state approximation to avoid time dependent fluid, heat and ionization computations. This approximation holds when the characteristic accretion timescale is much shorter than the Hubble timescale, which is fulfilled for PBHs with $M \lesssim 3 \times 10^4 M_\odot$ [59]. Since AHK formalism breaks down for $M > 10^4 M_\odot$, eq. (2.7) is valid only for EMDs which do not have significant contributions beyond that limit.

2.2 Important considerations

Several considerations are in order before we present our results and attempt their interpretation. First of all, the treatment of the effects of PBHs on the CMB (adopted from AHK) only considers changes in the ionization and Hydrogen thermal history via energy injection due to PBHs accretion. It does not consider any changes in the background history of the Universe. These changes would be mainly introduced because of the energy transfer from the matter component to the radiation one through black hole mergers, for instance. However there are several indications that these processes are not important in this context. In fact ref. [60] estimated that no more than 1% of the dark matter can be converted into gravitational waves after recombination; hence this mechanism cannot provide a significant "dark radiation" component affecting the early time expansion history and cosmological parameters estimation. It cannot be invoked therefore to reduce the tension between the inferred value of H_0 obtained using CMB observations and assuming ΛCDM [37] and its direct measurement coming from the distance ladder [61]. However, black hole mergers could affect the expansion history before recombination in a similar way than $N_{\rm eff}$. This effect would further affect recombination quantities, such as $r_{\rm s}$, which also affects the inferred value of H_0 [62, 63]. This avenue is left to study in future work.

Energy transfer from matter to radiation sectors is not the only effect of PBH mergers. When two PBHs merge, the final state is a single black hole with larger mass. Thus the merger history of the PBH population changes the initial EMD predicted by inflation theories. The extent of this effect depends on the merger rate which in turn depends on the initial clustering and mass and velocity distributions. Given current theoretical uncertainties and observational precision, neglecting changes in the EMD through time is not expected to bias current constraints. However, this may need to be accounted for in the future.

As PBHs behave like a cold dark matter fluid at sufficiently large scales, they only affect cosmological observables via energy injection because of the accreted matter. Therefore, the only other cosmological probe affected by PBHs is reionization. The rest of cosmological probes (i.e., cosmic shear, baryon acoustic oscillations, etc) will not be affected by a large $f_{\rm PBH}$. For this reason we have not considered other cosmological probes here. In practical applications they could certainly be used to further reduce parameter degeneracies.

While we assume spherical accretion, in [39] disk accretion is assumed. As the radiative efficiency when a disk is formed is much larger than if the accretion is spherical, their constraints are much stronger than ours and those appearing in AHK. However, both scenarios are possible in the early Universe: whether the accretion is spherical or a disk is formed depends on the value of the angular momentum of the accreted gas at the Bondi radius compared with the angular momentum at the innermost stable circular orbit. Given that it is difficult to estimate the angular momentum of the gas accreting onto a PBH, the best approach is to consider these as two limiting cases. We refer the reader to figure 3 and related discussion in Poulin et al. (2017) [39] in order to see the extent of the differences in the shape of the power spectra between both scenarios. Nonetheless, we expect that our results can be extrapolated to the disk accretion framework. Actually, the degeneracies between $f_{\rm PBH}$ and other parameters are expected to be approximately the same in both cases.

Therefore, it should be clear from the above discussion that uncertainties in the modelling of processes such as accretion mechanisms of PBHs or velocity distributions imply that any constraint should be interpreted as an order of magnitude estimate, rather than a precise quantity. However, the behaviour of parameters degeneracies as a function of the different data sets considered or ionization regime should be qualitatively captured by our analysis. For this reason, we will also report the ratio between the constraints using two different data sets or ionization models.

As the equivalence relation between the effects of PBH with an EMD and a monochromatic distribution derived in [50] is obtained assuming the formalism of AHK, it is subject to the same caveats as AHK modelling. In particular given that AHK modelling breaks down for $M > 10^4 M_\odot$, eq. (2.7) should be used strictly only for EMDs which do not have significant contributions beyond that limit. A criterion to decide if a EMD fullfil this condition can be found in ref. [50]. Finally, while in principle the choice of the parameter α in eq. (2.7) could be numerically optimized, the equivalent mass is relatively insensitive to small changes of its value for the EMDs considered here; therefore a slightly sub-optimal value of α does not bias our results.

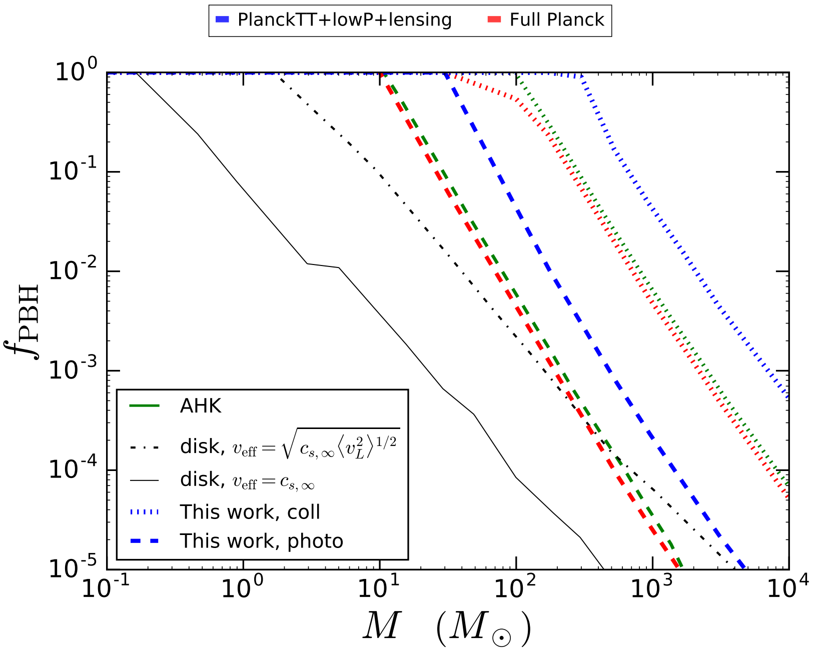

Figure 1. 68% confidence level marginalized constraints on $f_{\rm PBH}$ in the collisional ionization regime (dotted lines) and in the photoionization regime (dashed lines). The results using the full data set of Planck are shown in red and without including the high multipoles of polarization, in blue. We also show, as a reference, the 68% confidence level marginalized constraints of AHK (green) and the 95% confidence level marginalized constraints of [39] (black), where disk accretion is assumed. These external results are obtained including the high multipoles of Planck polarization power spectrum.

3 Results

3.1 Constraints on $f_{\rm PBH}$ for monochromatic distributions

We start by directly comparing our approach with that of AHK; we use the same data (Planck lite highℓTTTEEE + prior in τ) but a MCMC instead of a Fisher approach to estimate parameter constraints. The constraints we obtain are similar to those of AHK, with variations always below the 10% level, which is smaller than the theoretical uncertainty of the model. Although there is no significant effect introduced by using a Fisher approach, as we are interested in the posterior distribution in the whole parameter space, we use MCMC.

In figure 1 we show the 68% confidence level upper limits on $f_{\rm PBH}$ for monochromatic populations of PBHs with different masses for both the full Planck dataset (red) and removing the high multipoles of polarization power spectrum (blue). Note that this color coding is used in all the figures throughout the paper. We also show the results of AHK and the 95% confidence level upper limits obtained assuming disk accretion from [39]. The results using *full* Planck are very similar to those obtained in AHK. For the recommended baseline of Planck (which is the most conservative case) the constraints are weaker, widening the window where $f_{\rm PBH} \sim 1$ is allowed. The maximum masses for which $f_{\rm PBH} \sim 1$ is allowed (i.e., there is no upper limit at 68% confidence level) in each of the cases considered are reported in table 1.

	coll. Planck full	coll. baseline	photo. Planck full	photo. baseline
max. M with $f_{\rm PBH} \sim 1$	$30M_\odot$	$300M_\odot$	$10M_\odot$	$30M_\odot$

Table 1. Maximum mass for which $f_{\rm PBH} \sim 1$ is allowed at 68% confidence level for monochromatic distributions. We report the values for all possible combinations of data sets (either full Planck or baseline) and ionization regimes (either collisional ionization or photoionization). Note that (as it should be clear from the text and from figure 1) these values are approximated and limited by the discrete sampling in mass for which we compute the constraints.

	Planck full/ baseline (coll)	Planck full/baseline (photo)	photo/coll (Full Planck)	photo/coll (baseline)
$f_{\rm PBH}$ ratio	0.11	0.11	5.2×10^{-3}	$4.8\ \times10^{-3}$
Validity	$M > 300M_\odot$	$M > 30M_\odot$	$M > 100M_\odot$	$M > 300M_\odot$

Table 2. Ratio of 68% marginalized upper limits on $f_{\rm PBH}$. We compare the upper limits obtained using full Planck against using the baseline PlanckTT+lowP+lensing for the two ionization regimes and the constraints obtained assuming photoionization against assuming collisional ionization for both data sets. In all cases we report the mass range for which the correspondent ratio is valid.

To capture the effect of different data sets and assumptions on the ionization regime on the $f_{\rm PBH}$ limits, we use the ratio between two upper limits obtained with different assumptions or data. Table 2 highlights the effect of polarization high multipoles (first two columns) by reporting the ratio of the marginalised 68% confidence level on $f_{\rm PBH}$ obtained using the *full* Planck data to that obtained using the *baseline* Planck data set. The next two columns illustrate the effect of the ionization regime (ratio of assuming photoionization over collisional ionization). As it can be seen, ratios for the different data sets does not depend on the ionization limit and ratios for the ionization limits does not depend on the data. This suggests that the ratio between two marginalized upper limits on $f_{\rm PBH}$ can be used to isolate the effects of specific choices of modelling or data sets. In fact, including the high multipoles of polarization power spectra improves constraints by a factor of 10. On the other hand, assuming photoionization regime instead of collisional ionization, improve constraints by a factor of ∼200.

3.1.1 Constraints and degeneracies with cosmological parameters in ΛCDM

In addition to the constraints on $f_{\rm PBH}$, we also study the degeneracies of this parameter with the six standard cosmological parameters of the ΛCDM model.

The most notable degeneracy, as already noticed in [38], is between $f_{\rm PBH}$ and the scalar spectral index n_s. This positive correlation is induced by the energy injection of the PBH emission, which alters the tails of the CMB power spectra. As decoupling is delayed, the diffusion damping increases and the high multipoles are suppressed through Silk damping. In figures 2 and 3, we show the results for the collisional ionization and photoionization limits, respectively. We report 68% and 95% confidence level marginalized constraints on the $f_{\rm PBH} - n_s$ (left) and $f_{\rm PBH} - r_s$ (right) planes, for different masses, as these are the most affected parameters; in general, degeneracies become stronger for larger masses. For some cases, a scale independent or even blue tilted primordial power spectrum is allowed. Combined analyses with galaxy surveys can be used to constrain n_s, reducing the degeneracy; we will discuss this in more details elsewhere.

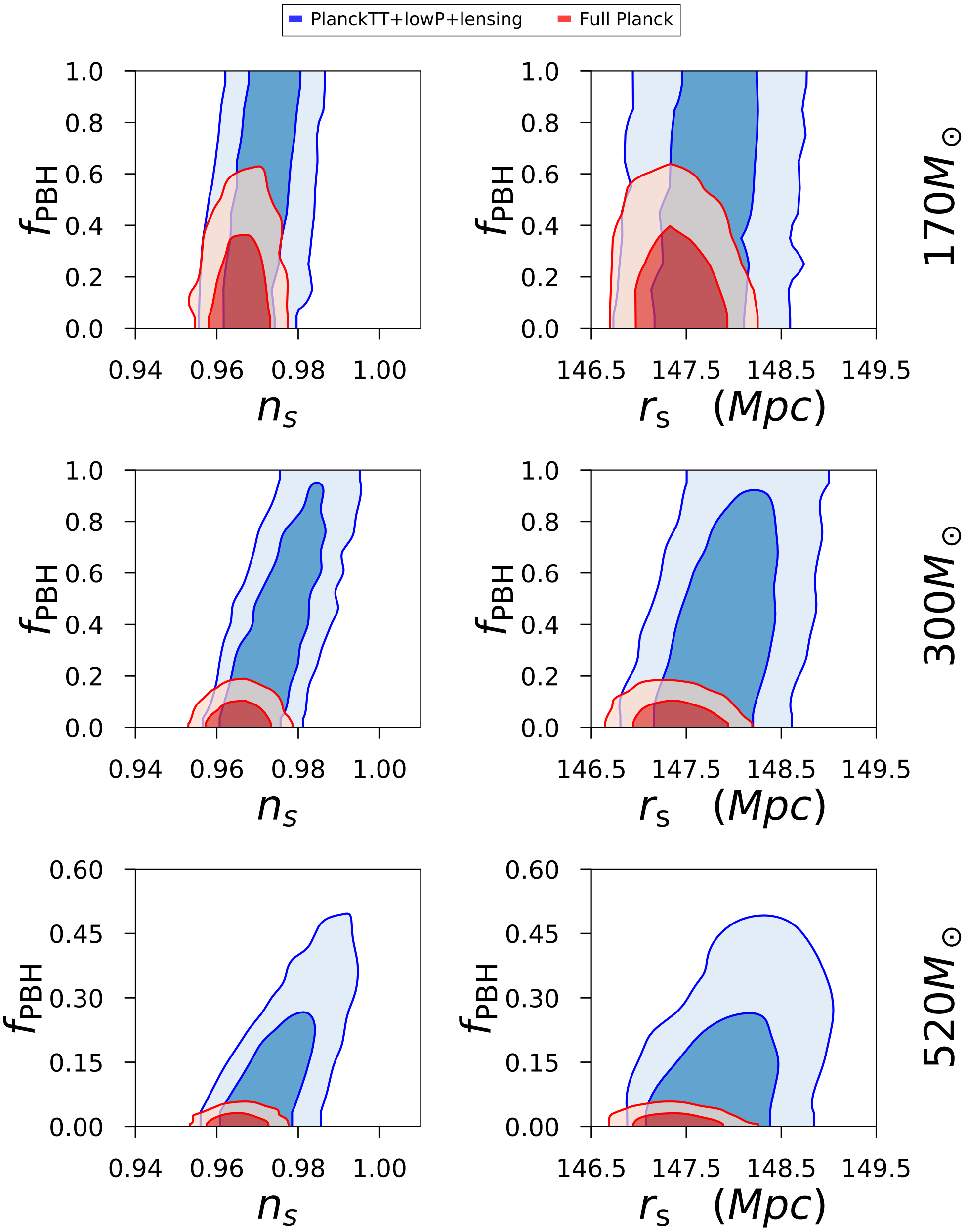

Figure 2. 68% and 95% confidence level marginalized constraints on the n_s-$f_{\rm PBH}$ plane (left) and r_s-$f_{\rm PBH}$ plane (right) for ΛCDM with PBHs as part of the dark matter (i.e., free $f_{\rm PBH}$) in the collisional ionization regime. We consider three monochromatic distributions: $170M_\odot$ (top), $300M_\odot$ (middle) and $520M_\odot$ (bottom). Results using the full data set of Planck are shown in red and using the recommended baseline, in blue. 68% upper limits on $f_{\rm PBH}$ correspond to the those shown in figure 1. Note the change of scale in y-axis.

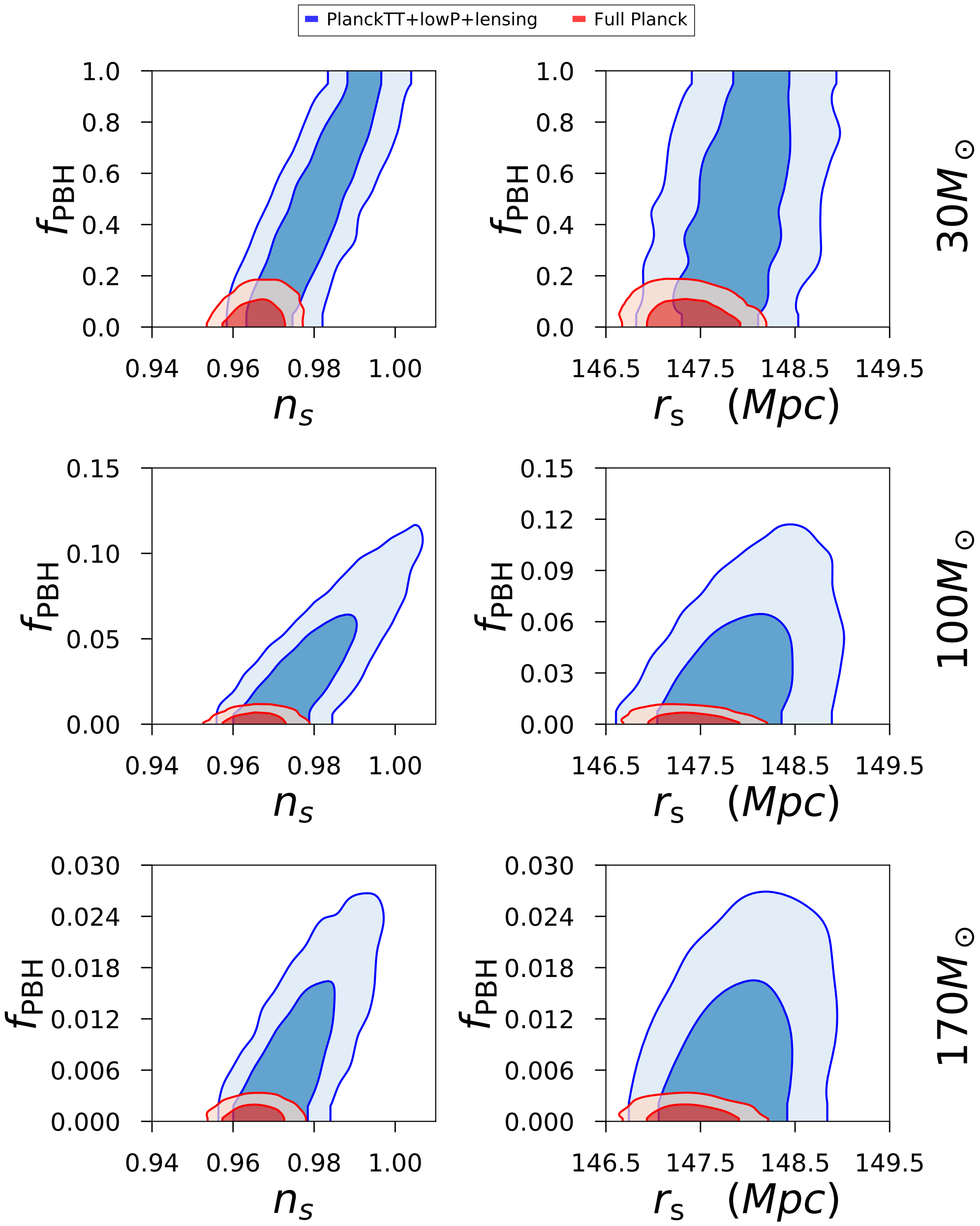

Figure 3. Same as figure 2, but in photoionization regime. In this case we consider $30M_\odot$ (top), $100M_\odot$ (middle) and $170M_\odot$ (bottom).

The $f_{\rm PBH} - r_{\rm s}$ degeneracy is the result of two competing effects. On one hand, the presence of PBHs delays recombination and shifts the peaks of CMB power spectra (see figure 13 of AHK). This yields a larger sound horizon at radiation drag, leading to a lower value of H_0 to fit the cosmic distance ladder of supernovae type Ia and Baryon Acoustic Oscillations (BAO), as shown in [62]. On the other hand, the effect of a delayed recombination on the value of r_s is compensated by small degeneracies in the density parameters of baryons and dark matter. Thus, a sizeable PBH component (with masses $\gtrsim 300 M_\odot$ for collisional ionization or $\gtrsim 30 M_\odot$ for photoionization) can change r_s by ~ 1 Mpc. This shift is of a magnitude comparable to other effects and, most importantly, non-negligible with current and future errors in distance measurements using the BAO scale.

The effect on the rest of ΛCDM parameters is smaller, mostly resulting in mild relaxations of the confidence regions. Beyond that, only the amplitude of the scalar modes in the primordial power spectrum, A_S, presents a small positive correlation with f_PBH.[2]

Perhaps unsurprisingly, the inclusion of the highℓ polarization data effectively remove the degeneracies; the effect on the TT damping tail can be mimicked by changes of the cosmological parameters, but this is not anymore the case once also the highℓ polarization is considered. It is well known that the highℓ polarization data has a similar effect in other models where, as in this model, the CMB damping tail is affected by the additional physics introduced (e.g., if dark radiation is allowed and for decaying dark matter models).

3.1.2 Implications for extended cosmologies

Here we explore the consequences of varying f_PBH in some common extensions of the ΛCDM model. In addition to an expected weakening of the constraints, we study the degeneracies with the additional parameters. We consider the following models: free equation of state of dark energy (wCDM), free sum of neutrino masses (ΛCDM+m_ν), free effective number of relativistic species (ΛCDM+N_eff) and free running of the spectral index (ΛCDM+α_s). Finally, we also allow the running of the running of the spectral index, β_s to be a free parameter (ΛCDM+α_s+β_s). We limit the study to the recommended baseline of Planck. Moreover, following the results from the previous section and in order to appreciate changes in f_PBH, we choose masses for which $f_\mathrm{PBH} \sim 0.1$: $520 M_\odot$ for collisional ionization and $100 M_\odot$ for photoionization.

Figure 4 shows 68% and 95% confidence level marginalized constraints on the plane of f_PBH and the additional parameters of the extended cosmologies. As it can be seen, there is a correlation between m_ν and f_PBH and between N_eff and f_PBH, and an anti-correlation between α_s and f_PBH, but no appreciable correlation with w. The degeneracies with m_ν, N_eff and α_s open the possibility that when limiting the theoretical framework to ΛCDM, one might hide the presence of PBHs. On the other hand, $f_\mathrm{PBH} = 0$ is always within the 68% confidence region.

The positive correlation between f_PBH and N_eff can be explained as follows. On one hand, as PBH energy injection delays recombination, r_s is higher (and CMB peaks are displaced towards larger scales). On the other hand, a value of N_eff different than the fiducial value changes the expansion history, especially in the early Universe, hence r_s is modified. Concretely, higher values of N_eff derive on lower values of r_s (and displacements of the CMB peaks towards smaller scales). This is why, if PBHs exist, larger values of f_PBH need larger values of N_eff to fit observations. Varying m_ν also changes the expansion history, the angular diameter distance to recombination and the redshift of equality, so the relation between f_PBH and m_ν is similar to that explained above.

We also consider the case in which the running of the spectral index, α_s, is scale dependent, hence there is an additional free parameter in this case: the running of the running, β_s,

---

[2] While in principle one may expect also a degeneracy with the optical depth to recombination τ_reio, this is not noticeable due to the tight constraints on this parameter imposed by the low ℓ polarization data and because f_PBH is positive definite.

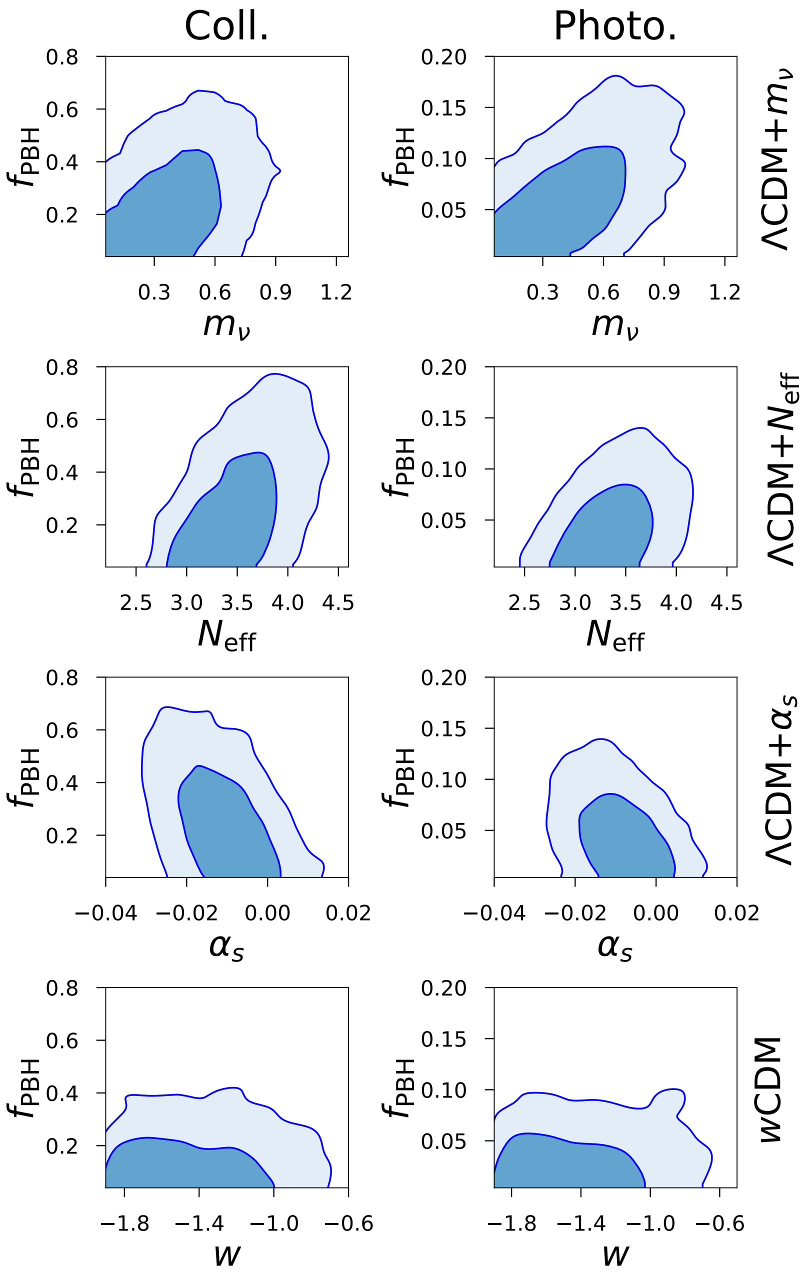

Figure 4. 68% and 95% confidence level marginalized constraints on the plane $f_{\rm PBH}$-x (x being the additional parameter to ΛPBH) for $520 M_\odot$ in the collisional ionization regime (left) and $100 M_\odot$ in the photoionization (right) for the following extended cosmologies (form top to bottom): ΛPBH+m_ν, ΛPBH+$N_{\rm eff}$, ΛPBH+α_s and wPBH.

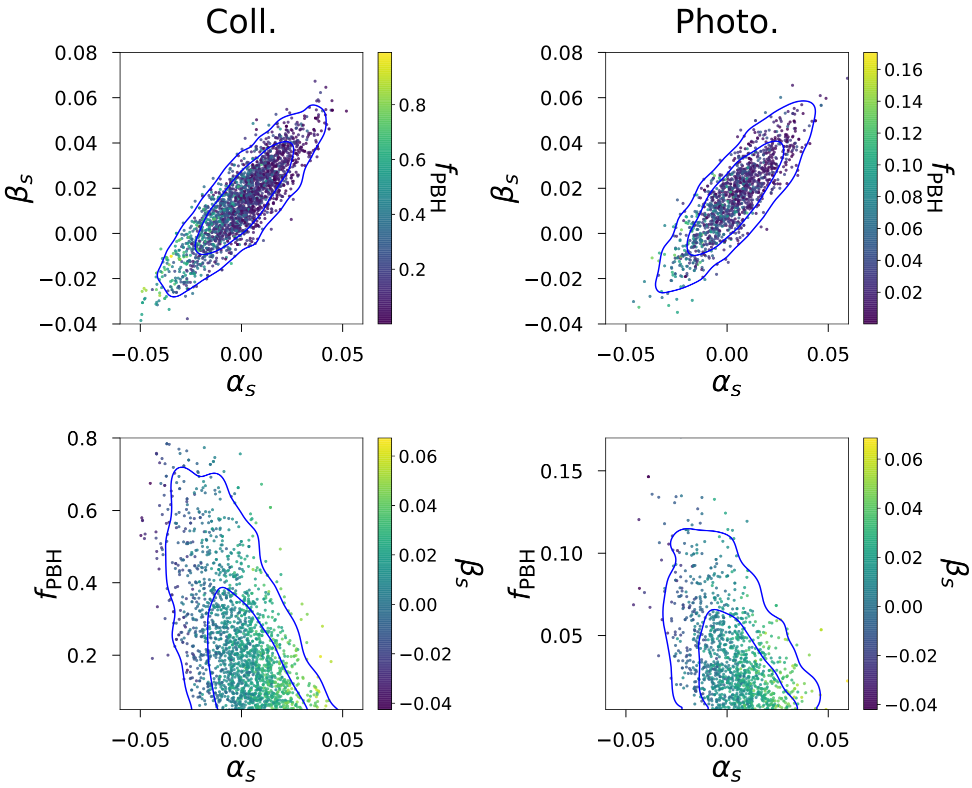

Figure 5. 68% and 95% confidence level marginalized constraints for a ΛCDM + α_s + β_s model for $520M_\odot$ in the collisional regime (left panels) and for $100M_\odot$ in the photoionization regime (right panels). Upper panels: constraints on the β_s-α_s plane with a color code to express the value of $f_{\rm PBH}$. Bottom panels: constraints on the $f_{\rm PBH}$-α_s plane with a color code to indicate the value of β_s. These results are obtained without including the high multipoles of the polarization power spectrum of Planck.

which we consider scale independent. As it can be seen in figure 5, varying β_s weakens the constraints on α_s and the parameters are highly correlated. What is more surprising is that for small values of $f_{\rm PBH}$, β_s is slightly different than 0. However, this trend is not strong enough to be statistically significant.

Although there is a strong correlation between $f_{\rm PBH}$ and n_s, the correlations with α_s and β_s are much smaller. This is due to the suppression of the CMB power spectra on the high ℓ tail produced by PBHs can be mimicked by a different constant value of n_s, without evidence of the need of a strong scale dependent variation.

Figure 6 shows how the degeneracies in extended cosmologies weaken the constraints on $f_{\rm PBH}$. Adding an extra cosmological parameter to the 6-ΛCDM ones, weakens the constraints on $f_{\rm PBH}$ approximately by a factor 2, except for wCDM, due to the lack of correlation. The shift of the parameters w and β from their ΛCDM-fiducial values is responsible for making the $f_{\rm PBH}$ constraints in the extended model slightly tighter.

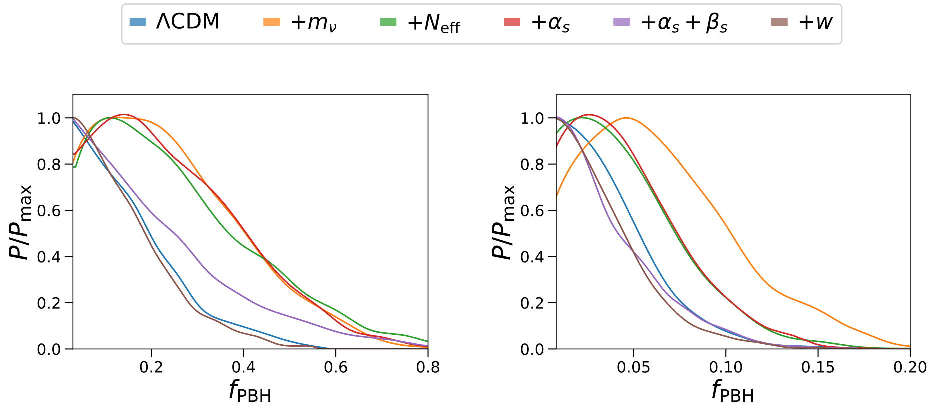

Figure 6. Margnialized probability distribution of $f_{\rm PBH}$ obtained assuming the extended cosmologies and those obtained assuming ΛCDM using PlanckTT+lowP+lensing for collisional ionization and $520M_\odot$ (left) and photoionization $100M_\odot$ (right).

3.2 Constraints on PBHs with extended mass distributions

So far, we have considered monochromatic populations of PBHs. Although this is an interesting first step, a more realistic case involves a distribution of masses. We follow [50] as described in section 2.1 and assess numerically the accuracy of the approximation in six specific cases: two Lognormal distributions and four Power Law distributions (two with $\gamma = 0$ and other two with $\gamma = -0.5$). For each EMD case, we consider a narrow and a wide distribution. Our aim is to test the approach of [50] by comparing the results obtained following their prescription with an exact calculation using MCMCs.

The resulting marginalized 68% and 95% confidence level upper limits on $f_{\rm PBH}$ using full Planck for the six EMDs are shown in table 3. In the second column we report results for a monochromatic distribution of $30M_\odot$ and in the following columns we report constraints for extended mass distributions chosen to have an effective equivalent mass (according to section 2.1) of $30M_\odot$. The differences in the upper limits are well below the theoretical uncertainties of the model. These results demonstrates that, within the current knowledge of how an abundant population of PBHs affects the CMB, there is no difference between computing the constraints using the actual EMD and using an effective equivalent mass following the approach of [50]. In the same spirit, the monochromatic upper limits on $f_{\rm PBH}$ can be used to constrain the parameters of the EMDs considered here; i.e., μ and σ for the Lognormal and γ for the Power Law (for which we consider different mass bounds). We use the marginalized 95% confidence level upper limits of $f_{\rm PBH}$ and translate these into limits for the EMDs parameters as follows. For every choice of EMD and its parameters, we compute the effective equivalent monochromatic mass and look up the $f_{\rm PBH}$ value corresponding to the 95% confidence upper limit (see section 2 and figure 1). The results for photoionization and collisional ionization limits using both full Planck and PlanckTT+lowP+lensing for a ΛCDM model are shown in figure 7 for a Lognormal EMD and figure 8 for Power Law EMDs. The black shaded region indicates parameters values for which the EMD extends significantly beyond the limit of $10^4M_\odot$ where the AHK formalism becomes invalid.

The above results can be understood as follows. If PBHs have an EMD, the largest contribution to the injected energy comes from the high mass tail [50]. Therefore for a large

C.L.	M=30$M_\odot$ $\equiv M_{\rm eq}$	LN (1)	LN (2)	PL, (1) $\gamma = 0$	PL, (2) $\gamma = 0$	PL, (1) $\gamma = -0.5$	PL, (2) $\gamma = -0.5$
$f_{\rm PBH} \leq (68\%)$	0.071	0.072	0.067	0.073	0.070	0.069	0.0725
$f_{\rm PBH} \leq (95\%)$	0.14	0.15	0.14	0.14	0.14	0.14	0.16

Table 3. Evaluation of the performance of the effective equivalent mass to match the results of accounting properly for EMDs. The result using the monochromatic approximation is shown in the second column (M=30$M_\odot$), results obtained using several extended distributions are shown in the following columns. We compare the 68% and 95% marginalized upper limits on $f_{\rm PBH}$ using full Planck and in the photoionization regime for six different EMDs with an equivalent mass of 30$M_\odot$ and the correspondent monochromatic case. We consider lognormal distributions (LN) with $\alpha = 0.2$ and $\{\mu, \sigma\} = \{22.8M_\odot, 0.5\}$ (1) and $\{\mu, \sigma\} = \{10M_\odot, 1.0\}$ (2). We also consider power law distributions with $\alpha = 0.3$ and $\gamma = 0$ with $\{M_{\rm min}, M_{\rm max}\} = \{1M_\odot, 82M_\odot\}$ (1) and $\{M_{\rm min}, M_{\rm max}\} = \{0.01M_\odot, 114M_\odot\}$ (2), and $\gamma = -0.5$ with $\{M_{\rm min}, M_{\rm max}\} = \{1M_\odot, 150M_\odot\}$ (1) and $\{M_{\rm min}, M_{\rm max}\} = \{0.01M_\odot, 564M_\odot\}$ (2). Note how similar the constraints are and how accurate is the monochromatic approximation.

width of a Lognormal mass distribution, μ is constrained to be small. In the case of the Power Law mass distribution, the flatter the distribution (i.e., the larger γ), the stronger the constraint on $f_{\rm PBH}$. In essence, this implies that the constraints on $f_{\rm PBH}$ for EMDs are stronger than for monochromatic distributions. Then, if PBHs are meant to be all the dark matter and have an EMD, this has to be peaked at $M \lesssim 1 - 50M_\odot$, hence the allowed window shrinks.

From eq. (2.7) and the results shown in table 1 it is possible to define a region in the parameter space of the EMDs for which $f_{\rm PBH} \sim 1$ is allowed (dark red in figures 7 and 8). Let us define $M_{\rm lim}$ to be the maximum mass of a monochromatic distribution for which there are no upper limits on $f_{\rm PBH}$ (values reported in table 1). We can then constrain the parameter space of EMDs by imposing $M_{\rm eq} \lesssim M_{\rm lim}$. For Lognormal distributions, there is an analytic solution:

$$\begin{cases} \mu \lesssim M_{\rm lim}, \\ \sigma \lesssim \sqrt{\dfrac{2}{2+\alpha} \log\left(\dfrac{M_{\rm lim}}{\mu}\right)}. \end{cases} \tag{3.1}$$

4 Discussion and conclusions

The presence of a population of PBHs constituting a large fraction of the dark matter (i.e., in what we call ΛPBH model) would have injected radiation in the primordial plasma affecting the Universe's thermal and ionization histories and leaving an imprint on e.g. the CMB. A robustly demonstrated absence of these signatures would put strong limits on the abundance of PBHs of masses $\gtrsim 10M_\odot$ and thus help to exclude a possible dark matter candidate. We find no evidence for the presence of such PBHs with an abundance large enough to be appreciable: $f_{\rm PBH} = 0$ is always inside the 68% confidence region in all the cases considered. However, the sensitivity of present experiments is still not good enough to rule out PBHs in this mass range as a sizeable fraction of the dark matter. Moreover, on the theoretical side, uncertainties in the modelling of processes such as accretion mechanisms of PBH or

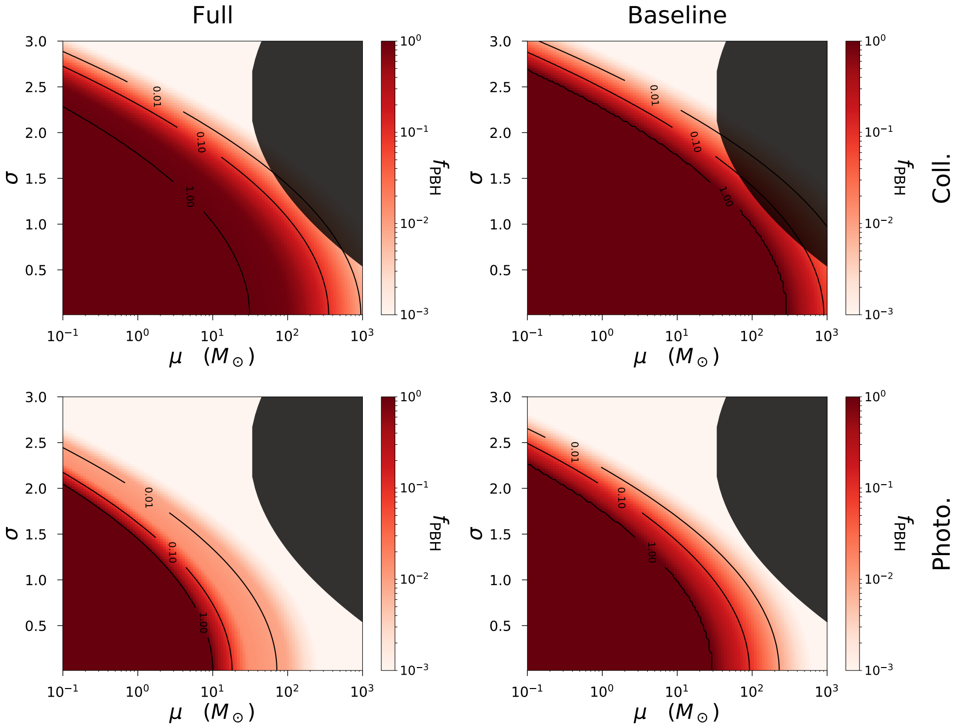

Figure 7. 95% confidence level marginalized constraints on $f_{\rm PBH}$ (in color code) for a Lognormal mass distribution as function of the two parameters of the distribution, μ and σ, in the collisional regime (upper panels) and in the photoionization regime (bottom panels). The black shaded region indicates the values of μ and σ for which EMDs extends beyond $10^4 M_\odot$ (the ratio between the values of the distribution in $M = 10^4 M_\odot$ and in the peak is 10^{-5}), masses for which AHK formalism breaks down and eq. (2.7) is not valid. Left panels: results obtained using full Planck. Right panels: results obtained without including the high ℓ of polarization.

velocity distribution imply that any constraint should be interpreted as an order of magnitude estimate, rather than a precise quantity.

In this work we use the formalism introduced in AHK [36], which assumes spherical accretion and two limiting scenarios in which either collisional or photoionization processes completely dominate. We build on AHK by performing a robust statistical analysis, considering extended mass distributions of PBHs and exploring cosmological parameter degeneracies and the cosmological consequences that a large $f_{\rm PBH}$ would have on other parameters. Beside confirming AHK findings, we note that the current allowed window of $f_{\rm PBH} \sim 1$ for monochromatic populations of PBHs with masses $\sim 10 - 100 M_\odot$ greatly depends on the dataset considered (see figure 1 and table 1). A significant component of the constraining power of CMB observations comes from the high multipoles of polarization power spectrum: the marginalized constraints on $f_{\rm PBH}$ are about ten times stronger when included.

For Planck's recommended baseline data (i.e., not including the high multipoles of polarization power spectrum), CMB observations allow $f_{\rm PBH} \sim 1$ for $M \lesssim 30 M_\odot$ for the most stringent case (photoionization) and $M \lesssim 300 M_\odot$ for the most conservative one (collisional ionization). The inclusion of highℓ polarization data shrinks significantly this window to $M \lesssim$

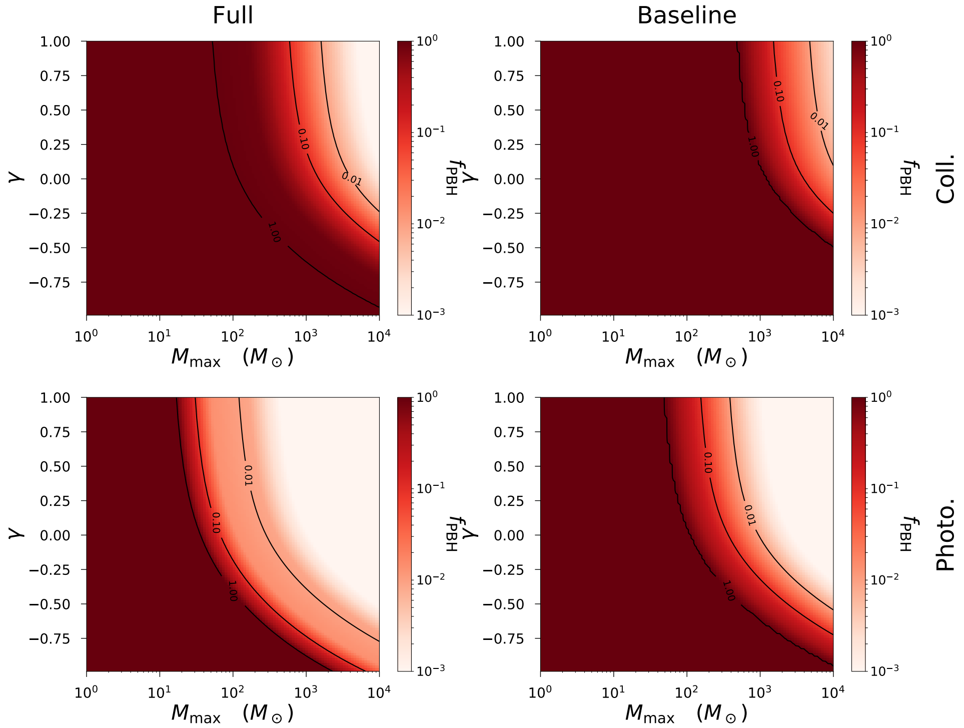

Figure 8. 95% confidence level marginalized constraints on $f_{\rm PBH}$ (in color code) for a Power Law mass distribution as function of two parameters of the distribution, $M_{\rm max}$ and γ, for a fixed $M_{\rm min} = 10^{-2} M_\odot$ in the collisional regime (upper panels) and in the photoionization regime (bottom panels). Left panels: results obtained using full Planck. Right panels: results obtained without including the high ℓ of polarization.

$10 M_\odot$ for photoionization and $M \lesssim 30 M_\odot$ for collisional ionization. The forthcoming release of Planck data with confirmation that the highℓ polarization power spectrum is suitable to be used in extended cosmologies will greatly constrain the models for PBHs and their role as a dark matter component.

We have also investigated degeneracies between $f_{\rm PBH}$ for PBH masses in the allowed ΛPBH model window of $\sim \mathcal{O}(10)\, M_\odot$ to $\sim \mathcal{O}(500)\, M_\odot$ and some cosmological parameters in a ΛPBH cosmology (figures 2 and 3). As expected, we find a large correlation with n_s, which gets stronger for larger $M_{\rm PBH}$, and allows even $n_s \approx 1$. Since future galaxy surveys will measure n_s with astonishing precision, it will become possible to limit this degeneracy and set an indirect constraint on $f_{\rm PBH}$. Interestingly, we find that, compared to the standard $f_{\rm PBH} = 0$ model, a sizeable $f_{\rm PBH}$ would yield a higher sound horizon at radiation drag, $r_{\rm s}$. A joint analysis with BAO would yield a lower value for H_0. Therefore a ΛPBH Universe do not ease some of the existing tensions of ΛCDM (and in particular the H_0 one, see e.g., [62]), and possibly even worsen them.

However, a sizeable $f_{\rm PBH}$, if ignored, would bias the determination of $r_{\rm s}$ by ~ 1 Mpc. It is important to note that this shift is non-negligible compared to expected errors in the determination of the BAO distance scale, hence this possibility should be kept in mind when interpreting forthcoming BAO data.

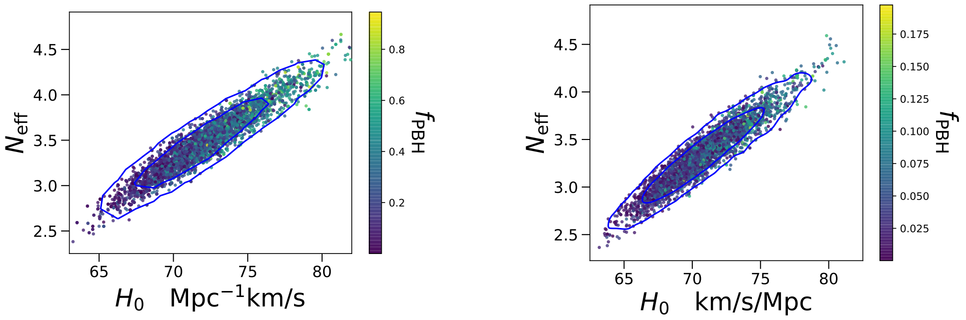

Figure 9. 68% and 95% constraints on the plane $N_{\rm eff}$-H_0 with a color code to express the value of $f_{\rm PBH}$ for collisional ionization and $520M_\odot$ (left) and for photoionization and $100M_\odot$ (right) using the baseline Planck data set. The marginalized constraints on the plane $N_{\rm eff}$-$f_{\rm PBH}$ can be seen in figure 4.

We have shown that the ratios between marginalized upper limits of $f_{\rm PBH}$ for two different data sets do not depend on the assumptions about the ionization regime. Moreover, the ratios between the constraints on $f_{\rm PBH}$ for different ionization regimes do not depend on the inclusion of the high multipoles of polarization power spectrum (table 2). This suggests that using the ratio between marginalized upper limits on $f_{\rm PBH}$ it is possible to isolate effects of specific choices of modelling or data sets, hence our findings can be reinterpreted for different modelling approaches, such as the disk accretion modelling of [39].

If PBHs as dark matter are studied in the framework of popular extensions to ΛCDM, the allowed parameter space is extended because of degeneracies between $f_{\rm PBH}$ and i.e., $N_{\rm eff}$ or the neutrino mass (figure 4). These degeneracies make it possible that PBH as dark matter might be hidden when assuming a ΛCDM background model, by forcing extended parameters to its fiducial values. The degeneracies with the parameters related with the neutrino sector can be explained by the fact that exotic neutrino physics would change the expansion history of the early Universe, therefore changing the epoch of recombination. A larger $f_{\rm PBH}$ requires a larger $N_{\rm eff}$, which yields a higher H_0 CMB-inferred value when ΛCDM+$N_{\rm eff}$ is assumed, as can be seen in figure 9. This could make the CMB inferred value of H_0 fully compatible with direct measurements [62, 64–66].

Finally, we successfully test the approach proposed in [50] to convert constraints computed for monochromatic distributions into constraints for EMDs in the case of CMB observations. Given the simplicity of the approach and the performance, we advocate using it to quickly get precise estimate for any EMD. We also present constraints on the properties of popular EMDs, as to being consistent with current CMB data.

Following this approach, we compute 95% confidence level upper limits on $f_{\rm PBH}$ as function of the parameters of the EMDs (figures 7 and 8). We find that CMB sets strong constraints on $f_{\rm PBH}$ for EMDs that extends towards large masses. If one takes into account microlensing constraints (which constrain PBHs in the $M \lesssim 1 - 10M_\odot$ range), $f_{\rm PBH} \sim 1$ and thus a ΛPBH cosmology is allowed only for narrow EMDs and only if most conservative assumptions and data are considered.

We eagerly await the release of the final Planck highℓ polarization data: in combination with other constraints it will be key to boost or rule out the hypothesis of PBHs as dark matter.

Acknowledgments

We thank Yacine Ali-Haïmoud for sharing his modified version of HyRec with us and for valuable discussions which help to improve this work. We also thank Valerie Domcke, Tommi Tenkanen, Julian B. Muñoz, Enrico Barausse and Ely Kovetz for useful comments on this manuscript. Funding for this work was partially provided by the Spanish MINECO under projects AYA2014-58747-P AEI/FEDER UE and MDM-2014-0369 of ICCUB (Unidad de Excelencia Maria de Maeztu). JLB is supported by the Spanish MINECO under grant BES-2015-071307, co-funded by the ESF. NB is supported by the Spanish MINECO under grant BES-2015-073372. AR has received funding from the People Programme (Marie Curie Actions) of the European Union H2020 Programme under REA grant agreement number 706896 (COSMOFLAGS). LV acknowledges support of European Union's Horizon 2020 research and innovation programme (BePreSySe, grant agreement 725327) and thanks the Radcliffe Institute for Advanced Study at Harvard University for hospitality.

Based on observations obtained with Planck (http://www.esa.int/Planck), an ESA science mission with instruments and contributions directly funded by ESA Member States, NASA, and Canada.

References

[1] Y.B. Zel'dovich and I.D. Novikov, *The hypothesis of cores retarded during expansion and the hot cosmological model*, *Sov. Astron.* **10** (1967) 602.

[2] G.F. Chapline, *Cosmological effects of primordial black holes*, *Nature* **253** (1975) 251.

[3] MACHO, EROS collaboration, C. Alcock et al., *EROS and MACHO combined limits on planetary mass dark matter in the galactic halo*, *Astrophys. J.* **499** (1998) L9 [`astro-ph/9803082`] [INSPIRE].

[4] C. Flynn, A. Gould and J.N. Bahcall, *Hubble deep field constraint on baryonic dark matter*, *Astrophys. J.* **466** (1996) L55 [`astro-ph/9603035`] [INSPIRE].

[5] B.J. Carr and M. Sakellariadou, *Dynamical constraints on dark compact objects*, *Astrophys. J.* **516** (1999) 195 [INSPIRE].

[6] P.N. Wilkinson et al., *Limits on the cosmological abundance of supermassive compact objects from a search for multiple imaging in compact radio sources*, *Phys. Rev. Lett.* **86** (2001) 584 [`astro-ph/0101328`] [INSPIRE].

[7] G. Jungman, M. Kamionkowski and K. Griest, *Supersymmetric dark matter*, *Phys. Rept.* **267** (1996) 195 [`hep-ph/9506380`] [INSPIRE].

[8] G. Arcadi et al., *The waning of the WIMP? A review of models, searches and constraints*, `arXiv:1703.07364` [INSPIRE].

[9] VIRGO, LIGO SCIENTIFIC collaboration, B.P. Abbott et al., *Observation of gravitational waves from a binary black hole merger*, *Phys. Rev. Lett.* **116** (2016) 061102 [`arXiv:1602.03837`] [INSPIRE].

[10] S. Bird et al., *Did LIGO detect dark matter?*, *Phys. Rev. Lett.* **116** (2016) 201301 [`arXiv:1603.00464`] [INSPIRE].

[11] M. Sasaki, T. Suyama, T. Tanaka and S. Yokoyama, *Primordial black hole scenario for the gravitational-wave event GW150914*, *Phys. Rev. Lett.* **117** (2016) 061101 [`arXiv:1603.08338`] [INSPIRE].

[12] S. Clesse and J. García-Bellido, *The clustering of massive primordial black holes as dark matter: measuring their mass distribution with advanced LIGO*, Phys. Dark Univ. **15** (2017) 142 [`arXiv:1603.05234`] [INSPIRE].

[13] K. Kohri, T. Nakama and T. Suyama, *Testing scenarios of primordial black holes being the seeds of supermassive black holes by ultracompact minihalos and CMB μ-distortions*, Phys. Rev. **D 90** (2014) 083514 [`arXiv:1405.5999`] [INSPIRE].

[14] J.L. Bernal, A. Raccanelli, J. Silk, E. Kovetz and L. Verde, *Primordial black holes as seeds of super massive black holes*, in preparation.

[15] J. Silk, *Feedback by massive black holes in gas-rich dwarf galaxies*, Astrophys. J. **839** (2017) L13 [`arXiv:1703.08553`] [INSPIRE].

[16] A. Raccanelli, E.D. Kovetz, S. Bird, I. Cholis and J.B. Muñoz, *Determining the progenitors of merging black-hole binaries*, Phys. Rev. **D 94** (2016) 023516 [`arXiv:1605.01405`] [INSPIRE].

[17] A. Raccanelli, *Gravitational wave astronomy with radio galaxy surveys*, Mon. Not. Roy. Astron. Soc. **469** (2017) 656 [`arXiv:1609.09377`] [INSPIRE].

[18] A. Raccanelli, F. Vidotto and L. Verde, *Effects of primordial black holes quantum gravity decay on galaxy clustering*, `arXiv:1708.02588` [INSPIRE].

[19] I. Cholis et al., *Orbital eccentricities in primordial black hole binaries*, Phys. Rev. **D 94** (2016) 084013 [`arXiv:1606.07437`] [INSPIRE].

[20] E.D. Kovetz, I. Cholis, P.C. Breysse and M. Kamionkowski, *Black hole mass function from gravitational wave measurements*, Phys. Rev. **D 95** (2017) 103010 [`arXiv:1611.01157`] [INSPIRE].

[21] J.B. Muñoz, E.D. Kovetz, L. Dai and M. Kamionkowski, *Lensing of fast radio bursts as a probe of compact dark matter*, Phys. Rev. Lett. **117** (2016) 091301 [`arXiv:1605.00008`] [INSPIRE].

[22] B. Carr, M. Raidal, T. Tenkanen, V. Vaskonen and H. Veermäe, *Primordial black hole constraints for extended mass functions*, Phys. Rev. **D 96** (2017) 023514 [`arXiv:1705.05567`] [INSPIRE].

[23] F. Kühnel and K. Freese, *Constraints on primordial black holes with extended mass functions*, Phys. Rev. **D 95** (2017) 083508 [`arXiv:1701.07223`] [INSPIRE].

[24] K. Schutz and A. Liu, *Pulsar timing can constrain primordial black holes in the LIGO mass window*, Phys. Rev. **D 95** (2017) 023002 [`arXiv:1610.04234`] [INSPIRE].

[25] Y. Ali-Haïmoud, E.D. Kovetz and M. Kamionkowski, *The merger rate of primordial-black-hole binaries*, `arXiv:1709.06576` [INSPIRE].

[26] E.D. Kovetz, *Probing primordial-black-hole dark matter with gravitational waves*, Phys. Rev. Lett. **119** (2017) 131301 [`arXiv:1705.09182`] [INSPIRE].

[27] K. Griest, A.M. Cieplak and M.J. Lehner, *Experimental limits on primordial black hole dark matter from the first 2 yr of kepler data*, Astrophys. J. **786** (2014) 158 [`arXiv:1307.5798`] [INSPIRE].

[28] H. Niikura et al., *Microlensing constraints on primordial black holes with the Subaru/HSC Andromeda observation*, `arXiv:1701.02151` [INSPIRE].

[29] EROS-2 collaboration, P. Tisserand et al., *Limits on the Macho Content of the Galactic Halo from the EROS-2 survey of the magellanic clouds*, Astron. Astrophys. **469** (2007) 387 [`astro-ph/0607207`] [INSPIRE].

[30] S. Calchi Novati, S. Mirzoyan, P. Jetzer and G. Scarpetta, *Microlensing towards the SMC: a new analysis of OGLE and EROS results*, Mon. Not. Roy. Astron. Soc. **435** (2013) 1582 [`arXiv:1308.4281`] [INSPIRE].

[31] E. Mediavilla et al., *Microlensing-based estimate of the mass fraction in compact objects in lens*, *Astrophys. J.* **706** (2009) 1451 [`arXiv:0910.3645`] [INSPIRE].

[32] D.P. Quinn et al., *On the reported death of the MACHO era*, *Mon. Not. Roy. Astro. Soc. Lett.* **396** (2009) L11 [`arXiv:0903.1644`].

[33] T.D. Brandt, *Constraints on MACHO dark matter from compact stellar systems in ultra-faint dwarf galaxies*, *Astrophys. J.* **824** (2016) L31 [`arXiv:1605.03665`] [INSPIRE].

[34] D. Gaggero et al., *Searching for primordial black holes in the radio and X-ray sky*, *Phys. Rev. Lett.* **118** (2017) 241101 [`arXiv:1612.00457`] [INSPIRE].

[35] G. Giesen, J. Lesgourgues, B. Audren and Y. Ali-Haimoud, *CMB photons shedding light on dark matter*, *JCAP* **12** (2012) 008 [`arXiv:1209.0247`] [INSPIRE].

[36] Y. Ali-Haïmoud and M. Kamionkowski, *Cosmic microwave background limits on accreting primordial black holes*, *Phys. Rev.* **D 95** (2017) 043534 [`arXiv:1612.05644`] [INSPIRE].

[37] PLANCK collaboration, P.A.R. Ade et al., *Planck 2015 results. XIII. Cosmological parameters*, *Astron. Astrophys.* **594** (2016) A13 [`arXiv:1502.01589`] [INSPIRE].

[38] M. Ricotti, J.P. Ostriker and K.J. Mack, *Effect of primordial black holes on the Cosmic Microwave Background and cosmological parameter estimates*, *Astrophys. J.* **680** (2008) 829 [`arXiv:0709.0524`] [INSPIRE].

[39] V. Poulin, P.D. Serpico, F. Calore, S. Clesse and K. Kohri, *Squeezing spherical cows: CMB bounds on disk-accreting massive Primordial Black Holes*, `arXiv:1707.04206` [INSPIRE].

[40] B.J. Carr, *The primordial black hole mass spectrum*, *Astrophys. J* **201** (1975) 1.

[41] S.W. Hawking, *Black holes from cosmic strings*, *Phys. Lett.* **B 231** (1989) 237.

[42] S.W. Hawking, I.G. Moss and J.M. Stewart, *Bubble collisions in the very early universe*, *Phys. Rev.* **D 26** (1982) 2681.

[43] S. Clesse and J. García-Bellido, *Massive primordial black holes from hybrid inflation as dark matter and the seeds of galaxies*, *Phys. Rev.* **D 92** (2015) 023524 [`arXiv:1501.07565`] [INSPIRE].

[44] M.W. Choptuik, *Universality and scaling in gravitational collapse of a massless scalar field*, *Phys. Rev. Lett.* **70** (1993) 9 [INSPIRE].

[45] J.C. Niemeyer and K. Jedamzik, *Near-critical gravitational collapse and the initial mass function of primordial black holes*, *Phys. Rev. Lett.* **80** (1998) 5481 [`astro-ph/9709072`] [INSPIRE].

[46] I. Musco, J.C. Miller and L. Rezzolla, *Computations of primordial black hole formation*, *Class. Quant. Grav.* **22** (2005) 1405 [`gr-qc/0412063`] [INSPIRE].

[47] I. Musco, J.C. Miller and A.G. Polnarev, *Primordial black hole formation in the radiative era: investigation of the critical nature of the collapse*, *Class. Quant. Grav.* **26** (2009) 235001 [`arXiv:0811.1452`] [INSPIRE].

[48] I. Musco and J.C. Miller, *Primordial black hole formation in the early universe: critical behaviour and self-similarity*, *Class. Quant. Grav.* **30** (2013) 145009 [`arXiv:1201.2379`] [INSPIRE].

[49] B. Carr, F. Kuhnel and M. Sandstad, *Primordial Black Holes as Dark Matter*, *Phys. Rev.* **D 94** (2016) 083504 [`arXiv:1607.06077`] [INSPIRE].

[50] N. Bellomo, J.L. Bernal, A. Raccanelli and L. Verde, *Primordial black holes as dark matter: converting constraints from monochromatic to extended mass distributions*, `arXiv:1709.07467` [INSPIRE].

[51] A.M. Green, *Microlensing and dynamical constraints on primordial black hole dark matter with an extended mass function*, *Phys. Rev.* **D 94** (2016) 063530 [`arXiv:1609.01143`] [INSPIRE].

[52] J. Lesgourgues, *The Cosmic Linear Anisotropy Solving System (CLASS) I: overview*, `arXiv:1104.2932` [INSPIRE].

[53] D. Blas, J. Lesgourgues and T. Tram, *The Cosmic Linear Anisotropy Solving System (CLASS) II: approximation schemes*, *JCAP* **07** (2011) 034 [`arXiv:1104.2933`] [INSPIRE].

[54] Y. Ali-Haimoud and C.M. Hirata, *Ultrafast effective multi-level atom method for primordial hydrogen recombination*, *Phys. Rev.* **D 82** (2010) 063521 [`arXiv:1006.1355`] [INSPIRE].

[55] Y. Ali-Haimoud and C.M. Hirata, *HyRec: A fast and highly accurate primordial hydrogen and helium recombination code*, *Phys. Rev.* **D 83** (2011) 043513 [`arXiv:1011.3758`] [INSPIRE].

[56] B. Audren, J. Lesgourgues, K. Benabed and S. Prunet, *Conservative constraints on early cosmology: an illustration of the Monte Python cosmological parameter inference code*, *JCAP* **02** (2013) 001 [`arXiv:1210.7183`] [INSPIRE].

[57] PLANCK collaboration, N. Aghanim et al., *Planck 2015 results. XI. CMB power spectra, likelihoods and robustness of parameters*, *Astron. Astrophys.* **594** (2016) A11 [`arXiv:1507.02704`] [INSPIRE].

[58] PLANCK collaboration, N. Aghanim et al., *Planck intermediate results. XLVI. Reduction of large-scale systematic effects in HFI polarization maps and estimation of the reionization optical depth*, *Astron. Astrophys.* **596** (2016) A107 [`arXiv:1605.02985`] [INSPIRE].

[59] M. Ricotti, *Bondi accretion in the early universe*, *Astrophys. J.* **662** (2007) 53 [`arXiv:0706.0864`] [INSPIRE].

[60] M. Raidal, V. Vaskonen and H. Veermäe, *Gravitational waves from primordial black hole mergers*, *JCAP* **09** (2017) 037 [`arXiv:1707.01480`] [INSPIRE].

[61] A.G. Riess et al., *A 2.4% determination of the local value of the Hubble constant*, *Astrophys. J.* **826** (2016) 56 [`arXiv:1604.01424`] [INSPIRE].

[62] J.L. Bernal, L. Verde and A.G. Riess, *The trouble with* H_0, *JCAP* **10** (2016) 019 [`arXiv:1607.05617`] [INSPIRE].

[63] L. Verde, J.L. Bernal, A.F. Heavens and R. Jimenez, *The length of the low-redshift standard ruler*, *Mon. Not. Roy. Astron. Soc.* **467** (2017) 731 [`arXiv:1607.05297`] [INSPIRE].

[64] C.L. Bennett, D. Larson, J.L. Weiland and G. Hinshaw, *The 1% concordance Hubble constant*, *Astrophys. J.* **794** (2014) 135 [`arXiv:1406.1718`] [INSPIRE].

[65] G. Efstathiou, *H0 revisited*, *Mon. Not. Roy. Astron. Soc.* **440** (2014) 1138 [`arXiv:1311.3461`] [INSPIRE].

[66] W.L. Freedman, *Cosmology at a crossroads*, *Nature Astron.* **1** (2017) 0121.

4. The next frontier for large scale structure

This Chapter discusses the great potential of future LSS surveys to probe and constrain deviations from ΛCDM through the study of clustering, focusing on radio-continuum surveys and intensity mapping experiments. The article Bernal et al. (2019) and the work in progress that is currently under collaboration review and soon will be submitted, Bernal et al. (2019a) and Bernal et al. (2019b), are included below.

Galaxy surveys, and LSS experiments in general, will live a golden era during the next decade. Several next-generation experiments (e.g., DESI, Euclid) will start surveying the sky in the coming years, with already planned projects ready to take over after they finish (e.g., SKA, LSST). This huge experimental effort will return game-changing observations and push the envelope of observational cosmology. Upcoming experiments will improve current surveys both in depth and sky coverage. For instance, DESI will reach $z \sim 1.7$ using spectroscopic observations of emission line galaxies (and $z \sim 3.5$ using the Lyman-α forest) covering 14000 deg^2 of the sky (DESI Collaboration et al., 2016a), while SKA will reach $z \sim 3$ in its HI galaxy survey (and $z \sim 5$ in its radio-continuum galaxy survey) being an all-sky survey (Square Kilometre Array Cosmology Science Working Group et al., 2018). These specifications of future galaxy surveys are to be compared with the 10000 deg^2 of the sky at $0.15 \lesssim z \lesssim 0.7$ and $2 \lesssim z \lesssim 3.2$ probed by BOSS. As a consequence, 30 million galaxies and quasars and 100 million galaxies are expected to be detected by DESI and SKA, respectively (to be compared with the 1.2 million galaxies used by BOSS, Alam et al. (2017b)).

Given the promising potential of future experiments to significantly improve the current state of the art, the survey strategy and the methodology to analyze the observations must be studied to optimize the extraction of cosmological information from the measurements, and avoid systematics or any other source of bias. In addition, thanks to the huge increase in the volumes probed, these surveys will have access for the first time to scales close to the horizon, where imprints of both the very early Universe (i.e., deviations from Gaussianity in the primordial density fluctuations) and relativistic corrections may dominate the signal (see e.g., Raccanelli et al. (2017) and Bertacca et al. (2012), respectively).

In Bernal et al. (2019), we estimate the potential of the Evolutionary Map of the Universe, an all-sky radio-continuum survey, to constrain models beyond ΛCDM. Radio-continuum experiments average the received radiation over all frequencies. This makes possible to survey the sky deeper and faster than photometric or spectroscopic surveys to achieve similar signal-to-noise ratio, yielding a larger number of sources (i.e., galaxies) surpassing the detection threshold. However, due to the average over frequencies, radio-continuum surveys cannot extract redshift information from their observations. Hence the need of external data to infer galaxy redshifts. The lack of precise redshift measurements forces us to project the galaxies along the line of sight, and use the angular power spectrum to measure galaxy clustering. In this work, both galaxy clustering and Integrated Sachs-Wolfe effect measurements are considered to forecast future constraints for EMU and SKA. Furthermore, multitracer techniques and different survey strategies are explored in order to maximize EMU's constraining power on the cosmological parameters. This work, carried out in collaboration with Alvise Raccanelli, Ely D. Kovetz, David Parkinson, Ray P. Norris, George Danforth and Courney Schmitt, was published in the Journal of Cosmology and Astroparticle Physics (JCAP) in February 2019.

On the other hand, if easy-to-identify lines in the received spectra are targeted (rather than averaging over all frequencies as radio-continuum experiments), tuning the frequency of the telescope facilitates precise redshift measurements. Afterwards, it is possible to use only the brightest resolved sources, those above a given detection threshold, and carry out a galaxy survey. However, it is also possible to use all the light received by the telescope and trace the underlying matter distribution with the measured radiation intensity (or brightness temperature) in a given frequency. This is what intensity mapping techniques propose. Since no individual source identification is needed, and faint sources are added to the measured intensity, much larger redshifts are accesible to intensity mapping. Therefore, intensity mapping is able to probe LSS at earlier times than any galaxy survey will ever reach.

In Bernal et al. (2019b), we provide an optimal methodology to analyze intensity mapping observations and optimize the extraction of cosmological information from the experiments without introducing any bias, and taking into account cosmological and astrophysical uncertainties. In the companion manuscript, Bernal et al. (2019a), we apply this methodology to planned and future intensity mapping experiments and highlight the great potential of these observations to measure the BAO scale and constrain the expansion history in regimes where there is no cosmological probe yet, as the epoch of reionization. On the other hand, in These two works, done in collaboration with Patrick Breysse, Ely D. Kovetz, and Héctor Gil-Marín (in the former) are currently under collaboration review, and will soon be submitted to Physical Review Letters and Physical Review D, respectively.

Altogether, the research included in this Chapter will guide the EMU collaboration and future intensity mapping experiments to use concrete survey strategies, depending on the priorities of each collaboration. Thus, it will be possible to maximize the cosmological information obtained from their observations.

Journal of Cosmology and Astroparticle Physics
An IOP and SISSA journal

Probing ΛCDM cosmology with the Evolutionary Map of the Universe survey

José Luis Bernal,[a,b] **Alvise Raccanelli,**[d,a,c] **Ely D. Kovetz,**[c]
David Parkinson,[e] **Ray P. Norris,**[f,g] **George Danforth**[c]
and Courtney Schmitt[c]

[a]ICC, University of Barcelona, IEEC-UB,
Martí i Franquès, 1, E08028, Barcelona, Spain
[b]Departament de Física Quàntica i Astrofísica, Universitat de Barcelona,
Martí i Franquès 1, E08028 Barcelona, Spain
[c]Department of Physics & Astronomy, Johns Hopkins University,
3400 N. Charles St., Baltimore, MD 21218, U.S.A.
[d]Theoretical Physics Department, CERN,
1 Esplanade des Particules, CH-1211 Geneva 23, Switzerland
[e]Korea Astronomy and Space Science Institute,
Yuseong-gu, Daedeok-daero 776, Daejeon 34055, Korea
[f]Western Sydney University, Locked Bag 1797, Penrith South, NSW 1797, Australia
[g]CSIRO Astronomy & Space Science, P.O. Box 76, Epping, NSW 1710, Australia
E-mail: joseluis.bernal@icc.ub.edu, alvise.raccanelli@cern.ch, ekovetz1@jhu.edu,
davidparkinson@kasi.re.kr, raypnorris@gmail.com, gdanfor1@jhu.edu,
cschmit6@jhu.edu

Received October 19, 2018
Accepted January 31, 2019
Published February 14, 2019

Abstract. The Evolutionary Map of the Universe (EMU) is an all-sky survey in radio-continuum which uses the Australian SKA Pathfinder (ASKAP). Using galaxy angular power spectrum and the integrated Sachs-Wolfe effect, we study the potential of EMU to constrain models beyond ΛCDM (i.e., local primordial non-Gaussianity, dynamical dark energy, spatial curvature and deviations from general relativity), for different design sensitivities. We also include a multi-tracer analysis, distinguishing between star-forming galaxies and galaxies with an active galactic nucleus, to further improve EMU's potential. We find that EMU could measure the dark energy equation of state parameters around 35% more precisely than existing constraints, and that the constraints on $f_{\rm NL}$ and modified gravity parameters will improve up to a factor ~ 2 with respect to Planck and redshift space distortions measurements. With this work we demonstrate the promising potential of EMU to contribute to our understanding of the Universe.

https://doi.org/10.1088/1475-7516/2019/02/030

Keywords: cosmological parameters from LSS, power spectrum, redshift surveys

ArXiv ePrint: 1810.06672

Contents

1 Introduction

Our current best description of the large-scale structure of the Universe relies on the standard cosmological model, Λ-Cold Dark Matter (ΛCDM), which posits that the energy density at present times is dominated by a cosmological constant and that the matter sector is composed mostly of dark matter. Although this model reproduces astonishingly well most observations [1, 2], there are still some persistent tensions, especially on the Hubble constant between direct local measurements [3, 4] and the Planck-inferred value assuming ΛCDM [1], which has been widely studied in the literature (see e.g., [5–10]). Moreover, there are also some theoretical issues within the model, such as the value of the cosmological constant, the nature of dark matter and dark energy, an accurate description of inflation and the scale of validity of General Relativity. All this motivates the development and study of models beyond ΛCDM+GR.

Up to this date, the strongest constraints on the parameters of ΛCDM have come from Cosmic Microwave Background (CMB) observations. However, the Planck satellite has almost saturated the cosmic variance limit in the measurement of the CMB temperature power spectrum. Moreover, low redshift observations are required in order to constrain models which extend ΛCDM to explain cosmic acceleration; in these cases, galaxy surveys are as of now the most powerful probe. The golden era of galaxy surveys is about to start, with some of the next generation experiments already observing or beginning in 2019. A huge experimental effort will provide game-changing galaxy catalogs, thanks to which galaxy-survey cosmology will reach full maturity. Contrary to photometric or spectroscopic surveys, radio-continuum surveys average over all frequency data to have larger signal to noise for each individual source, which enables them to deeply scan large areas of the sky very quickly and detect faint sources at high redshifts. This allows the detection of large number of galaxies, but with only minimal redshift information.

Radio surveys have been used for cosmological studies in the past, mainly with NVSS [11] (see e.g., [12–25]). Studies of cosmological models and beyond-ΛCDM parameter constraints using next generation radio surveys were spearheaded in [26] and then followed by subsequent works such as e.g., [27–37]. Forthcoming radio-continuum surveys have the unique ability to survey very large parts of the sky up to high-redshift, being therefore able to probe an unexplored part of the instrumental parameters space, not accessible to optical surveys for at least another decade. Thus, surveys like the Evolutionary Map of the Universe (EMU) and the Square Kilometer Array (SKA) continuum will be optimal for tests of non-Gaussianity, ultra-large scale effects and cosmic acceleration models, as we will see below.

EMU [38] is an all-sky radio-continuum survey using the Australian SKA Pathfinder (ASKAP) radio telescope [39–41]. Although ASKAP was planned as a precursor of SKA to test and develop the needed technology, it is a powerful telescope in its own right. In this work we aim to evaluate the potential of EMU as a cosmological survey, and in particular how powerful it can be in constraining extensions of ΛCDM. We pay special attention to primordial non-Gaussianity (PNG), since it manifests in the galaxy power spectrum on very large scales, accessible only by surveys like EMU, with large fractions of the sky observed. Constraining PNG is one of the few ways to observationally probe the epoch of inflation, and a precise measurement of its parameters might rule out a large fraction of inflationary models (e.g., slow-roll single-field inflation generally predicts small PNG, $f_{\rm NL} \ll 1$ for local PNG [42–44]). Therefore, we explore if EMU will be able to detect deviations from Gaussian initial conditions in the local limit below $f_{\rm NL} \lesssim 1$ [45]. Besides PNG, we also study a model of dark energy whose equation of state evolves with redshift; a model which does not fix the spatial curvature to be flat; and phenomenological, scale-independent modifications of General Relativity (GR).

Given the lack of detailed redshift information, the main observable to be used with continuum radio surveys is the full shape of the angular galaxy power spectrum. Besides considering the whole sample altogether, we also take advantage of the expected broad distribution of sources in redshift and the potential of machine-learning redshift measurements (e.g. [46, 47]) and clustering-based redshifts obtained by cross correlating EMU's sample with spectroscopic catalogues [48, 49] (whose performance in cosmological surveys was estimated in [50]). These methods will enable to split the sample into several redshift bins, and therefore we consider a second case where we use five redshift bins. We leave the determination of the best strategy to the EMU redshift group. In addition to the auto and cross angular power spectra among all possible combination of redshift bins, we use the Integrated Sachs-Wolfe (ISW) effect by cross correlating the galaxies observed by EMU in each redsfhit bin with the CMB.

This paper is organized as follows: in section 2 we discuss the relevant specifications of EMU and the estimated quantities required to compute the galaxy power spectrum, such as the source redshift distribution or galaxy bias; in section 3 we explain the observables considered and the models studied, and describe the methodology used; results are discussed in section 4. We conclude in section 5. A detailed and comprehensive report of the results can be found in appendix A, and a comparison between using T-RECS [51] or S^3 [52] can be read in appendix B.

2 EMU

The main goal of EMU is to make a deep radio-continuum survey throughout the entire Southern sky reaching $\delta = +30°$. This is roughly the same area covered by NVSS [11], but approximately 45 times more sensitive and with 4.5 times better angular resolution (it has a design sensitivity of 10 μJy/beam rms and 10 arc-sec resolution). It is expected to observe around 70 million galaxies by the end of the survey. Thanks to these advantages, and especially to the large fraction of the sky scanned and the depth of the survey, EMU (and future experiments of SKA) will be key for the study of galaxy clustering at very large scales. The corresponding catalog and the rest of radio data will be published once their quality has been assured.

We consider four different realizations of EMU, to compare the effectiveness of each:

- Design standard EMU: observing 30000 deg^2 of the sky (corresponding to a fraction of the whole sky $f_{\rm sky} = 0.727$), with a sensitivity of 10 μJy/beam rms.
- Pessimistic EMU: the same areal coverage (30000 deg^2), with a sensitivity of 20 μJy/beam rms.
- EMU-early: an early stage of the survey with only 2000 deg^2 surveyed and 100 μJy/beam rms.
- SKA-2 *like* survey: observing 30000 deg^2 of the sky with 1 μJy/beam rms, to compare it with the design sensitivity of EMU.

Like most of the studies regarding radio surveys, we adopt a 5σ threshold for a source to be detected.

We use the Tiered Radio Extragalactic Continuum Simulation (T-RECS) [51] to estimate the galaxy number density distribution as a function of redshift of both star forming galaxies (SFG) and galaxies with active galactic nucleus (AGN) and the corresponding galaxy and magnification biases. Throughout most of this paper, we work with the two population of galaxies together forming a single sample. However, we also estimate the gain of computing the auto power spectra of each population and their cross power spectrum using the multi-tracer technique [53, 54]. Although some studies distinguish between five different populations subdiving AGNs and SFGs (e.g., [32]), we prefer to be conservative and avoid that subdivision, since its robustness given the observational conditions is not very well quantified.

As discussed above, the redshift determination of the galaxies observed by EMU, as a radio-continuum survey, will be very poor. This prevents the use of EMU to measure radial baryon acoustic oscillations or redshift space distortions, without precise external redshift information. Without any external data, it is not possible to determine the redshift of the sources and so bin the galaxy catalogue in redshift. Therefore, we consider a case with a single redshift bin covering the whole galaxy sample observed by EMU. Nonetheless, binning in redshift and using auto and cross correlations between the galaxies of all possible combinations of redshift bins improves significantly the performance of a galaxy survey. We make a conservative choice and use five wide redshift bins with Gaussian window functions whose width is equal to the half width of the redshift bin, assuming that external data sets and the methodologies to infer the redshift are complete and mature enough to do so. Nonetheless, one should keep in mind that uncertainties in the galaxy properties as the galaxy bias degrades the quality of the inferred redshifts. We leave the study of the best redshift binning

JCAP02(2019)030

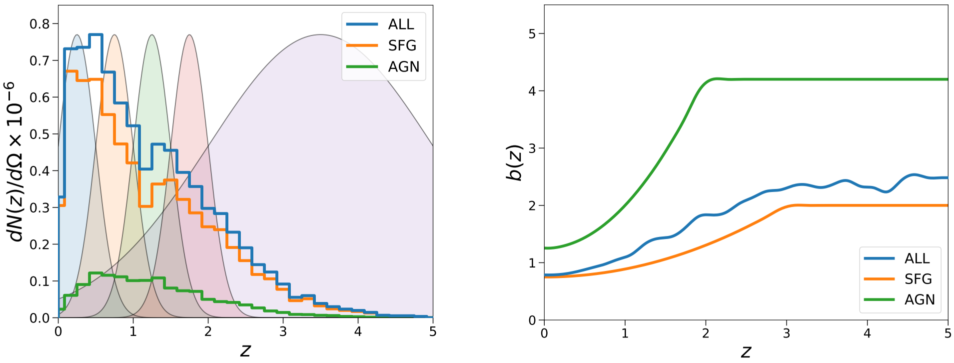

Figure 1. *Left*: $dN/dzd\Omega$ for the galaxies observed assuming a rms flux/beam of 10μJy, always requiring a 5-σ detection. We also plot the Gaussian window functions of the five redshift bins considered to compute the cosmological observables. *Right* theoretical galaxy bias for SFGs and AGNs and the corresponding weighted total. We show the quantities related to the whole sample in blue, with SFGs in orange and with AGNs in green.

strategy of EMU's observed galaxies for future work. We show the total number density redshift distribution of galaxies, $dN/dzd\Omega$, for each galaxy population and for the complete sample at design sensitivity in the left panel of figure 1, along with the corresponding Gaussian windows used for each redshift bin when computing the observables (see section 3.1).

In addition to modeling the galaxy redshift distribution, we need to model both the galaxy and magnification bias of our sample. We assume a different scale-independent galaxy bias model, which increases the bias monotonically with redshift, for each galaxy population in T-RECS. However, this trend becomes unphysical at high enough redshift, so here we follow [55] and keep a constant bias above a cut-off redshift. The true dependence of bias with redshfit at high-redshift, low-luminosity galaxies (where most of them are still undetected) is still unknown. On the other hand, the authors of [32] argue that the high-redshift cut-off is not physical. The choice of bias model is therefore a source of uncertainty, degenerate with the redshift distribution (see section 3.1 for further discussion). In order to compute the galaxy bias of the whole galaxy sample, we use the number-weighted average of both populations: $b(z) = [b_{\rm sfg}(z)N_{\rm sfg}(z) + b_{\rm agn}(z)N_{\rm agn}(z)]/N_{\rm all}(z)$. We show the galaxy bias of SFGs, AGNs and the whole sample assuming 10 μJy/beam rms sensitivity in the right panel of figure 1.

In order to estimate the magnification bias, we use the "observed" magnitudes from T-RECS to get the slope of the cumulative number counts for galaxies brighter than the survey magnitude limit $m_{\rm lim}$ evaluated at $m_{\rm lim}$ [56–58]:

$$s(z) = \frac{\partial}{\partial m}\left[\log_{10} n_{\rm cum}(m,z)\right]\Big|_{m_{\rm lim}} , \tag{2.1}$$

where $n_{\rm cum}$ is the cumulative number counts of galaxies as function of magnitude. As the number density evolves with redshift, this slope will also change, and so will the magnification bias. We compute the magnification bias for each population and the whole sample in the same way, using the corresponding $n_{\rm cum}(m,z)$ in each case.

3 Forecasts

In this section we describe the cosmological observables included in our forecasts, introduce the models we investigate and review the Fisher matrix formalism used to predict the constraints. In all cases we assume a complete understanding of foregrounds and other sources of observational systematics, which would allow for a clean and precise measurement of galaxy clustering. We use `Multi_CLASS`[1] [59], a modification of the public Boltzmann code `CLASS` [60] which allows to compute the cross power spectra of two different populations, to obtain the theoretical observables.

3.1 Cosmological observables

We aim to estimate the potential of EMU to use galaxy clustering (measuring angular power spectra) to constrain models beyond ΛCDM. In addition, we also consider ISW measurements by cross correlating each redshift bin of our galaxy sample with the CMB. In all cases, we set a conservative cut on the minimum scale included, in order to avoid non linearities and limit the analysis to multipoles within the interval $\ell_{\rm min} \leq \ell \leq 200$. The largest scales considered, $\ell_{\rm min}$, are limited by the fraction of sky surveyed ($f_{\rm sky}$): $\ell_{\rm min} = \pi/(2f_{\rm sky})$. For both observables we also consider the case where SFGs and AGNs can be discriminated, allowing to use multi-tracer techniques.

The galaxy distribution, as we observe it, is affected by gravitational perturbations along the line of sight [61]. Therefore, the total observed overdensity, $\Delta_{\rm obs}$, should include, in addition to the standard redshift-space distortions, large-scale and projection effects, namely lensing magnification, time-delays, ISW, doppler and gravitational potential effects [62–67]. In this work we neglect contributions from gravitational potentials; the interested reader can see the complete model and corresponding signal and contributions from each term for different configurations in e.g., [68]. In our case, the observed galaxy overdensity at a position $\mathbf{n}$ on the sky is computed as [63, 64]:

$$\Delta_{\rm obs}(\mathbf{n},z) = \Delta_\delta(\mathbf{n},z) + \Delta_{\rm rsd}(\mathbf{n},z) + \Delta_\kappa(\mathbf{n},z) + \Delta_{\rm Doppler}(\mathbf{n},z)\,, \tag{3.1}$$

where Δ_δ indicates the galaxy overdensity in the comoving gauge, $\Delta_{\rm rsd}$ accounts for peculiar velocity perturbations and redshift space distortions, Δ_κ contains the lensing convergence, and $\Delta_{\rm Doppler}$ refers to Doppler effects. The latter, although subdominant at small scales, is needed, since it is degenerate with $f_{\rm NL}$ [69]. Each of the terms in equation (3.1) is given by:

$$\begin{aligned}
\Delta_\delta(\mathbf{n},z) &= b(z)\delta_{\rm com}\left[r(z)\mathbf{n},\tau(z)\right]\,,\\
\Delta_{\rm rsd}(\mathbf{n},z) &= \frac{1}{\mathcal{H}(z)}\partial_r(\mathbf{v}\cdot\mathbf{n})\,,\\
\Delta_\kappa(\mathbf{n},z) &= \left[2-5s(z)\right]\kappa\,,\\
\Delta_{\rm Doppler} &= \left[\frac{\mathcal{H}'(z)}{\mathcal{H}^2(z)} + \frac{2-5s(z)}{r(z)\mathcal{H}(z)} + 5s(z) - f_{\rm evo}(z)\right](\mathbf{v}\cdot\mathbf{n})\\
&\quad + \left[3\mathcal{H}(z) - f_{\rm evo}(z)\right]\Delta^{-1}(\nabla\cdot\mathbf{v})\,,
\end{aligned} \tag{3.2}$$

---

[1] `Multi_CLASS` will be publicly available at https://github.com/nbellomo?tab=projects when the corresponding paper is published.

where $\delta_{\rm com}$ is the matter overdensity in the comoving gauge at a distance r and proper time τ, $\mathcal{H}$ is the conformal Hubble parameter, $\mathbf{v}$ is the peculiar velocity, κ is the lensing convergence and $f_{\rm evo}$ is the evolution bias.

Using equations (3.1) and (3.2), we define $\Delta_\ell^{W_{\rm i}}$, the transfer function of the observed number counts at wavenumber k, in the redshift bin i and using a window function $W_{\rm i}$ (Gaussian in our case) for each multipole ℓ, as in [70]. We refer the interested reader to appendix A of [67] for details on the calculation of $\Delta_\ell^{W_i}$. With all these pieces, the observed angular power spectrum of galaxies in redshift bins $\{i, j\}$ is given by:

$$C_\ell^{\rm ij} = 4\pi \int \frac{dk}{k} \Delta_\ell^{W_{\rm i}}(k) \Delta_\ell^{W_{\rm j}}(k) P_0(k)\,, \tag{3.3}$$

where $P_0(k)$ is the primordial power spectrum. Note that when two non-overlapping bins are cross correlated, the distance is too large to have a significant contribution from intrinsic density clustering (i.e., coming from $\Delta_{\ell,\delta}^{W_{\rm i}} \Delta_{\ell,\delta}^{W_{\rm j}}$). However, we do observe a significant cross correlation due to lensing contributions [71]. Concretely, the dominant term is always $\Delta_{\ell,\delta}^{W_{\rm j}} \Delta_{\ell,\kappa}^{W_i} \propto b(z_{\rm j}) s(z_{\rm i})$, which is the correlation between the magnification of background sources due to foreground lenses and the observed overdensities in the background. In some previous studies, magnification has been considered as a different signal than density perturbations (i.e., reporting the constraints from galaxy clustering and from magnification separately). However, this is not a realistic scenario, since these two contributions are difficult to disentangle, so we can only refer to the *observed* galaxy clustering and model the signal properly. The effects of not including the lensing magnification contribution when modeling the signal in a Fisher forecast, even for cosmological parameters that are not affected by gravitational lensing, are studied in [59].

When using the multi-tracer technique, we consider SFGs and AGNs as different galaxy populations, each with their corresponding redshift distribution, galaxy bias and magnification bias. Therefore, in this case we compute auto and cross correlations between different galaxy populations and redshift bins. Equation (3.3) can be modified so it also accounts for the two different galaxy populations. The transfer functions now become $\Delta_\ell^{{\rm X},W_i}$, where the X superscript refers to the type of galaxy, and they are computed as usual, but using the specifications corresponding for each subsample, as discussed in section 2. So, when using multiple tracers, we compute $C_\ell^{\rm X,i;Y,j}$.

In addition to the angular power spectrum, we also use the ISW effect to measure the matter overdensity field. The ISW effect is the gravitational shift that a photon suffers as it passes through matter density fluctuations while the gravitational potential evolves. In an Einstein-de Sitter Universe, where the gravitational potential does not evolve, the blueshift and redshift of the photon falling and going out from a well cancel each other. Nonetheless, if the gravitational potential evolves due to e.g., dark energy or modifications of GR, the cancellation is not perfect, so there is a net change in the photon temperature which accumulates along the photon path.

The ISW effect contributes to the CMB temperature fluctuations, but only on large scales, where the observations are limited by cosmic variance. However, it can also be detected in the cross correlation of the CMB anisotropies and the galaxy distribution. This correlation was detected for the first time almost simultaneously in several works using observations in radio from the NVSS survey [14, 15, 17, 18, 72]; near infra-red from the 2-MASS survey [73] and the APM survey [74]; optical from SDSS [75]; and X-ray for HEAO-I satellite [14].

Equation (3.3) can be used to compute the cross correlations between the galaxy distribution and the CMB anisotropies for each redshift bin of our galaxy catalog, $C_\ell^{\rm iT}$, using $\Delta_\ell^{W_{\rm i}}(k)\Delta_\ell^{W_{\rm T}}(k)$ instead of $\Delta_\ell^{W_{\rm i}}(k)\Delta_\ell^{W_{\rm j}}(k)$, where $\Delta_\ell^{W_{\rm T}}(k)$ is the transfer function for CMB temperature anisotropies. Moreover, one can use multiple tracers and compute the cross correlations of the CMB with each galaxy population separately, in a similar fashion as for the angular galaxy power spectra.

3.2 Models

In this work we focus on popular models beyond the standard model of cosmology, which have one or two extra model parameters, since a low redshift, wide field survey as EMU will help significantly to constrain them thanks to the breaking of degeneracies existing in the CMB measurements. We focus on the following extensions of ΛCDM: a model with local PNG in the distribution of the initial conditions; a model with an evolving dark energy equation of state; a model with scale-independent modifications of General Relativity; and a model where spatial curvature is not fixed to be flat.

3.2.1 Primordial non-Gaussianity

The ultra-large-scale modes of the matter power spectrum have remained outside the horizon since inflation. This is why they might preserve an imprint of primordial deviations from Gaussian initial conditions. Thanks to all-sky surveys, we can access those ultra large scales and probe inflation models with low-redshift observations. We model PNG in the local limit, the easiest case to detect, introducing the parameter $f_{\rm NL}$,[2] defined as the amplitude of the local quadratic contribution of a single Gaussian random field ϕ to the Bardeen potential Φ. We refer to this model as ΛCDM+$f_{\rm NL}$. Other PNG models and the corresponding predicted constraints from a SKA-*like* survey can be found in e.g., [33]. In the limit considered here, the Bardeen potential is obtained as:

$$\Phi(x) = \phi(x) + f_{\rm NL}\left(\phi^2(x) - \langle\phi^2\rangle\right) . \tag{3.4}$$

The quadratic contribution in equation (3.4) introduces skewness in the density probability distribution, which results in a modification of the number of massive objects. This can be modeled as a scale-dependent variation of the galaxy bias [77–80]. If $b_{\rm G}$ is the Gaussian galaxy bias, the total galaxy bias is given by:

$$b(k,z) = b_{\rm G}(z) + \left[b_{\rm G}(z) - 1\right] f_{\rm NL}\delta_{\rm ec}\frac{3\Omega_m H_0^2}{c^2k^2T(k)D(z)} , \tag{3.5}$$

where $\delta_{\rm ec} = 1.68$ is the critical value of the matter overdensity for spherical collapse, Ω_m is the matter density parameter at $z = 0$, $D(z)$ is the linear growth factor (normalized to 1 at $z = 0$) and $T(k)$ is the matter transfer function (which is 1 on large scales). Thus, the deviation from the Gaussian galaxy bias at small k is proportional to $f_{\rm NL}k^{-2}$, hence it contributes significantly only on large scales.

3.2.2 Dynamical dark energy

Dark energy can be modeled with a scalar field, instead of a cosmological constant as in ΛCDM. In that case, the equation of state of dark energy, w, may be different than -1 and

---

[2] here we use the large scale structure convention ($f_{\rm NL}^{\rm LSS} \approx 1.3 f_{\rm NL}^{\rm CMB}$ [76]).

also vary with redshift. The energy density of dark energy is then no longer constant and is given by

$$\rho_{\rm DE}(a) = \rho_{\rm DE,0} \exp\left[-3\int_1^a \frac{1+w(a')}{a'}da'\right] , \tag{3.6}$$

where $\rho_{\rm DE,0}$ is the density of dark energy today. We use the CPL parameterization [81, 82] to model $w(a)$ as:

$$w(a) = w_0 + (1-a)w_a, \tag{3.7}$$

where a is the scale factor. Therefore, we call this model $(w_0 w_a)$CDM.

3.2.3 Modified gravity

Although cosmic acceleration is normally modeled using dark energy, it can also be explained in theory with modifications to gravity. Moreover, GR might be a local approximation, and has only been tested precisely on scales ranging from millimeters to solar-system scales, with a compelling test at horizon scales yet to be done. This is what has motivated the theoretical development of alternative theories to GR, adding degrees of freedom. There is a huge variety of modified gravity theories, although a large fraction of them are ruled out after the recent measurement of the neutron-star merger and gravitational-wave counterpart (see e.g., [83] for an updated review). Moreover, consistency tests of GR using current data do not favour modifications (see e.g., [84]). Nonetheless, GR might not be the correct description of gravity at the ultra-large scales that will be surveyed by EMU. In order to model deviations from GR in a general way, we follow an effective description of the relation between the metric potentials and their relation with the energy density [85, 86]:

$$-2k^2\Psi = 8\pi G_N a^2 \rho\delta_{\rm com}\mu(a,k) , \qquad \frac{\Phi}{\Psi} = \gamma(a,k) , \tag{3.8}$$

where $\mu = \gamma = 1$ are the limiting values corresponding to GR, where ρ (the total energy density) and $\delta_{\rm com}$ are evaluated at a. We only consider scale independent modifications of GR, but there are several possible parameterizations of $\mu(z,k)$ and $\gamma(z,k)$ [1, 87]. We assume that deviations from GR are only significant at low redshifts, so we model them as being proportional to the dark energy density parameter, Ω_Λ

$$\mu(a,k) = 1 + \mu_0\frac{\Omega_\Lambda(a)}{\Omega_{\Lambda,0}}, \qquad \gamma(a,k) = 1 + \gamma_0\frac{\Omega_\Lambda(a)}{\Omega_{\Lambda,0}}, \tag{3.9}$$

where $\Omega_{\Lambda,0}$ is the dark energy density parameter today. Combining equations (3.8) and (3.9), we obtain that with this parameterization ΛCDM with GR corresponds to $\mu_0 = \gamma_0 = 0$. In this work, this model is referred to as ΛCDM+μ_0+γ_0. We follow `MGCLASS`[3] [87] and modify `Multi_CLASS` to include this parameterization of modified gravity in our computations.

Finally, we also consider a model in which the curvature of the spatial sector of the Universe is constant, but not fixed to be zero. We denote this model ΛCDM+Ω_k.

3.3 Fisher matrix formalism

In order to forecast the constraining power of EMU for the models discussed above, we use the Fisher matrix analysis [88, 89]. Accounting for SFGs and AGNs as different tracers of

---

[3] https://gitlab.com/philbull/mgclass

the dark matter field, we define $\tilde{C}_\ell^{\mathrm{X,i;Y,j}}$ as the angular power spectrum plus the shot noise as:

$$\tilde{C}_\ell^{\mathrm{X,i;Y,j}} = C_\ell^{\mathrm{X,i;Y,j}} + \frac{\delta^K_{\mathrm{ij}}\delta^K_{\mathrm{XY}}}{dN(z_{\mathrm{i}})/d\Omega}, \tag{3.10}$$

where δ^K is the Kronecker delta and $dN(z_{\mathrm{i}})/d\Omega$ denotes the average number of sources per steradian in the i-th redshift bin. If we assume a Gaussian likelihood, it is possible to define a covariance matrix for each multipole $\mathcal{C}_\ell$ built by blocks, so if each block is indexed by $\{X, Y\}$, $\left(\mathcal{C}_\ell\right)_{\mathrm{X,Y}} = \tilde{C}_\ell^{\mathrm{XY}}$. Then, each block is built as $\left(\tilde{C}_\ell^{\mathrm{XY}}\right)_{i,j} = \tilde{C}_\ell^{\mathrm{X,i;Y,j}}$. In this way, the Fisher matrix element corresponding to the parameters θ_α and θ_β for the galaxy angular power spectrum is given by:

$$F^{\mathrm{gg}}_{\alpha\beta} = \left\langle \frac{\partial^2 \log \mathcal{L}^{\mathrm{gg}}}{\partial\theta_\alpha \partial\theta_\beta} \right\rangle = f_{\mathrm{sky}} \sum_\ell \frac{2\ell+1}{2} \mathrm{Tr}\left[\frac{\partial \mathcal{C}_\ell}{\partial\theta_\alpha}\mathcal{C}_\ell^{-1}\frac{\partial \mathcal{C}_\ell}{\partial\theta_\beta}\mathcal{C}_\ell^{-1}\right]. \tag{3.11}$$

Using equation (3.11) ensures that the full covariance of all galaxy angular power spectra considered is accounted for properly. If the covariance between different power spectra was neglected, the results of the Fisher analysis may change dramatically, as shown in [59].

We consider the ISW effect as an independent cosmological probe. Moreover, the ISW computed for each redshift bin and each of the galaxy population is independent from the other (when considered separately). In this case, we also assume a Gaussian likelihood and then the Fisher matrix is obtained as:

$$F^{\mathrm{ISW}}_{\alpha\beta} = \sum_{\ell\ell',\mathrm{X,i}} \frac{\partial C_\ell^{\mathrm{X,i;T}}}{\partial\theta_\alpha}\frac{\partial C_{\ell'}^{\mathrm{X,i;T}}}{\partial\theta_\beta}\delta^K_{\ell\ell'}\sigma^{-2}_{C_\ell^{\mathrm{X,i;T}}}, \qquad \sigma_{C_\ell^{\mathrm{X,i;T}}} = \sqrt{\frac{\left(C_\ell^{\mathrm{X,i;T}}\right)^2 + \tilde{C}_\ell^{\mathrm{X,i;X,i}}C_\ell^{\mathrm{TT}}}{(2\ell+1)f_{\mathrm{sky}}}}, \tag{3.12}$$

where C_ℓ^{TT} is the CMB temperature angular power spectrum, and we neglect the error of the CMB measurement beyond cosmic variance, since it is much smaller than the shot noise of the galaxy power spectra.

Assuming a Gaussian likelihood for the C_ℓ is a good approximation for large ℓ, since the central limit theorem can be applied due to the large number of modes. However, on large scales, where the number of modes is limited, the true likelihood is better approximated by a lognormal likelihood (see e.g., [90]). Nonetheless, Fisher matrix analysis assumes Gaussianity; one should use the extension proposed in [91] to account for non Gaussian likelihood. In any case, we do not expect large changes, since Fisher forecasts overestimate errors in this case (compared with the lognormal likelihood) and we are considering a complete understanding and removal of systematics. As systematics affect more the observations on large scales, these effects cancel each other qualitatively, justifying the Gaussian approximation for the likelihood in this case. We leave the exploration of the effect of a non Gaussian likelihood to future work.

As discussed in section 3.2, we will explore motivated models beyond ΛCDM, focusing on the extra cosmological parameters. Nonetheless, we also vary the five relevant parameters of ΛCDM for the galaxy clustering. In addition, we consider different levels of knowledge about the properties of each galaxy population, regarding galaxy and magnification bias. First, we assume a complete knowledge of $b^{\mathrm{X}}(z)$ and $s^{\mathrm{X}}(z)$. Secondly we include a single parameter, $\Delta b^X_{\mathrm{all}}$, to model our ignorance with respect to the galaxy bias at all redshifts. Third, we repeat the same strategy, but having an independent Δb^X_{i} for each redshift bin. Finally, we

Parameter	Meaning	Equation
$f_{\rm NL}$	Non Gaussian parameter in the local limit	Eq. (3.4)
w_0	Equation of state of the dark energy fluid at redshift 0	Eq. (3.7)
w_a	Amplitude of the time varying contribution to the equation of state of the dark energy fluid	Eq. (3.7)
Ω_k	Spatial curvature energy density parameter	—
μ_0	Amplitude of the time varying ($\propto \Omega_\Lambda(a)$) deviation from $\mu = 1$ in modified gravity	Eq. (3.9)
γ_0	Amplitude of the time varying ($\propto \Omega_\Lambda(a)$) deviation from $\gamma = 1$ in modified gravity	Eq. (3.9)
$\Delta b^X_{\rm all}$	Uncertainty on the galaxy bias of tracer X (or all the sample when needed).	$b^X_{\rm true}(z) = b^X(z) + \Delta b^X_{\rm all}$
$\Delta b^X_{\rm i}$	Uncertainty on the galaxy bias of tracer X (or all the sample when needed) in the redshift bin i.	$b^X_{\rm true}(z_{\rm i}) = b^X(z_{\rm i}) + \Delta b^X_{\rm i}$
$\Delta s^X_{\rm i}$	Uncertainty on the magnification bias of tracer X (or all the sample when needed) in the redshift bin i.	$s^X_{\rm true}(z_{\rm i}) = bsX(z_{\rm i}) + \Delta s^X_{\rm i}$

Table 1. Reference and meaning of each of the symbols used to denote the parameters included in the Fisher Matrix analysis along with the five standard cosmological parameters needed to compute the galaxy clustering.

also add independent $\Delta s^X_{\rm i}$ in a similar fashion to model our ignorance with respect to the magnification bias. In summary, if $\vec{\beta}$ denotes the parameters included to model our ignorance about the galaxy populations properties, we will have four cases: $\vec{\beta} = \varnothing$; $\vec{\beta} = \{\Delta b^X_{\rm all}\}$; $\vec{\beta} = \{\Delta b^X_{\rm i}\}$; and $\vec{\beta} = \{\Delta b^X_{\rm i}, \Delta s^X_{\rm i}\}$. This range of possibilities is a fair estimate, since the galaxy and magnification biases cannot be perfectly measured, but we will not be completely ignorant about them either, which is the case corresponding to the marginalization over $\{\Delta b^X_{\rm i}, \Delta s^X_{\rm i}\}$. The most realistic scenario will be somewhere in between. All the definitions and relevant equations or corresponding references regarding the extra cosmological parameters and the nuisance galaxy bias and magnification bias parameters for each of the cases discussed above can be found in table 1.

Therefore, if a given model has $\vec{\Upsilon}$ extra cosmological parameters with respect to ΛCDM, we will consider the next set of parameters for the Fisher matrix:

$$\vec{\theta} = \left\{\Omega_{\rm b}h^2, \Omega_{\rm cdm}h^2, h, n_s, \log\left(10^{10}A_s\right), \vec{\Upsilon}, \vec{\beta}\right\}\,, \tag{3.13}$$

where $\Omega_{\rm b}h^2$ and $\Omega_{\rm cdm}h^2$ are the baryon and cold-dark-matter physical densities, respectively, h is $H_0/(100\,{\rm km/s/Mpc})$ (with H_0 being the Hubble constant), and n_s, A_s are the spectral index and the amplitude of the primordial power spectrum of scalar modes, respectively. We assume a ΛCDM model as our fiducial cosmology, setting the cosmological parameter fiducial values to the best fit of the analysis of the temperature, polarization and lensing power spectra [1] and BAO [2, 92, 93] assuming the base model:[4] $\Omega_{\rm b}h^2 = 0.022447$, $\Omega_{\rm cdm}h^2 = 0.11928$, $h = 0.67702$, $\log(10^{10}A_s) = 3.048$, and $n_s = 0.96824$.

---

[4] The results of this analysis are denoted as `base_plikHM_TTTEEE_lowl_lowE_lensing_post_BAO` at the public Planck repository http://pla.esac.esa.int/pla/, where also the public MCMC can be found.

4 Results

In this section, we discuss the results of the Fisher matrix analysis; a detailed report of the results can be found in tables 4, 5, 6, 7 and 8 in appendix A. As stated above, we forecast constraints from EMU considering four different realizations regarding the rms flux per beam (using always a threshold of five times the rms flux per beam to claim a detection) and the fraction of sky covered. We use two cosmological probes: the angular power spectrum of the observed galaxies (referred to as galaxy clustering, GC, in the plots and tables of this section) and the ISW effect (see section 3.1 for more details). We estimate the constraints for all realizations of EMU considered using all galaxies as a single tracer, but we also consider two different tracers for the design sensitivity case of EMU. We expect the gains obtained in this case thanks to the multi-tracer technique to be equivalent in the other realizations considered in this work.

In order to estimate the combined constraints with current observations, we add priors from the temperature, polarization and lensing CMB power spectra from Planck [1], combined with BAO observations from spectroscopic galaxy surveys [2, 92, 93] (except for ΛCDM+μ_0+γ_0, for which we use the constraints from Planck+BAO+RSD, as done in [1]). We take the priors from current observations from the publicly available Monte-Carlo Markov Chains (MCMCs) of Planck collaboration when possible. However there are no public MCMCs for any modified gravity model or ΛCDM+$f_{\rm NL}$. For these cases, we make use of the marginalized 68% confidence level constraints on each of the extra parameters reported in [1] and [94], respectively, to the ΛCDM parameter covariance matrix, only in the corresponding diagonal element. The main limitation of this procedure is the lack of information of the degeneracies between the extra parameters and the ΛCDM parameters (and also between the extra parameters in the case of the modified gravity model). However, we do not expect that our forecast depends significantly on these degeneracies. The exploration of the effect of these degeneracies is left for future work.

We show in figure 2 the marginalized forecast constraints for the extra parameters of each extension of ΛCDM discussed in section 3.2, assuming both the galaxy and magnification bias are completely understood. On the other hand, we also show in figure 3 similar constraints marginalizing over $\Delta b_{\rm i}^X$ and $\Delta s_{\rm i}^X$. The most realistic scenario lies between these two cases, since some knowledge of the galaxy and magnification biases of the observed sources is expected by the time EMU is finished. We consider EMU at design sensitivity (i.e. 10 μJy of rms flux per beam and 30000 deg^2 of sky scanned) for different data combinations: angular galaxy power spectra alone, adding ISW and adding ISW and priors of current constraints. In each case, we report results taking the whole sample in a single redshift bin (dotted lines with diamonds) and splitting the catalogue in five redshift bins (solid lines with circles); and also using SFGs and AGNs as the same tracer (blue lines) and as different tracers (orange lines). We moreover show current constraints with a green line in order to compare it with EMU's forecasts. In all cases (no matter the redshift binning, the number of tracers or the sensitivity of the survey), EMU will not be competitive with current constraints on Ω_k from Planck+BAO, so we will not discuss these results in this section. Results for constraints on curvature are shown in appendix A.

Assuming that the discrimination between SFGs and AGNs is not good enough to perform a multi-tracer analysis and that the redshift inference using external data sets is not reliable enough in order to split the sample in different redshift bins, EMU's constraints will not be competitive on their own with current observations.

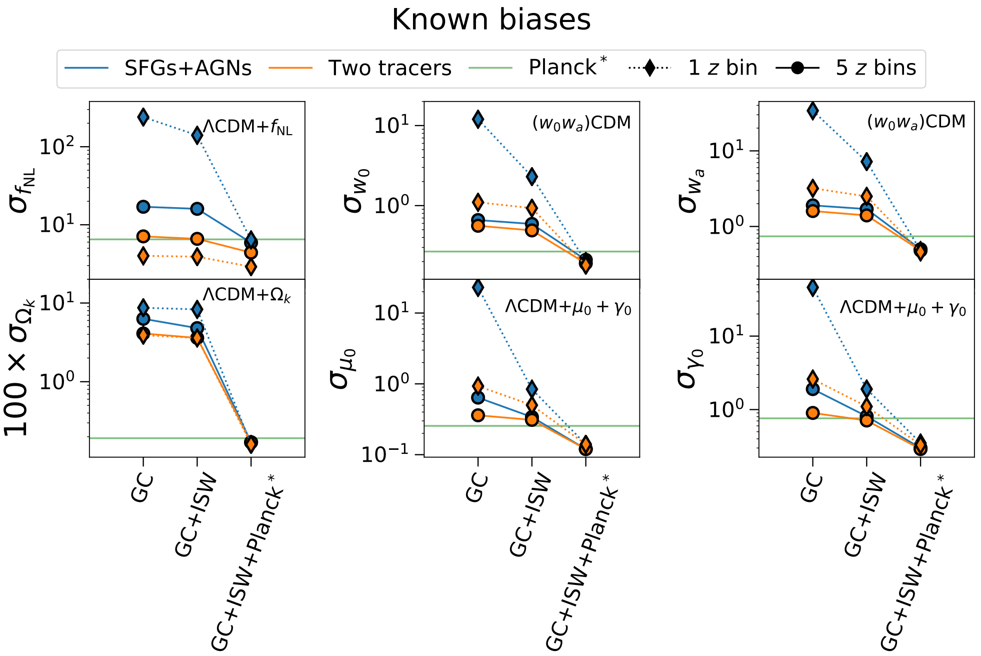

Figure 2. Marginalized 68% confidence level forecast constraints around the ΛCDM limit values on each of the extra cosmological parameters of the models discussed in section 3.2, for different data combinations, considering a realization of EMU at design sensitivity, without marginalizing over galaxy and magnification bias uncertainty parameters. We show results assuming one (dotted lines with diamonds) or five redshift bins (solid lines with circles) and using all the galaxies as a single tracer (blue lines) or discriminating between SFGs and AGNs (orange lines). We also show current constraints in green. "+Planck*" means Planck+BAO in all cases but in the ΛCDM+μ_0+γ_0 constraints, where it means Planck+BAO+RSD. Note the change of scale in the vertical axis in all cases.

10 μJy rms/beam, 1 Tracer, 1 Redshift bin					
	$f_{\rm NL}$	w_0	w_a	μ_0	γ_0
GC+ISW	140 (240)	2.3 (5.3)	7.2 (12)	0.84 (1.0)	1.9 (1.9)
GC+ISW+Planck*	6.4 (6.4)	0.20 (0.26)	0.48 (0.74)	0.14 (0.20)	0.35 (0.45)

Table 2. Marginalized 68% confidence level predicted constraints for the extra parameters of the models ΛCDM+$f_{\rm NL}$, $(w_0 w_a)$CDM and ΛCDM+$\mu_0 + \gamma_0$, from radio-continuum measurements with EMU, assuming design sensitivity and using one redshift bin and tracer. We report constraints assuming total knowledge about galaxy and magnification biases and marginalizing over the corresponding parameters $\Delta b_{\rm all}$ and $\Delta s_{\rm all}$, in parentheses. We show results including galaxy power spectra and ISW effect (GC+ISW), and also including Planck+BAO priors (Planck+BAO+RSD in the case of ΛCDM+$\mu_0 + \gamma_0$) denoted as Planck*.

Combining the angular galaxy power spectrum and the ISW effect and assuming a total knowledge of the galaxy and magnification bias (marginalizing over $\Delta b_{\rm all}$ and $\Delta s_{\rm all}$, we obtain the following forecasts: $\sigma(f_{\rm NL}) = 140$ (240), $\sigma(w_0) = 2.3$ (5.3), $\sigma(w_a) = 7.2$ (12), $\sigma(\mu_0) = 0.84$ (1.0) and $\sigma(\gamma_0) = 1.9$ (1.9), assuming the corresponding model.

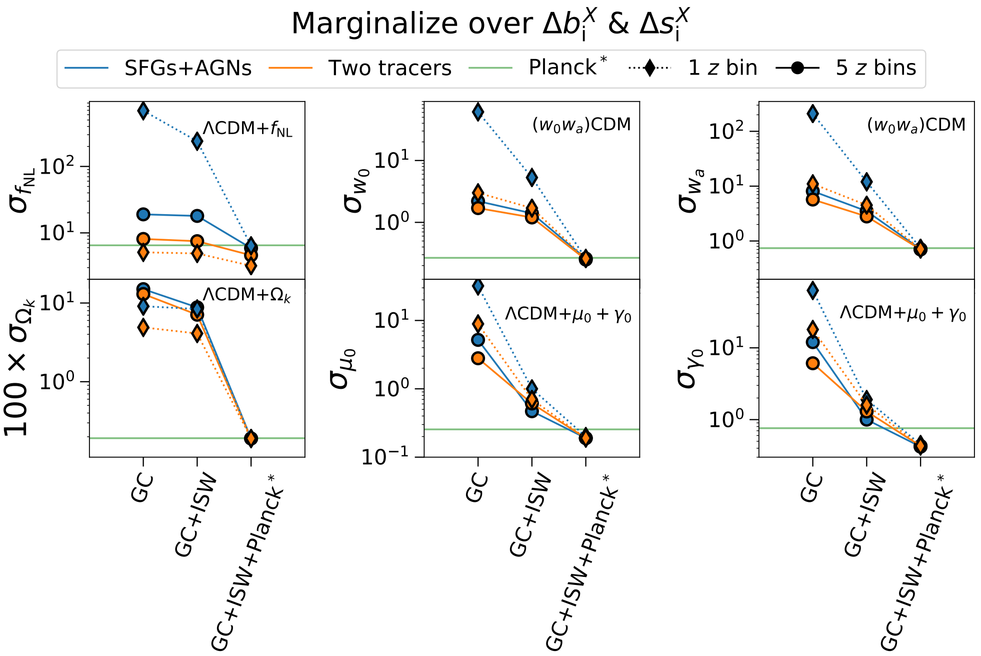

Figure 3. Same as figure 2 but marginalizing also over all the galaxy and magnification biases uncertainty parameters: Δb_i and Δs_i.

We report the predicted constraints on the extra parameters in table 2 assuming EMU observations at design sensitivity and using only one tracer and one redshift bin. We report results assuming total knowledge about the galaxy and magnification bias and also assuming total ignorance and marginalizing over the corresponding parameters, in parenthesis. In this configuration, EMU will not be competitive on its own. However, when combined with current constraints from CMB, BAO and RSD observations, EMU's measurements will improve current constraints on the modified gravity model a 45% (22%) for μ_0 and a 54% (41%) for γ_0. In this case, they will also improve mildly the constraints on (w_0w_a)CDM, only if the galaxy and magnification biases are completely known: 25% for w_0 and 35% for w_a.

Nonetheless, the improvement of redshift inference methodologies with external data sets and the advent of new galaxy catalogs with better sensitivity will allow to determine the redshifts with higher precision. Thanks to this, splitting EMU's catalogue in five redshift bins and using SFGs and AGNs as two different tracers is expected to be feasible. We report the resulting predicted constraints for this configuration in table 3, in a similar fashion as before. The strongest constraints set by the combination of EMU observations with current data will be a factor 2.3 (2.0) for f_NL, 33% (equal) and 37% (7%) stronger for w_0 and w_a, respectively, and a factor 2.1 (1.3) and 2.3 (1.8) smaller for μ_0 and γ_0, respectively, than current observations when the galaxy and magnification bias are assumed to be known (marginalizing over Δb_i^X and Δs_all^X).

As expected, using two tracers improves EMU's performance, especially for f_NL, where EMU alone constraints are stronger than current bounds. This is not surprising, since PNG imprints appear on the largest scales, those more affected by the cosmic variance, which is

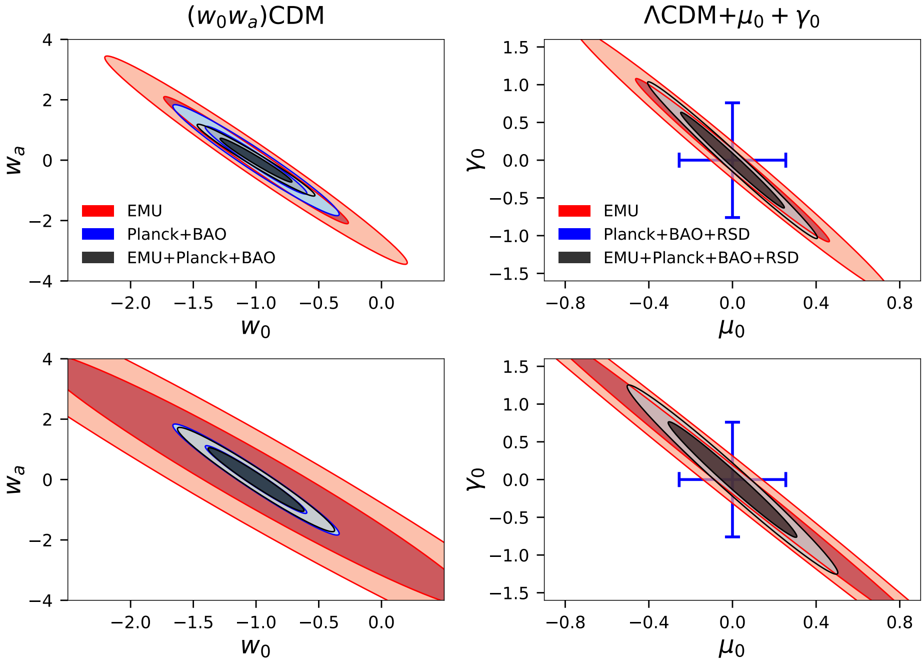

Figure 4. 68% and 95% confidence level forecast constraints around the ΛCDM limit values on w_0 and w_a in a $(w_0 w_a)$CDM cosmology (left panels) and on μ_0 and γ_0 for ΛCDM+μ_0+γ_0 (right panels). EMU at design sensitivity are in red, Planck+BAO in blue, and their combination in black. Upper panels assume total knowledge of galaxy and magnification bias, bottom panels marginalize over them. We only show one-dimensional marginalized 68% confidence level constraints from Planck+BAO+RSD in the right panels because there is no public result on the correlation between μ_0 and γ_0, nor public MCMC for this model.

10 μJy rms/beam, 2 Traces, 5 Redshift bins^a					
	$f_{\rm NL}$	w_0	w_a	μ_0	γ_0
GC+ISW	3.9 (4.9)	0.49 (1.2)	1.4 (2.8)	0.31 (0.61)	0.71 (1.3)
GC+ISW+Planck*	2.9 (3.2)	0.19 (0.25)	0.48 (0.70)	0.12 (0.19)	0.29 (0.43)

Table 3. Same as table 2 but using five redshift bins and two tracers. ^{a}: in the case of ΛCDM+$f_{\rm NL}$ we report the result using a single redshift bin, since it is stronger in this case.

partially overcome by the multi-tracer technique. What it is surprising is that using SFGs and AGNs as different tracers the constraints on $f_{\rm NL}$ are better using only one redshift bin. This is due to the fact that PNG imprints are very sensitive to $b(z)$. In figure 1 it is shown that AGN galaxy bias is much larger than SFG galaxy bias. However, EMU will observe many more SFGs than AGNs, and it will not detect enough AGNs in the high-redshift bins. Therefore, for the AGN power spectra at high redshifts, where the impact of PNG is larger, the shot noise is also larger and the final sensitivity of EMU to $f_{\rm NL}$ decreases with respect to having only one bin. Then, the strongest constraints on $f_{\rm NL}$ found in this work correspond to having two tracers with only one redshift bin. Something similar happens for other parameters, but at much less significance.[5]

In figure 4 we show marginalized 68% and 95% confidence level contours on the w_0-w_a plane from EMU forecasts (assuming the realization at design sensitivity and using two tracers), Planck+BAO and the combination of them (left panels), and contours on the μ_0-γ_0 plane from EMU and EMU combined with Planck+BAO+RSD in the corresponding right panels. Upper panels assume total knowledge of the galaxy and magnification bias, while bottom panels assume total ignorance and include a marginalization over $\Delta b_{\rm i}^X$ and $\Delta s_{\rm all}^X$. As can be seen, the degeneracy between w_0 and w_a is almost the same measured by EMU and Planck+BAO, hence the combination of both measurements do not break the existing degeneracy. We only show one-dimensional marginalized 68% constraints for μ_0 and γ_0 independently from Planck+BAO+RSD as there is no published value for the correlation between μ_0 and γ_0 nor a MCMC to compute it.

The fact that an early EMU data release covers only 2000 deg^2 limits considerably its performance in constraining cosmological parameters with galaxy clustering. Therefore, combining Planck+BAO with EMU-early does not improve the constraints. However, the impact of having a factor two worse sensitivity than in the design sensitivity (i.e., the pessimistic sensitivity of 20 μJy rms/beam) does not degrade critically the constraints. Using one single tracer and considering five redshift bins, the constraints are around $25-30\%$ weaker than at design sensitivity for all the parameters. In the case of $f_{\rm NL}$ using only one redshift bin, the constraints are even better, due to having a larger abundance ratio of AGNs with respect to SFGs, so the average bias is larger. This is no longer true using five redshift bins, since the effect of the larger shot noise with the pessimistic sensitivity is more important in this case. Finally, the improvement that SKA-2 will achieve (a factor 10 in sensitivity) will be crucial. SKA-2 forecast constraints on $f_{\rm NL}$ assuming five redshift bins and a single tracer are a factor ~ 3 stronger than those for EMU at design sensitivity, improving upon current bounds from Planck. In addition, in the cases of evolving dark energy and modified gravity models, the constraints on w_0, w_a, μ_0 and γ_0 will be a factor ~ 2 stronger than EMU at design sensitivity if ISW and galaxy clustering are combined.

However, EMU will not be able to measure $f_{\rm NL}$ below unity. In order to find the specifications needed by EMU to achieve the goal of having an uncertainty on local PNG measurements better than $\sigma(f_{\rm NL}) \sim 1$, we forecast the constraints on $f_{\rm NL}$ from EMU-*like* surveys as a function of the fraction of sky surveyed and the number of sources detected. We model the variation on the number of sources with a factor $N_{\rm factor}$ multiplying the number density $dN/dzd\Omega$ appearing in figure 1. We reckon that having a better sensitivity will allow to detect more new galaxies at larger redshift than at lower redshift, which would modify the shape of the redshift distribution. However, we expect this change in the shape of the redshift distribution to be small enough within the range of parameters considered here so as not to affect our results significantly. Therefore, changing the total number of detected sources maintaining the shape of the redshift distribution is a fair approximation for this study. The variation to $f_{\rm sky}$ and $N_{\rm factor}$ enter the covariance matrix in the Fisher matrix computation (equations (3.11) and (3.12)). This kind of study is important in order to guide the planning of the survey strategy, since in principle it may be more convenient to use the same total observing time on a smaller area to reduce the noise and detect more sources, or vice versa. For a similar investigation for spectroscopic surveys, see [95].

---

[5] As can be seen in the appendix B, the S^3 simulation predicts approximately the same number of SFGs and AGNs detected. Therefore, this effect is not present in the constraints obtained using S^3 as benchmark to predict the redshift distribution of galaxies and the galaxy and magnification bias.

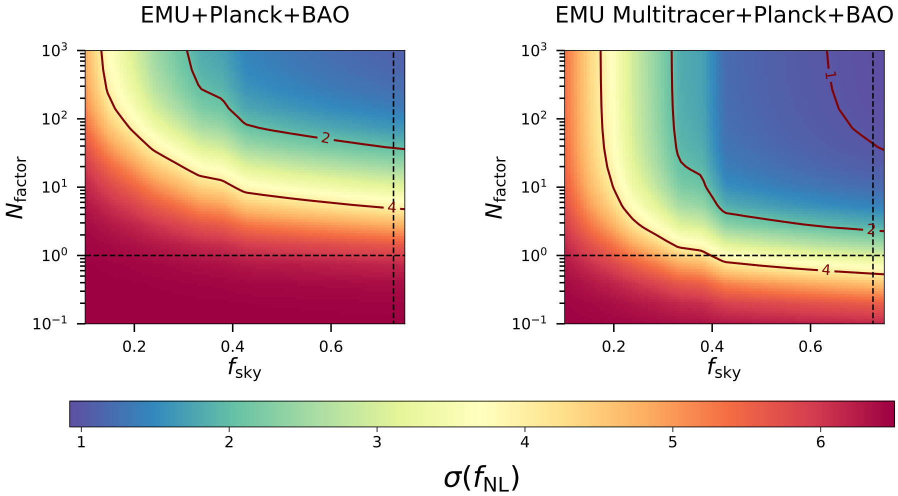

Figure 5. 68% confidence level forecast constraints for $f_{\rm NL}$ (assuming a fiducial $f_{\rm NL} = 0$) from measurements of the angular galaxy power spectra and the ISW effect, combined with the prior from Planck and BAO. We use five redshift bins when considering all galaxies as one single tracer (left), but only one redshift bin when distinguishing between SFGs and AGNs (right) since we find better constraints than binning the catalogues in redshift (see main text and table 8).

We show the dependence on $f_{\rm sky}$ and $N_{\rm factor}$ (starting from EMU at design sensitivity) for the predicted constraints on $f_{\rm NL}$ in figure 5, both considering all galaxies as the same kind of tracer (left panel) and using two tracers (right panel). In the multi-tracer case, we use a single redshift bin, since the constraints are better in this case. We use EMU forecasts assuming complete knowledge of the galaxy and magnification bias and the priors from current observations in both panels. We find that using all the galaxies as a single tracer, it will not be possible to measure local PNG with precision $\sigma(f_{\rm NL}) < 1$ even if EMU scans 75% of the sky and observes 1000 times more galaxies. However, it will be possible using two different tracers if EMU would be able to detect around 40 times more galaxies. In this the case, the total observing time of EMU should increase by a large factor in order to achieve this precision goal (note that reducing the rms/beam flux from 10 to 1 μJy corresponds to detecting around 13 times more galaxies). On the other hand, using the same total observing time, the sensitivity can be increased if $f_{\rm sky}$ is smaller. However, we find that the $N_{\rm factor}$ needed to reach $\sigma(f_{\rm NL}) \sim 1$ increases dramatically whenever $f_{\rm sky} < 0.65$, given that, as stated above, PNG effects shows on ultra-large scales. Nonetheless, it is important to keep in mind that this analysis is done keeping the same abundance ratio between AGNs and SFGs. If, by any cause, a significant increase of sensitivity will amount to increasing the relative abundance of AGNs, or by any change, the measured galaxy bias is larger than expected, the total number of sources observed would not have to be so large. As can be seen in i.e. tables 4 and 8, marginalizing over $\Delta b_{\rm i}^{X}$ and $\Delta s_{\rm i}^{X}$ does not have a large effect on the constraints on $f_{\rm NL}$, so the results are qualitatively similar in that case.

5 Conclusions

The Evolutionary Map of the Universe (EMU), an all-sky radio-continuum survey operating on the Australian SKA Pathfinder (ASKAP), will provide deep and wide observations with enough detected sources to study galaxy clustering at the ultra-large scales for the first time. In this work we use the Fisher matrix formalism to estimate the precision in measuring parameters of models beyond ΛCDM, using measurements of the angular galaxy power spectrum and the integrated Sachs-Wolfe effect. The cases under study include models with evolving dark energy equation of state, low redshift deviations from General Relativity, spatial curvature and primordial non-Gaussianity in the local limit.

We estimate the population of objects detected by EMU using the T-RECS catalogues [51] and assume that all observational systematics are under control and correctly accounted for. In this way, the main uncertainties left are the galaxy properties, such as the galaxy and magnification biases. We consider different levels of knowledge of these quantities throughout this work, having in mind that partial information will be available by the time EMU data is available. Regarding the observed sources, we first consider all the galaxies as the same kind of tracer of the density field, and then distinguish between Star-Forming galaxies and AGNs as different tracers and perform a multi-tracer analysis.

As a radio-continuum survey, EMU's redshift determination will be very poor. However, given the large numbers and the improvement of the redshift inference algorithms and external data sets, it will be possible to assign redshifts so that a tomographic analysis can be performed. While not being competitive using all galaxies as the same tracer and a single redshift bin, we find that using external observations to infer the redshifts and split the catalogue into five redshift bins (which is a conservative assumption) boosts EMU's constraining power. Moreover, if the observations allow a reliable distinction between SFGs and AGNs, a multi-tracer analysis will return the best from EMU: when combined with current observations from CMB observations and BAO analyses, EMU's observations at design sensitivity will improve the current bounds on evolving dark energy models and modified gravity by a factor of two.

As EMU will survey a large fraction of the sky, it will observe the largest scales to date. Since local PNG would have imprints on the largest scales, EMU is a perfect experiment to increase the precision of the measurements of $f_{\rm NL}$. However, it will need a multi-tracer analysis in order to overcome the cosmic variance. This way, EMU alone will set a bound twice smaller than the current bound, and slightly smaller if combined with current observations. In order to achieve the possibly game-changing threshold of an uncertainty on $f_{\rm NL}$ below 1, EMU will have to observe around 40 times more galaxies, which would need an out-of-range amount of time of observations (i.e. SKA-2 would detect a factor 13 more galaxies than EMU). However, if the fraction of the sky observed lies below ~ 0.65 (which will allow to use more observation time per pointing to increase sensitivity), the amount of galaxies needed increases dramatically. Therefore, other strategies (combination with other cosmological probes, improvements in the redshift estimation with external data such it is possible to split the catalogue in more redshift bins, increasing the number of tracers, etc.) will be needed to achieve this goal. Note that using S^3 instead of T-RECS the constraints are slightly better (see appendix B). Nonetheless, even in this case, achieving $\sigma(f_{\rm NL}) < 1$ with only EMU seems difficult and it will be needed to wait for more sensitive experiments such as the different surveys of SKA-2. This result is consistent with the findings reported for the SKA Phase 1 [96]. However, the possibility to find small deviations from Gaussian initial conditions with

SKA will only be possible if it follows an all-sky survey strategy. In any case, EMU's bound on $f_{\rm NL}$ will be the best in the near future and EMU's catalogues will be the main data set to combine with new measurements in the quest to measure PNG.

Although EMU is operating in ASKAP, a pathfinder for SKA, it will have scientific relevance on its own, since it will be the deepest all-sky survey (and with best angular resolution among similar surveys) by the time it will end. This will be an important step forward to constrain physics which manifests itselfs on the largest scales, such as primordial non-Gaussianity, but also relativistic corrections in the galaxy clustering statistics [97]. This makes EMU a critical stepping stone for our understanding of the early Universe, gravity and dark energy, and also for the preparation of future galaxy surveys.

Acknowledgments

We thank Nicola Bellomo for discussions during the development of this work. Funding for this work was partially provided by the Spanish MINECO under projects AYA2014-58747-P AEI/FEDER UE and MDM-2014-0369 of ICCUB (Unidad de Excelencia Maria de Maeztu). JLB is supported by the Spanish MINECO under grant BES-2015-071307, co-funded by the ESF. AR has received funding from the People Programme (Marie Curie Actions) of the European Union H2020 Programme under REA grant agreement number 706896 (COSMOFLAGS) and the John Templeton Foundation. This work was supported at Johns Hopkins by NSF Grant No. 0244990, NASA NNX17AK38G, and the Templeton foundation.

A Cosmological forecasts results

In this appendix we report the results of the cosmological forecast for radio-continuum surveys discussed in section 4 in detail (tables 4, 5, 6, 7 and 8. We consider the four models discussed in section 3.2 and four different surveys: EMU at design sensitivity (10 μJy rms flux/beam), a pessimistic realization (with twice rms flux/beam), EMU early results (100 μJy rms flux/beam) and SKA-2 (1 μJy rms flux/beam). For each survey, we consider a single redshift bin and five different redshift bins, as shown in section 2. Moreover, we consider different assumptions about our prior knowledge for the galaxy and magnification biases. Either we understand the biases completely, we marginalize over a single parameter which shifts $b(z)$, marginalize over parameters which shifts $b(z)$ for each bin or marginalize over parameters that shift both $b(z)$ and $s(z)$ in each bin.

B Comparison with S^3 simulation

Prior to the release of the T-RECS catalogues, most of the forecast analysis for galaxy radio surveys were done using the S^3 simulations [52]. In order to ease the comparison with those studies and also to illustrate the differences between both set of simulations we repeat the study using S^3 for the four models under considerations and assuming the design sensitivity realization of EMU. We consider a case with all the galaxies used as a single tracer and another one using them as two different tracers. The differences between the results using each simulation also gives an estimate of the inherent uncertainty of the cosmological forecast using simulations.

We show the relevant quantities obtained from S^3 in figure 6. S^3 further subdivides the SFGs into star burst galaxies and star forming galaxies, and the AGNs into radio quiet quasars and Fanoroff-Riley type-I and type-II radio galaxies. These five populations of galaxies have been used as different tracers for studies in the literature (e.g. [32]). However, an accurate discrimination among all five might be uncertain, so we prefer to proceed as with T-RECS and consider only two different tracers SFGs and AGNs. As star burst galaxies are far less abundant than star forming galaxies, we assume the galaxy bias model of the latter for the whole SFG population. Regarding AGNs, Fanoroff-Riley type-I galaxies abundance is negligible. Therefore, we only consider the bias model of the radio quiet quasars and Fanoroff-Riley type-II and use an approximated weighted mean. The galaxy bias for both radio quiet quasars and Fanoroff-Riley type-II are shown in red and purple dotted lines, respectively.

Survey	# redshift bins	Bias uncertainty	Data combination and constraints on ΛCDM+$f_{\rm NL}$		
			Galaxy Clustering (GC)	GC+ISW	GC+ISW+Planck+BAO
			$f_{\rm NL}$	$f_{\rm NL}$	$f_{\rm NL}$
EMU Design Sensitivity (10 μJy rms/beam)	1 bin	Known	240	140	6.4
		$\Delta b_{\rm all}$	320	170	6.4
		$\Delta b_{\rm all}$ & $\Delta s_{\rm all}$	690	240	6.4
	5 bins	Known	17	16	5.9
		$\Delta b_{\rm all}$	17	16	5.9
		Δb_i	17	16	5.9
		Δb_i & Δs_i	19	18	5.9
EMU Pessimistic Sensitivity (20 μJy rms/beam)	1 bin	Known	160	130	6.4
		$\Delta b_{\rm all}$	360	140	6.4
		$\Delta b_{\rm all}$ & $\Delta s_{\rm all}$	360	160	6.5
	5 bins	Known	23	21	6.1
		$\Delta b_{\rm all}$	23	21	6.1
		Δb_i	24	22	6.1
		Δb_i & Δs_i	27	24	6.1
EMU Early Results (100 μJy rms/beam, 2000 deg^2)	1 bin	Known	6200	3000	6.5
		$\Delta b_{\rm all}$	50000	4000	6.5
		$\Delta b_{\rm all}$ & $\Delta s_{\rm all}$	74000	4400	6.5
	5 bins	Known	360	360	6.5
		$\Delta b_{\rm all}$	360	360	6.5
		Δb_i	400	390	6.5
		Δb_i & Δs_i	490	470	6.5
SKA-2 (1 μJy rms/beam)	1 bin	Known	130	70	6.4
		$\Delta b_{\rm all}$	130	70	6.4
		$\Delta b_{\rm all}$ & $\Delta s_{\rm all}$	270	73	6.4
	5 bins	Known	5.5	5.5	4.0
		$\Delta b_{\rm all}$	5.6	5.5	4.0
		Δb_i	5.7	5.6	4.1
		Δb_i & Δs_i	5.9	5.8	4.1

Table 4. Marginalized 68% confidence level predicted constraints on $f_{\rm NL}$ assuming ΛCDM+$f_{\rm NL}$ from radio-continuum measurements with EMU. We show results of galaxy clustering by itself (GC), galaxy clustering combined with ISW (GC+ISW), and when Planck+BAO priors are also added (GC+ISW+Planck+BAO),both not binning in redshift and with five redshift bins. We consider four different surveys: EMU at design sensitivity, a pessimistic realization of EMU with twice the rms flux/beam, EMU early and SKA-2. We assume different cases for the knowledge of the bias, either known or marginalizing over the galaxy bias and the magnification bias. $\Delta b_{\rm all}$ refers to marginalizing over a single parameter Δb_all which shifts the whole $b(z)$.

Survey	# redshift bins	Bias uncertainty	Data combination and constraints on (w_0w_a)CDM					
			GC		GC+ISW		GC+ISW+Planck+BAO	
			w_0	w_a	w_0	w_a	w_0	w_a
EMU Design Sensitivity (10 μJy rms/beam)	1 bin	Known	12	34	2.3	7.2	0.20	0.48
		Δb_{all}	19	70	5.0	9.6	0.26	0.72
		Δb_{all} & Δs_{all}	61	210	5.3	12	0.26	0.74
	5 bins	Known	0.66	1.9	0.59	1.7	0.20	0.50
		Δb_{all}	0.78	2.9	0.60	1.9	0.23	0.66
		Δb_i	1.8	6.5	1.0	2.9	0.25	0.69
		Δb_i & Δs_i	2.2	8.1	1.4	3.5	0.26	0.71
EMU Pessimistic Sensitivity (20 μJy rms/beam)	1 bin	Known	6.9	23	2.5	8.3	0.21	0.51
		Δb_{all}	29	120	3.5	8.7	0.25	0.71
		Δb_{all} & Δs_{all}	65	230	3.5	9.4	0.26	0.72
	5 bins	Known	0.95	2.9	0.80	2.4	0.22	0.58
		Δb_{all}	1.0	3.9	0.81	2.5	0.24	0.68
		Δb_i	2.4	9.9	1.2	3.5	0.25	0.71
		Δb_i & Δs_i	3.2	13	2.0	4.8	0.26	0.72
EMU Early Resuls (100 μJy rms/beam, 2000 deg^2)	1 bin	Known	2100	6600	51	130	0.26	0.73
		Δb_{all}	2800	9900	270	550	0.27	0.74
		Δb_{all} & Δs_{all}	5400	33000	280	580	0.27	0.74
	5 bins	Known	8.3	26	6.3	17	0.27	0.74
		Δb_{all}	9.1	35	8.8	18	0.27	0.74
		Δb_i	28	100	16	36	0.27	0.74
		Δb_i & Δs_i	58	170	20	44	0.27	0.74
SKA-2 (1 μJy rms/beam)	1 bin	Known	18	63	2.8	7.3	0.18	0.43
		Δb_{all}	21	94	3.2	7.7	0.27	0.74
		Δb_{all} & Δs_{all}	22	120	7.2	16	0.27	0.74
	5 bins	Known	0.33	0.87	0.31	0.80	0.15	0.36
		Δb_{all}	0.44	1.3	0.37	1.1	0.21	0.60
		Δb_i	0.79	2.2	0.61	1.6	0.24	0.64
		Δb_i & Δs_i	0.94	2.9	0.68	1.7	0.24	0.66

Table 5. Same as table 4 but for w_0 and w_a assuming a (w_0w_a)CDM model.

Survey	# redshift bins	Bias uncertainty	Data combination and constraints on ΛCDM+Ω_k		
			GC	GC+ISW	GC+ISW+Planck+BAO
			$100 \times \Omega_k$	$100 \times \Omega_k$	$100 \times \Omega_k$
EMU Design Sensitivity (10 μJy rms/beam)	1 bin	Known	8.7	8.3	0.16
		$\Delta b_{\rm all}$	9.1	8.4	0.19
		$\Delta b_{\rm all}$ & $\Delta s_{\rm all}$	9.1	8.4	0.19
	5 bins	Known	6.3	4.8	0.17
		$\Delta b_{\rm all}$	9.6	7.8	0.19
		Δb_i	13	8.0	0.19
		Δb_i & Δs_i	15	8.8	0.19
EMU Pessimistic Sensitivity (20 μJy rms/beam)	1 bin	Known	12	11	0.17
		$\Delta b_{\rm all}$	13	11	0.19
		$\Delta b_{\rm all}$ & $\Delta s_{\rm all}$	13	11	0.19
	5 bins	Known	9.7	6.7	0.18
		$\Delta b_{\rm all}$	18	12	0.19
		Δb_i	23	12	0.19
		Δb_i & Δs_i	28	13	0.19
EMU Early Results (100 μJy rms/beam, 2000 deg^2)	1 bin	Known	130	88	0.19
		$\Delta b_{\rm all}$	130	110	0.19
		$\Delta b_{\rm all}$ & $\Delta s_{\rm all}$	130	110	0.19
	5 bins	Known	87	45	0.19
		$\Delta b_{\rm all}$	150	77	0.19
		Δb_i	160	82	0.19
		Δb_i & Δs_i	160	82	0.19
SKA-2 (1 μJy rms/beam)	1 bin	Known	5.4	4.4	0.16
		$\Delta b_{\rm all}$	6.0	4.9	0.19
		$\Delta b_{\rm all}$ & $\Delta s_{\rm all}$	6.0	5.3	0.19
	5 bins	Known	2.3	2.0	0.15
		$\Delta b_{\rm all}$	2.6	2.4	0.18
		Δb_i	3.8	2.9	0.18
		Δb_i & Δs_i	4.3	3.1	0.18

Table 6. Same as table 4 but for Ω_k assuming a ΛCDM+Ω_k model.

Survey	# redshift bins	Bias uncertainty	Data combination and constraints on ΛCDM+μ_0+γ_0					
			GC		GC+ISW		GC+ISW+Planck+BAO+RSD	
			μ_0	γ_0	μ_0	γ_0	μ_0	γ_0
EMU Design Sensitivity (10 μJy rms/beam)	1 bin	Known	23	46	0.84	1.9	0.14	0.35
		Δb_{all}	25	51	1.0	1.9	0.20	0.44
		Δb_{all} & Δs_{all}	32	63	1.0	1.9	0.20	0.45
	5 bins	Known	0.64	1.9	0.34	0.81	0.12	0.30
		Δb_{all}	1.1	2.8	0.43	0.95	0.18	0.40
		Δb_i	3.9	8.8	0.46	1.0	0.19	0.42
		Δb_i & Δs_i	5.2	12	0.47	1.0	0.19	0.42
EMU Pessimistic Sensitivity (20 μJy rms/beam)	1 bin	Known	20	39	0.96	2.2	0.15	0.36
		Δb_{all}	20	39	1.1	2.2	0.20	0.44
		Δb_{all} & Δs_{all}	27	54	1.1	2.2	0.20	0.45
	5 bins	Known	1.0	3.0	0.47	1.1	0.14	0.35
		Δb_{all}	2.3	5.5	0.59	1.3	0.19	0.43
		Δb_i	5.1	12	0.60	1.3	0.19	0.43
		Δb_i & Δs_i	8.4	19	0.61	1.4	0.19	0.44
EMU Early Results (100 μJy rms/beam, 2000 deg^2)	1 bin	Known	430	870	6.1	14	0.23	0.62
		Δb_{all}	13000	27000	7.1	14	0.23	0.62
		Δb_{all} & Δs_{all}	15000	31000	9.2	14	0.23	0.62
	5 bins	Known	6.2	19	2.9	7.1	0.23	0.64
		Δb_{all}	61	140	3.5	7.8	0.23	0.64
		Δb_i	88	200	3.5	7.9	0.23	0.64
		Δb_i & Δs_i	100	220	3.5	7.9	0.23	0.65
SKA-2 (1 μJy rms/beam)	1 bin	Known	12	24	0.79	1.8	0.15	0.35
		Δb_{all}	46	91	0.82	1.8	0.20	0.44
		Δb_{all} & Δs_{all}	48	96	1.0	1.9	0.20	0.44
	5 bins	Known	0.20	0.59	0.17	0.39	0.092	0.21
		Δb_{all}	0.29	0.80	0.20	0.46	0.13	0.29
		Δb_i	1.4	3.2	0.32	0.73	0.17	0.39
		Δb_i & Δs_i	1.7	4.0	0.33	0.74	0.17	0.39

Table 7. Same as table 4 but for μ_0 and γ_0 assuming a phenomenological parameterization of modified gravity as a ΛCDM+μ_0+γ_0 model. In this case, the external data is Planck+BAO+RSD.

Survey	# redshift bins	Bias uncertainty	Data combination and constraints on extended models					
			Galaxy Clustering (GC)		GC+ISW		GC+ISW+Planck*	
EMU with multi-tracer Design Sensitivity (10 μJy rms/beam) Using T-RECS			$f_{\rm NL}$		$f_{\rm NL}$		$f_{\rm NL}$	
	1 bin	Known	4.0		3.9		2.9	
		$\Delta b_{\rm all}$	4.2		4.0		3.0	
		$\Delta b_{\rm all}$ & $\Delta s_{\rm all}$	5.1		4.9		3.2	
	5 bins	Known	7.1		6.6		4.4	
		$\Delta b_{\rm all}$	7.3		6.7		4.5	
		Δb_i	7.6		7.0		4.6	
		Δb_i & Δs_i	8.1		7.5		4.6	
			w_0	w_a	w_0	w_a	w_0	w_a
	1 bin	Known	1.1	3.2	0.93	2.5	0.18	0.46
		$\Delta b_{\rm all}$	1.2	4.8	0.98	0.27	0.19	0.47
		$\Delta b_{\rm all}$ & $\Delta s_{\rm all}$	3.0	11	1.7	4.5	0.26	0.71
	5 bins	Known	0.56	1.6	0.49	1.4	0.19	0.48
		$\Delta b_{\rm all}$	0.57	1.7	0.50	1.4	0.19	0.49
		Δb_i	1.2	4.4	0.78	2.1	0.25	0.68
		Δb_i & Δs_i	1.7	5.7	1.2	2.8	0.25	0.70
			$100 \times \Omega_k$		$100 \times \Omega_k$		$100 \times \Omega_k$	
	1 bin	Known	3.9		3.6		0.16	
		$\Delta b_{\rm all}$	4.9		3.9		0.16	
		$\Delta b_{\rm all}$ & $\Delta s_{\rm all}$	4.9		4.1		0.19	
	5 bins	Known	4.1		3.6		0.17	
		$\Delta b_{\rm all}$	4.5		3.8		0.17	
		Δb_i	11		6.7		0.19	
		Δb_i & Δs_i	13		7.1		0.19	
			μ_0	γ_0	μ_0	γ_0	μ_0	γ_0
	1 bin	Known	0.93	2.6	0.50	1.1	0.14	0.33
		$\Delta b_{\rm all}$	3.1	6.4	0.69	1.6	0.15	0.34
		$\Delta b_{\rm all}$ & $\Delta s_{\rm all}$	8.9	18	0.70	1.6	0.19	0.43
	5 bins	Known	0.36	0.90	0.31	0.71	0.12	0.29
		$\Delta b_{\rm all}$	0.39	0.95	0.33	0.75	0.13	0.31
		Δb_i	2.4	5.2	0.60	1.3	0.19	0.43
		Δb_i & Δs_i	2.8	6.1	0.61	1.3	0.19	0.43

Table 8. Same as in tables 4, 5, 6 and 7, but only for the EMU survey at design sensitivity and using SFGs and AGNs as different tracers. "+Planck*" means Planck+BAO in all case but in the ΛCDM+μ_0+γ_0 constraints, where means Planck+BAO+RSD.

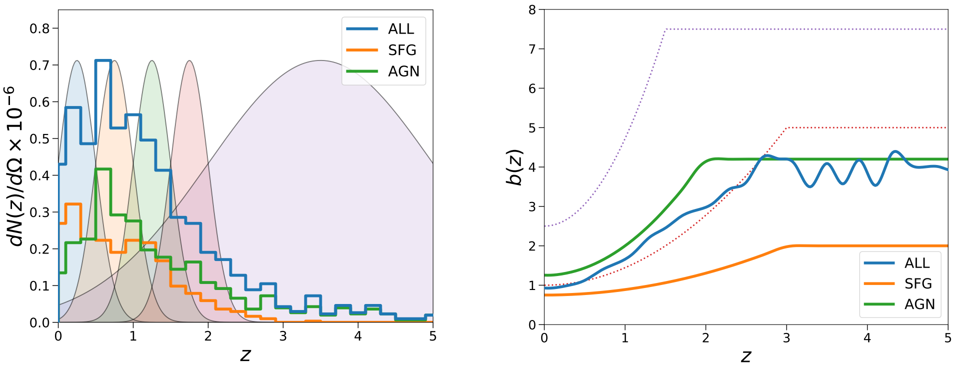

Figure 6. *Left*: $dN/dzd\Omega$ for the galaxies observed assuming a rms flux/beam of 10μJy from S^3 simulation, always requiring a signal of the flux of five times larger than the rms/beam to consider a detection. We also plot the Gaussian window functions of the five redshift bins considered to compute the cosmological observables. *Right* theoretical galaxy bias for SFGs and AGNs and the corresponding weighted total from S^3. We show the quantities related to the whole sample in blue, with SFGs alone in orange and with AGNs alone in green. We also show the galaxy bias for radio quiet quasars and Fanoroff-Riley type-II in red and purple dotted lines, respectively.

The quantities shown in figure 6 are to be compared with their equivalents using T-RECS (figure 1). The total number of galaxies above the threshold of detection is similar for both galaxies. However, the distribution in S^3 is broader than in T-RECS, and there are also more AGNs than SFGs, especially at large redshifts. This is very important, since it affects significantly the values of the weighted mean of $b(z)$ when all galaxies are considered as a single tracer. It also reverses which tracer has more weight in the multi-tracer analysis. These differences are the responsible of the discrepancies between S^3 and T-RECS.

The results using S^3 are reported in table 9 and 10. Since the average bias is larger in S^3, the signal to noise ratio of the galaxy power spectra and ISW are larger too. Therefore, the constraints on w_0 and w_a coming only from the galaxy power spectra are $\sim 30\%$ better using S^3, although the difference is negligible when ISW is included in the analysis. Also the magnitude of the impact of marginalizing over the galaxy and magnification biases is similar using both simulations. The gains using two different tracers to constrain $(w_0 w_a)$CDM are similar too. In the case of ΛCDM+μ_0+γ_0, the differences between using S^3 and T-RECS are not significant.

However, since the galaxy bias has so large impact in the signal of local PNG, there is a significant difference in the constraints on $f_{\rm NL}$ using each simulation. Using S^3 the constraints are $\sim 3-4$ times better using all galaxies as a single tracer and combining the galaxy power spectra and the ISW. Then, EMU alone would be able to improve current bounds on $f_{\rm NL}$, even without performing a multi-tracer analysis , measuring $\sigma_{f_{\rm NL}} \sim 5$. Using two different tracers, the difference between the results from each simulation assuming a single redshift bin is negligible. However, as considering S^3 AGNs are more abundant than SFGs and they do not suffer from low numbers in the high redshift bins, the constraints using five redhsift bins improve with respect to those using only one (as it was the case considering T-RECS).

Survey	# redshift bins	Bias uncertainty	Data combination and constraints on extended models					
			Galaxy Clustering (GC)		GC+ISW		GC+ISW+Planck*	
EMU Design Sensitivity (10 μJy rms/beam) Using S^3 simulation			$f_{\rm NL}$		$f_{\rm NL}$		$f_{\rm NL}$	
	1 bin	Known	19		18		5.4	
		$\Delta b_{\rm all}$	29		19		5.5	
		$\Delta b_{\rm all}$ & $\Delta s_{\rm all}$	49		40		6.0	
	5 bins	Known	5.7		5.5		3.6	
		$\Delta b_{\rm all}$	5.8		5.6		3.6	
		Δb_i	6.0		5.8		3.8	
		Δb_i & Δs_i	6.3		6.1		3.8	
			w_0	w_a	w_0	w_a	w_0	w_a
	1 bin	Known	6.5	35	2.0	6.0	0.19	0.45
		$\Delta b_{\rm all}$	13	66	2.3	6.1	0.25	0.71
		$\Delta b_{\rm all}$ & $\Delta s_{\rm all}$	15	79	3.0	7.7	0.26	0.73
	5 bins	Known	0.43	1.3	0.40	1.1	0.17	0.43
		$\Delta b_{\rm all}$	0.44	2.0	0.40	1.2	0.19	0.57
		Δb_i	1.0	4.0	0.71	2.0	0.24	0.67
		Δb_i & Δs_i	1.6	5.8	1.0	2.6	0.25	0.70
			$100 \times \Omega_k$		$100 \times \Omega_k$		$100 \times \Omega_k$	
	1 bin	Known	7.6		7.1		0.16	
		$\Delta b_{\rm all}$	7.8		7.1		0.19	
		$\Delta b_{\rm all}$ & $\Delta s_{\rm all}$	7.9		7.2		0.19	
	5 bins	Known	4.7		3.5		0.16	
		$\Delta b_{\rm all}$	8.3		5.7		0.18	
		Δb_i	9.0		5.8		0.19	
		Δb_i & Δs_i	9.9		6.0		0.19	
			μ_0	γ_0	μ_0	γ_0	μ_0	γ_0
	1 bin	Known	10	23	1.1	2.6	0.15	0.35
		$\Delta b_{\rm all}$	10	23	1.2	2.6	0.20	0.45
		$\Delta b_{\rm all}$ & $\Delta s_{\rm all}$	12	26	1.3	2.7	0.20	0.45
	5 bins	Known	0.37	1.1	0.28	0.67	0.12	0.28
		$\Delta b_{\rm all}$	1.2	2.8	0.46	1.0	0.18	0.40
		Δb_i	2.9	6.4	0.49	1.1	0.19	0.42
		Δb_i & Δs_i	4.4	9.8	0.50	1.1	0.19	0.42

Table 9. Same as in tables 4, 5, 6 and 7, but only for the EMU survey at design sensitivity and using the S^3 simulation [52] instead of T-RECS to obtain the redshift distribution of sources and the bias. "+Planck*" means Planck+BAO in all case but in the ΛCDM+μ_0+γ_0 constraints, where means Planck+BAO+RSD.

Survey	# redshift bins	Bias uncertainty	Data combination and constraints on extended models					
			Galaxy Clustering (GC)		GC+ISW		GC+ISW+Planck*	
EMU with multi-tracer Design Sensitivity (10 μJy rms/beam) Using S^3			$f_{\rm NL}$		$f_{\rm NL}$		$f_{\rm NL}$	
	1 bin	Known	4.3		4.3		3.0	
		$\Delta b_{\rm all}$	4.6		4.3		3.1	
		$\Delta b_{\rm all}$ & $\Delta s_{\rm all}$	6.1		5.7		3.1	
	5 bins	Known	3.8		3.7		3.0	
		$\Delta b_{\rm all}$	4.0		3.8		3.2	
		Δb_i	4.9		4.6		3.5	
		Δb_i & Δs_i	4.8		3.7		3.2	
			w_0	w_a	w_0	w_a	w_0	w_a
	1 bin	Known	1.2	3.5	0.85	2.4	0.17	0.43
		$\Delta b_{\rm all}$	1.5	6.2	1.0	2.9	0.20	0.47
		$\Delta b_{\rm all}$ & $\Delta s_{\rm all}$	2.8	12	1.3	3.6	0.26	0.71
	5 bins	Known	0.40	1.2	0.35	1.0	0.16	0.43
		$\Delta b_{\rm all}$	0.41	1.3	0.36	1.1	0.18	0.47
		Δb_i	0.98	3.8	0.55	1.6	0.24	0.65
		Δb_i & Δs_i	1.4	5.9	0.67	1.8	0.24	0.67
			$100 \times \Omega_k$		$100 \times \Omega_k$		$100 \times \Omega_k$	
	1 bin	Known	4.3		3.7		0.16	
		$\Delta b_{\rm all}$	6.0		4.5		0.16	
		$\Delta b_{\rm all}$ & $\Delta s_{\rm all}$	6.1		4.6		0.19	
	5 bins	Known	3.2		2.8		0.16	
		$\Delta b_{\rm all}$	3.7		3.1		0.17	
		Δb_i	9.6		5.3		0.19	
		Δb_i & Δs_i	11		5.7		0.19	
			μ_0	γ_0	μ_0	γ_0	μ_0	γ_0
	1 bin	Known	0.74	1.9	0.45	1.0	0.14	0.31
		$\Delta b_{\rm all}$	3.1	6.3	0.64	1.4	0.14	0.32
		$\Delta b_{\rm all}$ & $\Delta s_{\rm all}$	5.8	12	0.65	1.5	0.19	0.43
	5 bins	Known	0.29	0.73	0.24	0.56	0.12	0.29
		$\Delta b_{\rm all}$	0.32	0.77	0.26	0.60	0.12	0.29
		Δb_i	1.2	2.7	0.44	0.99	0.18	0.41
		Δb_i & Δs_i	1.7	3.7	0.46	1.0	0.19	0.41

Table 10. Same as in table 8, but using the S^3 simulation [52] instead of T-RECS to obtain the redshift distribution of sources and the bias.

References

[1] PLANCK collaboration, *Planck 2018 results. VI. Cosmological parameters*, arXiv:1807.06209 [INSPIRE].

[2] BOSS collaboration, *The clustering of galaxies in the completed SDSS-III Baryon Oscillation Spectroscopic Survey: cosmological analysis of the DR12 galaxy sample*, *Mon. Not. Roy. Astron. Soc.* **470** (2017) 2617 [arXiv:1607.03155] [INSPIRE].

[3] A.G. Riess et al., *A 2.4% determination of the local value of the Hubble constant*, *Astrophys. J.* **826** (2016) 56 [arXiv:1604.01424] [INSPIRE].

[4] A.G. Riess et al., *Milky Way Cepheid standards for measuring cosmic distances and application to Gaia DR2: implications for the Hubble constant*, *Astrophys. J.* **861** (2018) 126 [arXiv:1804.10655] [INSPIRE].

[5] J.L. Bernal, L. Verde and A.G. Riess, *The trouble with* H_0, *JCAP* **10** (2016) 019 [arXiv:1607.05617] [INSPIRE].

[6] J. Luis Bernal and J.A. Peacock, *Conservative cosmology: combining data with allowance for unknown systematics*, *JCAP* **07** (2018) 002 [arXiv:1803.04470] [INSPIRE].

[7] V. Poulin, K.K. Boddy, S. Bird and M. Kamionkowski, *Implications of an extended dark energy cosmology with massive neutrinos for cosmological tensions*, *Phys. Rev.* **D 97** (2018) 123504 [arXiv:1803.02474] [INSPIRE].

[8] E. Di Valentino, A. Melchiorri and O. Mena, *Can interacting dark energy solve the* H_0 *tension?*, *Phys. Rev.* **D 96** (2017) 043503 [arXiv:1704.08342] [INSPIRE].

[9] E. Di Valentino, A. Melchiorri and J. Silk, *Reconciling Planck with the local value of* H_0 *in extended parameter space*, *Phys. Lett.* **B 761** (2016) 242 [arXiv:1606.00634] [INSPIRE].

[10] F. D'Eramo, R.Z. Ferreira, A. Notari and J.L. Bernal, *Hot axions and the* H_0 *tension*, *JCAP* **11** (2018) 014 [arXiv:1808.07430] [INSPIRE].

[11] J.J. Condon et al., *The NRAO VLA sky survey*, *Astrophys. J.* **115** (1998) 1693.

[12] S.P. Boughn and R.G. Crittenden, *Cross-correlation of the cosmic microwave background with radio sources: constraints on an accelerating universe*, *Phys. Rev. Lett.* **88** (2002) 021302 [astro-ph/0111281] [INSPIRE].

[13] R.A. Overzier, H.J.A. Rottgering, R.B. Rengelink and R.J. Wilman, *The spatial clustering of radio sources in nvss and first: implications for galaxy clustering evolution*, *Astron. Astrophys.* **405** (2003) 53 [astro-ph/0304160] [INSPIRE].

[14] S. Boughn and R. Crittenden, *A correlation of the cosmic microwave sky with large scale structure*, *Nature* **427** (2004) 45 [astro-ph/0305001] [INSPIRE].

[15] WMAP collaboration, *First year Wilkinson Microwave Anisotropy Probe (WMAP) observations: dark energy induced correlation with radio sources*, *Astrophys. J.* **608** (2004) 10 [astro-ph/0305097] [INSPIRE].

[16] K.M. Smith, O. Zahn and O. Dore, *Detection of gravitational lensing in the Cosmic Microwave Background*, *Phys. Rev.* **D 76** (2007) 043510 [arXiv:0705.3980] [INSPIRE].

[17] A. Raccanelli et al., *A reassessment of the evidence of the Integrated Sachs-Wolfe effect through the WMAP-NVSS correlation*, *Mon. Not. Roy. Astron. Soc.* **386** (2008) 2161 [arXiv:0802.0084].

[18] S. Ho, C. Hirata, N. Padmanabhan, U. Seljak and N. Bahcall, *Correlation of CMB with large-scale structure: I. ISW tomography and cosmological implications*, *Phys. Rev.* **D 78** (2008) 043519 [arXiv:0801.0642] [INSPIRE].

[19] N. Afshordi and A.J. Tolley, *Primordial non-Gaussianity, statistics of collapsed objects and the Integrated Sachs-Wolfe effect*, *Phys. Rev.* **D 78** (2008) 123507 [arXiv:0806.1046] [INSPIRE].

[20] J.-Q. Xia et al., *A cross-correlation study of the Fermi-LAT γ-ray diffuse extragalactic signal*, *Mon. Not. Roy. Astron. Soc.* **416** (2011) 2247 [arXiv:1103.4861].

[21] M. Rubart and D.J. Schwarz, *Cosmic radio dipole from NVSS and WENSS*, *Astron. Astrophys.* **555** (2013) A117 [arXiv:1301.5559] [INSPIRE].

[22] T. Giannantonio et al., *Improved primordial non-gaussianity constraints from measurements of galaxy clustering and the integrated Sachs-Wolfe effect*, *Phys. Rev.* **D 89** (2014) 023511 [arXiv:1303.1349] [INSPIRE].

[23] A. Nusser and P. Tiwari, *The clustering of radio galaxies: biasing and evolution versus stellar mass*, *Astrophys. J.* **812** (2015) 85 [arXiv:1505.06817] [INSPIRE].

[24] PLANCK collaboration, *Planck 2015 results. XXI. The integrated Sachs-Wolfe effect*, *Astron. Astrophys.* **594** (2016) A21 [arXiv:1502.01595] [INSPIRE].

[25] A. Raccanelli, *Gravitational wave astronomy with radio galaxy surveys*, *Mon. Not. Roy. Astron. Soc.* **469** (2017) 656 [arXiv:1609.09377] [INSPIRE].

[26] A. Raccanelli et al., *Cosmological measurements with forthcoming radio continuum surveys*, *Mon. Not. Roy. Astron. Soc.* **424** (2012) 801 [arXiv:1108.0930].

[27] S. Camera et al., *Impact of redshift information on cosmological applications with next-generation radio surveys*, *Mon. Not. Roy. Astron. Soc.* **427** (2012) 2079 [arXiv:1205.1048].

[28] A. Raccanelli et al., *Probing primordial non-Gaussianity via iSW measurements with SKA continuum surveys*, *JCAP* **01** (2015) 042 [arXiv:1406.0010] [INSPIRE].

[29] D. Bertacca et al., *CMB-galaxy correlation in unified dark matter scalar field cosmologies*, *JCAP* **03** (2011) 039 [arXiv:1102.0284] [INSPIRE].

[30] M.J. Jarvis et al., *Cosmology with SKA radio continuum surveys*, arXiv:1501.03825 [INSPIRE].

[31] S. Camera, M.G. Santos and R. Maartens, *Probing primordial non-Gaussianity with SKA galaxy redshift surveys: a fully relativistic analysis*, *Mon. Not. Roy. Astron. Soc.* **448** (2015) 1035 [*Erratum ibid.* **467** (2017) 1505] [arXiv:1409.8286] [INSPIRE].

[32] L.D. Ferramacho, M.G. Santos, M.J. Jarvis and S. Camera, *Radio galaxy populations and the multitracer technique: pushing the limits on primordial non-Gaussianity*, *Mon. Not. Roy. Astron. Soc.* **442** (2014) 2511 [arXiv:1402.2290] [INSPIRE].

[33] A. Raccanelli et al., *Future constraints on angle-dependent non-Gaussianity from large radio surveys*, *Phys. Dark Univ.* **15** (2017) 35.

[34] D. Karagiannis et al., *Constraining primordial non-Gaussianity with bispectrum and power spectrum from upcoming optical and radio surveys*, *Mon. Not. Roy. Astron. Soc.* **478** (2018) 1341 [arXiv:1801.09280] [INSPIRE].

[35] G. Scelfo et al., *GW×LSS: chasing the progenitors of merging binary black holes*, *JCAP* **09** (2018) 039 [arXiv:1809.03528] [INSPIRE].

[36] M. Ballardini, F. Finelli, R. Maartens and L. Moscardini, *Probing primordial features with next-generation photometric and radio surveys*, *JCAP* **04** (2018) 044 [arXiv:1712.07425] [INSPIRE].

[37] D. Alonso, E. Bellini, P.G. Ferreira and M. Zumalacárregui, *Observational future of cosmological scalar-tensor theories*, *Phys. Rev.* **D 95** (2017) 063502 [arXiv:1610.09290] [INSPIRE].

[38] R.P. Norris et al., *EMU: Evolutionary Map of the Universe*, *Publ. Astron. Soc. Austral.* **28** (2011) 215 [arXiv:1106.3219] [INSPIRE].

[39] S. Johnston et al., *Science with the Australian Square Kilometre Array Pathfinder*, *PASA* **24** (2007) 174.

[40] S. Johnston et al., *Science with ASKAP. The Australian Square-Kilometre-Array Pathfinder*, *Exp. Astron.* **22** (2008) 151.

[41] R.P. Norris et al., *Radio continuum surveys with Square Kilometre Array Pathfinders*, *Publ. Astron. Soc. Austral.* **30** (2013) 20 [`arXiv:1210.7521`] [INSPIRE].

[42] N. Bartolo, E. Komatsu, S. Matarrese and A. Riotto, *Non-Gaussianity from inflation: theory and observations*, *Phys. Rept.* **402** (2004) 103 [`astro-ph/0406398`] [INSPIRE].

[43] E. Komatsu, *Hunting for primordial non-gaussianity in the Cosmic Microwave Background*, *Class. Quant. Grav.* **27** (2010) 124010 [`arXiv:1003.6097`] [INSPIRE].

[44] D. Wands, *Local non-Gaussianity from inflation*, *Class. Quant. Grav.* **27** (2010) 124002 [`arXiv:1004.0818`] [INSPIRE].

[45] M. Alvarez et al., *Testing inflation with large scale structure: connecting hopes with reality*, `arXiv:1412.4671` [INSPIRE].

[46] R. P. Norris, M. Salvato and G. Longo, , in preparation.

[47] K.J. Luken, R.P. Norris, and L.A.F. Park, *Preliminary results of using k-nearest neighbours regression to estimate the redshift of radio selected datasets*, `arXiv:1810.10714`.

[48] B. Ménard et al., *Clustering-based redshift estimation: method and application to data*, `arXiv:1303.4722` [INSPIRE].

[49] M. Rahman et al., *Clustering-based redshift estimation: comparison to spectroscopic redshifts*, *Mon. Not. Roy. Astron. Soc.* **447** (2015) 3500 [`arXiv:1407.7860`] [INSPIRE].

[50] E.D. Kovetz, A. Raccanelli and M. Rahman, *Cosmological constraints with clustering-based redshifts*, *Mon. Not. Roy. Astron. Soc.* **468** (2017) 3650 [`arXiv:1606.07434`] [INSPIRE].

[51] A. Bonaldi et al., *The Tiered Radio Extragalactic Continuum Simulation (T-RECS)*, *Mon. Not. Roy. Astron. Soc.* **482** (2019) 2 [`arXiv:1805.05222`] [INSPIRE].

[52] R.J. Wilman et al., *A semi-empirical simulation of the extragalactic radio continuum sky for next generation radio telescopes*, *Mon. Not. Roy. Astron. Soc.* **388** (2008) 1335.

[53] U. Seljak, *Extracting primordial non-Gaussianity without cosmic variance*, *Phys. Rev. Lett.* **102** (2009) 021302 [`arXiv:0807.1770`] [INSPIRE].

[54] P. McDonald and U. Seljak, *How to measure redshift-space distortions without sample variance*, *JCAP* **10** (2009) 007 [`arXiv:0810.0323`] [INSPIRE].

[55] A. Raccanelli et al., *Cosmological measurements with forthcoming radio continuum surveys*, *Mon. Not. Roy. Astron. Soc.* **424** (2012) 801.

[56] T. Matsubara, *The gravitational lensing in redshift-space correlation functions of galaxies and quasars*, *Astrophys. J.* **537** (2000) L77 [`astro-ph/0004392`] [INSPIRE].

[57] M. Bartelmann and P. Schneider, *Weak gravitational lensing*, *Phys. Rept.* **340** (2001) 291.

[58] J. Liu, Z. Haiman, L. Hui, J.M. Kratochvil and M. May, *The Impact of Magnification and Size Bias on Weak Lensing Power Spectrum and Peak Statistics*, *Phys. Rev.* **D 89** (2014) 023515 [`arXiv:1310.7517`] [INSPIRE].

[59] N. Bellomo, J.L. Bernal, A. Raccanelli, L. Verde and G. Scelfo, *On the importance of a correct modelling in the multitracer era*, in preparation.

[60] J. Lesgourgues, *The Cosmic Linear Anisotropy Solving System (CLASS) I: Overview*, `arXiv:1104.2932` [INSPIRE].

[61] J. Yoo, A.L. Fitzpatrick and M. Zaldarriaga, *A new perspective on galaxy clustering as a cosmological probe: general relativistic effects*, *Phys. Rev.* **D 80** (2009) 083514 [`arXiv:0907.0707`] [INSPIRE].

[62] J. Yoo, *General relativistic description of the observed galaxy power spectrum: do we understand what we measure?*, *Phys. Rev.* **D 82** (2010) 083508 [`arXiv:1009.3021`] [INSPIRE].

[63] C. Bonvin and R. Durrer, *What galaxy surveys really measure*, *Phys. Rev.* **D 84** (2011) 063505 [`arXiv:1105.5280`] [INSPIRE].

[64] A. Challinor and A. Lewis, *The linear power spectrum of observed source number counts*, *Phys. Rev.* **D 84** (2011) 043516 [`arXiv:1105.5292`] [INSPIRE].

[65] D. Jeong, F. Schmidt and C.M. Hirata, *Large-scale clustering of galaxies in general relativity*, *Phys. Rev.* **D 85** (2012) 023504 [`arXiv:1107.5427`] [INSPIRE].

[66] D. Bertacca, R. Maartens, A. Raccanelli and C. Clarkson, *Beyond the plane-parallel and Newtonian approach: Wide-angle redshift distortions and convergence in general relativity*, *JCAP* **10** (2012) 025 [`arXiv:1205.5221`] [INSPIRE].

[67] A. Raccanelli et al., *Cosmological measurements with general relativistic galaxy correlations*,' *JCAP* **05** (2016) 009.

[68] A. Raccanelli, D. Bertacca, R. Maartens, C. Clarkson and O. Doré, *Lensing and time-delay contributions to galaxy correlations*, *Gen. Rel. Grav.* **48** (2016) 84 [`arXiv:1311.6813`] [INSPIRE].

[69] A. Raccanelli, D. Bertacca, D. Jeong, M.C. Neyrinck and A.S. Szalay, *Doppler term in the galaxy two-point correlation function: wide-angle, velocity, Doppler lensing and cosmic acceleration effects*, *Phys. Dark Univ.* **19** (2018) 109 [`arXiv:1602.03186`] [INSPIRE].

[70] E. Di Dio, F. Montanari, J. Lesgourgues and R. Durrer, *The CLASSgal code for relativistic cosmological large scale structure*, *JCAP* **11** (2013) 044 [`arXiv:1307.1459`] [INSPIRE].

[71] A. Raccanelli et al., *Lensing and time-delay contributions to galaxy correlations*, *Gen. Rel. Grav.* **48** (2016) 84 [`arXiv:1311.6813`] [INSPIRE].

[72] T. Giannantonio et al., *Combined analysis of the integrated Sachs-Wolfe effect and cosmological implications*, *Phys. Rev.* **D 77** (2008) 123520 [`arXiv:0801.4380`] [INSPIRE].

[73] N. Afshordi, Y.-S. Loh and M.A. Strauss, *Cross-correlation of the Cosmic Microwave Background with the 2MASS galaxy survey: signatures of dark energy, hot gas and point sources*, *Phys. Rev.* **D 69** (2004) 083524 [`astro-ph/0308260`] [INSPIRE].

[74] P. Fosalba and E. Gaztanaga, *Measurement of the gravitational potential evolution from the cross-correlation between wmap and the apm galaxy survey*, *Mon. Not. Roy. Astron. Soc.* **350** (2004) L37 [`astro-ph/0305468`] [INSPIRE].

[75] SDSS collaboration, *Physical evidence for dark energy*, `astro-ph/0307335` [INSPIRE].

[76] K. Kotera, D. Allard and A.V. Olinto, *Cosmogenic neutrinos: parameter space and detectabilty from PeV to ZeV*, *JCAP* **10** (2010) 013 [`arXiv:1009.1382`] [INSPIRE].

[77] S. Matarrese, L. Verde and R. Jimenez, *The abundance of high-redshift objects as a probe of non-Gaussian initial conditions*, *Astrophys. J.* **541** (2000) 10 [`astro-ph/0001366`] [INSPIRE].

[78] N. Dalal, O. Dore, D. Huterer and A. Shirokov, *The imprints of primordial non-Gaussianities on large-scale structure: scale dependent bias and abundance of virialized objects*, *Phys. Rev.* **D 77** (2008) 123514 [`arXiv:0710.4560`] [INSPIRE].

[79] S. Matarrese and L. Verde, *The effect of primordial non-Gaussianity on halo bias*, *Astrophys. J.* **677** (2008) L77 [`arXiv:0801.4826`] [INSPIRE].

[80] V. Desjacques and U. Seljak, *Primordial non-Gaussianity from the large scale structure*, *Class. Quant. Grav.* **27** (2010) 124011 [`arXiv:1003.5020`] [INSPIRE].

[81] M. Chevallier and D. Polarski, *Accelerating universes with scaling dark matter*, *Int. J. Mod. Phys.* **D 10** (2001) 213.

[82] E.V. Linder, *Exploring the expansion history of the universe*, *Phys. Rev. Lett.* **90** (2003) 091301 [`astro-ph/0208512`] [INSPIRE].

[83] J.M. Ezquiaga and M. Zumalacárregui, *Dark energy in light of multi-messenger gravitational-wave astronomy*, *Front. Astron. Space Sci.* **5** (2018) 44 [`arXiv:1807.09241`].

[84] J.L. Bernal, L. Verde and A.J. Cuesta, *Parameter splitting in dark energy: is dark energy the same in the background and in the cosmic structures?*, *JCAP* **02** (2016) 059 [`arXiv:1511.03049`] [INSPIRE].

[85] L. Amendola, M. Kunz and D. Sapone, *Measuring the dark side (with weak lensing)*, *JCAP* **04** (2008) 013 [`arXiv:0704.2421`] [INSPIRE].

[86] G.-B. Zhao et al., *Probing modifications of general relativity using current cosmological observations*, *Phys. Rev.* **D 81** (2010) 103510 [`arXiv:1003.0001`] [INSPIRE].

[87] T. Baker and P. Bull, *Observational signatures of modified gravity on ultra-large scales*, *Astrophys. J.* **811** (2015) 116 [`arXiv:1506.00641`] [INSPIRE].

[88] R.A. Fisher, *The fiducial argument in statistical inference*, *Annals Eugen.* **6** (1935) 391.

[89] M. Tegmark, A. Taylor and A. Heavens, *Karhunen-Loeve eigenvalue problems in cosmology: How should we tackle large data sets?*, *Astrophys. J.* **480** (1997) 22 [`astro-ph/9603021`] [INSPIRE].

[90] L. Verde et al., *First-year Wilkinson Microwave Anisotropy Probe (WMAP) observations: parameter estimation methodology*, *Astrophys. J. Suppl. Ser.* **148** (2003) 195.

[91] E. Sellentin, M. Quartin and L. Amendola, *Breaking the spell of Gaussianity: forecasting with higher order Fisher matrices*, *Mon. Not. Roy. Astron. Soc.* **441** (2014) 1831 [`arXiv:1401.6892`] [INSPIRE].

[92] F. Beutler et al., *The 6dF galaxy survey: baryon acoustic oscillations and the local Hubble constant*, *Mon. Not. Roy. Astron. Soc.* **416** (2011) 3017 [`arXiv:1106.3366`].

[93] A.J. Ross et al., *The clustering of the SDSS DR7 main Galaxy sample — I. A 4 per cent distance measure at* $z = 0.15$, *Mon. Not. Roy. Astron. Soc.* **449** (2015) 835 [`arXiv:1409.3242`] [INSPIRE].

[94] PLANCK collaboration, *Planck 2015 results. XVII. Constraints on primordial non-Gaussianity*, *Astron. Astrophys.* **594** (2016) A17 [`arXiv:1502.01592`] [INSPIRE].

[95] A. Raccanelli, O. Dore and N. Dalal, *Optimization of spectroscopic surveys for testing non-Gaussianity*, *JCAP* **08** (2015) 034 [`arXiv:1409.1927`] [INSPIRE].

[96] SKA collaboration, *Cosmology with phase 1 of the Square Kilometre Array: Red Book 2018: technical specifications and performance forecasts*, *Submitted to: Publ. Astron. Soc. Austral.* (2018) [`arXiv:1811.02743`] [INSPIRE].

[97] M. Borzyszkowski, D. Bertacca and C. Porciani, *LIGER: mock relativistic light-cones from Newtonian simulations*, *Mon. Not. Roy. Astron. Soc.* **471** (2017) 3899 [`arXiv:1703.03407`] [INSPIRE].

4.2 Optimal extraction of cosmological information from line-intensity mapping

Line-intensity mapping (IM) provides a promising way to probe cosmology, reionization and galaxy evolution. However, being so sensitive to cosmology and astrophysics at the same time may become a nuisance. Here we propose a methodology to optimally extract cosmological information from the anisotropic IM power spectrum, accounting for the uncertainties in astrophysical sector. We parametrize astrophysical contributions to the IM power spectrum and marginalize over them so that the impact on the cosmological measurements is minimized. In addition, we account for redshift space distortions, the Alcock-Paczynski effect, different regimes in the mode counting depending on the dimensions of the volume observed, and provide an accurate analytic prescription for the covariance matrix of the multipoles of the IM power spectrum. Although we mostly focus on the auto-power spectrum, we also discuss the adaptation of the methodology to cross-correlations for completeness. Altogether, our formalism facilitates cosmological constraints robust to astrophysics.

We study the gains of including the hexadecapole of the IM power spectrum in the analysis, finding a 25%-75% increase in the precision of the BAO scale measurements when included. As an illustration of the potential of our formalism, we estimate future constraints from IM power spectrum measurements on the sum of neutrino masses and local primordial non Gaussianiaties. We find that an experiment targeting CO at high redshift, observing a quarter of the sky during $\sim$ 30000, hours can achieve 68% confidence level marginalized errors $\sigma\left(\sum m\nu\right) \sim 0.05$ eV and $\sigma\left(f_{\rm NL}\right) \sim 5$, respectively.

Considering the power of the formalism presented in this work, we recommend its use for cosmological analyses of the IM power spectrum to fulfill the promising potential of IM experiments.

4.2.1 Introduction

An impressive experimental effort put in galaxy surveys, in combination with Cosmic Microwave Background (CMB) observations, has achieved percent level precision in the inferred cosmological parameters of the standard cosmological model, Λ-Cold Dark Matter (ΛCDM), and provided stringent constraints on possible deviations from it (Planck Collaboration et al., 2018; Alam et al., 2017b). This success has encouraged further investment for the coming years on experiments measuring the large scale structure, whose outcome will further constrain or detect physics beyond ΛCDM (Bernal et al., 2019; DESI Collaboration et al., 2016a; Amendola et al., 2018; Doré et al., 2014; Square Kilometre Array Cosmology Science Working Group et al., 2018).

Galaxy surveys rely on resolving individual galaxies to trace the matter density field, which naturally limits their scope to $z \lesssim 2$, reaching $z \lesssim 3$ only thanks to Lyman-α forest measurements (see e.g., de Sainte Agathe et al. (2019); Blomqvist et al. (2019)). Although there are proposals motivating the use of spectroscopic observations of Lyman-break galaxies to reach $z \sim 5$ (Wilson & White, 2019; Ferraro et al., 2019), it is extremely unlikely that a galaxy survey. This is mainly because galaxy surveys only use sources brighter than a given threshold and treat them as number counts, while galaxies at high redshift are sparse and faint. In addition, the need of observing individual resolved sources with a high signal-to-noise ratio (S/N) slows down the sky coverage, and therefore increases the budget required to carry out the survey.

On the other hand, intensity mapping (IM) experiments propose a great alternative. IM techniques use all the observed flux coming from the sky, hence exploiting unresolved and much fainter sources, too. These faint sources would not satisfy the requirements to be claimed as a detected source in a galaxy survey. Basically, IM integrates all the emission along the line of sight. This way, IM techniques grant access to significantly larger redshifts than galaxy surveys. The dark ages could also be probed thanks to IM (theoretically, up to $z \lesssim 500$ (Breysse et al., 2018)), which would provide strong constraints on deviations from ΛCDM, as explored in Bernal et al. (2018); Short et al. (2019); Furlanetto et al. (2019a).

Conveniently, no resolved sources are needed, which softens the angular resolution requirements and allows to survey the sky fast. Targeting easily-identifiable spectral lines and tuning the frequency of the receivers makes possible to measure the redshift of the emission along a line of sight. On the other hand, the intensity of each line is intimately related with various astrophysical processes, so targeting different lines allows to study reionization and galaxy evolution. Moreover, since these lines are sourced in halos, they act as a biased tracer of the underlying density distribution, with the bias depending on the specific line. In this way, accurate three-dimensional maps of the large scale structure of the Universe over huge volumes can be obtained. Altogether, IM experiments hold great promise both for cosmology and astrophysics (Kovetz et al., 2017, 2019).

Several lines can be targeted with IM. Probably, the most study line to date is HI 21, first detected by Chang et al. (2010). Some 21 cm IM experiments will target the epoch of reionization (Bandura et al., 2014; DeBoer et al., 2017), while the planned Square Kilometer Array has great potential for cosmology at low redshift (Bull et al., 2015; Square Kilometre Array Cosmology Science Working Group et al., 2018), and is expected to probe fundamental physics, too (Bull et al., 2018). However, HI line is weak, especially when compared with galactic foregrounds in the frequency range of interest. Other lines have also been subject of study, such as the rotational lines of CO (Li et al., 2016; Padmanabhan, 2018a), CII (Silva et al., 2015; Pullen et al., 2018; Padmanabhan, 2018b), Hα and Hβ (Gong et al., 2017; Silva et al., 2018), oxygen lines (Gong et al., 2017), and Lymanα (Silva et al., 2013), among others. Some of them have been already detected at intermediate redshifts (Keating et al., 2015, 2016), at least tentatively (Pullen et al., 2018; Croft et al., 2016). A significant effort is being invested preparing the stage 2 of IM, with some experiments which have already started observing and some others which soon will do it, as COMAP (Cleary et al., 2016), TIME (Crites et al., 2014), and SPHEREx (Doré et al., 2014), among others.

The plethora of possible targeted lines facilitates multitracer techniques, which reduces cosmic variance (Seljak, 2009; McDonald & Seljak, 2009). Nonetheless, non-targeted spectral lines may also introduce contamination in the observed signal acting as interlopers, due to redshift confussion. This contamination, as well as galactic foregrounds, must be subtracted and corrected for. Cross-correlations of different spectral lines, or between one line and galaxy number counts, are one of the most optimal techniques to identify and remove foregrounds and interlopers (see e.g., Sun et al. (2018); Silva et al. (2013)). Other strategies to remove foreground and interloper contaminations include the identification of a distorted Alcock-Paczynski effect (Cheng et al., 2016) and blindly masking the brightest sources (Breysse et al., 2015).

The dependence of the spectral line intensity on both astrophysical processes and cosmology entails degeneracies in the observed signal. Given the high level of ignorance regarding the luminosity function of spectral lines at high redshift, being able to disentangle cosmology and astrophysics is of utmost importance. Otherwise, these degeneracies hinder the extraction of clean information from the observations. Nevertheless, the interrelation between cosmology and astrophysics is often neglected when IM observations are analyzed or forecasted, fixing the sector that is not targeted. Ignoring the astrophysical uncertainties when extracting cosmological constraints from IM observations may result in a considerable underestimation of the errors.

Here we propose and develop a general formalism applicable to any spectral line, to optimally extract cosmological information from the IM power spectrum. This methodology builds upon some concepts imported from galaxy surveys, and marginalizes over the astrophysical uncertainties. We primarily focus on the best strategy to maximize the precision of the BAO scale measurements through the Alcock-Paczynski effect. We take into account redshift space distortions and that the anisotropic observed power spectrum will need to be compressed in Legendre multipoles (or in angular wedges). Applying our methodology, the measured BAO scale becomes robust to astrophysics. On the other hand, constraining the growth rate would need prior information about the mean brightness temperature. We also discuss how this formalism can be extended to infer the value of other cosmological parameters, as the sum of neutrino masses and primordial non Gaussianity in the local limit. For completeness, we also provide the optimal parametrization for cross-correlations between spectral lines or between one line and galaxy number counts.

In any case, it is important to bear in mind that brightness temperature fluctuations are far from following a Gaussian distribution. Therefore, not all the information contained in the IM signal is encoded in the corresponding power spectrum. Alternative summary statistics, as the bispectrum or the voxel intensity distribution, are then needed in order to exhaust the information encoded in IM observations. Concretely, the voxel intensity distribution is more sensitive to the line luminosity function than the IM power spectrum, as shown in Breysse et al. (2017), and it may very well provide a prior on the astrophysics. Of course, both the IM power spectrum and the voxel intensity distribution can be measured and analyzed at the same time, taking into account the correlation between them (Ihle et al., 2019).

In a companion paper (Bernal et al., 2019a), we propose the use of BAO measurements obtained from IM observations to obtain cosmic rulers at the epoch of reionization. We also highlight the great potential of the methodology presented in this work to optimize the BAO measurements and constrain the expansion history without contamination from astrophysical uncertainties. In addition, our formalism could be adapted to measure the velocity-induced acoustic oscillations (Muñoz, 2019b), recently proposed as standard ruler during the cosmic dawn in Muñoz (2019a), in a more robust way.

We modify the public code `LIM`[1] to analytically compute the anisotropic IM power spectrum and the corresponding covariance. This modified version uses outputs from `CAMB`[2] (Lewis et al., 2000) and `Pylians`[3] (Villaescusa-Navarro, 2018) to obtain the matter power spectrum and other cosmological quantities, and the halo mass function and halo bias, respectively.

This manuscript is structured as follows. In Section 4.2.2 we review the basics of the anisotropic IM power spectrum in redshift space. Afterwards, the optimal parametrization to measure the Legendre multipoles of the IM power spectrum and maximize the extraction of cosmological information is discussed in Section 4.2.3, with an accurate analytic prescription of the corresponding covariance between the multipoles presented in Section 4.2.4. Finally, the application of this methodology is discussed in Section 4.2.5, including a motivation to include the hexadecapole in the analysis, as well as illustrative examples of forecasts regarding models beyond ΛCDM. Finally, the conclusions can be found in Section 4.2.6, and an adaptation of our formalism to be applied to cross-correlations is included in Appendix 4.2.7.

---

[1] `https://github.com/pcbreysse/lim`

[2] `https://camb.info/`

[3] `https://github.com/franciscovillaescusa/Pylians`

4.2.2 Intensity Mapping Power Spectrum Modeling

One of the most powerful summary statistics to probe the large scale clustering is the power spectrum. Therefore, here we focus on the brightness temperature, T, (or intensity, I) fluctuations power spectrum. Depending on the frequency band of the experiment, either brightness temperature or intensity are conventionally used to quantify the observed flux. Brightness temperature and intensity depend on the luminosity, L, of a spectral line with rest fram frequency ν at a given redshift as:

$$T(z) = \frac{c^3(1+z)^2}{8\pi k_B \nu^3 H(z)} L, \qquad I(z) = \frac{c}{4\pi\nu H(z)}, \tag{4.1}$$

where c is the speed of light, k_B is the Boltzmann constant and $H(z)$ is the Hubble parameter at redshift z. Both brightness temperature and intensity are continuous fields which trace the matter density field in a different, biased way, depending on the line (e.g., while HI line traces neutral hydrogen, CO rotation lines are found in star forming regions, etc.). This is due to the emission being sourced in halos. Hereinafter, we will use the brightness temperature in order to homogenize the nomenclature, but all the expressions are equally valid if intensity is used instead.

In many cases, it is possible to relate the luminosity of a spectral line to the mass of the host halo, $L(M)$. For instance, it is possible to estimate the hydrogen fraction, or the star formation rate, in a halo of a given mass. This way, the luminosity function can be computed using the halo mass function, $\mathrm{d}n/\mathrm{d}M$, and $L(M)$. Although the luminosity function can be parametrized directly with a fitting function, we consider the former option. An effective linear bias for IM can be computed as a luminosity-averaged halo bias for the targeted line, given by:

$$b = \frac{\int \mathrm{d}M L(M) b_{\mathrm{h}}(M) \frac{\mathrm{d}n}{\mathrm{d}M}}{\int \mathrm{d}M L(M) \frac{\mathrm{d}n}{\mathrm{d}M}}, \tag{4.2}$$

where b_{h} is the halo bias. Since in this work we focus on fairly large scales, we neglect any scale dependence of the halo bias.

In addition, it is important to take into account that these observations are made on redshift space, i.e., the radial coordinate is only given by the redshift of the signal. Therefore, the real space prediction of the IM power spectrum has to be converted into redshift space. This introduces anisotropies in the a priori isotropic real space power spectrum. At linear scales, peculiar velocities boost the power spectrum in redshift space by the Kaiser effect. In turn, small-scale velocities suppress the clustering at small scales, effect known as the fingers of God. We use a Lorentzian damping factor whose scale dependence is driven by the parameter σ_{FoG}, related with the halo velocity dispersion. This damping factor can be also a Gaussian function. We have checked that the results of this work do not depend on the choice between these two options.

The relation between the density perturbations in real and redshift space (δ^r and δ^s, respectively) can be approximated with a linear redshift space distortion factor, such as $\delta^s = F_{\mathrm{RSD}}\delta^r$. The redshift space distortion factor, accounting for Kaiser term and the fingers of God, is given by:

$$F_{\mathrm{RSD}} = \left(1 + \frac{f(z)}{b(z)}\mu^2\right) \frac{1}{1 + 0.5\left(k\mu\sigma_{\mathrm{FoG}}\right)^2}, \tag{4.3}$$

where $f(z)$ is the logarithmic derivative of the growth factor (also known as the growth rate), k is the module of the wavenumber, and $\mu = \hat{k} \cdot \hat{k}_{\parallel}$ is the cosine of the angle between the wavenumber $\vec{k}$ and the line of sight ($\mu \in [-1, 1]$).

Finally, the brightness temperature is a continuous field, hence there is no shot noise contribution due to the discreteness of the field (as happens in galaxy surveys). Nonetheless, there is still a scale-independent contribution to the IM power spectrum sourced by the variance of the brightness temperature, which would be still present even in the absence of clustering. This has been called the shot noise contribution, P_{shot}, due to historical reasons.

Taking all these contributions into account, we can express the anisotropic IM power spectrum as function of k and μ as as the sum of a clustering and shot noise contributions:

$$\begin{aligned} &P(k,\mu) = P_{\mathrm{clust}}(k,\mu) + P_{\mathrm{shot}}; \\ &P_{\mathrm{clust}}(k,\mu) = \langle T\rangle^2 b^2 F_{\mathrm{RSD}}^2(k,\mu) P_{\mathrm{m}}(k); \\ &P_{\mathrm{shot}} = \langle T^2\rangle, \end{aligned} \tag{4.4}$$

where all quantities depend on redshift, P_m is the matter power spectrum, and the moments of the brightness temperature distribution are computed using the halo mass function (as in the denominator of Equation (4.2)).

4.2.3 Measuring the intensity mapping power spectrum

Any IM experiment will have a limited angular and spectral resolution. Therefore, every observation returns a voxelized map of brightness temperature so that the measured power spectrum is always smoothed with respect to the signal that arrives to the telescope. In other words, the *observed* clustering is the result of the convolution of the *true* signal and the voxel window function of the experiment. In Fourier space: $\tilde{P}(k,\mu) = P(k,\mu)W(k,\mu)$, where $\tilde{P}(k,\mu)$ is the power spectrum computed from the *observed* signal, $P(k,\mu)$ is the *true* power spectrum, and $W(k,\mu)$ is the voxel window function. The smoothing due to the voxel window function introduces further anisotropies, and modifies the ratio between $P_{\rm clust}$ and $P_{\rm shot}$. This might facilitate the detection of the IM power spectrum in some cases, as explicitly computed in Chung (2019). However, the cosmological and astrophysical information encoded in this measurement is polluted by some artificial signal introduced by the experiment.

Here we consider a different avenue. If the voxel window function is modeled well enough, it is possible to *deconvolve* the *observed* power spectrum and recover the *true* signal. In this case, we can still use Equation (4.4) to model the IM power spectrum which will be analyzed, since $P(k,\mu) = \tilde{P}(k,\mu)W^{-1}(k,\mu)$. Following this approach, we preserve the cosmological and astrophysical signal in the IM power spectrum unpolluted. As discussed in Section 4.2.4, the voxel window has instead an effect in the noise of the IM power spectrum. Note that in order to avoid the inclusion of observational systematics, an accurate description of the voxel window function is needed, no matter the approach chosen.

As mentioned in Section 4.2.2, to measure the three-dimensional IM power spectrum, it is necessary to transform redshifts into distances. Hence, a further artificial anisotropy is introduced if the fiducial cosmology assumed to apply this transformation does not match the actual cosmology. This effect, known as the Alcock-paczynski effect, distorts radial and transverse distances in a different way (Alcock & Paczynski, 1979). In order to model this effect in the theoretical power spectrum, rescaling parameters are use to redefine the distances:

$$\alpha_\perp = \frac{D_A(z)/r_{\rm s}}{\left(D_A(z)/r_{\rm s}\right)^{\rm fid}}, \qquad \alpha_\parallel = \frac{\left(H(z)r_{\rm s}\right)^{\rm fid}}{H(z)r_{\rm s}}, \tag{4.5}$$

where $D_A(z)$ is the angular diameter distance, and r_s is the sound horizon at radiation drag; the superscript 'fid' denotes the corresponding values in the assumed fiducial cosmology. Due to this distortion, the *true* wave numbers are related to the *observed* ones by $k_\perp^\mathrm{tr} = k_\perp^\mathrm{obs}/\alpha_\perp$ and $k_\parallel^\mathrm{tr} = k_\parallel^\mathrm{obs}/\alpha_\parallel$. This relation can be expressed in terms of k and μ (Ballinger et al., 1996):

$$\begin{aligned} k^\mathrm{tr} &= \frac{k^\mathrm{obs}}{\alpha_\perp}\left[1 + \left(\mu^\mathrm{obs}\right)^2\left(F_\mathrm{AP}^{-2} - 1\right)\right]^{-1/2}, \\ \mu^\mathrm{tr} &= \frac{\mu^\mathrm{obs}}{F_\mathrm{AP}}\left[1 + \left(\mu^\mathrm{obs}\right)^2\left(F_\mathrm{AP}^{-2} - 1\right)\right]^{-1/2}, \end{aligned} \tag{4.6}$$

where $F_\mathrm{AP} = \alpha_\parallel/\alpha_\perp$. In addition, the power spectrum needs to be corrected for the modification of the volumes multiplying by the factor: $H(z)/H^\mathrm{fid}(z) \times \left(D_A^\mathrm{fid}(z)/D_A(z)\right)^2$.

Finally, the information encoded in the anisotropic power spectrum can be optimally compressed using Legendre polynomials, $\mathcal{L}_\ell$. Accounting also for the Alcock-Paczynski effect, we can compute the multipoles of the IM power spectrum as:

$$P^\ell(k^\mathrm{obs}) = \frac{H(z)}{H^\mathrm{fid}(z)}\left(\frac{D_A^\mathrm{fid}(z)}{D_A(z)}\right)^2 \frac{2\ell+1}{2}\int_{-1}^{1} \mathrm{d}\mu^\mathrm{obs} P(k^\mathrm{tr}, \mu^\mathrm{tr})\mathcal{L}_\ell(\mu^\mathrm{obs}), \tag{4.7}$$

where $P(k^\mathrm{tr}, \mu^\mathrm{tr})$ is given by Equation (4.4). Another option is to compress the information in bins in μ (wedges), rather than using Legendre multipoles (see e.g., Kazin et al. (2012)). In this work we will focus on the Legendre multipoles of the IM power spectrum, and leave the exploration of the angular wedges for future work.

Equation (4.7) must be used in a smart way in order to maximize the outcome of the observations for cosmology. This is not trivial, since one needs to identify where the information lies and if it is astrophysical or cosmological. First of all, the overall shape of $P_m(k)$ is not very sensitive to small variations of most of the standard cosmological parameters. Taking this into account, it is preferable to use a template for $P_m(k)$ computed on the fiducial cosmology used to transform redshift into distances. Then, the impact of the cosmological model on the IM power spectrum can be modeled only varying terms that relate P_m and $P^\ell(k^\mathrm{obs})$.

The only exception for which this procedure breaks down is when a cosmological parameter clearly modifies P_m, as it could be the sum of neutrino masses, $\sum m_\nu$.

In addition to the growth rate, the amplitude of the clustering contribution of the IM power spectrum at large scales depends on three factors: the luminosity-averaged bias, the amplitude of the matter power spectrum (which can be parametrized with the root mean square of the density fluctuations within 8 $h\mathrm{Mpc}^{-1}$, σ_8), and the mean brightness temperature (see Equation (4.4)). In turn, the amplitude of the shot noise contribution depends solely in $\langle T^2\rangle$. This contrasts with the galaxy power spectrum, which does not have any prefactor for the clustering part, and for which the shot noise is the inverse of the galaxy number density (when the shot noise is assumed to be Poissonian).

Therefore, the terms σ_8, b, and $\langle T\rangle$ are completely degenerate within a measurement of the IM power spectrum at a given single redshift, as well as σ_8, $(1+f\mu^2)$, and $\langle T\rangle$. These degeneracies could be broken using tomography if a cosmological model is assumed, given that each of these quantities evolve in a different way as function of redshift. However, we prefer to remain as model independent as possible and only assume a fiducial cosmology, needed to obtain radial distances and for the template of $P_m(k)$. Another way to break these degeneracies, at least partially, is to measure higher order statistics in combination with the IM power spectrum. We leave the study of higher order statistics for future work.

Taking all this into account, we group all degenerate parameters, and reparametrize the IM power spectrum from Equation (4.4) as:

$$P(k,\mu) = \left(\frac{\langle T\rangle b\sigma_8 + \langle T\rangle f\sigma_8\mu^2}{1+0.5\left(k\mu\sigma_{\mathrm{FoG}}\right)^2}\right)^2 \frac{P_m(k)}{\sigma_8^2} + \langle T^2\rangle, \tag{4.8}$$

where, again, all quantities depend on z. From Equation 4.8, the set of combination of parameters that can be directly measured from the IM power spectrum for each independent redshift bin and patch of the sky observed is:

$$\vec{\theta} = \{\alpha_\perp, \alpha_\parallel, \langle T\rangle f\sigma_8, \langle T\rangle b\sigma_8, \sigma_{\mathrm{FoG}}, \langle T^2\rangle, \vec{\varsigma}\}, \tag{4.9}$$

where $\vec{\varsigma}$ includes all parameters that significantly modify P_m, as discussed above.

In that case, the template used in Equation (4.8) would be $P_m(k, \vec{\varsigma})$ instead (where $\vec{\varsigma}$ woud be varied as free parameters too). Note that in some cases, the parameters embedded in $\vec{\varsigma}$ will be common to all redshifts and patches of the sky, and hence need to be treated differently than the rest. In any case, each IM power spectrum measurement from each sky patch and redshift bin can still be considered independent from the rest, whenever each of these volumes does not overlap with the rest.

Now, we need to ascertain which of the parameters entering Equation (4.9) contain cosmological information and which can be considered as nuisance parameters. Let us begin for $F_{\rm RSD}$: while its contribution at large scales is dominated by f, the small scales, where the fingers of God dominate RSD, are controlled by $\sigma_{\rm FoG}$. It is obvious that f contains cosmological information (it is very sensitive to modifications of General Relativity), but the situation for $\sigma_{\rm FoG}$ is not so clear. Although $\sigma_{\rm FoG}$ is related with the halo velocity dispersion, and therefore contains cosmological information, this is very difficult to trace. Therefore, we prefer to be conservative and consider $\sigma_{\rm FoG}$ as a nuisance parameter.

The luminosity-averaged bias and the moments of the brightness temperature depend mostly on astrophysics, rather than on cosmology. In fact, the only cosmological dependence existing in these quantities is through the halo mass function and the halo bias. Since the exact dependence of both the halo bias and the halo mass function on cosmology is uncertain, we neglect any possible cosmological information that could be obtained from these quantities. As can be seen in Equations (4.1) and (4.2), the key quantity is $L(M)$. Therefore, the measurement of $\langle T\rangle$, $\langle T^2\rangle$ and b would be very useful to constrain luminosity function, which is still very unknown for any line at high redshift. The question is how much astrophysical information can be recovered from the IM power spectrum.

$L(M)$ can be parametrized in many different ways, depending on the specific line and model. Let us illustrate the potential of the IM power spectrum to constrain the shape of $L(M)$ by considering the CO emission line assuming the model introduced in Li et al. (2016). In Figure 4.1, we show the CO IM power spectrum at $z = 2.73$ using the fiducial values for the parameters of the model reported in Li et al. (2016), and compare it with the resulting CO IM power spectra when each of these parameters are varied 5% one by one.

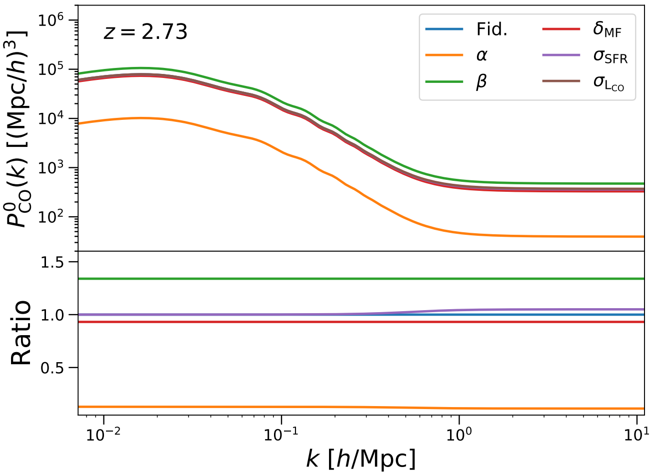

Figure 4.1: CO IM power spectrum at $z = 2.73$ assuming the fiducial astrophysical model used in Li et al. (2016) (blue) and varying 5% each of the parameters entering $L(M)$ separately (top), and the corresponding ratio with respect to the fiducial case (bottom).

It can be seen how, with the exception of $\sigma_{\rm SFR}$, all parameter variations produce just a change in the amplitude of the power spectrum. The particularity of $\sigma_{\rm SFR}$ is that it changes $P_{\rm shot}$ and $P_{\rm clust}$ in a different way, hence the scale dependence appreciable on the ratio. Figure 4.1 evidences that individual parameters of the luminosity function or astrophysical model cannot be constrained using the IM power spectrum. Therefore, the only accessible information is indeed $\langle T\rangle$, $\langle T^2\rangle$ and b, rather than the underlying astrophysics. Although Figure 4.1 represents a specific example, this result is expected to be qualitatively similar for most models and spectral lines.

Since significant cosmological information is only present in $\alpha_\perp$, $\alpha_\parallel$, and $\langle T\rangle f\sigma_8$ (and $\vec{\varsigma}$), we consider the rest of parameters in Equation (4.9) as nuisance parameters and marginalize over them. Moreover, using a prior on $\langle T\rangle$ is the only way to constrain $f\sigma_8$.

Small scales are dominated by $P_{\rm shot}$ (as can be seen in e.g., Figure 4.1), so extending the analysis until very small scales does not entail great benefits in terms of cosmological information. Note however that this regime of the IM power spectrum is not affected by non-linearities (since $P_{\rm shot}$ does not depend on clustering), hence small scales are not limited by theoretical systematics. Therefore, this regime can be used to attempt IM detection, as done in e.g., Keating et al. (2016). However, if brightness temperature and galaxy number counts are cross-correlated, considering a scale dependent bias might be necessary.

Finally, in order to improve the coverage of the BAO scale, while maintaining the control over the modes included in each k bin, we use a linear binning in k, unless otherwise stated.

The parametrization introduced in Equation (4.8) is especially useful since it disentangles astrophysics and cosmology. Given the intrinsic correlation of astrophysics and cosmology existent in IM, this parametrizations allows for marginalization over the astrophysics without affecting to the features depending on cosmology. This facilitates robust cosmological constraints, especially for BAO measurements.

Note that we choose the parametrization of the IM power spectrum depicted in Equation (4.8) in order to separate b and f. However, the IM power spectrum can be reparametrized in a different way to target other parameter combinations. For example, if a measurement of $\beta = f/b$ is wanted, one could use:

$$P(k,\mu) = \left(\frac{(\langle T\rangle b\sigma_8)\left(1+\beta\mu^2\right)}{1+0.5\left(k\mu\sigma_{\rm FoG}\right)^2}\right)^2 \frac{P_m(k)}{\sigma_8^2} + \langle T^2\rangle. \tag{4.10}$$

In this case, the measured quantities would be β and $\langle T\rangle b\sigma_8$, instead of $\langle T\rangle f\sigma_8$ and $\langle T\rangle b\sigma_8$. However, we consider the parametrization of Equation (4.8), which allows us to measure the parameters appearing in Equation (4.9), more suitable for cosmology, avoiding any contamination from b on the measurement of f.

4.2.4 Covariance of the measured intensity mapping power spectrum

While precise measurements of the galaxy power spectrum at small scales are limited by the shot noise, in the case of IM power specturm, $P_{\rm shot}$ contains information of interest (mostly astrophysical). Nonetheless, IM power spectrum still has three contributions to its error budget: the cosmic variance (common to the galaxy power spectrum), the instrumental noise, that introduces an artificial floor brightness temperature in the observed map, and potential non-corrected foregrounds or interlopers.

The size of the impact of foregrounds and interlopers in the observed IM power spectrum greatly depends on the emission line and redshifts of interest. For instance, galactic foregrounds are several orders of magnitude larger than the signal in HI, while the ratio is significantly smaller for CO. Moreover, the foreground subtraction and interloper identification techniques are quite general in terms of the measured emission line. Therefore, we expect great advances in this part of the observational analysis in the coming years. Therefore, in this work we assume a complete control of foregrounds and interlopers, considering that the signal has been successfully cleaned and neglecting this contribution to the measurement errors. In addition, we assume a Gaussian covariance without mode coupling.

As mentioned in the previous section, the experiment returns a voxelized map of brightness temperature. We consider that the pixel size (i.e., the size of the angular grid) is given by the full width half maximum of the beam of the experiment, $\theta_{\rm FWHM}$, so that each observed patch of the sky will have $\Omega_{\rm field}/\theta^2_{\rm FWHM}$ pixels, with $\Omega_{\rm field}$ being the solid angle of the patch observed. The radial binning, in turn, is given by the spectral resolution of the experiment and the corresponding width of a frequency channel, $\delta\nu$. Thus, the total number of voxels in an observed field is given by the product of the number of pixels and the number of channels, $\Delta\nu/\delta\nu$, where $\Delta\nu$ is the bandwidth of the experiment.

We consider the voxel window function associated with the limited resolution of the experiment, $W(k,\mu)$ to be well described by a Gaussian function. The Gaussian voxel window widths in the transverse and radial directions are given by:

$$\sigma_\parallel = \frac{c(1+z)\delta\nu}{H(z)\nu_{\rm obs}}; \qquad \sigma_\perp = \chi(z)\theta_{\rm FWHM}, \tag{4.11}$$

where $\nu_{\rm obs}$ is the observed frequency, and $\chi(z)$ is the radial comoving distance. The corresponding voxel window function is (Li et al., 2016):

$$W(k,\mu) = \exp\left\{-k^2\left[\sigma_\perp^2(1-\mu^2)+\sigma_\parallel^2\mu^2\right]\right\}. \tag{4.12}$$

Although we have assumed $W(k,\mu)$ to be Gaussian, the beam profile might not be a perfect Gaussian, and the frequency channels are discrete bins (corresponding to a top-hat window). Nonetheless, this approximation is enough for the scope of this work. In any case, an exhaustive characterization of both the beam profile and spectral binning will provide an accurate determination of $W(k)$, hence a correct deconvolution of the *observed* IM power spectrum (see Section 4.2.3). The exact description of $W(k)$ does not affect the conclusions of this work.

The instrumental noise is related with instrumental limitations of the experiment. For instance, the system temperature of the experiment, $T_{\rm sys}$, limits its sensitivity. The noise power spectrum for a total observing time $t_{\rm obs}$ with $N_{\rm feeds}$ independent detectors, is:

$$P_n = \frac{T_{\rm sys}^2 V_{\rm field}}{N_{\rm vox} N_{\rm feeds} \delta\nu t_{\rm pix}} = \frac{T_{\rm sys}^2 V_{\rm field}}{\Delta\nu N_{\rm feeds} t_{\rm obs}}, \tag{4.13}$$

where $t_{\rm pix}$ is the time invested in observing each pixel. Equation (4.13) describes the instrumental noise of the *observed* power spectrum. However, since we want to analyze the *deconvolved* power spectrum, the inverse of $W(k)$ should be applied to P_n. This is equivalent to directly model the effect of the voxelization only in the noise, which limits the significance of the signal at small scales, those close to the dimensions of the voxel and whose information cannot be resolved.

Finally, these uncertainties are statistically suppressed as more modes of the power spectrum are measured. It is only possible to access the information at scales between the size of the survey and the dimensions of the voxel. Therefore, the number of observed modes, $N_{\rm modes}$, depends on the total volume surveyed and on the size of the voxels. An observed patch of the sky has a volume:

$$V_{\rm field} = \left[\chi^2(z)\Omega_{\rm field}\right]\left[\frac{c(1+z)^2\Delta\nu}{H(z)\nu}\right]. \tag{4.14}$$

Each term in Equation (4.14) corresponds to the transverse area and the length of the radial side of the volume observed, respectively (i.e. $V_{\rm field} \sim L_\perp^2 L_\parallel$). Then, each of these dimensions set the minimum accessible wavenumbers for an experiment: $k_\perp^{\rm min} = 2\pi/L_\perp$ and $k_\parallel^{\rm min} = 2\pi/L_\parallel$. Likewise, the voxel size determines the maximum k accessible in each direction, $k_\perp^{\rm max}$ and $k_\parallel^{\rm max}$. Taking into account possible ignorance about the voxel window function, we prefer to be conservative and set the smallest scales probed to $k_{\perp,\parallel}^{\rm max} = 2/\sigma_{\perp,\parallel}$ to avoid the introduction of observational systematics coming from a poor modeling of the voxel window function.

Considering the accessible scales either in the transverse or radial directions, the number of modes per bin in k and μ has three different regimes. Let us assume $k_\perp^{\rm min} < k_\parallel^{\rm min}$ and $k_\perp^{\rm max} < k_\parallel^{\rm max}$ for illustration. In this example, while the modes $k \in \left[k_\parallel^{\rm min}, k_\perp^{\rm max}\right]$ are completely accessible (so that we can access the full three-dimensional information), for $k < k_\parallel^{\rm min}$, the experiment can only probe the Universe observed as in a two-dimensional survey (i.e., it has no access to the radial information because these scales are larger than the depth of the survey). Similarly, for $k > k_\perp^{\rm max}$ the survey cannot resolve transverse modes (since these scales are smaller than the size of the pixel), hence only one-dimensional information can be recovered. Thus, the number of modes per bin in k and μ in an observed field corresponding to these three regimes is:

$$\begin{aligned} N_{\rm modes}^{(3{\rm D})}(k) &= \frac{k^2\Delta k\Delta\mu}{8\pi^2}V_{\rm field}; \\ N_{\rm modes}^{(2{\rm D})}(k) &= \frac{k\Delta k}{2\pi}S_{\rm field}; \\ N_{\rm modes}^{(1{\rm D})}(k) &= \frac{\Delta k}{4\pi}L_{\parallel,{\rm field}}, \end{aligned} \tag{4.15}$$

with Δk and $\Delta\mu$ referring to the width of the wave number and μ bins, respectively, and $S_{\rm survey}$ is the transverse area of the field. Following this logic, the measurements are limited to $k \in \left[\min(k_\perp^{\rm min}, k_\parallel^{\rm min}), \max(k_\perp^{\rm max}, k_\parallel^{\rm max})\right]$.

Now we have all the necessary pieces to compute the covariance per k and μ bin, $\sigma^2(k,\mu)$:

$$\sigma^2(k,\mu) = \frac{1}{N_{\rm modes}(k,\mu)}\left(P(k,\mu) + \frac{P_n}{W(k,\mu)}\right)^2. \tag{4.16}$$

Since the multipoles of the IM power spectrum are the summary statistics of interest, we need to compute the covariance of each multipole, and the covariance among them. This is necessary to perform the combined analysis of the IM power spectrum multipoles correctly, accounting for all possible correlations between the multipoles. We refer the interested reader to Grieb et al. (2016) for a thorough derivation of the analytic multipole covariance for the galaxy power spectrum under the Gaussian assumption. Here, we extrapolate those results to the case of the IM power spectrum. The total covariance matrix is formed by the blocks of each of the auto- and cross-covariance matrices. These blocks, corresponding to multipoles ℓ

and ℓ', are given by (Grieb et al., 2016):

$$\mathcal{C}_{\ell\ell'}(k_i,k_j) = \frac{(2\ell+1)(2\ell'+1)}{2} \times \int_{-1}^{1} \mathrm{d}\mu\sigma^2(k_i,\mu)\mathcal{L}_\ell(\mu)\mathcal{L}_{\ell'}(\mu)\delta^K_{ij}, \tag{4.17}$$

where δ^K is the Kronecker delta.

If we build the vectors $\vec{\Theta} = [P^0(k_0), P^0(k_1), ..., P^2(k_0), P^2(k_1), ...]$, and $\vec{\Theta}(k) = [P^0(k), P^2(k), ...]$, we can compute the total signal-to-noise ratio, S/N, and S/N(k) per k bin as:

$$(\mathrm{S/N})^2 = \vec{\Theta}^T\mathcal{C}\vec{\Theta}, \qquad (\mathrm{S/N}(\,k))^2 = \vec{\Theta}^T(k)\mathcal{C}(k)\vec{\Theta}(k), \tag{4.18}$$

where the superscript T denotes the transpose operator and $\mathcal{C}(k_i)$ is a $N_\ell \times N_\ell$ matrix (with N_ℓ being the number of multipoles included in the analysis) built with the corresponding elements of $\mathcal{C}_{\ell\ell'}(k_i,k_i)$. Similarly, we can compute the χ^2 of the IM power spectrum for a given experiment defining $\Delta\vec{\Theta}$ as the difference between the model prediction for the IM power spectrum multipoles and the measurements (or, in the case of performing a Fisher matrix forecast, the fiducial IM power spectrum multipoles), using:

$$\chi^2 = \Delta\vec{\Theta}^T\mathcal{C}\Delta\vec{\Theta}. \tag{4.19}$$

4.2.5 Application

In this section we illustrate the application of the formalism presented in Sections 4.2.3 and 4.2.4. First of all, we present our assumed experiment, as well as the Fisher matrix formalism and the models considered. Afterwards, we study the impact of adding the hexadecapole to the monopole and quadrupole in the analysis of the IM power spectrum, as well as different correlations between the measured parameters. Finally, we forecast cosmological constraints for the models previously introduced, and discuss the best possible strategies to improve such constraints.

4.2.5.1 Assumed experiment

While the formalism introduced above is completely general for any given emission line, we need to consider a specific experiment in order to compute the covariance of the IM power spectrum and discuss different strategies for future IM observations. For this work, we choose a future CO experiment within the Intensity Mapping Stage 3 observational effort, introduced in Bernal et al. (2019a), in order to illustrate how the results change with redshift.

CO line has a rest frame frequency $\nu_{\rm CO} = 115.27$ GHz. For our assumed experiment, we consider a wide frequency band ($\Delta\nu = 12 - 36$ GHz) split in five non-overlapping, independent redshift bins such as $\log_{10}[\Delta(1+z)] = \log_{10}[\Delta(\nu_{\rm CO}/\nu_{\rm obs})] = 0.1$. Furthermore, we consider 10000 hours of observations along 1000 deg^2 of the sky with 500 dual polarization feeds (i.e., effectively $N_{\rm feeds} = 1000$), with an angular and spectral resolutions corresponding to $\theta_{\rm FWHM} = 4$ arcmin and $\delta\nu = 2$ MHz. Finally, we assume a $T_{\rm sys}$ model from the performance of heterodyne-based instruments for centimeter radioastronomy (see e.g., (Prestage, 2006; Murphy, 2018)):

$$T_{\rm sys} = \max\left[20,\, \nu_{\rm obs}\,({\rm K/GHz})\right]. \tag{4.20}$$

We choose $\Omega_{\rm field} = 1000$ deg^2 to maximize the S/N maintaining the rest of survey parameters fixed.

4.2.5.2 Fisher matrix and considered models

We use the Fisher matrix formalism (Fisher, 1935; Tegmark et al., 1997) to evaluate different strategies regarding IM power spectrum measurements in terms of the forecasted constraints. The Fisher matrix is the average of the second partial derivatives of the logarithm of the likelihood around the best fit (the fiducial model in our case):

$$F_{\vartheta_a\vartheta_b} = \left\langle \frac{\partial^2 \log\mathcal{L}}{\partial\vartheta_a\partial\vartheta_b}\right\rangle = \sum_i \left(\frac{\partial\Theta^T}{\partial\vartheta_a}\mathcal{C}^{-1}\frac{\partial\Theta}{\partial\vartheta_b}\right)_{i,j}, \tag{4.21}$$

where ϑ_a and ϑ_b denote the parameters entering the analysis. We assume the halo mass function and halo bias presented in Tinker et al. (2010), and follow the CO emission model (with the corresponding fiducial parameter values) introduced in Li et al. (2016). Regarding the cosmological model, we assume the Planck baseline ΛCDM model and take the best fit value parameters from the combined analysis of the full Planck 2018 and galaxy BAO measurements assuming ΛCDM (Planck Collaboration et al., 2018; Alam et al., 2017b): baryon and dark matter physical densities at $z = 0$, $\Omega_{\rm b}h^2 = 0.0224$ and $\Omega_{\rm cdm}h^2 = 0.1193$, respectively; spectral index $n_s = 0.967$; amplitude of the primordial power spectrum of scalar perturbations at the pivot scale $\log\left(A_s 10^{10}\right) = 3.047$; Hubble constant $H_0 = 67.67$ km/s/Mpc; and sum of neutrino masses $\sum m_\nu = 0.06$ eV. When combining forecasts from IM power spectrum measurements with current observations, we use priors obtained from the public results of the Planck collaboration legacy data release[1] Planck Collaboration et al. (2018).

We first consider a ΛCDM model, with no parameters in $\vec{\varsigma}$. As an example of a case where the template for $P_m(k)$ should be varied, we also consider a sum of the neutrinos masses that can be larger than 0.06 eV. In this case, $\vec{\varsigma} = \sum m_\nu$. In addition, since IM has been claimed to be a powerful way to constrain primordial non Gaussianity, especially in the local limit (Moradinezhad Dizgah et al., 2019; Moradinezhad Dizgah & Keating, 2019), we consider also local primordial non-Gaussianity and the potential of our assumed experiment to constrain deviations from Gaussian initial conditions.

Any imprint caused by primordial deviations from Gaussian initial conditions would have been preserved in the ultra-large scales of the matter power spectrum, since these modes have remained outside of the horizon since inflation. In the local limit, primordial non Gaussianity can be parametrized with $f_{\rm NL}$[2] as the amplitude of the local quadratic contribution of a single Gaussian random field ϕ to the Bardeen potential Φ:

$$\Phi(x) = \phi(x) + f_{\rm NL}\left(\phi^2(x) - \langle\phi^2\rangle\right) , \tag{4.22}$$

where we have assumed a fiducial value of $f_{\rm NL} = 0$, i.e., the Gaussian limit. The skewness introduced in the density probability distribution by local primordial non Gaussianity increases the number of massive objects, hence introducing a scale-dependence on the halo bias (Matarrese et al., 2000; Dalal et al., 2008; Matarrese & Verde, 2008; Desjacques & Seljak, 2010). Denoting the Gaussian halo bias with $b_h^{\rm G}$, the total halo bias appearing in Equation (4.2) is given by

---

[1] The specific Monte Carlo Markov Chains can be found in the public Planck repository (`http://pla.esac.esa.int/pla`). The data combination is denoted as `plikHM_TTTEEE_lowl_lowE_lensing` and `plikHM_TTTEEE_lowl_lowE_lensing_post_BAO` (whether galaxy BAO are included or not), or equivalent for extended models.

[2] Here we assume the convention of large scale structure rather than the one for CMB ($f_{\rm NL}^{\rm LSS} \approx 1.3 f_{\rm NL}^{\rm CMB}$ (Xia et al., 2010)).

$b_h(k,z) = b_h^{\mathrm{G}}(z) + \Delta b_h(k,z)$, with $\Delta b_h(k,z)$ being:

$$\Delta b_h(k,z) = \left[b_h^{\mathrm{G}}(z) - 1\right] f_{\mathrm{NL}} \delta_{\mathrm{ec}} \frac{3\Omega_m H_0^2}{c^2 k^2 T_m(k) D(z)}\,, \tag{4.23}$$

where Ω_m is the matter density parameter at $z = 0$, $\delta_{\mathrm{ec}} = 1.68$ is the critical value of the matter overdensity for ellipsoidal collapse, $D(z)$ is the linear growth factor (normalized to 1 at $z = 0$) and $T_m(k)$ is the matter transfer function (~ 1 at large scales). Equation (4.23) evidences a $f_{\mathrm{NL}} k^{-2}$ dependence on the luminosity-averaged bias. Note that varying f_{NL} does not exactly fall under the definition of $\vec{\varsigma}$ inEquation 4.9, since f_{NL} does not modify the shape of $P_m(k)$. However, we include it in $\vec{\varsigma}$ for simplicity.

Note that varying either $\sum m_\nu$ or f_{NL} would also slightly modify the halo mass function and therefore alter the IM power spectrum via modifications of $\langle T\rangle$, $\langle T^2\rangle$ and b. We do not model this dependence, but our findings are not affected by this: the halo mass function would affect just in a minimal way the amplitude of P_{clust} and the P_{shot} contribution, which are marginalized over. We left the exploration of these effects to future work.

4.2.5.3 IM power spectrum multipoles

Contrary to most of the IM research in the literature[1], we use the Legendre multipoles of the IM power spectrum as our summary statistics (Equation (4.7)).

For the simplest redshift space distortions prescription, including only the Kaiser effect, all the information enconded in the power spectrum is contained in the monopole, quadrupole and hexadecapole. This is no longer true when a small scale damping due to the fingers of God is included. However, while measuring the monopole and quadrupole is relatively easy, given their reasonably high S/N, detecting the hexadecapole is challenging, since usually the signal is well below the noise. Focusing only on the astrophysics and considering the *observed* power spectrum (i.e., before deconvolving the voxel window function), Chung (2019) finds

---

[1] Most examples in the literature only considers the spherically averaged IM power spectrum, or unrealistically study directly the two-dimensional IM power spectrum as function of k and μ without any data compression

that including the hexadecapole ($\ell = 4$) does not significantly improve the estimated constraints.

However, regarding cosmology, including the hexadecapole might be useful. Even if the hexadecapole does not add information for the BAO determination (especially if the errors are dominated by cosmic variance), it might help to break degeneracies between the BAO rescaling parameters and RSD. This is because a non-detection of the hexadecapole is also informative, since its amplitude is mostly independent of the luminosity-averaged bias and provides a distinct feature which facilitates to disentangle the anistropies sourced by RSD and the Alcock-Paczynski effect. For instance, including the hexadecapole in the analysis of the quasar power spectrum in eBOSS (Gil-Marín et al., 2018), resulted in smaller degeneracies between $\alpha_{\parallel}$ and $\alpha_{\perp}$, and between $\alpha_{\parallel}$ and $f\sigma_8$, compared with the case without including the hexadecapole.

Moreover, the hexadecapole can be measured and estimated at the same time as the lower order multipoles, not requiring additional computing time. However, the hexadecapole is more sensitive to potential systematics related with the radial direction ($\mu \sim 1$). This would impose stronger requirements on experiments to ensure a clean and robust measurement. In order to assess the benefits of adding the hexadecapole to the IM power spectrum analysis, we compare the projected results with and without its inclusion.

We explore the gain of adding the hexadecapole to the IM power spectrum studies and discuss if the effort of correcting the corresponding systematic errors is worthy.

First of all we evaluate the straightforward gain of including the quadrupole and hexadecapole: we compare the S/N(k) of the IM power spectrum using only the monopole and adding one by one the other two multipoles (Equation (4.18)). The results for our assumed experiment in each of the five redshift bins are shown in Figure 4.2.

As can be seen, while adding the quadrupole returns an increase in the S/N(k) at scales below the BAO scale, the further gain obtained by adding the hexadecapole is negligible (except at very small scales). It is also evident that the S/N(k) decreases with redshift. This is because the amplitude of the IM power spectrum decreases with redshift, added to the fact that the noise power spectrum, P_n, stops decreasing at $z \gtrsim 4.7$, due to the minimum reached by $T_{\rm sys}$ (Equation (4.20)). In addition,

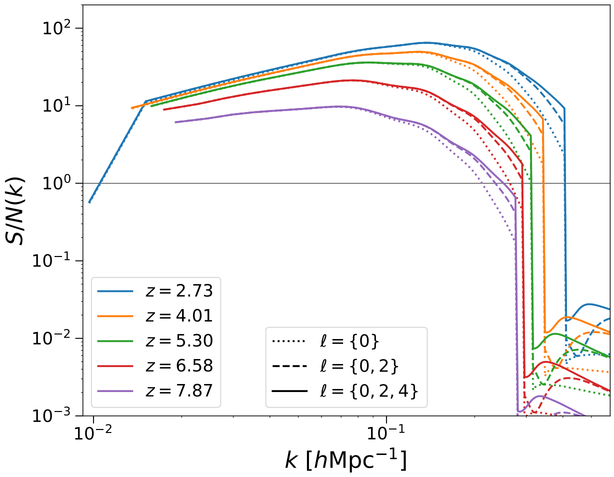

Figure 4.2: Signal-to-noise ratio per k bin for each redshift bin of the IMS3 CO experiment considered in this work (color coded) including only the monopole (dotted lines), the monopole and the quadrupole (dashed lines) and adding also the hexadecapole (solid lines). The S/N(k) exhibits a drastic cut-off at large k (i.e., when $k > k_{\perp}^{\max}$) because the survey becomes efficiently one-dimensional. At very small k for the lowest redshift bin, $k < k_{\parallel}^{\min}$, hence the survey is efficiently two-dimensional.

we can see a drastic drop in S/N(k) at large, k, different for each redshift. This happens at $k > k_{\perp}^{\max}$ (for our assumed experiment, the angular resolution is poorer that the spectral resolution), hence passing from a three-dimensional to an one-dimensional survey, with the subsequent reduction of N_{modes} (see the discussion around Equation (4.15)). This also occurs at large scales for the lowest redshift bin, where $k < k_{\parallel}^{\max}$; however, in this case the reduction is smaller because the transition is from a three-dimensional to a two-dimensional survey. Note that the maximum and minimum scales change with redshift, since the relation between angular and spectral resolution with the physical dimensions of the voxel depends on redshift. While the general behaviour shown in Figure 4.2 when all three dimensions are accessible is completely general, the scales at which S/N(k) drastically drops are of course very dependent on the specific experiment.

Nonetheless, adding multipoles beyond the monopole yields more benefits that just and increase of the S/N. First of all, adding at least the quadrupole is necessary to measure the anisotropic BAO, and so $D_A(z)/r_{\rm s}$ and $H(z)r_{\rm s}$. Secondly, we need to

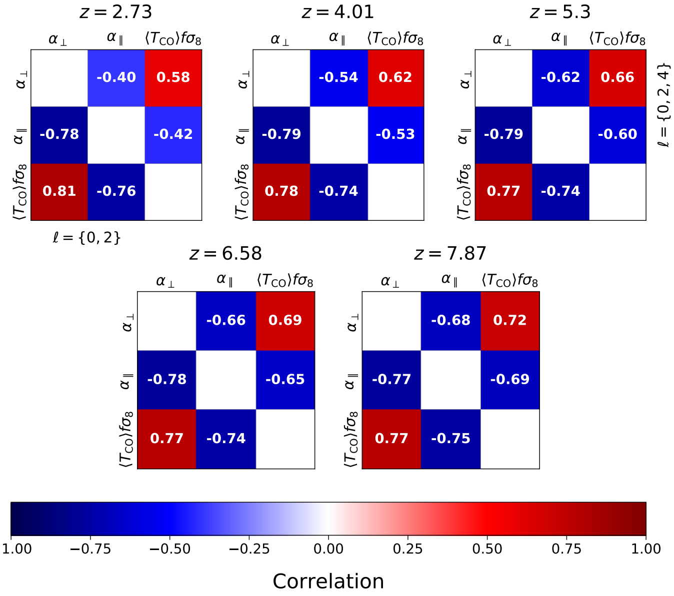

Figure 4.3: Correlation matrices of the parameters $\alpha_\perp$, $\alpha_\parallel$ and $\langle T\rangle f\sigma_8$, marginalized over the nuisance parameters, for each redshift bin of the IMS3 CO experiment. The correlations in the upper triangular matrix correspond to the case where monopole, quadrupole and hexadecapole are included, and the lower triangular matrix, without including the hexadecapole.

study how the correlation between the cosmological quantities measured change with the inclusion of the hexadecapole. The correlation matrices for each redshift bin after marginalizing over nuisance parameters (i.e., only remaining $\alpha_\perp$, $\alpha_\parallel$ and $\langle T\rangle f\sigma_8$) are shown in Figure 4.3, comparing the results including or not the hexadecapole. This figure shows a reduction of the correlation between the cosmological parameter when the hexadecapole is included with respect to the case in which it is not. Note that this reduction is smaller for larger redshifts (where the global S/N, and especially that of the hexadecapole is smaller).

Lower correlations have a positive impact on the final marginalized constraints. Table 4.1 reports the forecasted 68% confidence level marginalized precision of the measurements of the BAO rescaling parameters and the parameter combination $\langle T\rangle f\sigma_8$ for each of the redshift bins of our assumed experiment. While the fiducial value of $\alpha_\perp$ and $\alpha_\parallel$ is 1 for all redshifts, the corresponding fiducial value of $\langle T\rangle f\sigma_8$ at each redshift bin is: {0.78, 0.67, 0.56, 0.43, 0.29} μK (for increasing z).

Exp.	z	$\sigma_{\rm rel}\left(\alpha_\perp\right)$ (%)		$\sigma_{\rm rel}\left(\alpha_\parallel\right)$ (%)		$\sigma_{\rm rel}\left(\langle T\rangle f\sigma_8\right)$ (%)	
		$\ell\leq 2$	$\ell\leq 4$	$\ell\leq 2$	$\ell\leq 4$	$\ell\leq 2$	$\ell\leq 4$
IMS3(CO)	2.73	1.5	0.88	2.2	1.3	1.1	0.71
	4.01	1.4	0.097	2.3	1.5	1.1	0.83
	5.30	1.8	1.3	2.8	2.1	1.2	0.97
	6.58	3.4	2.7	5.7	4.4	1.6	1.3
	7.87	8.4	7.0	14.2	11.6	2.1	1.9

Table 4.1: Forecasted 68% confidence level marginalized relative constraints from an IMS3 CO experiment on the BAO parameters and $\langle T\rangle f\sigma_8$, expressed as percentages. We show results using only the monopole and quadrupole and adding also the hexadecapole.

The worsening of the precision with redshift is expected, given the decreasing of S/N with redshift (as shown in Figure 4.2). Interestingly, the marginalized constraints on the BAO rescaling parameters are between a 25% and 75% stronger when including the hexadecapole. The improvement obtained by including the hexadecapole decreases with redshift, as expected by the reduction of the difference between correlations with and without the hexadexapole shown in Figure 4.3.

The BAO rescaling parameters can be interpreted in a cosmological frameworks using Equation (4.32), yielding measurements of the angular diameter distance and the Hubble expansion rate. We show projected constraints on the D_A-H plane in the left panel of Figure 4.4 derived from the results shown in Table 4.1 and Figure 4.3. It can be seen how the correlation between these parameter changes with redshift, as well as the improvement obtained by including the hexadecapole.

As noted in Section 4.2.3, any IM experiment needs a prior on $\langle T\rangle$ to provide a reliable constrain on redshift space distortions. Always that the IM power spectrum is measured with enough S/N, as is the case considered here, the precision of the measured $\langle T\rangle f\sigma_8$ will be very good (in the 1%-2% level for our assumed experiment). Therefore, the error budget on the inference of $f\sigma_8$ will be dominated by the error on $\langle T\rangle$ (which is expected to be much larger than percent level, at least in the coming years).

Of course, inferred constraints on $f\sigma_8$ will be correlated with the luminosity-averaged bias. We show in the right panel of Figure 4.4 forecasted 68% and 95% confidence level marginalized inferred constraints on the plane $f\sigma_8$-$b_{\rm CO}\sigma_8$ for all

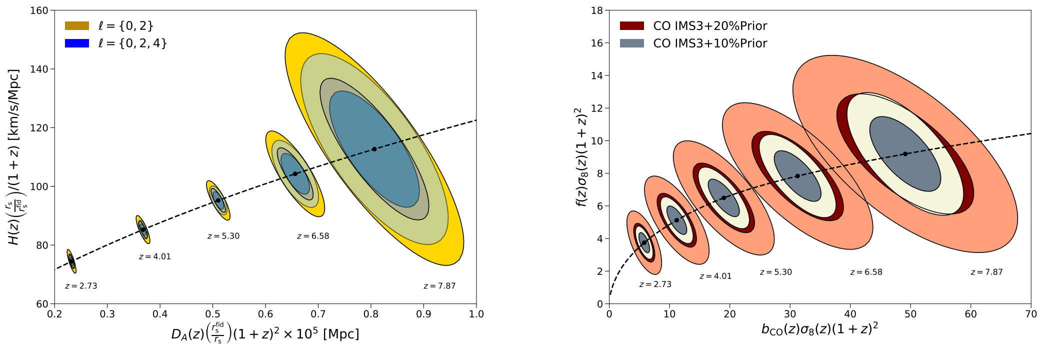

Figure 4.4: *Left*: Forecasted 68% and 95% confidence level marginalized constraints on the plane $(D_A(z)/r_s)\, r_s^{\rm fid} \times (1+z)^2 - (H(z) r_s)/r_s^{\rm fid} \times (1+z)^{-1}$ from each redshift bin of the IMS3 CO experiment, obtained from the constraints on the plane $\alpha_\perp - \alpha_{||}$ using Equation (4.32). We show results using only the monopole and quadrupole (yellow contours), as well as including also the hexadecapole (blue). *Right*: Forecasted 68% and 95% confidence level marginalized constraints in the plane $b(z)\sigma_8(z) \times (1+z)^2 - f(z)\sigma_8(z) \times (1+z)^2$ from each redshift bin of the IMS3 CO experiment. We show results using a 20% prior and a 10% prior on $\langle T\rangle(z)$ in maroon and grey, respectively. The black dashed line corresponds to the prediction of the fiducial model.

redshift bins from the CO experiment within IMS3. We consider a 20% and a 10% precision prior on $\langle T_{\rm CO}\rangle$ on each redshift bin. As expected, the uncertainty in the prior on $\langle T_{\rm CO}\rangle$ dominates the budget error of $f\sigma_8$ and $b\sigma_8$. The degeneracy between $\langle T\rangle$ and $f\sigma_8$ compromises the potential of IM to constrain the growth rate. This Figure shows that also the degeneracy between f and b changes with redshift.

However, cross-correlations of different spectral lines, or with galaxy number counts, might be able to partially break the degeneracy between $\langle T\rangle$ and $f\sigma_8$ by investigating the values of $\langle T\rangle f\sigma_8$ and $\langle T\rangle b\sigma_8$ for the auto- and cross-correlations. This is because, while f is a cosmological quantity, common to any tracer, b is unique for every line.

Note that the redshift range shown in both panels of Figure 4.4 is completely unconstrained to date. Therefore, any measurement on this regime would be very informative. While the errors on $f\sigma_8$ are quite large (they are essentially the error of the prior on $\langle T\rangle$), the precision of the $D_A(z)$ and $H(z)$ measurements (although the last bin is in the $\sim$ 10% level) is very good. The potential of IM to provide precise standard ruler measurements at high redshift is studied and highlighted in Bernal

Extra parameter	$\sigma\left(\sum m_\nu\right)$	$\sigma\left(f_{\rm NL}\right)$
IMS3(CO)*	0.20	29
Planck	0.078	6.6
Planck+galBAO	0.038	6.6
IMS3(CO)*+Planck	0.065	6.4
IMS3(CO)*+Planck+galBAO	0.036	6.4

Table 4.2: Forecasted 68% confidence level marginalized constraints from an IMS3 CO experiment on the extra parameters for the corresponding models beyond ΛCDM, using the monopole, quadrupole and hexadecapole of the intensity mapping power spectrum. $\sum m_\nu$ values are given in electronvolts. * Here we consider $\Omega_{\rm field} = 1000$ deg^2 and $t_{\rm obs} = 10000$ hours for our CO experiment within IMS3; Figure (4.5) show the corresponding projected constraints for other survey specifications.

et al. (2019a).

Although measuring higher multipoles might still concur some gain, the improvement would be marginal, and the level of observational systematics would be too high to consider these measurements reliable. This is why we limit our study to $\ell \leq 4$.

4.2.5.4 Constraining ΛCDM

The measured $\alpha_\perp$ and $\alpha_\parallel$, as well as $f\sigma_8$ (using a prior on $\langle T\rangle$) can be used to constrain cosmological parameters. However, here we focus on constraining parameters which are measured in a different way, studying their effect on the template of $P_m(k)$, or the scale dependence of the luminosity-averaged bias. Then, we forecast constraints on $\sum m_\nu$ and $f_{\rm NL}$ from our assumed CO experiment within IMS3. Note that the imprints of both a higher sum of neutrino masses and primordial non Gaussianity are more significant at very large scales. In addition, $\sum m_\nu$ and $f_{\rm NL}$ do not evolve with time, yielding the same value over all redshift bins. Therefore, in order to optimize the constraints on these parameters, rather than on the BAO scale, we choose a different strategy than the one discussed in 4.2.5.1. We consider a single redshift bin over the whole bandwidth of our experiment, centered at 24 GHz ($z = 3.80$), and a logarithmic binning in k, so that the coverage of the largest scales probed is maximized. Furthermore, we also marginalize over $\langle T\rangle f\sigma_8$, so that the constraints obtained are robust to astrophysics.

Table 4.2 shows the estimated 68% confidence level marginalized constraints on $\sum m_\nu$ and $f_{\rm NL}$ from our assumed experiment, Planck (with and without current galaxy BAO measurements) and the combination of both. The projected constraint on $\sum m_\nu$ from just IMS3 yields 0.20 eV of uncertainty. When combined with current CMB and galaxy BAO constraints, the constraint tightens to 0.035 eV. Moreover, these constraints improve even more with a (optimistic) 1% prior on $\langle T\rangle$ (and using the corresponding inferred measurement on $f\sigma_8$) to 0.15 eV and 0.028 eV, from IMS3 on its own and when combined with current constraints, respectively. These result may provide a 2σ detection of $\sum m_\nu$ in the best case scenario, but the constraints would be still weaker than e.g., the combination of DESI and Planck (DESI Collaboration et al., 2016a), which has the potential of achieven a 3σ detection. On the other hand, forecasted constraints on $f_{\rm NL}$ will not be competitive with current constraints from current CMB measurements (Planck Collaboration et al., 2019).

At this point, it is worthy to remember that we have envisioned IMS3 optimized to measure the BAO scale, hence choosing $\Omega_{\rm field}$ to maximize the overall S/N. Therefore, we now explore the dependence of the projected constraints on $\Omega_{\rm field}$. In addition, we also increase the observing time to reduce the noise power spectrum (varying $t_{\rm obs}$ has exactly the same effect as varying $N_{\rm feeds}$). The projected 68% marginalized constraints are shown in Figure 4.5.

As expected, the constraints on $f_{\rm NL}$ and $\sum m\nu$ improve as both $\Omega_{\rm field}$ and $t_{\rm obs}$ increase. In the case of $f_{\rm NL}$, our assumed experiment could improve over current constraints if it would cover ~ 8000 deg^2 of the sky during 20000 hours. Regarding the sum of neutrino masses, a similar experiment than the one assumed here, but observing a quarter of the sky during 25000 hours could reach a 1σ constraint on $\sum m_\nu$ of $\sim$ 0.06 eV without a CMB prior, which is an extremely powerful measurement for a constraint coming from large scale structure.

Note that we only consider modifications on $\Omega_{\rm field}$ and $t_{\rm obs}$ to improve the forecasted constraints. A more detailed analysis is beyond the scope of this work. We refer the interested reader to Moradinezhad Dizgah & Keating (2019), where a comprehensive study of the survey optimizations to reach a 1σ constraint on $f_{\rm NL}$ of order unity is carried out. However, note that Moradinezhad Dizgah & Keating (2019) use an inaccurate expression for the covariance, ignore the correlation between

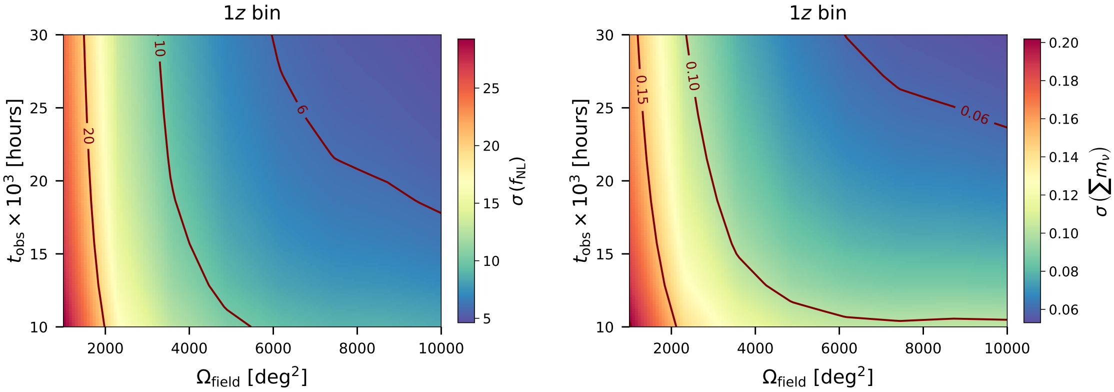

Figure 4.5: Forecast 68% confidence level marginalized constraints on $f_{\rm NL}$ (left) and $\sum m_\nu$ (right) from the IMS3 CO experiment using the monopole, quadrupole and hexadecapole, as function of $\Omega_{\rm field}$ and $t_{\rm obs}$. $\sum m_\nu$ constraints are given in electronvolts. The bottom left corner of each panel corresponds to the values reported in Table 4.2.

different μ bins or multipoles, fix the astrophysical parameters as if there was a complete knowledge about the luminosity function, and consider $f_{\rm NL}^{\rm fid}=1$.

Finally, we emphasize that these results are only an illustration of the potential of IM experiments for cosmology when the formalism proposed in this work is used. These results have room for improvement with more optimized surveys, as well as with cross-correlations between several spectral lines or galaxy number counts. We leave this study for future work.

4.2.5.5 Further improvement

In this work, we have focused on the optimal parametrization of the IM power spectrum and provided an accurate analytic prescription for its covariance to maximize the extraction of cosmological information robust to astrophysics. However, there is also room for improvement in the treatment of the brightness temperature maps, when analyzing the observed IM power spectrum.

One possibility would be to assign an arbitrary weight, w, to each of the observed voxels. Then, $w(\vec{r})$ can be chosen to maximize the S/N of the measured IM power spectrum. Thanks to the introduction of these weights, a minimal variance estimator can be derived. This would be an analogy of the FKP weights used on galaxy surveys (Feldman et al., 1994).

Overlapping or narrower redshift bins may be used to compute the IM power spectrum, and actually be more optimal than non overlapping independent bins, depending on the main objectives of the survey. However, in this case, each redshift bin cannot be considered independent from the rest anymore, and potential correlations must be taken into account. Moreover, the actual optimal frequency band of the experiment depends on the targeted parameters. We leave the exploration of redshift binning optimization and tomographic analysis strategies for future work.

Finally, in this work we have enforced the redshift bins to be narrow enough such that the redshift evolution of the large scale brightness temperature fluctuations do not change significantly (except in Section 4.2.5.4). However, this can be somehow taken into account thanks to the redshift weighting techniques (Zhu et al., 2015). In this case, redshift dependent weights are chosen in order to minimize the projected error on the target cosmological or astrophysical parameter using a Fisher matrix forecast, so that the constraining power is maximized. These techniques can become specially useful when wide redshift bins are needed, as for primordial non Gaussianity (see e.g., Mueller et al. (2019)).

4.2.6 Conclusions

Intensity mapping has the potential to become one of the most powerful cosmological probes in the coming years, as well as providing key observations to study galaxy evolution and reionization. IM is experiencing an intense observational effort, with many planned experiments. While most of the focus is centered on HI line, experiments targeting other emission lines are maturing quickly. Although foregrounds and interlopers may contaminate the signal and hinder its exploitation, having so many spectral lines to target and the potential to survey ever larger volumes at ever higher redshifts, makes IM an incredibly attractive way to probe the Universe.

However, the cosmological information encoded in the IM signal is always intrinsically related with astrophysics. Nevertheless, most previous cosmological studies of IM ignore this degeneracy and fix the astrophysical parameters, as if the processes driving the emission of the line were completely known. This is far from true. Although IM is also extremely interesting to characterize galaxies and study their evolution, this work focuses on cosmology and provides a way to isolate the cosmological information of the IM power spectrum. This allows for a marginalization over the astrophysical and other nuisance parameters.

We introduce a general pipeline applicable to the IM power spectrum of any spectral line. We propose to use the Legendre multipoles of the IM power spectrum in order to compress the anisotropic information, and we account for RSD and the Alcock-Paczyinski effect. We also derive an accurate analytic covariance to consider the correlation between multipoles, which is necessary for a correct parameter inference or Fisher matrix forecast. We also extend the formalism to the case of cross-correlations for completeness.

Thanks to the parametrization proposed in Equation (4.8), we avoid the contribution of astrophysics to the measurable cosmological parameters (except for $f\sigma_8$). Then, marginalizing over the rest of the parameters, precise and robust constraints can be obtained, especially regarding the BAO scale. This will allow to probe the expansion history of the Universe with really competitive precision at redshifts unobserved so far (i.e. $3 \lesssim z \lesssim 10$), as proposed in Bernal et al. (2019a). Moreover, with complementary measurements constraining the mean brightness temperature of a given line, it will be possible to set constraints on the growth of structures by inferring $f\sigma_8$.

We also study the benefits of including the hexadecapole in the IM power spectrum analysis. We find that, even although its S/N is very low, including it in the analysis will be very convenient. We find that marginalized constraints on the BAO rescaling parameters and $\langle T\rangle f\sigma_8$ improve between a 25% and a 75% when the hexadecapole is included, with respect to when it is not. This is because even a non-detection of the hexadecapole partially breaks the degeneracy between these parameters and significantly reduces the correlations.

Finally, we forecast constraints on $\sum m_\nu$ and $f_{\rm NL}$ independently on the astrophysics. This serves as an example of possible models beyond ΛCDM which can be efficiently constrained by IM experiments. We find extremely promising results for a wide CO experiment within IMS3. $\sum m_\nu$ can be constrained to 0.06 eV at 68% confidence level just using the IM power spectrum, if a quarter of the sky is observed during 25000 hours. Moreover, our assumed experiment, covering

~ 8000 deg^2 during 20000 hours, is has the potential to improve current constraints on $f_{\rm NL}$ on its own.

Note that these results are only an illustration. IM observations have much room to improve thanks to cross correlations of different spectral lines and with galaxy number counts, and applying the strategies mentioned in Section 4.2.5.5.

Unfortunately, there is still much unknown about the luminosity function of most emission lines at high redshift, with a large number of plausible models spanning a wide variety of amplitudes and shapes. This affects mainly to $\langle T\rangle$, b and $P_{\rm shot}$, hence the amplitude of the power spectrum. However, this will never affect the robustness of the cosmological measurements, only their S/N, by having an error more or less dominated by cosmic variance. Therefore, the actual S/N may change considerably with respect to theoretical expectations until precise determinations of the luminosity functions are achieved.

Contributing to the promising future of IM for cosmology, the formalism and findings presented in this work will allow for a robust, independent and optimal extraction of cosmological information from IM observations. Therefore, we recommend its use for future exploitation of IM power spectrum measurements.

4.2.7 Appendix: measuring cross-power spectra

The formalism discussed in this work focuses on the auto-power spectrum of brightness temperature fluctuations. Nonetheless, this formalism can be straightforwardly generalized for the case when two different lines, or IM and galaxy number counts, are cross-correlated. For completeness, we discuss here these cases and recommend the use of this formalism to measure the multipoles of the cross-power spectra.

Let us consider two generic brightness temperature maps of two different spectral lines, and a galaxy catalog, denoted by X, Y and g, respectively. In this case, the Kaiser effect present in the RSD factor is different for each tracer. For instance, in $F^X_{\rm RSD} \propto (1+f\mu^2/b_X)$, with b_X being the luminosity-averaged bias for the line X. In the case of galaxy number counts, we can use the same expression, substituting b_X by the galaxy bias, b_g. Then, the intensity mapping cross-power spectra of the X and Y lines, and the cross-power spectrum of galaxy number counts and intensity mapping, are given by:

$$\begin{aligned} P^{XY} &= P^{XY}_{\rm clust} + P^{XY}_{\rm shot}\,; \\ P^{XY}_{\rm clust} &= \langle T_X\rangle\langle T_Y\rangle b_X b_Y F^X_{\rm RSD} F^Y_{\rm RSD} P_{\rm m}; \\ P_{\rm shot} &= \langle T_X T_Y\rangle\,; \end{aligned} \tag{4.24}$$

$$\begin{aligned} P^{Xg} &= P^{Xg}_{\rm clust} + P^{Xg}_{\rm shot}\,; \\ P^{Xg}_{\rm clust} &= \langle T_X\rangle b_X b_g F^X_{\rm RSD} F^g_{\rm RSD} P_{\rm m}\,; \\ P^{Xg}_{\rm shot} &= \frac{\langle T_X\rangle_g}{n_g}\,; \end{aligned} \tag{4.25}$$

where we have dropped the explicit notation regarding dependence on k and μ (as will be done hereinafter). In Equation (4.25), $\langle T\rangle_g$ is the mean brightness temperature sourced by the galaxies belonging to the galaxy catalog used, and n_g is the number density of such galaxies. Note the difference in the shot noise terms in Equation (4.25) with respect to Equations (4.4) and (4.24). This is because contributions to $P^{Xg}_{\rm shot}$ come only from the locations occupied by the galaxies targeted by the galaxy survey, and the shot noise between the galaxy distribution and the luminosity sourced elsewhere vanishes.

Here we also assume that the shot noise of the galaxy power spectrum is Poissonian (i.e., $P^{gg}_{\rm shot} = 1/n_g$). Nonetheless, clustering and halo exclusion introduce deviations from a Poissonian shot noise. This non Poissonian contribution may change the amplitude of the shot noise and even induce a small scale dependence (Ginzburg et al., 2017; Schmittfull et al., 2018).

In any case, the parametrization of the cross-power spectra can be equally optimized. Following the same arguments as in Section 4.2.3, we express the power spectrum of two different lines as:

$$\begin{aligned} P^{XY} =& \frac{P_m/\sigma_8^2}{\left(1+0.5\left[k\mu\sigma_{\rm FoG}\right]^2\right)^2}\left(\tilde{T}^{1/2}_{XY} b_X\sigma_8 + \tilde{T}^{1/2}_{XY} f\sigma_8\mu^2\right)\times \\ &\times\left(\tilde{T}^{1/2}_{XY} b_Y\sigma_8 + \tilde{T}^{1/2}_{XY} f\sigma_8\mu^2\right) + \langle T_X T_Y\rangle, \end{aligned} \tag{4.26}$$

where $\tilde{T}_{XY} = \langle T_X\rangle\langle T_Y\rangle$. Since we have two different biases and two different brightness temperatures (one per each line), the combination of parameters that can be measured is:

$$\vec{\theta}_{XY} = \{\alpha_\perp, \alpha_\parallel, \tilde{T}_{XY}^{1/2} f\sigma_8, \tilde{T}_{XY}^{1/2} b_X\sigma_8, \tilde{T}_{XY}^{1/2} b_Y\sigma_8, \sigma_{\rm FoG}, \langle T_X T_Y\rangle, \vec{\varsigma}\}\,. \tag{4.27}$$

Similarly to Equation (4.26), we prefer to express the cross-power spectrum of IM and the galaxy number counts as:

$$\begin{aligned} P^{Xg} =& \frac{P_m/\sigma_8^2}{\left(1+0.5\left[k\mu\sigma_{\rm FoG}\right]^2\right)^2}\left(\langle T_X\rangle^{1/2} b_X\sigma_8 + \langle T_X\rangle^{1/2} f\sigma_8\mu^2\right)\times \\ &\times\left(\langle T_X\rangle^{1/2} b_g\sigma_8 + \langle T_X\rangle^{1/2} f\sigma_8\mu^2\right) + \frac{\langle T_X\rangle_g}{n_g}. \end{aligned} \tag{4.28}$$

In this case, the parameter combinations measured would be:

$$\vec{\theta}_{Xg} = \{\alpha_\perp, \alpha_\parallel, \langle T_X\rangle^{1/2} f\sigma_8, \langle T_X\rangle^{1/2} b_X\sigma_8, \langle T_X\rangle^{1/2} b_g\sigma_8, \sigma_{\rm FoG}, \langle T_X\rangle_g/n_g, \vec{\varsigma}\}\,. \tag{4.29}$$

The possible extra variation of the amplitude of $P^{Xg}_{\rm shot}$ due to non-Poissonian contributions mentioned above is already accounted for, since it is implicitly embedded in $\langle T_X\rangle_g$ when we marginalize over $\langle T_X\rangle_g/n_g$. Note that if the goal is to measure $\langle T_X\rangle_g$, the non-Poissonian contribution to the shot noise needs to be explicitly modeled. We neglect the potential scale dependence introduced, which is a good approximation at this stage.

The covariance of the cross-power spectra is also slightly different than for the auto-power spectrum. Although the two tracers (no matter if they are two lines or one line and galaxies) can be observed by the same experiment, let us consider without loss of generality the case in which each tracer is observed by a different experiment. In this case, most of the quantities introduced in Section 4.2.4 would be specific of each experiment. The covariance per μ and k bin of the cross-power spectra of two different lines is given by:

$$\sigma^2_{XY} = \frac{1}{2}\left(\frac{P^2_{XY}}{N_{\rm modes}} + \sigma_X\sigma_Y\right), \tag{4.30}$$

where σ_X and σ_Y are the square root of the covariance reported in Equation (4.16), computed using the power spectrum and survey specifications corresponding to the tracer X and Y, respectively. In the case of cross-correlating one line and galaxy number counts, the covariance can be computed as:

$$\sigma_{Xg}^2 = \frac{1}{2}\left(\frac{P_{Xg}^2}{N_{\rm modes}} + \sigma_X \frac{P_{gg} + \frac{1}{n_g}}{\sqrt{N_{\rm modes}}}\right), \tag{4.31}$$

where $\left(P_{gg} + 1/n_g\right)/\sqrt{N_{\rm modes}}$ is the square root of the covariance of the galaxy power spectrum (when Poissonian shot noise is assumed). In addition, $V_{\rm field}$ (which enters in the $N_{\rm modes}$ calculation) would be determined by the overlap of the two volumes surveyed using each tracer. It is possible to use a more detailed description of $V_{\rm field}$ by accounting for the two different volumes probed by each tracer (not only the overlap) and then compute the power spectrum taking into account the fact the some region would not overlap. We leave the exploration of this option for future work.

Finally, the computation of χ^2 (and, similarly, the S/N) when cross-correlations are considered needs to be adapted. If the cross-power spectrum of two tracers can be measured, also the corresponding auto-power spectra can be. Therefore, when comparing the model to the observations, all this information needs to be taken into account. In this case, Equations (4.18) and (4.19) are still correct, but both the data vector and covariance matrix need changes. The former will include both auto- and cross-power spectra, hence $\vec{\Theta}$ is the concatenation of $\vec{\Theta}_{XX}$, $\vec{\Theta}_{XY}$ and $\vec{\Theta}_{YY}$. In turn, the covariance matrix will be formed by four square submatrices of the same size, where the diagonal blocks would be $\mathcal{C}_{XX}$ and $\mathcal{C}_{YY}$, and the off-diagonal blocks, $\mathcal{C}_{XY}$. Note that in this case, Y can be line intensity mapping signal or galaxy number counts.

4.3 Cosmic rulers at the Epoch of Reionization with Intensity Mapping

Baryon acoustic oscillations (BAO) provide cosmic standard rulers to probe the expansion of the Universe across time. However, galaxy surveys are not able to reach redshifts beyond $z \sim 3-5$. We propose the use of line-intensity mapping (IM) observations to access redshifts beyond this limit and measure the BAO scale at the epoch of reionization. In a companion paper, we present an unbiased methodology to optimally extract cosmological information from the IM power spectrum marginalizing over the astrophysical uncertainties, which is especially suitable for measuring the BAO scale. We consider the planned experiments SPHEREx and COMAP, which will target the Hα and Lyman-α, and the CO spectral lines, respectively. We also envision a CO experiment within the next generation of IM observational effort, the Intensity Mapping Stage 3 (IMS3). We show that SPHEREx has the potential to measure the BAO scale with a precision of $\sim 7-20\%$ at $0.5 \lesssim z \lesssim 6.5$, and COMAP, with a precision of $\sim 3-4\%$ at $z \sim 2.8$. On the other hand, the IMS3 CO experiment will provide percent level measurements of the BAO scale at $2 \lesssim z \lesssim 7$, and with a $7-11\%$ error at $z \sim 8$. These measurements will be of paramount importance to probe the Universe in an unexplored regime, and test exotic models of dark matter, dark energy and modified gravity.

Introduction

Constraining the expansion of the Universe is one of the most powerful ways to probe dark energy. Understanding how the Universe expands equals to improve our knowledge about the curvature of the Universe and to detect any extra specie whose energy density evolves in a different manner than that of the matter or radiation. The expansion history can be constrained measuring directly the expansion rate or the distance-redshift relation (which is the integral of the Hubble parameter). And the best way to measure these quantities after recombination is using standard distance indicators. Among them, the most powerful ones are the BAO (as standard rulers) and the SNeIa (as standard candles). However, the latter only give relative measurements because the Hubble constant and the absolute magnitude of the SNeIa are completely degenerate. In addition, gravitational waves from neutron star mergers with electromagnetic counterparts (Abbott et al., 2017a,b) provide well-calibrated distance measurements with accompanying redshifts, hence acting as standard sirens (Abbott et al., 2017). Standard sirens have a great potential to constrain the expansion rate of the Universe in the near future (see e.g., Feeney et al. (2019)).

BAO can be used as standard rulers because the BAO scale is robustly determined by the sound horizon at radiation drag, r_s. Before recombination, dark matter clusters due to its own gravity, but baryons are impeded to fall into the gravitational potentials due to their interaction with photons. This unbalance produces acoustic oscillations in the matter density field: the BAO. After recombination, this pattern is frozen in the density distribution, given that the photon mean free path becomes larger than the Hubble length. Then, as the Universe evolves, overdensities grow keeping the BAO feature: a small enhancement of the correlation function at a distance corresponding to r_s. These oscillations and their corresponding scale are extremely well measured in the CMB, and can be also measured at low redshift using large scale structure experiments.

All existing BAO measurements have been obtained using observations from galaxy surveys, mostly using galaxy clustering (see e.g., Eisenstein et al. (2005); Cole et al. (2005); Alam et al. (2017b); Bautista et al. (2017); The Dark Energy Survey Collaboration & Abbott (2017)), but also quasar clustering (Gil-Marín et al., 2018), the Lyman-α forest (de Sainte Agathe et al., 2019), and the cross-correlation of quasars and the Lyman-α forest (Blomqvist et al., 2019). Planned future galaxy surveys, such as DESI (DESI Collaboration et al., 2016a), Euclid (Amendola et al., 2018) or SKA (Square Kilometre Array Cosmology Science Working Group et al., 2018) will improve over these measurements. However, any of these measurements are restricted to $z \lesssim 2$ ($z \lesssim 3$ for quasars and the Lyman-α forest). Even recent, ambitious proposals for future experiments would present an upper bound in redshift at $z \sim 5$ (Wilson & White, 2019; Ferraro et al., 2019). This is not a fundamental restriction to measure BAO, whose feature is of course present in the large scale structure at higher redshift. This upper bound is due to observational limitations of galaxy surveys: galaxies are too sparse and faint at high redshifts for galaxy surveys to have enough number density and yield meaningful measurements.

Alternative tracers or observational techniques are then required to measure the BAO at $z \gtrsim 3-5$. Line-intensity mapping (IM) experiments integrate all the light received by the telescope along the line of sight, adding the emission of every source. This makes possible to use much fainter sources than in galaxy surveys, where they would be discarded as they would not surpass the detection threshold. IM experiments target easily-identifiable spectral lines so that the redshift can be precisely determined by tuning the frequency of the receivers. The intensity of these lines traces the large scale structure, since they are sourced in halos. Taking all this into account, IM experiments return a biased map of the large scale structure of the Universe (where the actual bias depends on the line), reaching much higher redshifts than galaxy surveys. Then, BAO obtained from IM observations have the potential to become a very powerful probe of the expansion history of the Universe at high redshifts, even reaching the epoch of reionization.

BAO from the IM power spectrum

The BAO scale at high redshift can be constrained using future measurements of the IM power spectrum. To transform redshifts into distances and then be able to measure the power spectrum from the observations, a fiducial cosmology must be assumed. However, if the assumed fiducial cosmology does not match the actual one, the distances reconstructed from the observations would be distorted. This is known as the Alcock-Paczynski effect (Alcock & Paczynski, 1979). Rather than a nuisance, this effect is the key to interpret the measured BAO scale in a cosmological framework.

In Fourier space, we denote the true and observed wavenumbers as $k^{\rm tr}$ and $k^{\rm obs}$, respectively. Their relation along the line of sight and transverse directions is given by $k_{\parallel}^{\rm tr} = k_{\parallel}^{\rm obs}/\alpha_{\parallel}$ and $k_{\perp}^{\rm tr} = k_{\perp}^{\rm obs}/\alpha_{\perp}$. The rescaling parameters relating the observed and true scales are defined as:

$$\alpha_{\perp} = \frac{D_A(z)/r_{\rm s}}{\left(D_A(z)/r_{\rm s}\right)^{\rm fid}}, \qquad \alpha_{\parallel} = \frac{\left(H(z)r_{\rm s}\right)^{\rm fid}}{H(z)r_{\rm s}}, \tag{4.32}$$

where $D_A(z)$ and $H(z)$ are the angular diameter distance and the Hubble expansion rate at redshift z, respectively, and fiducial quantities are denoted by the superscript 'fid'. The BAO feature, probably the most prominent in the power spectrum at the observed scales (unless the turnover due to matter-radiation equality is observable), helps to correct any distortion produced by the Alcock-Paczynski effect, hence increasing the precision of the measurements of $\alpha_\perp$ and $\alpha_\parallel$. Therefore, comparing this measurements with the fiducial expectations directly provides a measurement of $D_A(z)/r_{\rm s}$ and $H(z)r_{\rm s}$. Afterwards, an external prior on $r_{\rm s}$ can be applied to infer absolute measurements of the expansion history of the Universe.

Disentangling cosmological and astrophysical information is one of the main challenges that appear when analyzing the IM power spectrum. Cosmology and astrophysics are intrinsically intertwined in the IM signal, since the astrophysical processes involving the emission or absorption of the spectral line determine the way the underlying matter distribution is traced. This difficulty is addressed by Bernal et al. (2019b), who propose an optimal way to extract cosmological information from the IM power spectrum. This methodology accounts for the astrophysical degeneracies and marginalizes over them, models redshift space distortions and the Alcock-Paczynski effect, and provide an accurate analytic covariance. Thanks to this methodology, it is then possible to obtain measurements of the BAO scale robust to astrophysics. In addition, if a prior on the mean brightness temperature is available, this methodology provides a way to measure the parameter combination $f\sigma_8$, too.

Spectral lines targeted

HI is the spectral line that has received more attention, due to its great potential to probe reionization (Furlanetto et al., 2019b) and constrain cosmology at low redshift (Bull et al., 2015; Square Kilometre Array Cosmology Science Working Group et al., 2018). However, HI line is quite weak, so that foregrounds may impede cosmological measurements at high redshifts. On the other hand other atomic and molecular lines have been detected at $z \sim 3$. Some examples include the CO auto-power spectrum detection at small scales (Keating et al., 2016), and tentative detections of the CII line (Pullen et al., 2018) and the Lyman-α line (Croft et al., 2016). In this work, we focus on these spectral lines, which are brighter than HI with respect to the corresponding foregrounds, hence more promising to provide higher signal-to-noise measurements of the large scale structure at the epoch of reionization.

CO is the second most abundant molecule in the Universe, and it can be found in cool and warm, metal-enriched molecular gas where stars form efficiently. Although there is a whole cascade of rotational lines, here we focus on the ground level ($J = 1 \to 0$), with has a rest frame frequency of 115.27 GHz. On the other hand, emitting CII photons (with rest wavelength of 158 μm) is one of the most efficient cooling mechanism in photodissociating regions powered by UV emission. The Lyman-α line (rest wavelength of 121.6 nm) is mostly sourced by hydrogen recombinations, although it can be triggered by collisional excitations, too. The hydrogen ionizes mostly due to UV photons emitted by young stars. But since hydrogen recombination timescales are small, it is a good approximation to consider the number of recombinations to be the same as the number of ionizations. Besides Lyman-α, other lines are also emitted as hydrogen recombines. Hα, with a rest frame wavelength of 656.3 nm, is one of the brightest among these. Although the physical processes that trigger the emission of these four lines are different, all of them can be considered as tracers of the star formation rate, with Lyman-α and Hα signal extending along the halo of star forming galaxies, contrarily to CO and CII.

IM experiments considered

We propose to use the power spectrum of star formation spectral lines, as CO, CII, Lyman-α and Hα to measure the BAO scale and extend the cosmic distance ladder up to reionization, reaching $z \sim 8$. To estimate the potential of IM BAO measurements, we forecast measurements of IM power spectrum from planned and future IM experiments targeting star formation spectral lines.

SPHEREx (Doré et al., 2014), in addition to be a galaxy survey, will carry out IM surveys. Launching in 2023, this satellite's IM missions will target Lyman-α and Hα emission, as well as Hβ and the oxygen lines OII and OIII. However, the power spectra of the first two lines are expected to yield higher significance and lower contamination from foregrounds and interlopers, which makes them more suitable for cosmological analyses. SPHEREx's wide survey will observe the whole sky, but the corresponding IM observations are expected to have low signal-to-noise ratios. Hence, we focus on the deep IM survey, which will cover 200 deg^2, but with much higher sensitivity. SPHEREx will have an angular resolution of 6.2 arcsec at full-width half maximum, and a spectral resolution $R = \delta_\nu/\nu_{\rm obs} = 41.4$ at $0.75 < \lambda_{\rm obs} < 4.1$ μm and $R = 150$ at $4.1 < \lambda < 4.8$ μm (where $\delta\nu$ is the width of the frequency channel, and $\nu_{\rm obs}$ and $\lambda_{\rm obs}$ are the observed frequency and wavelength, respectively). We restrict ourselves to $0.75 < \lambda_{\rm obs} < 4.1$ μm, since a spectral resolution of $R = 150$ is too low for our interest. Note that SPHEREx will observe the Lyman-α line at $5 \lesssim z \lesssim 8$, and Hα emission, at $z \lesssim 5$. Although Hα and Lyman-α emission from higher redshifts enters into the observable frequency band of SPHEREx, the corresponding noise will be too high to achieve significant measurements.

On the other hand, COMAP (Cleary et al., 2016), already under construction, is a single-dish, ground-based telescope targeting the CO lines in the frequency band $26-34$ GHz (which corresponds to $2.4 \lesssim z \lesssim 3.4$ for the first CO rotational line). The experiment's telescopes include 19 single-polarization detectors with an angular resolution of 4 arcmin at full-width half maximum and channel width of $\delta\nu = 15.6$ MHz. The expected system temperature is $T_{\rm sys} \sim 40$ K. In its first phase, COMAP1, the experiment will employ one telescope. However, due to the small volume observed (only 2.25 deg^2 of the sky will be probed), its observations will not be suitable for cosmological analyses. The second phase of COMAP (COMAP2) will observe during $t_{\rm obs} = 10000$ hours with four identical, additional telescopes. The spectral resolution of the five telescopes used by COMAP2 will be improved to $\delta\nu = 8$ MHz. The precise survey strategy for COMAP2 has not been decided yet. Therefore, we optimize the total signal-to-noise ratio and assume a sky coverage $\Omega_{\rm field} = 60$ deg^2.

There are promising CII planned experiments, such as TIME (Crites et al., 2014). It is expected that in the coming years, these experiments will confirm tentative CII detections with significant measurements of the power spectrum. However, the sky coverage of the planned surveys will be so small that large enough scales will not be accessible. Unfortunately, this means that the BAO scale will not be measured.

We also envision the next generation of IM experiments, the Intensity Mapping Stage 3 (IMS3). One of the primary goals of the IMS3 observational effort will be to probe cosmology at the epoch of reionization. Therefore, IMS3 must involve a

Instr. Paramater	COMAP 1	COMAP 2	IMS3 (CO)
$T_{\rm sys}$ [K]	40	40	max(20,$\nu_{\rm obs}$)
# detectors	19	95	500*
Ang. resolution (FWHM) [arcmin]	4	4	4
Frequency band [GHz]	26-34	26-34	12-36
$\delta\nu$ [MHz]	15.6	8.0	2.0
$t_{\rm obs}$ [h]	6000	10000	10000
$\Omega_{\rm field}$ [deg^2]	2.25	60	1000

Table 4.3: Experimental specifications for COMAP 1 (under construction), the planned COMAP 2 and the CO experiment within the IMS3. * These are dual polarization detectors, which double the effective number of detectors.

coordinated experimental effort developing several experiments to target different spectral lines over large volumes at higher redshifts.

Among all the lines that will be targeted by IMS3, we focus on CO, the only spectral line that has been robustly detected at intermediate redshifts using IM. We conceive this ground-based CO experiment as an upgrade of COMAP. Taking the upgrades between the two phases of COMAP described above as benchmark, we consider 500 dual-polarization detectors, and a frequency channel width of $\delta\nu = 2$ MHz. The great upgrade in spectral resolution is easy to achive, since, as noted by Ihle et al. (2019), COMAP's spectrometer can operate at higher spectral resolution than 15.6 MHz, having a basic resolution of ~ 1.95 MHz. COMAP will not be able to exploit such great resolution due to limited signal-to-noise per voxel, but this will not be the case for a CO experiment within IMS3.

We assume that the CO experiment within IMS3 will observe at frequencies between $12-36$ GHz ($2.2 \lesssim z \lesssim 8.6$) during 10000 hours. Finally, we use a model based on the performance of heterodyne-based instruments for radioastronomy at centimeter wavelengths to model $T_{\rm sys} = \max\left[20,\, \nu_{\rm obs}\,({\rm K/GHz})\right]$ (see e.g., Prestage (2006); Murphy (2018)). As done for COMAP2, we choose $\Omega_{\rm field} = 1000$ deg^2 in order to optimize the total signal-to-noise ratio of the CO IM power spectrum. We compare the experimental specifications of both phases of COMAP and the IMS3 CO experiment in Table 4.3.

The evolution of the large scale structure and the luminosity function of the spectral lines as function of redshift is non negligible over the wide redshift ranges

	SPHx (Hα)				SPHx (Lyα)		COMAP2	IMS3				
z	0.55	1.90	3.20	4.52	5.74	7.00	2.84	2.73	4.01	5.30	6.58	7.87
$D_A(z)/r_{\rm s}$	11.0	6.9	9.6	19.8	11.4	37.9	3.1	0.88	0.98	1.3	2.7	7.0
$H(z)r_{\rm s}$	15.1	10.6	16.1	36.5	21.9	76.4	4.5	1.3	1.5	2.1	4.4	11.6

Table 4.4: Forecasted 68% confidence level relative marginalized relative constraints on $D_A(z)/r_{\rm s}$ and $H(z)r_{\rm s}$ from COMAP2, an IMS3 CO experiment and SPHEREx observations of the Hα and the Lyman-α lines. The relative constraints are expressed in percentages. Note that all these constraints are independent among them, except those of COMAP2 and the first bin of the IMS3 CO experiment.

probed by the experiments that we consider. Therefore, we need to bin the volumes observed in different redshift bins. We consider in every case non-overlapping, independent redshift bins such as $\log_{10}[\Delta(1+z)] = \log_{10}[\Delta(\nu/\nu_{\rm obs})] = 0.1$ (where ν is the rest frame frequency), with the corresponding effective redshift located in the center of the frequency bin. This results in four bins for the SPHEREx Hα observations (with effective redshifts $z = \{0.55, 1.90, 3.20, 4.52\}$), two bins for the volume probed by SPHEREx using the Lyman-α line ($z = \{5.74, 7.00\}$), a single redshift bin for COMAP2 at $z = 2.84$, and five redshift bins for the CO experiment within IMS3 ($z = \{2.73, 4.01, 5.30, 6.58, 7.87\}$).

Results

We apply the Fisher matrix formalism (Fisher, 1935; Tegmark et al., 1997) to forecast constraints on the BAO measurements using the IM power spectrum multipoles up to the hexadecapole, as measured by SPHEREx, COMAP2 and a CO experiment within IMS3. We model Lyman-α, Hα and CO emissions following the models and prescriptions of Silva et al. (2013), Gong et al. (2017) and Li et al. (2016), respectively. Regarding the cosmological model, we assume the Planck baseline ΛCDM model with the bestfit to the full Planck data set and BAO from galaxies as fiducial values for the cosmological parameters. Finally, we use the halo mass function and halo bias fitting function introduced in Tinker et al. (2010). We use the methodology proposed by Bernal et al. (2019b) to model the multipoles of the IM power spectrum and their corresponding covariance.

In table 4.4, we report forecasted marginalized 68% confidence level relative constraints on $D_A(z)/r_{\rm s}$ and $H(z)r_{\rm s}$ from the surveys considered. We find that

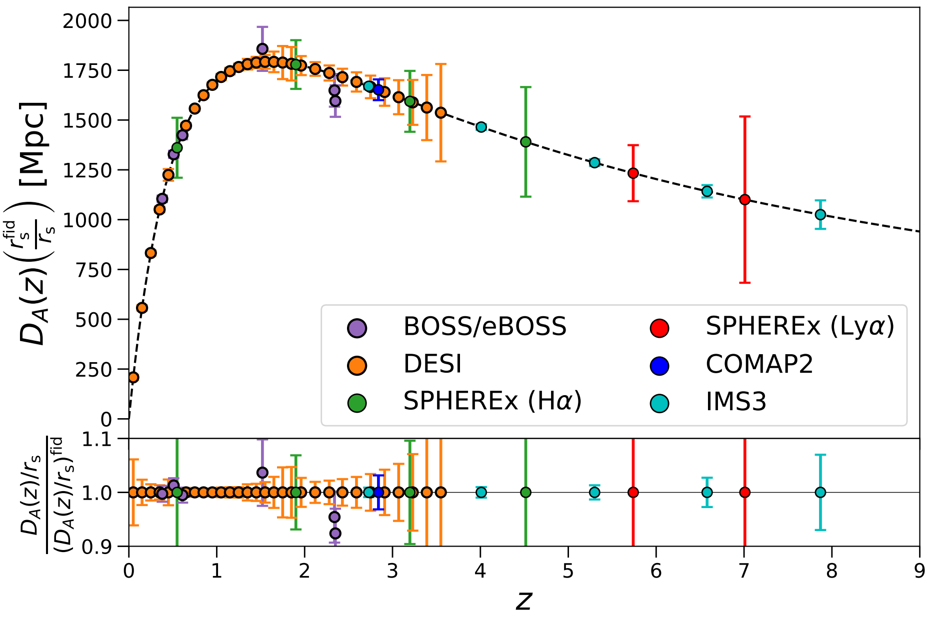

Figure 4.6: 68% confidence level marginalized measurements and forecasted constraints of the angular diameter distance as a function of redshift, weighted by the ratio between the actual sound horizon at radiation drag and its fiducial value. Estimated constraints from IM observations of Hα (green) and Lyman-α (red) lines using SPHEREx, and of CO line using COMAP2 (blue) and IMS3 (cyan) are included. We also show current measurements from BOSS and eBOSS collaborations (purple), and projected constraints from DESI (orange).

SPHEREx's IM BAO measurements will not be very precise: the precision of the strongest constraint would be of 6.9% at $z = 1.9$, while most of the remaining measurements would have errors above the 10%. The estimated low precision of SPHEREx is caused by the poor spectral resolution of the experiment.

In turn, COMAP2 will measure BAO scale at a redshift similar to that of the Lyman-α forest, and with competitive precision (3.1% and 4.5% errors in the transverse and radial directions, respectively). IMS3 CO experiment, on the other hand, will provide very precise measurements at $2 \lesssim z \lesssim 6$ (some even below the percent level), while the precision degrades at larger redshifts. At the last redshift bin ($z = 7.87$), IMS3 will measure $D_A/r_{\rm s}$ and $Hr_{\rm s}$ with a precision of 7% and 11.6%, respectively.

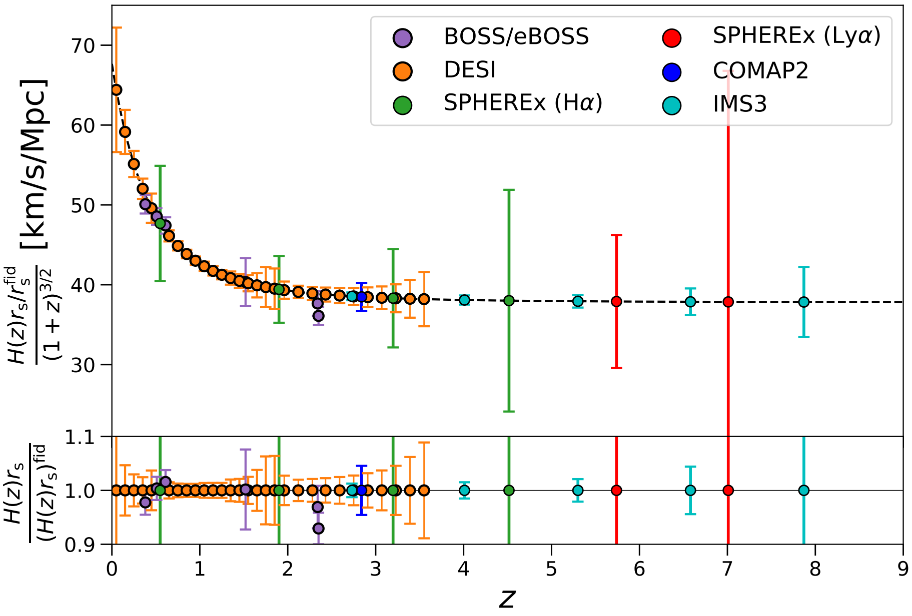

Figure 4.7: Same as Figure 4.6, but for the Hubble expansion rate over $(1+z)^{3/2}$ as function of redshift.

In Figure 4.6 and Figure 4.7, we present a comparison of the forecasted precision of the angular diameter distances and Hubble expansion rates to be measured by IM experiments, with existing and projected measurements from galaxy surveys. We show the results weighted by the ratio of the fiducial $r_{\rm s}$ and its actual value, to avoid the inclusion of external information in the analysis in the form of a prior on $r_{\rm s}$. We include existing measurements from the BOSS (Alam et al., 2017b) and eBOSS (Gil-Marín et al., 2018; de Sainte Agathe et al., 2019; Blomqvist et al., 2019) galaxy surveys, as well as forecasted constraints from the DESI galaxy survey (DESI Collaboration et al., 2016a). For all of them, we include results from galaxy or quasar BAO ($z \lesssim 2$), and BAO from the Lyman-α forest and its cross-correlation with quasars ($2 \lesssim z \lesssim 3.5$).

As can be seen from these comparisons, COMAP2 measurements will be really competitive, improving current eBOSS measurements and having the same level of precision than DESI estimates. In turn, SPHEREx precision at the intermediate redshift bins is comparable to current constraints from eBOSS using the quasar power spectrum at $z = 1.52$, but worse than constraints from the Lyman-α forest.

Interestingly, while BAO measured from the IM power spectrum (and from galaxy clustering) usually yield stronger constraints on the transverse direction (i.e., D_A) than in the radial direction (i.e., H), measurements using the Lyman-α are more precise on the radial direction. Therefore, it is very likely that the degeneracies between D_A and H as measured from these two observables are very different. Then, if IM and Lyman-α forest BAO are combined, we expect that degeneracies will be broken and the final constraints will be much stronger. In addition, there is no expectation of measuring the BAO scale at $z \gtrsim 4$ in the coming years besides IM observations, so that SPHEREx measurements, even if with large errors, can be really meaningful until more precise experiments become available.

Conversely, the CO experiment within the IMS3 envisioned in this work would yield incredibly precise results at very high redshifts, increasing the determination of the expansion of the Universe beyond reionization. Only the first redshift bin of the IMS3 CO experiment would overlap with existing or projected measurements from the Lyman-α forest, and the forecasted constraints from IMS3 are $3 - 5$ times and $2 - 3$ times stronger than those from eBOSS and DESI, respectively. Furthermore, IMS3 would maintain the same level of precision until $z = 5.30$, where it starts to degrade, yielding a $3 - 4$ times worse constraints at $z = 6.58$ than at lower redshifts.

Finally, we also consider the case in which we have access to a prior on the mean brightness temperature or intensity of the spectral lines. In this scenario, as proposed by Bernal et al. (2019b), it would be possible to obtain inferred constraints on $f\sigma_8$ after marginalizing over astrophysics. We show the forecasted precision of the inferred values from IM experiments in Figure 4.8, assuming different precisions for the brightness temperature prior. As above, we include existing measurements from galaxy surveys, from BOSS and eBOSS, but also from 2dFGRS Percival et al. (2004), 6dFGRS (Beutler et al., 2012) and WiggleZ Kazin et al. (2014), and the estimated results of DESI.

Note that it is not possible to obtain reliable $f\sigma_8$ measurements from the Lyman-α forest, hence existing and coming galaxy surveys measurements can only reach $z \lesssim 2$. Therefore, if robust measurements from IM are to be obtained, these experiments will be able to study the growth of structure in regimes where galaxy surveys are still very far from probing, and maybe never reach. As can be seen, if

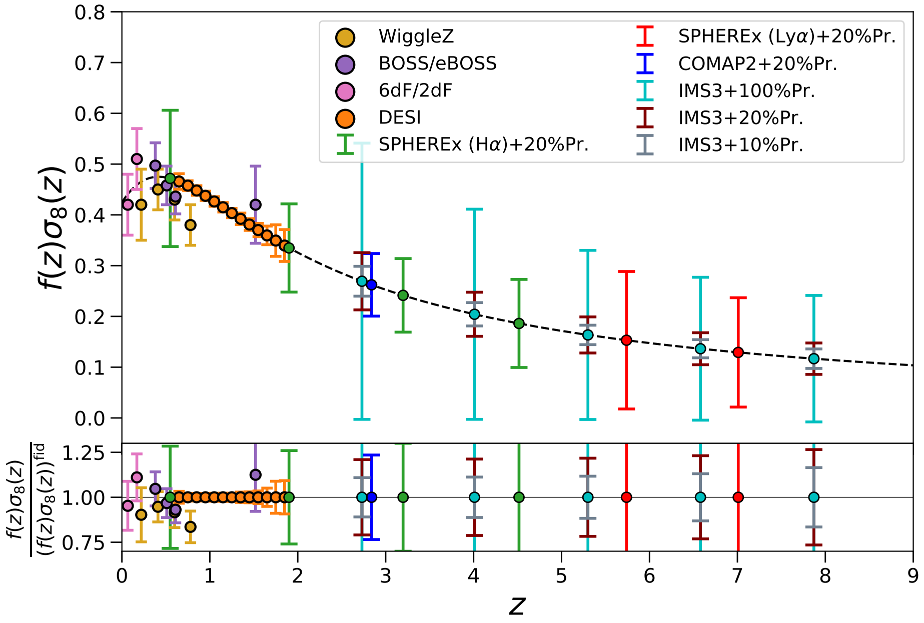

Figure 4.8: Same as Figure 4.6, but for the parameter combination $f\sigma_8$ (considering different possibilities for the prior on $\langle T\rangle$), and also including existing constraints from WiggleZ (yellow) and 6dF and 2dF surveys (pink).

the measurement of $\langle T\rangle f\sigma_8$ (the quantity that can be directly measured from the IM power spectrum (Bernal et al., 2019b)) is precise enough, the error is completely dominated by the uncertainty in $\langle T\rangle$. This is the case for COMAP2 and IMS3 measurements. This further motivates precise measurements of the luminosity function of star forming spectral lines.

As mentioned above, the forecasted constraints from IM experiments we report are completely independent, due to our chosen redshift binning. In the case of SPHEREx, IM targeting Lyman-α and Hα will not overlap in redshift. SPHEREx and COMAP, will observe different patches of the sky, so they will be independent, too. The only exception involves COMAP2 and the first redshift bin of the CO experiment within IMS3. As we consider the IMS3 experiment an upgrade of COMAP, we assume that their volumes would overlap. Finally, for a fair comparison with galaxy surveys, one does need to bear in mind that most of the measurements presented in Figures 4.6, 4.7 and 4.8 are correlated, especially for BOSS and eBOSS (only the measurements close in redshift) and WiggleZ, but probably also for the final measurements of DESI if so many redshift bins are used.

Conclusions

Throughout this letter, we have demonstrated the potential of planned and future IM experiments to constrain the expansion history of the Universe up to the epoch of reionization. This would be an incredible achievement for cosmology and almost the only way to directly measure how the Universe expands beyond $z \sim 3-5$, since galaxy surveys cannot reach higher redshifts. Standard sirens (Abbott et al., 2017) might also achieve this goal, although the sensitivity needed to obtain precise measurements of neutron star mergers and their electromagnetic counterparts at these redshifts is considerably more exigent than current and coming experiments. Another option is to measure the velocity-induced acoustic oscillations at cosmic dawn, as proposed in Muñoz (2019a); however, these measurements are complementary to those proposed here, since they probe different epochs of the Universe.

In order to asses the potential importance of these future measurements, one can assume a cosmological model and forecast constraints using them. We show forecasted relative constraints on the total abundance of matter at $z = 0$, $\Omega_{\rm M}$, and the Hubble constant, H_0, assuming ΛCDM, in Figure 4.9. We combine all redshift bins, lines and experiments as independent measurements (avoiding the combination between COMAP2 and IMS3), and also combine them with existing results from the legacy results of Planck and their combination with measured galaxy BAO[1](Planck Collaboration et al., 2018).

While IMS3 can constrain H_0 around the percent level, IM BAO constraints are a factor $\sim 2-3$ worse than Planck's. For instance, Planck's marginalized 68% confidence level relative constraints on $\Omega_{\rm M}$ and H_0 are $\sim 2\%$ and $\sim 0.8\%$, respectively ($\sim 1.6\%$ and $\sim 0.6\%$ when galaxy BAO are included); if we combine them with the IM constraints, we obtain $\sim 1.8\%$ and $\sim 0.6\%$, respectively ($\sim 1.4\%$ and $\sim 0.5\%$). Adding $f\sigma_8$ measurements from IM observations using a conservative

---

[1] We obtain the priors from the public Planck repository (`http://pla.esac.esa.int/pla`), using the data combination denoted as `plikHM_TTTEEE_lowl_lowE_lensing` and `plikHM_TTTEEE_lowl_lowE_lensing_post_BAO`.

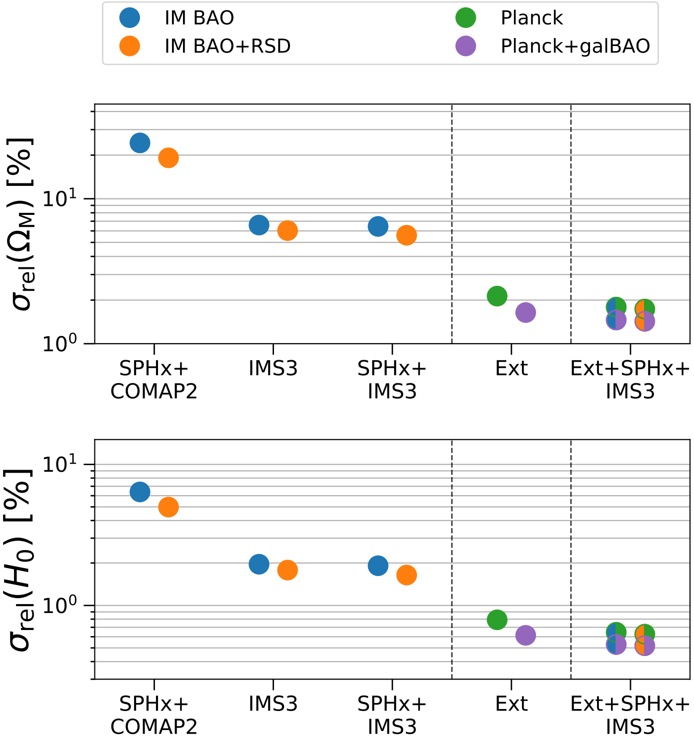

Figure 4.9: Forecasted marginalized 68% confidence level relatived constraints on $\Omega_{\rm M}$ and H_0 assuming ΛCDM from the CO experiment of the IMS3, using only BAO (marginalizing over the amplitude of the power spectrum) and using also $f\sigma_8$ measurements (+RSD), using a 100% prior on $\langle T\rangle$. We also include current constraints from Planck and BAO from galaxies, as well as their combination. Markers with two colors denote the combination of the corresponding data sets.

prior on the mean brightness temperature of the lines (i.e. 100% error), does not improve significantly the measurements. In addition, the projected measurements reported here have little constraining power on standard parametrizations of dark energy, such as wCDM or the CPL parametrization, using w_0 and w_a (Chevallier & Polarski, 2001). This is because IM BAO are measured at high redshift. These measurements are not going to set strong constraints on standard deviations from ΛCDM. On the contrary, given that all these models predict an expansion history fully determined by the matter abundance from $z\sim 2$ until recombination, and accounting for Planck's strong constraints on $\Omega_{\rm M}h^2$, *consistent* high redshift measurements of the expansion history will not improve cosmological constraints significantly. SKA is expected to yield precise BAO measurements from IM observations at low redshift (Square Kilometre Array Cosmology Science Working Group et al., 2018).

We emphasize 'consistent results' because there is no cosmological probe between $z \sim 2.5$ and recombination. Therefore, blindly assuming that the expansion of the Universe during this period was matter-dominated without any deviation from ΛCDM requires assuming that the nature of dark matter and dark energy is very well known. There are models that predict other behaviors, including modified gravity theories or decayind dark matter into lighter dark particles (see e.g., Raveri (2019) or Vattis et al. (2019)). These models, or alternative modifications of the cosmic expansion in the matter dominated era, could reduce the tension between the direct measurement of H_0 (Riess et al., 2019) and the corresponding inferred value found by Planck assuming ΛCDM (Planck Collaboration et al., 2018). In the end, model independent reconstructions of the Hubble parameter are unconstrained beyond $z \sim 0.7$ (Bernal et al., 2016b; Verde et al., 2017). Moreover, measuring $f\sigma_8$ at high z will allow to constrain modified gravity theories beyond the $\Omega_{\rm M}^{\gamma}$ parametrization.

During this work, we have considered that by the time IM observations over large volumes are available, there will be enough control over foregrounds and line interlopers. In this case, a successful subtraction could be achieved, hence foregrounds and interlopers would not hinder the signal. Accounting for foregrounds might degrade the results reported here, but we emphasize that in the coming years there will be several IM observations which will overlap with galaxy surveys. Cross-correlations between different tracers will make possible the subtraction of this contamination from the IM signal (see e.g., Silva et al. (2013); Sun et al. (2018)). Finally, the luminosity functions of spectral lines at high redshift are highly unknown, which would affect the amplitude of the IM power spectrum. Although this will not bias the BAO measurements (because they are marginalized over the astrophysical uncertainties), it will certainly affect the precision of the measurement by modifying the signal-to-noise ratio. We have account for this fact by choosing line emission models whose predictions are not too optimistic nor too conservative.

In summary, IM experiments will provide precise and robust measurements of the BAO scale up to the epoch of recombination $z \lesssim 8$. These observations will provide constraints on the expansion of the Universe at redshifts which are not accessible otherwise, and test key assumptions of the most common cosmological models, as well as probing exotic models of dark energy and gravity.

5. Conclusions and future prospects

This Chapter summarizes the main conclusions of the research collected in this thesis, and discusses its relevance and impact in a broader context. Finally, potential avenues for research worthy to pursue as follow ups of this work are discussed.

5.1 The tension on H_0 and the role of r_s

The nature and origin of the tension on the Hubble constant, H_0, has been one of the most intriguing enigmas in cosmology during the last few years. H_0 is a crucial quantity in cosmology, since it provides an absolute scale for the expansion history of the Universe. Starting from H_0, the distance-redshift relation is measured using distance indicators such as standard candles (e.g., SNeIa) or standard rulers (e.g., BAO). This procedure builds the direct cosmic distance ladder. However, the distance-redshift relation can be measured starting from an early-Universe quantity, too. The sound horizon at radiation drag, r_s, provides the calibration of BAO as standard rulers, hence normalizing the BAO distance measurements. When r_s instead of H_0 is used to anchor the expansion history of the Universe, the inverse distance ladder is built. Of course, both the direct and inverse cosmic distance ladders must yield consistent results.

The strongest constraints on the anchors of the cosmic distance ladder, H_0 and r_s, come from the CMB angular power spectra measurements. However, CMB can measure H_0 and r_s only in an indirect way. CMB observations probe the Universe at recombination, and therefore require a cosmological model to reconstruct the evolution of the Universe to infer low redshift quantities such as H_0. On the other hand, the CMB angular power spectra measure extremely well the angular acoustic scale. However, the conversion from the angular scale to the physical sound horizon requires an assumption about the expansion history and the sound speed of the early Universe. Due to these reasons, both measurements are model-dependent.

There have been claims of internal inconsistencies in the Planck data sets, which might affect the inferred values of $r_{\rm s}$ and H_0 (Addison et al., 2016). These claims are based on analyses of the large and small scales of the Planck temperature angular power spectrum by separate (i.e., $\ell < 1000$ and $\ell \geq 1000$) yielding inconsistent results. This discrepancy is aligned with the shift in the best fit of the cosmological parameters measured by Planck with respect to WMAP results (which only measured $\ell \lesssim 1000$ with enough signal-to-noise ratio). However, the shifts between Planck and WMAP results are not unusually large according to the expectations obtained from simulated data sets (Planck Collaboration et al., 2016c), so the discrepancies found in Addison et al. (2016) fall within the expectations.

While the anchors of the cosmic distance ladder cannot be directly measured from CMB observations, they can be inferred using other probes. Unfortunately, there is no known direct, independent way to measure $r_{\rm s}$ without assuming any model. The best attempts include model-independent measurements of the low redshift standard ruler, $r_{\rm s}h$, (Verde et al., 2017); and indirect measurements of $r_{\rm s}$ using inferred values of $\Omega_b h^2$ (obtained from primordial deuterium estimates (Cooke et al., 2017)) and BAO, requiring the assumption of a cosmology before recombination (Addison et al., 2017). On the other hand, H_0 can be measured directly in the local Universe using the distance ladder without the need of assuming any cosmological model (Riess et al., 2011). Since the first Planck data release, direct measurements and CMB inferred values assuming ΛCDM have shown increasing levels of discrepancy: from 2-2.5σ (Planck Collaboration et al., 2014) to the current $\sim 4.4\sigma$ (Planck Collaboration et al., 2018; Riess et al., 2019), as more precise measurements did not show significant shifts of the best-fit values.

However, building the distance ladder to directly measure H_0 requires a set of astrophysical assumptions, especially related with the homogeneity of the standard candles used. Recent studies of the Tip of the Red Giant Branch (which can be also used as standard candle) confirm distance measurements using cepheids (see e.g., Hatt et al. (2018)), which dissipates doubts about the homogeneity of cepheids. Moreover, it has been shown that the H_0 measurement is robust against different cepheid callibration modeling choices (Follin & Knox, 2018), and other collaborations beyond SH0ES have measured H_0 with independent SNeIa observations, yielding similar results (Burns et al., 2018).

Nevertheless, SNeIa are not perfect standard candles. After light-curve standardization, it is possible to differentiate between at least two populations in terms of their brightness. While the convention is to separate these two populations by the stellar mass of the host galaxy, Rigault et al. (2018) prove that the age of the SN environment is a better tracer to distinguish the two populations. Interestingly, using the stellar mass as an indicator of the two populations concurs in an underestimation of the difference between the brightness after light-curve standarization of SNeIa belonging to each population. Therefore, the conventional SNeIa analysis might introduce a systematic bias which would affect the distance ladder and, therefore, the H_0 measurements (Rigault et al., 2015). In any case, a definitive quantification of this bias on the SH0ES's measurement requires the application of the analysis using the age of the SN environment to the SNeIa sample used by this collaboration. Meanwhile, statistical reanalyses of the SH0ES measurements have confirmed the original result, without finding any systematic error which explains the tension (Feeney et al., 2017; Cardona et al., 2017).

Since CMB inferred values of H_0 are model-dependent, new physics may alleviate the tension. Several models have been advocated to ease this tension, but none of them has been favoured over ΛCDM by observations. One of the preferred candidates over the past few years to solve the H_0 tension was the introduction of extra relativistic species, which lowers the inferred value of $r_{\rm s}$ and increases the derived H_0. However, CMB polarization power spectrum strongly constraints this model, even with theory motivated priors such as those coming from QCD axions (D'Eramo et al., 2018). These results have been confirmed by the corrected CMB polarization power spectrum of the Planck legacy data release (Planck Collaboration et al., 2018). Other models beyond the standard deviations of ΛCDM were studied in e.g., Di Valentino et al. (2016, 2017, 2018); Chiang & Slosar (2018); Renk et al. (2017).

When it proves hard to find a cosmological model to explain the tension, one of the best options, in my opinion, is to use model-independent analyses. With this agnostic approach, it is possible to extract conclusions from the data in the big picture, isolate the sources of the discrepancy and develop strategies to mitigate it. Then, model-independent analyses have the potential to lead theoretical research to alleviate the tension.

With this in mind, and taking into account that the inverse and direct cosmic distance ladder must coincide, model-independent determinations of the two anchors of the cosmic distance ladder are of utmost importance. Only using BAO and SNeIa, and assuming that they can be treated as standard rulers and standard candles, respectively, we measure the low redshift standard ruler, $r_{\rm s}h$, with a precision of $\sim 2\%$ in a model-independent way, even without imposing spatial flatness (Verde et al., 2017).

Then, the measurement of the low redshift standard ruler allows to infer the values of one the anchors of the cosmic distance ladder by using a prior on the other. This was explored in Bernal et al. (2016b), obtaining a $r_{\rm s}$ value significantly lower than the CMB inferred value when the local measurement of H_0 is imposed. The resulting tension with respect to the CMB inferred value of $r_{\rm s}$ is $\sim 2.6\sigma$. In turn, when $r_{\rm s}$ from CMB is applied to the measured $r_{\rm s}^h$, a low value of H_0 is obtained, resulting in a similar tension with SH0ES's H_0 measurement than between Planck's and SH0ES's. This evidences that the H_0 tension is in reality a mismatch between the two anchors of the cosmic distance ladder.

Besides, the shape of the expansion history of the Universe obtained from model-independent analyses does not deviate more than 5% within a 68% confidence level for $z \lesssim 0.7$ (at higher redshifts, SNeIa measurements are sparser and less precise), as we reported in Bernal et al. (2016b). Therefore, SNeIa and BAO alone, analyzed in the most agnostic way possible, strongly constrain any dynamical dark energy or deviation from the expansion history of the Universe predicted by ΛCDM at very low redshift (precisely at the dark energy dominated epoch). This result disfavors modifications in the dark energy sector as a way to alleviate the H_0 tension.

Our work in Bernal et al. (2016b) changed the way to address the tension on H_0. Later works confirmed these results focusing on the dark energy density instead of the Hubble parameter (Poulin et al., 2018b), or solely on $r_{\rm s}$ (Aylor et al., 2019). Now that it has been shown that no changes in the late Universe will reduce the tension, most of the theoretical efforts are focused on early Universe modifications yielding lower values of $r_{\rm s}$ with respect to the ΛCDM prediction. However, state-of-the-art observations still favours ΛCDM over them. Standard extra relativistic species, for instance, cannot ease this tension due to the changes they produce in the growth of perturbations prior to recombination by changing the diffusion scale.

Some examples of promising models to ease the H_0 tension include self interacting neutrinos (Kreisch et al., 2019), axionic early dark energy (Poulin et al., 2018a), or evolving scalar fields which add energy to the Universe at a narrow redshift window around recombination (Agrawal et al., 2019).

On the other hand, unknown systematics might be always present in the data, and therefore source this kind of tensions. There is an extensive literature in cosmology related to the definition and evaluation of tensions between data sets (see e.g., Verde et al. (2013); Charnock et al. (2017); Lin & Ishak (2017)). However, subjectivity is always involved when defining the threshold between consistency and tension. In addition, if two data sets are considered in tension, one of them needs to be discarded. Usually, this is also a subjective decision. When a way to reconcile these data sets is not found (as happens currently in the case on H_0), there should be a procedure capable to analyze the data accounting for the inconsistencies and extract robust, although weaker, constraints. In the epoch of precision cosmology, accuracy must really be the goal.

This was the main motivation to develop a formalism to perform joint analysis of several data sets in a conservative way, no matter the level of discrepancy between them, as well as accounting for the presence of unknown systematics. We introduce this methodology, along with the the release of a public code, `BACCUS`, in Bernal & Peacock (2018). It involves extra parameters to model possible unaccounted-for systematics of two types: misestimation of the covariance of the data (already introduced in Hobson et al. (2002)) and a bias in the best fit (introduced in a consistent way for the first time in this work).

Thanks to these two types of parameters, the methodology is completely flexible and can account for any kind of discrepancy or systematic errors affecting the data sets. This methodology provides a way to obtain conservative and agnostic constraints from the data. Of course, the resulting constraints will be pessimistic, since potential systematic errors are considered and marginalized over. However, this avenue works as a sanity check to avoid any false claim of new physics. In this sense, this approach should be always used in parallel with standard, more aggressive analysis. In addition, this methodology has the power to ascertain which data set might be contaminated by non-accounted systematics.

Besides introducing introduce the methodology, we apply it to the tension in H_0, using every independent existing observation at low redshift providing a constraint on the expansion history of the Universe. The results obtained applying the conservative approach peak at larger values than the standard approach. Nevertheless, the conservative uncertainties are so large that there is no tension with either the CMB inferred value or the direct measurement, nor it is possible to ascertain whether any of the data sets included is affected by systematics.

Finally, this methodology has been proved useful to use external data from a different probe, when different experiments or assumptions provide inconsistent results. In this case, rather than choosing between them, `BACCUS` can be used to obtain a conservative result from all existing measurements and use it as prior. For instance, `BACCUS` was used for this purpose in Jimenez et al. (2019b) to combine the age of globular clusters obtained assuming different stellar models.

5.2 The role of primordial black holes in cosmology

PBHs may form in the very early Universe (before matter-radiation equality) from high peaks in the density perturbations within the horizon. Therefore, the abundance and mass distribution of PBHs carry information about the primordial power spectrum. Moreover, if the abundance of PBHs is high, they might be a significant fraction of the dark matter. There has been an increasing interest in PBHs since the first detections of graviational waves. However, the vast majority of these studies consider that all PBHs have the same mass. This assumption is unrealistic, not only because not all of the PBHs would form at the very same time, but also because each PBH would experience a different accretion and merger history, which also produces an extended mass distribution. Furthermore, any correlation between the fraction of dark matter as PBHs, $f_{\rm PBH}$, and the cosmological parameters is often ignored. Of course, correctly considering these two facts has a large impact in the observational constraints on $f_{\rm PBH}$.

As PBHs accrete gas, they inject energy in form of radiation into the medium. This affects the thermal and ionization histories of the Universe and, if abundant enough, leave observable imprints on the CMB anistropies (as suggested by Ricotti et al. (2008) and revised by Ali-Haïmoud & Kamionkowski (2017)) and the 21 cm intensity mapping signal (as we studied in Bernal et al. (2018)). The more massive the PBHs, the faster they accrete matter, hence the stronger the energy injection into the medium. Starting from the modeling of the impact of PBHs on the CMB (Ali-Haïmoud & Kamionkowski, 2017), we perform a robust statistical analysis (improving the treatment used in Ali-Haïmoud & Kamionkowski (2017)), and study the degeneracies with the rest of parameters Bernal et al. (2017). A strong degeneracy with the spectral index n_s and a mild degeneracy with $r_{\rm s}$ are found. Moreover, there are strong degeneracies with additional parameters of models beyond ΛCDM, especially the number of relativistic species. These degeneracies, common to other energy injecting mechanisms, such as annihilating dark matter (see e.g., Green et al. (2019)), open the possibility to impose stronger constraints on $f_{\rm PBH}$ combining CMB with other observations such as galaxy clustering.

Furthermore, we set constraints on $f_{\rm PBH}$ from CMB anisotropies explicitly accounting for PBH extended mass distributions for the first time in Bernal et al. (2017). This result also tests with success the methodology to convert $f_{\rm PBH}$ constraints assuming that all PBHs have the same mass to cases with extended mass distributions, introduced in Bellomo et al. (2018). Whenever the mass distribution extends towards high masses, CMB angular power spectra set stronger constraints on $f_{\rm PBH}$ than in the unrealistic scenario of a monochromatic distribution located at the same mass where the extended mass distribution peaks. As shown by Bellomo et al. (2018), this also happens for microlensing constraints when the mass distribution extends toward lower masses. This way, and taking into account other constraints, as those obtained from SNeIa magnifications (Zumalacárregui & Seljak, 2018b), the hypothesis of PBHs of $M_{\rm PBH} \gtrsim 10^{-8} M_\odot$ being a significant fraction of the dark matter is disfavored.

On the other hand, even if the abundance of PBHs is significantly lower than the abundance of dark matter, massive PBHs ($10^2 M_\odot \lesssim M_{\rm PBH} \lesssim 10^4 M_\odot$) could provide a solution for a long-lasting open question in astrophysics and cosmology: the origin and formation mechanism of supermassive black holes. In this scenario, PBHs would be the seeds that, after growing significantly since $z \sim 20$, become the supermassive black holes that are located in the center of the galaxies. These massive seeds (no matter if they are primordial or astrophysical, as direct collapsed black holes) are needed to explain the observed population supermassive black holes with $M \sim 10^8 - 10^9 M_\odot$ at $z \sim 8$.

In Bernal et al. (2018), we propose the first robust and unequivocal probe to test if the massive seeds are primordial, independently of the dark matter nature. Kohri et al. (2014) propose the use of CMB spectral distortions or the cosmic ray background to rule out this hypothesis. However, their results present a set of caveats. First, they assume an incorrect model of the effects of PBHs on the CMB, which leads to an overestimation of the PBH contribution to spectral distortions. This constrain vanishes when a better model is used. We refer the interested reader to Ali-Haïmoud & Kamionkowski (2017) for the discussion of the incorrect model which obtains such overestimate. On the other hand, the argument related with the cosmic ray background is only valid if WIMPs are most of the dark matter, so that they would annihilate around the PBHs and produce a more intense flux than that observed.

Given that the $f_{\rm PBH}$ needed to explain the supermassive black hole populations is so small ($f_{\rm PBH} \sim 10^{-8} - 10^{-6}$), the imprints on the CMB would be undetectable. Moreover, the required $f_{\rm PBH}$ on the mass range of interest is unconstrained by current observations. Nevertheless, this sparse population of PBHs could be detectable using 21 cm intensity mapping, since 21 cm emission is extremely sensitive to the baryon temperature and neutral fraction. Then, if a signal from the dark ages (before the first stars formed) consistent with a black hole is detected, such black hole must be primordial. Conveniently, the 21 cm brightness temperature during the dark ages is an extremely clean signal, with no contamination from astrophysical surveys. This is why this probe is so robust.

Considering the radial profile of the 21 cm brightness temperature around each PBH, we added their global contribution to the standard emission. Afterwards, the total sky-averaged emission and 21 cm intensity mapping angular power spectrum were computed, accounting for the angular structure of the PBH contribution for the first time. The contribution of PBHs is much larger in the angular power spectrum, where an enhancement of the signal at small scales is predicted. Even so, these imprints would be very difficult to detect with SKA, due to the low signal-to-noise ratio of its measurements at so high redshift. An experiment with a longer baseline, which would entail lower noise and provide access to smaller scales, would be needed to achieve a detection of the PBH contribution.

Thanks to more ambitious experiments, such as an upgraded SKA and a radio array on the far side of the Moon (which would avoid the opacity of the atmosphere at the frequencies corresponding to 21 cm radiation emitted at $z \gtrsim 30$), the PBHs contribution could be characterized very well. Therefore, besides providing a robust and powerful avenue to probe if PBHs are the seeds of the supermassive black holes, we motivate an upgrade of the HI intensity mapping experiments proposing this science case.

5.3 Radio-continuum and intensity mapping surveys

After the great success of Planck, the next decade will bring a golden era for large scale structure experiments. In order to achieve the ambitious goals expected, a tremendous observational effort will be needed. Therefore, in addition to the more common spectroscopic and photometric galaxy surveys, the coming years will witness the comeback of radio-continuum galaxy surveys, as well as the rise of intensity mapping (IM) experiments.

Both radio-continuum observations and IM techniques propose different strategies to survey the sky deeper and faster than standard optical spectroscopic and photometric galaxy surveys. Radio-continuum galaxy surveys achieve it by averaging the received light over all frequencies to boost the signal-to-noise ratio, at expenses of losing redshift information. On the other hand, IM techniques use all the light received to trace the underlying density distribution, rather than selecting only the sources brighter than a given threshold, as galaxy surveys do.

These two strategies have some advantages over spectroscopic or photometric galaxy surveys. The increased sky coverage speed also facilitates that larger fractions of the sky are surveyed, granting access to larger and larger volumes. In addition, radio-continuum galaxy surveys have the potential to detect many more galaxies, which decreases the impact of the shot noise. On the other hand, IM experiments can target any easily-identifiable spectral line, which naturally makes possible cross-correlation between line brightness temperature maps, as well as with galaxy number counts. This is incredibly useful to mitigate systematics, foregrounds and line interlopers, as well as allows us to carry out multitracer analyses. Moreover, IM grants access to high redshifts, where the galaxies are so sparse and faint than a galaxy survey is not possible: in theory, IM could probe also the dark ages, even reaching $z \lesssim 500$ (Breysse et al., 2018). This makes IM the perfect way to probe the Universe and study galaxy evolution during and before reionization.

In Bernal et al. (2019), we estimate the potential of all-sky radio-continuum galaxy surveys like EMU or SKA to constrain deviations from ΛCDM. Given the huge volumes that will be probed by these surveys and the poor redshift sensitivity, their constraining power peaks for models whose deviations from ΛCDM in the galaxy clustering appear at the largest scales, such as local primordial non Gaussianity, parametrized with $f_{\rm NL}$. We show that EMU has the potential to improve CMB constraints on $f_{\rm NL}$ by a factor two, approximately. However, this goal will only be achieved if external data can be used to infer the galaxy redshifts (hence enabling us to carry out tomographic analyses) and distinguishing between two populations of galaxies to carry out multitracer analyses and reduce cosmic variance.

However, the precision goal of achieving an error on $f_{\rm NL}$ below unity, needed to discriminate between different models of inflation, is still out of reach for radio-continuum surveys on their own. The only way to achieve it would be to probe the whole sky detecting $\sim 30-40$ times more galaxies than EMU. This upgrade will be very hard to achieve, since only ~ 13 times more galaxies are expected to be detected with 10 times better sensitivity than EMU (i.e., a SKA-2-like survey). This being the case, radio-continuum surveys will need to be combined with other galaxy surveys, IM experiments, or other probes (as, for example, the Sunyaev-Zeldovic effect) to achieve a precision on $f_{\rm NL}$ below unity. In addition EMU will also be able to improve current constraints on modified gravity models and, marginally, on dynamical dark energy.

The results of this work are less optimistic than previous works studying radio-continuum surveys, but this is due to the adoption of a more realistic simulation of the radio-continuum signal (T-RECS (Bonaldi et al., 2019) instead of S^3 (Wilman et al., 2008)) to estimate the number of sources detected and the relative abundance of each galaxy population. Finally, I shall emphasize that a similar technique was used to forecast the results of radio-continuum surveys of the phase 1 of SKA (Square Kilometre Array Cosmology Science Working Group et al., 2018).

On the other hand, the work in progress presented in this thesis about IM highlights the great promise that this technique has for probing the Universe at high redshift. Together with the current huge experimental effort that is being carried out, theoretical work developing the tools and methodologies required to ensure the correct exploitation of this kind of observations is needed. In concrete, in Bernal et al. (2019b) we focus on the optimization of the extraction of cosmological information from measurements of the IM power spectrum. This is not a trivial question, since each spectral line is subject to a whole different plethora of astrophysical processes. This makes that the dependence of the observed signal on cosmology and on astrophysics is highly intertwined.

Therefore, the work presented here is timely and needed. Compared with previous cosmological analyses of the IM power spectrum, this is the first time in which the degeneracy between cosmology and astrophysics is considered. In addition, we compress the anisotropic IM power spectrum on Legendre multipoles and provide an accurate analytic prescription for the covariance. Finally, we propose an optimal parametrization to maximize the precision of the cosmological measurements and avoid degeneracies between key cosmological parameters.

The main result of this work is the possibility to measure the BAO scale, and parameters which significantly modify the shape of the matter or the halo power spectrum (such as $\sum m_\nu$ or $f_{\rm NL}$) independently of the astrophysical uncertainties in a robust way. In addition, the product of the growth rate and the amplitude of the density perturbations, $f\sigma_8$, may be measured if an external prior on the mean of the brightness temperature is provided. This is not an unrealistic requirement, since other techniques, such as the voxel intensity distribution, are specifically designed to constrain the luminosity function (Breysse et al., 2017). We also show that including the hexadecapole of the IM power spectrum results in a 25% and a 75% improvement in the cosmological constraints. This is because the hexadecapole helps to to break parameter degeneracies, even if it is not detected.

Finally, thanks to this methodology, IM has a great potential to provide cosmic ruler measurements at the epoch of reionization. In Bernal et al. (2019a) he highlight this opportunity and forecast constraints on the expansion history from planned

IM experiments such as SPHEREx (Doré et al., 2014) and the second phase of COMAP (Cleary et al., 2016), as well as a future CO experiment within the Intensity Mapping Stage 3. We reach percent level with COMAP at $z \sim 2.8$, and especially with the future CO experiment, at $2 \lesssim z \lesssim 8$, while SPHEREx will soon provide $\sim 7 - 20\%$ constraints at $0.5 \lesssim 7$. These measurements are crucial for model-independent analyses of the expansion history, which, as shown above, are key to study the tension on H_0. Furthermore, these measurements will be able to constrain decaying dark matter models (see e.g., Vattis et al. (2019) and dynamical dark energy and modified gravity theories that go beyond standard parametrizations, as that proposed in Raveri (2019).

5.4 Future prospects

This thesis collects research focused on the theoretical problems of ΛCDM and the discrepancies between the results from independent experiments obtained assuming this model. These might be smoking guns of the need of new physics; however, ΛCDM is still favoured over any other model considered to date. This is why these inconsistencies and open questions should be studied at the same time in a global context. This subsection is focused on possible further work along these lines.

5.4.1 Studying the H_0 tension

Throughout this thesis, it has been shown that the tension on H_0 is in reality a mismatch between the two anchors of the cosmic distance ladder. Moreover, SNeIa and BAO observations constrain deviations from a cosmological constant, hence it is difficult that new physics in the late Universe can ease this tension. Therefore, there are only two ways to reconcile H_0 measurements: either finding a physical way to lower the value of $r_{\rm s}$ by modifying the physics before recombination, or modifying the expansion history of the Universe in the non-probed period of the Universe between recombination and $z \approx 3$.

The CMB power spectrum is measured with exquisite precision. This is why any extra component that modifies the expansion history to achieve a lower value of $r_{\rm s}$ cannot affect the CMB power spectra peaks. Since the CMB power spectra is very sensitive to the diffusion scale, the reduction of r_s needs to be achieved before the damping scale grows too much. However, $r_\mathrm{s} \lesssim 10$ Mpc at $z \approx 2.5 \times 10^4$. This is why the modification in r_s evolution needs to happen during a narrow window around $z \approx 10^4$. Otherwise, a way to avoid modifications of the diffusion scale is needed. Moreover, the CMB power spectrum is also sensitive to the supersonic neutrino phase shift, so any modification of the cosmology should keep this unchanged. Early dark energy (Poulin et al., 2018a), self-interacting neutrinos models (Kreisch et al., 2019) or evolving scalar fields injecting energy before recombination (Agrawal et al., 2019) are some of the models explored which fulfill these requirements. However, there is no evidence of any of them being favored over ΛCDM. In any case, these models show promising results, and further research along these lines might lead to a reduction of the tension.

There is no a priori physical motivation to modify the expansion history at $3 \lesssim z \lesssim 1000$, when matter is supposed to completely dominate the expansion rate. However, it is important to bear in mind that we have no measurement of $H(z)$ at these redshifts and that there are models that predict these deviations, such as decaying dark matter into lighter dark matter particles (Vattis et al., 2019), or some modified gravity theories (Raveri, 2019).

Fortunately, future experiments will provide standard ruler measurements in this redshift range. While there are some proposals for spectroscopic surveys reaching $z \sim 5$ (Ferraro et al., 2019; Wilson & White, 2019), the noticeable improvement will be brought about by IM surveys, providing BAO measurements up to $z \approx 8 - 9$ with better, or at least competitive, precision (as we show in Bernal et al. (2019a)). Standard ruler measurements using velocity-induced acoustic oscillations at the cosmic dawn ($z \sim 15-20$) (Muñoz, 2019a,b)) would be complementary to BAO from IM and extend the cosmic distance ladder even to larger redshifts. Therefore, low redshift standard ruler measurements up to much higher redshift will be possible. The higher this upper limit on the redshift is, less time there will be for the expansion history of the Universe to accommodate changes in order to match the two anchors of the cosmic distance ladder.

Finally, in order to definitively address the tension on H_0, alternative, independent and competitive probes of the expansion history are needed. The obvious candidates are the standard sirens: gravitational waves with electromagnetic counterparts which provide very precise redshift measurements (Abbott et al., 2017). It is expected that the number of detections during the coming decade is high enough to discriminate between the two competing measurements of H_0 (Feeney et al., 2019). In addition, other alternatives include the so-called cosmic chronometers (Jimenez & Loeb, 2002; Moresco et al., 2016) or the measurements of the age of the Universe using the oldest globular clusters (Jimenez et al., 2019b). Further work in the modeling of these two avenues is needed, so that they become robust and reliable tracers of the expansion history of the Universe and H_0, competitive with current standard probes.

Once we have several independent measurements of H_0, as most model-independent as possible, and coming from the largest number of different physical phenomena, it will be possible to fully address the tension on H_0 in a global, agnostic way. This way, the source of the tension, being either cosmological or artificial, will arise.

5.4.2 Primordial black holes

Taking into account current observational constraints on the abundance of PBHs, the possibility that PBHs are a significant fraction of the dark matter is very unlikely, except for very light PBHs. Nonetheless, through the quest for detecting PBHs or ruling them out, our understanding of astrophysical processes related with lensing, accretion, and binary black hole mergers, among others, has increased.

On the other hand, the abundance and masses of PBHs are intimately related with the amplitude of the primordial power spectrum at a given scale, respectively. This makes PBHs a very powerful probe of the primordial power spectrum, especially at the smallest scales; actually light PBHs abundances are one of the very few observational consequences of the amplitude of the primordial perturbations in this regime. Therefore, pursuing black hole observational detection is still very relevant for cosmology, even if f_{PBH} is constrained to very small values. Nevertheless, further understanding of the exact relation between the shape of the primordial power spectrum, curvature and density perturbations, and the formation of PBHs and their abundance is needed in order to set robust constraints on the primordial power spectrum from PBHs (Germani & Musco, 2019; Musco, 2018).

It is possible to improve the prospects of constraining PBHs as seeds of the supermassive black holes, too. While in Bernal et al. (2018) we restrict attention to the 21 cm emission coming from the dark ages, motivated by considering cleaner signal, this probe can also be extended towards lower redshifts. Although at lower redshifts the signal is polluted by other astrophysical sources and astrophysical black holes may be already formed, this redshift range will be measured by planned experiments like SKA, HERA or JWST. Furthermore, mergers of PBHs of these masses produce graviational waves that may be detected by future gravitational waves interferometers, such as LISA and the Einstein Telescope. While the former is sensitive to higher masses, the latter will be able to detect mergers at higher redshifts. Following a similar logic as for the 21 cm signal from the dark ages, if a binary black hole merger is detected at redshifts higher to those corresponding to the formation of the first stars, those black holes must be primordial. Therefore, improving the phenomenological descriptions of all these processes will help to ascertain the origin of the supermassive black holes.

Finally, the existence of massive PBHs, even if they are not a significant fraction of the dark matter, may have tremendous consequences for other dark matter candidates, such as WIMPs. As first proposed by Lacki & Beacom (2010) and then revised by Adamek et al. (2019) and Bertone et al. (2019), these two candidates for dark matter cannot coexist, given current observations. If PBHs exist but they are not all of the dark matter, they would be at the center of ultra compact mini halos, formed in the early Universe as the rest of the dark matter clusters around them. These ultra compact mini halos would have very steep density profiles, with incredibly large densities in their cores. In this scenario, if the dark matter that is not made by PBHs is composed of WIMPs (or annihilates somehow to energetic electromagnetic species), the annihilation rate around the PBHs should be very high. This would originate many gamma rays point sources, clearly surpassing the abundance observed. Thus, detecting PBHs can rule a significant region of the parameter space of weak-scale theories beyond the standard model which attempt to explain the nature of dark matter. Nonetheless, this argument also works in the other direction: if WIMPs are to be detected, the abundance of massive PBHs must be extremely low. This fact further motivates the research on PBHs.

5.4.3 The future of large scale structure surveys

DESI and Euclid will measure the BAO scale and the growth of structures at $z \lesssim 3$ with unparalleled precision. But they will also provide, along with EMU (and later on SKA and LSST), the largest volumes surveyed to date. This will not only improve the statistics for standard measurements, but will also grant access to the largest observable scales, those close to the horizon.

At these ultra-large scales, contributions to the observed clustering beyond the standard density and peculiar velocity terms, dominate the signal. In this regime, relativistic corrections (redshift space distortions along the light-cone accounting for relativistic processes such as lensing and gravitational redshifts) and eventual signatures from primordial non Gaussianity dominate (Bertacca et al., 2012, 2018; Raccanelli et al., 2016, 2018, 2017). The former can be used as a test for GR, and the latter provides one of the few possible ways to probe inflation. For instance, single field slow roll inflation predicts negligible local non Gaussianity (i.e., $f_{\rm NL} \ll 1$). Therefore, strong constraints on $f_{\rm NL}$ may rule out a whole family of inflationary models.

However, primordial non Gaussianities and relativistic corrections contributions to the observed clustering are degenerate (Raccanelli et al., 2018). Therefore, a very careful modeling of the relativistic corrections and a suitable analysis should be included and performed in order to avoid any bias in the measurement and robustly measure primordial non Gaussianity from LSS.

Radio-continuum surveys have the potential to probe large enough volumes to make these searches possible. However, they are limited by the degradation of redshift measurements. Therefore, a global strategy involving different collaborations should be implemented in order to maximize the overlap between spectroscopic and photometric surveys with radio-continuum observations. This would ensure a more reliable redshift inference for radio-continuum galaxy surveys.

The dominant contributions to the ultra large scales (especially primordial non Gaussianity) grow with redshift. Furthermore, since these contributions are only dominant at the very large scales, both the angular and redshift resolution can be moderately degraded with no significant loss. Then, primordial non Gaussianity is a natural target for IM (see e.g., Square Kilometre Array Cosmology Science Working Group et al. (2018); Moradinezhad Dizgah et al. (2019); Moradinezhad Dizgah &

Keating (2019) and Bernal et al. (2019b)). Unfortunately, the largest scales are more susceptible to be affected by foregrounds which may contaminate and impossibilitate the measurements. Nevertheless, there are already some procedures for foreground removal (see e.g. Silva et al. (2013); Breysse et al. (2015); Sun et al. (2018); Cheng et al. (2016) and Kalus et al. (2019b)). Observational efforts to build upon these works and ensure clean IM measurements by the time the experiments are ready is therefore of utmost importance.

Finally, for IM experiments to achieve the promised potential, a significant theoretical and observational effort must be carried out. After achieving the first detections of HI (Chang et al., 2010) and CO (Keating et al., 2016), other lines must be detected, and better determinations of the astrophysical processes and spectral lines luminosity functions are needed to fully exploit IM for cosmology. In any case, in Bernal et al. (2019b), we show that the BAO scale can be robustly measured without knowledge about the astrophysics, yielding impressive potential to constrain the expansion history at the epoch of reionization (as we highlight in Bernal et al. (2019a)). Therefore, further research along these lines will prove extremely useful in order to carry observational cosmology to unexplored epochs and regimes.

References

Abazajian, K.N. et al. *CMB-S4 Science Book, First Edition.* arXiv e-prints, arXiv:1610.02743, 2016.

Abbott, B.P., et al. *Gw151226: Observation of gravitational waves from a 22-solar-mass binary black hole coalescence.* Phys. Rev. Lett., 116, 241103, 2016a.

Abbott, B.P. et al. *Observation of gravitational waves from a binary black hole merger.* Phys. Rev. Lett., 116, 061102, 2016b.

Abbott, B.P., et al. *A gravitational-wave standard siren measurement of the Hubble constant.* Nature, 551 (7678), 85–88, 2017.

Abbott, B.P., et al. *Gw170104: Observation of a 50-solar-mass binary black hole coalescence at redshift 0.2.* Phys. Rev. Lett., 118, 221101, 2017a.

Abbott, B.P., et al. *GW170608: Observation of a 19 solar-mass binary black hole coalescence.* Astrophys. J., 851 (2), L35, 2017b.

Abbott, B.P., et al. *Gw170814: A three-detector observation of gravitational waves from a binary black hole coalescence.* Phys. Rev. Lett., 119, 141101, 2017c.

Abbott, B.P., et al. *GW170817: Observation of Gravitational Waves from a Binary Neutron Star Inspiral.* Physical Review Letters, 119 (16), 161101, 2017a.

Abbott, B.P., et al. *Multi-messenger Observations of a Binary Neutron Star Merger.* Astrophys. J. Letters, 848, L12, 2017b.

Adamek, J., et al. *WIMPs and stellar-mass primordial black holes are incompatible.* arXiv e-prints, arXiv:1901.08528, 2019.

Addison, G.E., et al. *Quantifying Discordance in the 2015 Planck CMB Spectrum.* Astrophys. J., 818, 132, 2016.

Addison, G.E., et al. *Elucidating ΛCDM: Impact of Baryon Acoustic Oscillation Measurements on the Hubble Constant Discrepancy.* ArXiv e-prints, 2017.

Agarwal, B., et al. *The First Billion Years project: birthplaces of direct collapse black holes.* MNRAS, 443, 648–657, 2014.

Agrawal, P., et al. *Rock 'n' Roll Solutions to the Hubble Tension.* arXiv e-prints, arXiv:1904.01016, 2019.

Alam, S., et al. *Testing gravity on large scales by combining weak lensing with galaxy clustering using CFHTLenS and BOSS CMASS.* MNRAS, 465 (4), 4853–4865, 2017a.

Alam, S. et al. *The clustering of galaxies in the completed SDSS-III Baryon Oscillation Spectroscopic Survey: cosmological analysis of the DR12 galaxy sample.* MNRAS, 470, 2617–2652, 2017b.

Alcock, C. & Paczynski, B. *An evolution free test for non-zero cosmological constant.* Nature, 281, 358, 1979.

REFERENCES

Alcock, C., et al. *EROS and MACHO Combined Limits on Planetary-Mass Dark Matter in the Galactic Halo.* Astrophys. J., 499 (1), L9–L12, 1998.

Ali-Haïmoud, Y. & Kamionkowski, M. *Cosmic microwave background limits on accreting primordial black holes.* Phys. Rev. D, 95 (4), 043534, 2017.

Ali-Haïmoud, Y., et al. *The merger rate of primordial-black-hole binaries.* ArXiv e-prints, 2017.

Amendola, L., et al. *Cosmology and fundamental physics with the Euclid satellite.* Living Reviews in Relativity, 21 (1), 2, 2018.

Aubourg, É. et al. *Cosmological implications of baryon acoustic oscillation measurements.* Phys. Rev. D, 92 (12), 123516, 2015.

Aylor, K., et al. *Sounds Discordant: Classical Distance Ladder and* Λ*CDM-based Determinations of the Cosmological Sound Horizon.* Astrophys. J., 874 (1), 4, 2019.

Bañados, E., et al. *An 800-million-solar-mass black hole in a significantly neutral Universe at a redshift of 7.5.* Nature, 553 (7689), 473–476, 2018.

Ballinger, W.E., et al. *Measuring the cosmological constant with redshift surveys.* MNRAS, 282, 877, 1996.

Bandura, K., et al. *Canadian Hydrogen Intensity Mapping Experiment (CHIME) pathfinder.* In *Ground-based and Airborne Telescopes V*, vol. 9145 of *SPIE Conference Series*, 914522, 2014.

Barnacka, A., et al. *New constraints on primordial black holes abundance from femtolensing of gamma-ray bursts.* Phys. Rev. D, 86 (4), 043001, 2012.

Bautista, J.E. et al. *The SDSS-IV extended Baryon Oscillation Spectroscopic Survey: Baryon Acoustic Oscillations at redshift of 0.72 with the DR14 Luminous Red Galaxy Sample.* ArXiv e-prints, 2017.

Bellomo, N., et al. *Primordial black holes as dark matter: converting constraints from monochromatic to extended mass distributions.* JCAP, 2018 (1), 004, 2018.

Bennett, C.L., et al. *Nine-year Wilkinson Microwave Anisotropy Probe (WMAP) Observations: Final Maps and Results.* Astrophys.J.Sup., 208, 20, 2013.

Bernal, J.L. & Peacock, J.A. *Conservative cosmology: combining data with allowance for unknown systematics.* JCAP, 7, 002, 2018.

Bernal, J.L., et al. *Parameter splitting in dark energy: is dark energy the same in the background and in the cosmic structures?* JCAP, 2, 059, 2016a.

Bernal, J.L., et al. *The trouble with* H_0. JCAP, 10, 019, 2016b.

Bernal, J.L., et al. *Cosmological implications of primordial black holes.* JCAP, 2017 (10), 052, 2017.

Bernal, J.L., et al. *Signatures of primordial black holes as seeds of supermassive black holes.* JCAP, 2018 (5), 017, 2018.

Bernal, J.L., et al. *Cosmic rulers at the epoch of reionization with intensity mapping.* In preparation, 2019a.

Bernal, J.L., et al. *Optimal extraction of cosmological information from line-intensity mapping.* In preparation, 2019b.

Bernal, J.L., et al. *Probing ΛCDM cosmology with the Evolutionary Map of the Universe survey.* JCAP, 2019 (2), 030, 2019.

Bertacca, D., et al. *Beyond the plane-parallel and Newtonian approach: wide-angle redshift distortions and convergence in general relativity.* JCAP, 10, 025, 2012.

Bertacca, D., et al. *Relativistic wide-angle galaxy bispectrum on the light cone.* Phys. Rev. D, 97 (2), 023531, 2018.

Bertone, G., et al. *Primordial Black Holes as Silver Bullets for New Physics at the Weak Scale.* arXiv e-prints, arXiv:1905.01238, 2019.

Betoule, M. et al. *Improved cosmological constraints from a joint analysis of the SDSS-II and SNLS supernova samples.* Astron. Astrophys., 568, A22, 2014.

Beutler, F., et al. *The 6dF Galaxy Survey: $z \approx 0$ measurements of the growth rate and σ_8.* MNRAS, 423 (4), 3430–3444, 2012.

Bird, S., et al. *Did LIGO Detect Dark Matter?* Physical Review Letters, 116 (20), 201301, 2016.

Blomqvist, M., et al. *Baryon acoustic oscillations from the cross-correlation of Lyα absorption and quasars in eBOSS DR14.* arXiv e-prints, 2019.

Bonaldi, A., et al. *The Tiered Radio Extragalactic Continuum Simulation (T-RECS).* MNRAS, 482, 2–19, 2019.

Bonvin, V., et al. *H0LiCOW - V. New COSMOGRAIL time delays of HE 0435-1223: H_0 to 3.8 per cent precision from strong lensing in a flat ΛCDM model.* MNRAS, 465 (4), 4914–4930, 2017.

Brandt, T.D. *Constraints on macho dark matter from compact stellar systems in ultra-faint dwarf galaxies.* The Astrophysical Journal Letters, 824 (2), L31, 2016.

Breysse, P.C., et al. *Masking line foregrounds in intensity-mapping surveys.* MNRAS, 452 (4), 3408–3418, 2015.

Breysse, P.C., et al. *Insights from probability distribution functions of intensity maps.* MNRAS, 467, 2996–3010, 2017.

Breysse, P.C., et al. *Ultimate frontier of 21-cm cosmology.* Phys. Rev. D, 98 (4), 043520, 2018.

Bromm, V. & Loeb, A. *Formation of the First Supermassive Black Holes.* Astrophys. J., 596, 34–46, 2003.

Bugaev, E. & Klimai, P. *Constraints on amplitudes of curvature perturbations from primordial black holes.* Phys. Rev. D, 79 (10), 103511, 2009.

Bull, P., et al. *Late-time Cosmology with 21 cm Intensity Mapping Experiments.* Astrophys. J., 803 (1), 21, 2015.

Bull, P., et al. *Fundamental Physics with the Square Kilometer Array.* arXiv e-prints, arXiv:1810.02680, 2018.

Burns, C.R., et al. *The Carnegie Supernova Project: Absolute Calibration and the*

Hubble Constant. Astrophys. J., 869 (1), 56, 2018.

Cardona, W., et al. *Determining H_0 with Bayesian hyper-parameters.* JCAP, 3, 056, 2017.

Carr, B.J. & Sakellariadou, M. *Dynamical Constraints on Dark Matter in Compact Objects.* Astrophys. J., 516 (1), 195–220, 1999.

Chang, T.C., et al. *An intensity map of hydrogen 21-cm emission at redshift z˜0.8.* Nature, 466 (7305), 463–465, 2010.

Chapline, G.F. *Cosmological effects of primordial black holes.* Nature, 253, 251, 1975.

Charnock, T., et al. *Planck data versus large scale structure: Methods to quantify discordance.* Phys. Rev. D, 95 (12), 123535, 2017.

Cheng, Y.T., et al. *Spectral Line De-confusion in an Intensity Mapping Survey.* Astrophys. J., 832 (2), 165, 2016.

Chevallier, M. & Polarski, D. *Accelerating Universes with Scaling Dark Matter.* International Journal of Modern Physics D, 10, 213–223, 2001.

Chiang, C.T. & Slosar, A. *Inferences of H_0 in presence of a non-standard recombination.* arXiv e-prints, arXiv:1811.03624, 2018.

Chung, D.T. *A partial inventory of observational anisotropies in single-dish line-intensity mapping.* arXiv e-prints, arXiv:1905.00209, 2019.

Cleary, K., et al. *The CO Mapping Array Pathfinder (COMAP).* In *American Astronomical Society Meeting Abstracts #227*, vol. 227 of *American Astronomical Society Meeting Abstracts*, 426.06, 2016.

Cole, S., et al. *The 2dF Galaxy Redshift Survey: power-spectrum analysis of the final data set and cosmological implications.* MNRAS, 362 (2), 505–534, 2005.

Cooke, R., et al. *A one percent determination of the primordial deuterium abundance.* ArXiv e-prints, 2017.

Crites, A.T., et al. *The TIME-Pilot intensity mapping experiment.* In *Millimeter, Submillimeter, and Far-Infrared Detectors and Instrumentation for Astronomy VII*, vol. 9153 of *SPIE Conference Series*, 91531W, 2014.

Croft, R.A.C., et al. *Large-scale clustering of Lyman α emission intensity from SDSS/BOSS.* MNRAS, 457 (4), 3541–3572, 2016.

Dalal, N., et al. *Imprints of primordial non-Gaussianities on large-scale structure: Scale-dependent bias and abundance of virialized objects.* Phys. Rev. D, 77 (12), 123514, 2008.

de Sainte Agathe, V., et al. *Baryon acoustic oscillations at $z = 2.34$ from the correlations of Lyα absorption in eBOSS DR14.* arXiv e-prints, 2019.

DeBoer, D.R., et al. *Hydrogen Epoch of Reionization Array (HERA).* Pub. of the Astron. Soc. of the Pacific, 129 (974), 045001, 2017.

D'Eramo, F., et al. *Hot axions and the H_0 tension.* JCAP, 2018, 014, 2018.

DESI Collaboration, et al. *The DESI Experiment Part I: Science,Targeting, and Survey Design.* ArXiv e-prints, 2016a.

DESI Collaboration, et al. *The DESI Experiment Part II: Instrument Design.* arXiv e-prints, 2016b.

Desjacques, V. & Seljak, U. *Primordial non-Gaussianity from the large-scale structure.* Classical and Quantum Gravity, 27 (12), 124011, 2010.

Di Valentino, E., et al. *Reconciling Planck with the local value of H_0 in extended parameter space.* Physics Letters B, 761, 242–246, 2016.

Di Valentino, E., et al. *Can interacting dark energy solve the H_0 tension?* Phys. Rev D, 96 (4), 043503, 2017.

Di Valentino, E., et al. *Reducing the H_0 and σ_8 tensions with dark matter-neutrino interactions.* Phys. Rev. D, 97 (4), 043513, 2018.

Dijkstra, M., et al. *Feedback-regulated supermassive black hole seed formation.* MNRAS, 442, 2036–2047, 2014.

Doré, O., et al. *Cosmology with the SPHEREX All-Sky Spectral Survey.* arXiv e-prints, arXiv:1412.4872, 2014.

Douspis, M., et al. *On the tension between Large Scale Structures and Cosmic Microwave Background.* arXiv e-prints, arXiv:1901.05289, 2019.

Eisenstein, D.J., et al. *Detection of the Baryon Acoustic Peak in the Large-Scale Correlation Function of SDSS Luminous Red Galaxies.* Astrophys. J., 633 (2), 560–574, 2005.

Erben, T., et al. *CFHTLenS: the Canada-France-Hawaii Telescope Lensing Survey - imaging data and catalogue products.* MNRAS, 433, 2545–2563, 2013.

Event Horizon Telescope Collaboration, et al. *First M87 Event Horizon Telescope Results. I. The Shadow of the Supermassive Black Hole.* Astrophys. J. Letters, 875, L1, 2019.

Ezquiaga, J.M. & Zumalacárregui, M. *Dark Energy After GW170817: Dead Ends and the Road Ahead.* Phys. Rev. Letters, 119, 251304, 2017.

Fan, X., et al. *A Survey of z¿5.8 Quasars in the Sloan Digital Sky Survey. I. Discovery of Three New Quasars and the Spatial Density of Luminous Quasars at z∼6.* Astronom. J., 122, 2833–2849, 2001.

Feeney, S.M., et al. *Clarifying the Hubble constant tension with a Bayesian hierarchical model of the local distance ladder.* ArXiv e-prints, 2017.

Feeney, S.M., et al. *Prospects for Resolving the Hubble Constant Tension with Standard Sirens.* Phys. Rev. Letters, 122 (6), 061105, 2019.

Feldman, H.A., et al. *Power-Spectrum Analysis of Three-dimensional Redshift Surveys.* Astrophys. J., 426, 23, 1994.

Ferraro, S., et al. *Inflation and Dark Energy from spectroscopy at $z > 2$.* arXiv e-prints, arXiv:1903.09208, 2019.

Fisher, R.A. *The Fiducial Argument in Statistical Inference.* Annals Eugen., 6, 391–398, 1935.

Flynn, C., et al. *Hubble Deep Field Constraint on Baryonic Dark Matter.* Astrophys. J., 466, L55, 1996.

Follin, B. & Knox, L. *Insensitivity of the distance ladder Hubble constant determination to Cepheid calibration modelling choices.* MNRAS, 477 (4), 4534–4542, 2018.

Furlanetto, S., et al. *Astro 2020 Science White Paper: Fundamental Cosmology in the Dark Ages with 21-cm Line Fluctuations.* arXiv e-prints, arXiv:1903.06212, 2019a.

Furlanetto, S., et al. *Astro2020 Science White Paper: Insights Into the Epoch of Reionization with the Highly-Redshifted 21-cm Line.* arXiv e-prints, arXiv:1903.06204, 2019b.

Germani, C. & Musco, I. *Abundance of Primordial Black Holes Depends on the Shape of the Inflationary Power Spectrum.* Phys. Rev. D, 122 (14), 141302, 2019.

Giannantonio, T., et al. *Combined analysis of the integrated Sachs-Wolfe effect and cosmological implications.* Phys. Rev. D, 77 (12), 123520, 2008.

Giannantonio, T., et al. *Improved primordial non-Gaussianity constraints from measurements of galaxy clustering and the integrated Sachs-Wolfe effect.* Phys. Rev. D, 89 (2), 023511, 2014.

Gil-Marín, H., et al. *The clustering of the SDSS-IV extended Baryon Oscillation Spectroscopic Survey DR14 quasar sample: structure growth rate measurement from the anisotropic quasar power spectrum in the redshift range 0.8 ¡ z ¡ 2.2.* MNRAS, 477, 1604–1638, 2018.

Ginzburg, D., et al. *Shot noise and biased tracers: A new look at the halo model.* Phys. Rev. D, 96 (8), 083528, 2017.

Gonçalves, R.S., et al. *Cosmic homogeneity: a spectroscopic and model-independent measurement.* MNRAS, 475 (1), L20–L24, 2018.

Gong, Y., et al. *Intensity Mapping of Hα, Hβ, [OII], and [OIII] Lines at z < 5.* Astrophys. J., 835 (2), 273, 2017.

Graham, P.W., et al. *Dark matter triggers of supernovae.* Phys. Rev. D, 92 (6), 063007, 2015.

Green, D., et al. *Aspects of dark matter annihilation in cosmology.* JCAP, 2019 (4), 025, 2019.

Grieb, J.N., et al. *Gaussian covariance matrices for anisotropic galaxy clustering measurements.* MNRAS, 457, 1577–1592, 2016.

Hajian, A. & Souradeep, T. *Measuring the Statistical Isotropy of the Cosmic Microwave Background Anisotropy.* Astrophys. J. Letters, 597, L5–L8, 2003.

Hanany, S. et al. *MAXIMA-1: A Measurement of the Cosmic Microwave Background Anisotropy on Angular Scales of 10’-5°.* Astrophys. J., 545 (1), L5–L9, 2000.

Hatt, D., et al. *The Carnegie-Chicago Hubble Program. IV. The Distance to NGC 4424, NGC 4526, and NGC 4356 via the Tip of the Red Giant Branch.* Astrophys. J., 861 (2), 104, 2018.

Heavens, A.F., et al. *Testing homogeneity with the fossil record of galaxies.* JCAP, 2011 (9), 035, 2011.

Heymans, C., et al. *CFHTLenS: the Canada-France-Hawaii Telescope Lensing Survey.* MNRAS, 427, 146–166, 2012.

Hildebrandt, H., et al. *KiDS-450: cosmological parameter constraints from tomographic weak gravitational lensing.* Mon. Not. Roy. Astron. Soc., 465, 1454–1498, 2017.

Hinshaw, G., et al. *Nine-year Wilkinson Microwave Anisotropy Probe (WMAP) Observations: Cosmological Parameter Results.* Astrophys.J.Sup, 208, 19, 2013.

Ho, S., et al. *Correlation of CMB with large-scale structure. I. Integrated Sachs-Wolfe tomography and cosmological implications.* Phys. Rev. D, 78 (4), 043519, 2008.

Hobson, M.P., et al. *Combining cosmological data sets: hyperparameters and Bayesian evidence.* Mon. Not. Roy. Astron. Soc., 335, 377–388, 2002.

Hoyle, B., et al. *Testing Homogeneity with Galaxy Star Formation Histories.* Astrophys. J., 762 (1), L9, 2013.

Ihle, H.T., et al. *Joint Power Spectrum and Voxel Intensity Distribution Forecast on the CO Luminosity Function with COMAP.* Astrophys. J., 871, 75, 2019.

Inayoshi, K., et al. *Hyper-Eddington accretion flows on to massive black holes.* MNRAS, 459, 3738–3755, 2016.

Iršič, V., et al. *New constraints on the free-streaming of warm dark matter from intermediate and small scale Lyman-α forest data.* Phys. Rev. D, 96 (2), 023522, 2017.

Jimenez, R. & Loeb, A. *Constraining Cosmological Parameters Based on Relative Galaxy Ages.* Astrophys. J., 573, 37–42, 2002.

Jimenez, R., et al. *Measuring the Homogeneity of the Universe.* arXiv e-prints, arXiv:1902.11298, 2019a.

Jimenez, R., et al. *The local and distant Universe: stellar ages and H_0.* JCAP, 2019 (3), 043, 2019b.

Josan, A.S., et al. *Generalized constraints on the curvature perturbation from primordial black holes.* Phys. Rev. D, 79 (10), 103520, 2009.

Kalus, B., et al. *A map-based method for eliminating systematic modes from galaxy clustering power spectra with application to BOSS.* MNRAS, 482, 453–470, 2019a.

Kalus, B., et al. *A map-based method for eliminating systematic modes from galaxy clustering power spectra with application to BOSS.* MNRAS, 482 (1), 453–470, 2019b.

Katz, A., et al. *Femtolensing by dark matter revisited.* Journal of Cosmology and

Astro-Particle Physics, 2018 (12), 005, 2018.

Kazin, E.A., et al. *Improving measurements of H(z) and D_A (z) by analysing clustering anisotropies.* MNRAS, 419 (4), 3223–3243, 2012.

Kazin, E.A., et al. *The WiggleZ Dark Energy Survey: improved distance measurements to $z = 1$ with reconstruction of the baryonic acoustic feature.* Mon. Not. Roy. Astron. Soc., 441, 3524–3542, 2014.

Keating, G.K., et al. *First Results from COPSS: The CO Power Spectrum Survey.* Astrophys. J., 814 (2), 140, 2015.

Keating, G.K., et al. *COPSS II: The Molecular Gas Content of Ten Million Cubic Megaparsecs at Redshift $z\sim 3$.* Astrophys. J., 830, 34, 2016.

Kilbinger, M., et al. *CFHTLenS: combined probe cosmological model comparison using 2D weak gravitational lensing.* MNRAS, 430, 2200–2220, 2013.

Kohri, K., et al. *Testing scenarios of primordial black holes being the seeds of supermassive black holes by ultracompact minihalos and CMB μ distortions.* Phys. Rev. D, 90 (8), 083514, 2014.

Kovac, J.M., et al. *Detection of polarization in the cosmic microwave background using DASI.* Nature, 420, 772–787, 2002.

Kovetz, E.D., et al. *Line-Intensity Mapping: 2017 Status Report.* arXiv e-prints, arXiv:1709.09066, 2017.

Kovetz, E.D., et al. *Astrophysics and Cosmology with Line-Intensity Mapping.* arXiv e-prints, 2019.

Kreisch, C.D., et al. *The Neutrino Puzzle: Anomalies, Interactions, and Cosmological Tensions.* arXiv e-prints, arXiv:1902.00534, 2019.

Kuo, C.L. et al. *High-Resolution Observations of the Cosmic Microwave Background Power Spectrum with ACBAR.* Astrophys. J., 600 (1), 32–51, 2004.

Lacki, B.C. & Beacom, J.F. *Primordial Black Holes as Dark Matter: Almost All or Almost Nothing.* Astrophys. J., 720 (1), L67–L71, 2010.

Latif, M.A., et al. *How realistic UV spectra and X-rays suppress the abundance of direct collapse black holes.* MNRAS, 446, 3163–3177, 2015.

Lewis, A., et al. *Efficient Computation of Cosmic Microwave Background Anisotropies in Closed Friedmann-Robertson-Walker Models.* Astrophys. J., 538 (2), 473–476, 2000.

Li, T.S., et al. *Farthest Neighbor: The Distant Milky Way Satellite Eridanus II.* Astrophys. J., 838 (1), 8, 2017.

Li, T.Y., et al. *Connecting CO Intensity Mapping to Molecular Gas and Star Formation in the Epoch of Galaxy Assembly.* Astrophys. J., 817, 169, 2016.

Lin, W. & Ishak, M. *Cosmological discordances: A new measure, marginalization effects, and application to geometry versus growth current data sets.* Phys. Rev. D, 96 (2), 023532, 2017.

Lopez-Honorez, L., et al. *Warm dark matter and the ionization history of the*

Universe. Phys. Rev. D, 96 (10), 103539, 2017.

Madau, P. & Rees, M.J. *Massive Black Holes as Population III Remnants.* Astrophys. J. Letters, 551, L27–L30, 2001.

Marinoni, C., et al. *The scale of cosmic isotropy.* JCAP, 2012 (10), 036, 2012.

Matarrese, S. & Verde, L. *The Effect of Primordial Non-Gaussianity on Halo Bias.* Astrophys. J. Letters, 677, L77, 2008.

Matarrese, S., et al. *The Abundance of High-Redshift Objects as a Probe of Non-Gaussian Initial Conditions.* Astrophys. J., 541, 10–24, 2000.

McDonald, P. & Seljak, U. *How to evade the sample variance limit on measurements of redshift-space distortions.* JCAP, 10, 007, 2009.

Moradinezhad Dizgah, A. & Keating, G.K. *Line Intensity Mapping with [C II] and CO(1-0) as Probes of Primordial Non-Gaussianity.* Astrophys. J., 872, 126, 2019.

Moradinezhad Dizgah, A., et al. *Probing Cosmic Origins with CO and [C II] Emission Lines.* Astrophys. J., 870, L4, 2019.

Moresco, M., et al. *A 6% measurement of the Hubble parameter at z˜0.45: direct evidence of the epoch of cosmic re-acceleration.* JCAP, 5, 014, 2016.

Mortlock, D.J., et al. *A luminous quasar at a redshift of z = 7.085.* Nature, 474, 616–619, 2011.

Muñoz, J.B. *A Standard Ruler at Cosmic Dawn.* arXiv e-prints, arXiv:1904.07868, 2019a.

Muñoz, J.B. *Velocity-induced Acoustic Oscillations at Cosmic Dawn.* arXiv e-prints, arXiv:1904.07881, 2019b.

Mueller, E.M., et al. *Optimizing primordial non-Gaussianity measurements from galaxy surveys.* MNRAS, 485, 4160–4166, 2019.

Murphy, E.J. *A next-generation Very Large Array.* In A. Tarchi, M.J. Reid, & P. Castangia, eds., *Astrophysical Masers: Unlocking the Mysteries of the Universe*, vol. 336 of *IAU Symposium*, 426–432, 2018.

Musco, I. *The threshold for primordial black holes: dependence on the shape of the cosmological perturbations.* arXiv e-prints, arXiv:1809.02127, 2018.

Netterfield, C.B. et al. *A Measurement by BOOMERANG of Multiple Peaks in the Angular Power Spectrum of the Cosmic Microwave Background.* Astrophys. J., 571 (2), 604–614, 2002.

Niikura, H., et al. *Microlensing constraints on primordial black holes with the Subaru/HSC Andromeda observation.* arXiv e-prints, arXiv:1701.02151, 2017.

Niikura, H., et al. *Constraints on Earth-mass primordial black holes from OGLE 5-year microlensing events.* Phys. Rev. D, 99 (8), 083503, 2019.

Padmanabhan, H. *Constraining the CO intensity mapping power spectrum at intermediate redshifts.* MNRAS, 475 (2), 1477–1484, 2018a.

Padmanabhan, H. *Constraining the evolution of CII intensity through the end stages of reionization.* arXiv e-prints, arXiv:1811.01968, 2018b.

REFERENCES

Percival, W.J., et al. *The 2dF Galaxy Redshift Survey: spherical harmonics analysis of fluctuations in the final catalogue.* MNRAS, 353 (4), 1201–1218, 2004.

Perlmutter, S., et al. *Measurements of* Ω *and* Λ *from 42 High-Redshift Supernovae.* Astrophys. J., 517 (2), 565–586, 1999.

Planck Collaboration, et al. *Planck 2013 results. XVI. Cosmological parameters.* Astron. Astrophys., 571, A16, 2014.

Planck Collaboration, et al. *Planck 2015 results. XIV. Dark energy and modified gravity.* A&A, 594, A14, 2016a.

Planck Collaboration, et al. *Planck 2015 results. XVI. Isotropy and statistics of the CMB.* A&A, 594, A16, 2016b.

Planck Collaboration, et al. *Planck 2016 intermediate results. LI. Features in the cosmic microwave background temperature power spectrum and shifts in cosmological parameters.* ArXiv e-prints, 2016c.

Planck Collaboration, et al. *Planck intermediate results. XLVI. Reduction of large-scale systematic effects in HFI polarization maps and estimation of the reionization optical depth.* A&A, 596, A107, 2016d.

Planck Collaboration, et al. *Planck 2018 results. VI. Cosmological parameters.* ArXiv e-prints, 2018.

Planck Collaboration, et al. *Planck 2018 results. IX. Constraints on primordial non-Gaussianity.* arXiv e-prints, arXiv:1905.05697, 2019.

Poulin, V., et al. *Early Dark Energy Can Resolve The Hubble Tension.* arXiv e-prints, arXiv:1811.04083, 2018a.

Poulin, V., et al. *Implications of an extended dark energy cosmology with massive neutrinos for cosmological tensions.* Phys. Rev D, 97, 123504, 2018b.

Prestage, R.M. *The Green Bank Telescope.* In *Society of Photo-Optical Instrumentation Engineers (SPIE) Conference Series*, vol. 6267 of *Society of Photo-Optical Instrumentation Engineers (SPIE) Conference Series*, 626712, 2006.

Pullen, A.R., et al. *Probing gravity at large scales through CMB lensing.* MNRAS, 449 (4), 4326–4335, 2015.

Pullen, A.R., et al. *Search for C II emission on cosmological scales at redshift Z*$\sim$*2.6.* MNRAS, 478 (2), 1911–1924, 2018.

Raccanelli, A., et al. *Lensing and time-delay contributions to galaxy correlations.* General Relativity and Gravitation, 48, 84, 2016.

Raccanelli, A., et al. *Future constraints on angle-dependent non-Gaussianity from large radio surveys.* Physics of the Dark Universe, 15, 35–46, 2017.

Raccanelli, A., et al. *Doppler term in the galaxy two-point correlation function: Wide-angle, velocity, Doppler lensing and cosmic acceleration effects.* Physics of the Dark Universe, 19, 109–123, 2018.

Raveri, M. *Reconstructing Gravity on Cosmological Scales.* arXiv e-prints, arXiv:1902.01366, 2019.

Renk, J., et al. *Galileon gravity in light of ISW, CMB, BAO and H_0 data.* JCAP, 2017 (10), 020, 2017.

Ricotti, M., et al. *Effect of primordial black holes on the cosmic microwave background and cosmological parameter estimates.* The Astrophysical Journal, 680 (2), 829, 2008.

Riess, A.G., et al. *Observational Evidence from Supernovae for an Accelerating Universe and a Cosmological Constant.* Astronom. J., 116 (3), 1009–1038, 1998.

Riess, A.G., et al. *A 3% Solution: Determination of the Hubble Constant with the Hubble Space Telescope and Wide Field Camera 3.* Astrophys. J., 730, 119, 2011. [Erratum: Astrophys. J.732,129(2011)].

Riess, A.G., et al. *A 2.4% Determination of the Local Value of the Hubble Constant.* ApJ, 826, 56, 2016.

Riess, A.G., et al. *Large Magellanic Cloud Cepheid Standards Provide a 1% Foundation for the Determination of the Hubble Constant and Stronger Evidence for Physics Beyond LambdaCDM.* arXiv e-prints, 2019.

Rigault, M., et al. *Confirmation of a Star Formation Bias in Type Ia Supernova Distances and its Effect on the Measurement of the Hubble Constant.* Astrophys. J., 802 (1), 20, 2015.

Rigault, M., et al. *Strong Dependence of Type Ia Supernova Standardization on the Local Specific Star Formation Rate.* arXiv e-prints, arXiv:1806.03849, 2018.

Salvaterra, R., et al. *Limits on the high redshift growth of massive black holes.* A&A, 545, L6, 2012.

Sasaki, M., et al. *Primordial Black Hole Scenario for the Gravitational-Wave Event GW150914.* Physical Review Letters, 117 (6), 061101, 2016.

Schmittfull, M., et al. *Modeling Biased Tracers at the Field Level.* arXiv e-prints, arXiv:1811.10640, 2018.

Scolnic, D.M., et al. *The Complete Light-curve Sample of Spectroscopically Confirmed SNe Ia from Pan-STARRS1 and Cosmological Constraints from the Combined Pantheon Sample.* Astrophys. J., 859 (2), 101, 2018.

Seljak, U. *Extracting Primordial Non-Gaussianity without Cosmic Variance.* Physical Review Letters, 102 (2), 021302, 2009.

Seo, H.J. & Eisenstein, D.J. *Probing Dark Energy with Baryonic Acoustic Oscillations from Future Large Galaxy Redshift Surveys.* Astrophys. J., 598 (2), 720–740, 2003.

Short, K., et al. *Shedding light into dark matter from the dark ages.* In preparation, 2019.

Silk, J. *Feedback by Massive Black Holes in Gas-rich Dwarf Galaxies.* Astrophys. J., 839 (1), L13, 2017a.

Silk, J. *Feedback by Massive Black Holes in Gas-rich Dwarf Galaxies.* Astrophys.

J. Letters, 839, L13, 2017b.

Silva, B.M., et al. *Tomographic intensity mapping versus galaxy surveys: observing the Universe in H α emission with new generation instruments.* MNRAS, 475 (2), 1587–1608, 2018.

Silva, M., et al. *Prospects for Detecting C II Emission during the Epoch of Reionization.* Astrophys. J., 806 (2), 209, 2015.

Silva, M.B., et al. *Intensity Mapping of Lyα Emission during the Epoch of Reionization.* Astrophys. J., 763 (2), 132, 2013.

Singh, S., et al. *Probing gravity with a joint analysis of galaxy and CMB lensing and SDSS spectroscopy.* MNRAS, 482 (1), 785–806, 2019.

Smoot, G.F., et al. *Structure in the COBE differential microwave radiometer first-year maps.* Astrophys. J. Letters, 396, L1–L5, 1992.

Square Kilometre Array Cosmology Science Working Group, et al. *Cosmology with Phase 1 of the Square Kilometre Array; Red Book 2018: Technical specifications and performance forecasts.* arXiv e-prints, arXiv:1811.02743, 2018.

Starobinsky, A.A. *How to determine an effective potential for a variable cosmological term.* Soviet Journal of Experimental and Theoretical Physics Letters, 68 (10), 757–763, 1998.

Sugiyama, N.S., et al. *Limits on statistical anisotropy from BOSS DR12 galaxies using bipolar spherical harmonics.* MNRAS, 473, 2737–2752, 2018.

Sun, G., et al. *A Foreground Masking Strategy for [C II] Intensity Mapping Experiments Using Galaxies Selected by Stellar Mass and Redshift.* Astrophys. J., 856 (2), 107, 2018.

Suyu, S.H., et al. *H0LiCOW - I. H_0 Lenses in COSMOGRAIL's Wellspring: program overview.* MNRAS, 468 (3), 2590–2604, 2017.

Tegmark, M., et al. *Karhunen-Loève Eigenvalue Problems in Cosmology: How Should We Tackle Large Data Sets?* Astrophys. J., 480, 22–35, 1997.

The Dark Energy Survey Collaboration & Abbott, T.M.C.e.a. *Dark Energy Survey Year 1 Results: Measurement of the Baryon Acoustic Oscillation scale in the distribution of galaxies to redshift 1.* ArXiv e-prints, 2017.

Tinker, J.L., et al. *The Large-scale Bias of Dark Matter Halos: Numerical Calibration and Model Tests.* Astrophys. J., 724 (2), 878–886, 2010.

Troxel, M.A., et al. *Dark Energy Survey Year 1 results: Cosmological constraints from cosmic shear.* Phys. Rev. D, 98 (4), 043528, 2018.

Vattis, K., et al. *Late universe decaying dark matter can relieve the H_0 tension.* arXiv e-prints, arXiv:1903.06220, 2019.

Verde, L., et al. *Planck and the local Universe: Quantifying the tension.* Physics of the Dark Universe, 2, 166–175, 2013.

Verde, L., et al. *The length of the low-redshift standard ruler.* MNRAS, 467, 731–736, 2017.

Villaescusa-Navarro, F. *Pylians: Python libraries for the analysis of numerical simulations.* ascl:1811.008, 2018.

Volonteri, M., et al. *The evolution of massive black hole seeds.* MNRAS, 383, 1079–1088, 2008.

Wilkinson, P.N., et al. *Limits on the Cosmological Abundance of Supermassive Compact Objects from a Search for Multiple Imaging in Compact Radio Sources.* Phys. Rev. Letters, 86 (4), 584–587, 2001.

Wilman, R.J., et al. *A semi-empirical simulation of the extragalactic radio continuum sky for next generation radio telescopes.* MNRAS, 388, 1335–1348, 2008.

Wilson, M.J. & White, M. *Cosmology with dropout selection: Straw-man surveys and CMB lensing.* arXiv e-prints, arXiv:1904.13378, 2019.

Wu, X.B., et al. *An ultraluminous quasar with a twelve-billion-solar-mass black hole at redshift 6.30.* Nature, 518, 512–515, 2015.

Xia, J.Q., et al. *Constraining primordial non-Gaussianity with high-redshift probes.* JCAP, 2010, 013, 2010.

Zel'dovich, Y.B. & Novikov, I.D. *The Hypothesis of Cores Retarded during Expansion and the Hot Cosmological Model.* Soviet Astronomy, 10, 602, 1967.

Zhu, F., et al. *Optimal redshift weighting for baryon acoustic oscillations.* MNRAS, 451 (1), 236–243, 2015.

Zumalacárregui, M. & Seljak, U. *Limits on Stellar-Mass Compact Objects as Dark Matter from Gravitational Lensing of Type Ia Supernovae.* Phys. Rev. Letters, 121 (14), 141101, 2018a.

Zumalacárregui, M. & Seljak, U. *Limits on Stellar-Mass Compact Objects as Dark Matter from Gravitational Lensing of Type Ia Supernovae.* Phys. Rev. Letters, 121 (14), 141101, 2018b.